



Fakultät für Maschinenwesen  
Lehrstuhl für Angewandte Mechanik

# **Multibody systems with lubricated contacts**

## *Cavitation, interface coupling, reduction and quasi-Newton techniques*

**Andreas Ludwig Krinner**

Vollständiger Abdruck der von der Fakultät für Maschinenwesen der Technischen Universität München zur Erlangung des akademischen Grades eines

**Doktor-Ingenieurs (Dr.-Ing.)**

genehmigten Dissertation.

**Vorsitzender:** Prof. Dr.-Ing. Georg Wachtmeister

**Prüfer der Dissertation:**

1. Prof. Dr. ir. Daniel Rixen
2. Assoc. Prof. Dr. ir. Ron van Ostayen

Die Dissertation wurde am 16. Januar 2018 bei der Technischen Universität München eingereicht und durch die Fakultät für Maschinenwesen am 6. April 2018 angenommen.



## Danksagung

Die vorliegende Dissertation entstand während meiner wissenschaftlichen Tätigkeit am Lehrstuhl für Angewandte Mechanik der Technischen Universität München im Zeitraum vom März 2013 bis April 2017. Ohne die Unterstützung einiger Leute wäre diese Arbeit nicht möglich gewesen.

An erster Stelle gilt mein Dank meinem Doktorvater Professor Daniel Rixen. Dein entgegengebrachtes Vertrauen, die eingeräumten Freiheiten und die fruchtbaren fachlichen Diskussionen trugen erheblich zum Entstehen dieser Arbeit bei. Ich schätzte Deine offene Art für Fragestellungen jeglicher Art und genoss die äußerst positive Atmosphäre am Lehrstuhl unter Deiner Leitung. Vielen Dank dafür!

Weiterhin möchte ich Professor Georg Wachtmeister für die Übernahme des Vorsitzenden der Prüfungskommission sowie Professor Ron van Ostayen für das intensive Interesse an meiner Arbeit und die Übernahme des Zweitgutachtens danken.

Mein gesonderter Dank gilt Thomas Thümmel für die stete Unterstützung während meiner Zeit am Lehrstuhl. Ich danke Dir für das in mich gesetzte Vertrauen und die Möglichkeiten, die du mir in Forschung und Lehre, aber auch in verschiedensten Industrieprojekten eröffnet hast.

Die zahlreichen Kollegen, die mich in meiner Zeit am Lehrstuhl begleitet haben, werde ich in bester Erinnerung behalten. Ich bin nicht nur dankbar für die stets positive fachliche Zusammenarbeit, sondern auch für die schönen Erlebnisse rund um den Lehrstuhl. Einzelnen Personen möchte ich besonders danken: Thorsten Schindler danke ich für die fachliche Unterstützung und das Korrekturlesen meiner Dissertation. Meinem Bürokollegen Markus Roßner danke ich für die Unterstützung vor allem zu Beginn meiner Zeit am Lehrstuhl und seine wertvollen Antworten zu fachlichen und außerfachlichen Themen. Michael Häußler danke ich ebenfalls für die schöne gemeinsame Zeit im Büro sowie für das Korrekturlesen meiner Dissertation. Der Rotordynamik Gruppe um Christian Wagner und Johannes Maierhofer danke ich für die lebhaften und zahlreichen Diskussionen. Der elf-Uhr-Mensa-Gruppe um Christian Wagner, Oliver Hofmann, Michael Leistner und Fabian Gruber danke ich dafür, dass der tägliche Mensabesuch nicht nur ein kulinarisches Highlight war.

Weiterhin bedanke ich mich bei all den Studenten, die in Form von Studienarbeiten oder hilfswissenschaftlichen Tätigkeiten ihren Beitrag zu dieser Arbeit geleistet haben.

Tiefe Dankbarkeit empfinde ich für die Unterstützung, die ich Zeit meines Lebens durch meine Eltern Elisabeth und Hans-Jörg sowie meine Brüder Maximilian und Sebastian erfahren habe. Die Gewissheit um Eure Unterstützung ist von unschätzbarem Wert.

München, Mai 2018

Andreas Krinner

## Abstract

Elastohydrodynamic lubricated contacts occur in various machine elements and allow for a wear resistant power transmission while motion of rolling elements is present. Their accurate modeling and simulation enables better system and component designs with respect to lifetime, wear, vibration and material.

This work treats numerical methods for a more efficient simulation of multibody systems with elastohydrodynamic contacts. It deals with a stationary and a mass-conservative cavitation model, which are reformulated using methods of convex analysis. It suggests a monolithic solution strategy for the coupled problem of mechanic and hydrodynamic equations. A quasi-Newton method is analyzed as a solution technique. Different interface coupling methodologies are investigated for non-conforming fluid and structural meshes for the elastohydrodynamic problem and a novel load dependent approach is developed to reduce the elastic degrees of freedom of the lubricated interfaces. Numerical examples as well as an experimental validation of a rotor test rig demonstrate the applicability of the developed calculation methods.

---

## Zusammenfassung

Elastohydrodynamisch geschmierte Kontakte treten in einer Vielzahl von Maschinenelementen auf und ermöglichen die reibungsarme Übertragung von Kräften und Momenten bei vorhandener Bewegung von Wälzkörpern. Ihre detaillierte Abbildung in der Simulation ermöglicht eine verbesserte Auslegung von Systemen und Komponenten hinsichtlich Lebensdauer, Verschleiß, Schwingungsverhalten und Material.

Diese Arbeit behandelt numerische Methoden für die effiziente Simulation von Mehrkörpersystemen mit elastohydrodynamischen Kontakten. Behandelt werden ein stationäres sowie ein masse-erhaltendes Kavitationsmodell, welche mit Hilfe der konvexen Analysis neu formuliert werden. Es wird ein monolithischer Lösungsansatz für das mechanisch-hydrodynamisch gekoppelte System vorgeschlagen. Als Lösungstechnik wird u. a. eine quasi-Newton Methode untersucht. Verschiedene Kopplungsmethoden für nicht-konforme Fluid- und Strukturnetze für das elastohydrodynamische Problem werden analysiert und ein neuer Ansatz zur Reduktion der Schnittstellenfreiheitsgrade der geschmierten Oberflächen entwickelt. Numerische Beispiele sowie ein experimenteller Abgleich eines Rotorprüfstandes verdeutlichen die Anwendbarkeit der entwickelten Berechnungsmethoden.



# Table of Contents

<b>Table of Contents</b>	<b>v</b>
<b>Lists</b>	<b>ix</b>
<b>1 Introduction</b>	<b>1</b>
1.1 State-of-the-art in elastohydrodynamic lubrication . . . . .	2
1.1.1 General developments . . . . .	2
1.1.2 Solution strategies and methods . . . . .	5
1.2 Aim and outline of this work . . . . .	6
<b>2 The elastohydrodynamic lubricated contact</b>	<b>9</b>
2.1 REYNOLDS equation . . . . .	9
2.2 Numerical discretization . . . . .	12
2.2.1 Finite element (FE) discretization . . . . .	12
2.2.2 FE stabilization . . . . .	15
2.3 Cavitation conditions . . . . .	17
2.3.1 Review on cavitation models . . . . .	17
2.3.2 FE solution of the SWIFT-STIEBER cavitation condition . . . . .	21
2.3.3 FE solution of the mass-conservative JFO cavitation condition . . . . .	27
2.4 Kinematics and forces in the fluid film . . . . .	29
2.4.1 Fluid film kinematics . . . . .	29
2.4.2 Fluid film forces . . . . .	33
2.5 Extended REYNOLDS equation and mixed lubrication . . . . .	34
2.5.1 Mixed lubrication . . . . .	35
2.5.2 Inertia effects . . . . .	35
2.5.3 Temperature effects . . . . .	36
2.6 Numerical examples . . . . .	37
2.6.1 SWIFT-STIEBER condition: comparison of cavitation algorithms . . . . .	37
2.6.2 JFO condition: validation with solution from the literature . . . . .	39
2.6.3 SWIFT-STIEBER condition: SUPG stabilization . . . . .	39
<b>3 Coupled system</b>	<b>41</b>
3.1 Multi-body system dynamics with lubricated contacts . . . . .	41
3.1.1 Rigid body motion . . . . .	42
3.1.2 Flexible multibody dynamics . . . . .	43
3.1.3 Coupled system equations . . . . .	46
3.2 Interface coupling methodologies . . . . .	48
3.2.1 Consistent and conservative coupling strategy . . . . .	48
3.2.2 Transfer methods . . . . .	50
3.3 Discretized form . . . . .	53
3.4 Numerical example . . . . .	56

<b>4</b>	<b>Interface reduction methods</b>	<b>63</b>
4.1	CRAIG BAMPTON reduction method . . . . .	64
4.2	Two-step CRAIG BAMPTON method . . . . .	65
4.3	Dual reduction approach . . . . .	66
4.4	Numerical applications . . . . .	69
4.4.1	Simulation example 1: flexible slider-crank mechanism . . . . .	69
4.4.2	Simulation example 2: elastic rotor in flexible journal bearing . . . . .	72
4.4.3	Concluding remarks . . . . .	75
<b>5</b>	<b>Time integration and solution techniques</b>	<b>77</b>
5.1	Formulations and time discretization . . . . .	78
5.1.1	Partitioned formulation . . . . .	79
5.1.2	DAE formulation by projection function . . . . .	82
5.1.3	DAE formulation for mass-conservative cavitation condition . . . . .	84
5.2	Numerical Example . . . . .	87
5.2.1	Comparison of IQN-ILS and simplified Newton: partitioned formulation . . . . .	89
5.2.2	Comparison partitioned formulation and DAE formulation: simplified Newton . . . . .	90
5.2.3	Comparison partitioned formulation and DAE formulation: IQN-ILS . . . . .	91
5.2.4	DAE formulation with mass-conservative cavitation . . . . .	92
5.2.5	Time convergence and scaling . . . . .	93
5.2.6	Concluding remarks . . . . .	94
<b>6</b>	<b>Numerical-experimental case studies</b>	<b>95</b>
6.1	Slider-crank mechanism revised . . . . .	95
6.2	Experimental validation of a rotor test rig . . . . .	100
6.3	EHL point contact . . . . .	107
<b>7</b>	<b>Conclusion and outlook</b>	<b>111</b>
7.1	Summary . . . . .	111
7.2	New contributions . . . . .	112
7.3	Conclusions . . . . .	112
7.4	Recommendations for future work . . . . .	113
<b>A</b>	<b>Derivation of the REYNOLDS equation</b>	<b>115</b>
<b>B</b>	<b>Finite element shape functions</b>	<b>117</b>
B.1	Dual bi-linear LAGRANGE shape functions . . . . .	117
B.2	Modified bi-quadratic serendipity shape functions . . . . .	117
B.3	Dual bi-quadratic serendipity shape functions . . . . .	118
<b>C</b>	<b>Finite element discretization of the mass-conservative cavitation problem</b>	<b>119</b>
C.1	Standard-GALERKIN discretization . . . . .	119
C.2	PETROV-GALERKIN discretization . . . . .	121
<b>D</b>	<b>Kinematics for cylindrical joint</b>	<b>123</b>
<b>E</b>	<b>Parameter for simulaton examples</b>	<b>125</b>
E.1	Simulation example of Section 2.6.1 . . . . .	125
E.2	Simulation example of Section 2.6.2 . . . . .	125
E.3	Simulation example of Section 2.6.3 . . . . .	125

---

<b>F Solution techniques</b>	<b>127</b>
F.1 Scheme of solution strategy for DAE formulation with IQN-ILS method .	127
<b>References</b>	<b>141</b>



# Lists

## Abbreviations

<b>CMS</b> component mode synthesis	<b>MBS</b> multibody system
<b>DAE</b> differential algebraic equation	<b>NBC</b> NEUMANN boundary condition
<b>DBC</b> DIRICHLET boundary condition	<b>NCP</b> nonlinear complementarity problem
<b>DOF</b> degree of freedom	<b>NN</b> nearest neighbor
<b>EHL</b> elastohydrodynamic lubricated	<b>NNPro</b> nearest neighbor projected
<b>FDM</b> finite difference method	<b>SUPG</b> streamline upwind PETROV-GALERKIN
<b>FE</b> finite element	
<b>FEM</b> finite element method	<b>TEHL</b> thermal elastohydrodynamic lubricated
<b>FFR</b> floating frame of reference	<b>THL</b> thermal hydrodynamic lubricated
<b>FSI</b> fluid structure interaction	
<b>IQN-ILS</b> interface quasi Newton - inverse least squares	<b>VI</b> variational inequality
<b>JFO</b> JACOBSSON-FLOBERG-OLSSON	<b>WR</b> weighted residual
<b>LCP</b> linear complementarity problem	<b>wrt.</b> with respect to

## Figures

1.1	Different machine elements with lubricated contacts from [85]. . . . .	3
1.2	Schematic overview of EHL simulation and outline of topics addressed in this thesis. . . . .	7
2.1	Notations in the lubricated contact. . . . .	10
2.2	Cavitation conditions. . . . .	18
2.3	Pressure and density distribution in a bearing with JFO condition (assuming incompressible fluid behavior and $p_c = 0$ ) . . . . .	20
2.4	NCP and regularized NCP . . . . .	23
2.5	Projection function. . . . .	27
2.6	Notations in the lubricated contact. . . . .	30
2.7	Kinematics in cylindrical journal bearing. . . . .	31
2.8	Kinematics in the EHL point contact. . . . .	33
2.9	Pressure distribution for eccentric journal bearing. . . . .	38
2.10	Convergence of the discretization error for NCP and penalty formulation using quadratic finite elements. . . . .	38

2.11	Distributions of pressure and film content in angular direction of a grooved journal bearing. . . . .	39
2.12	Numerical pressure solution with and without SUPG stabilization in angular direction of a journal bearing. . . . .	40
3.1	Kinematics and external forces in floating frame of reference formulation. . . . .	43
3.2	Computational domains for the coupled system. . . . .	47
3.3	Discretized surfaces and computational domain for the coupled system. . . . .	49
3.4	Simulation example of a rigid shaft in a flexible bearing. . . . .	56
3.5	Convergence of discretization error for pressure on fluid and deformation on structural mesh respectively, using matching meshes. . . . .	58
3.6	Convergence of the discretization error of the pressure on the fluid and the deformation on the structural mesh respectively, for non-matching meshes with <b>consistent</b> coupling technique. . . . .	59
3.7	Convergence of the discretization error of the pressure on the fluid and the deformation on the structural mesh respectively, for non-matching meshes with <b>conservative</b> coupling technique. . . . .	60
3.8	Convergence of the discretization error in the pressure on the structural mesh for non-matching meshes with different coupling techniques. . . . .	61
3.9	Pressure distributions on the structural mesh for different coupling techniques. . . . .	62
4.1	Pressure distributions for infinitely long (middle) and infinitely short bearing (right), computed in a discrete $(FX, FZ)$ -plane (left). . . . .	68
4.2	Slider-crank mechanism with flexible connecting rod and lubricated joint. . . . .	69
4.3	Reference solution with (M3) by using $P_{c,1} = I_{cc}$ , $n_r = 60$ residual modes and $n_v = 6$ vibration modes. . . . .	70
4.4	CRAIG BAMPTON scheme (M1). . . . .	71
4.5	Two-step CRAIG BAMPTON scheme (M2). . . . .	71
4.6	Load dependent reduction scheme (M3) with $P_{c,2}^S$ ( $p_m = 1$ and $p_0 = 1.5$ ). . . . .	72
4.7	Elastic rotor with unbalance in flexible journal bearing. . . . .	73
4.8	Comparison of the three reduction methods, each with 30 overall modes. . . . .	74
4.9	Comparison of the three reduction methods, each with 50 overall modes. . . . .	74
5.1	Maximal pressure (left) and orbit (right) for steady-state and mass-conservative cavitation model. . . . .	87
5.2	Pressure distribution for steady-state cavitation model at $t = 0.0067$ s. . . . .	88
5.3	Pressure (left) and density (right) distribution for mass-conservative cavitation model at $t = 0.0067$ s. . . . .	88
5.4	Comparison of number of iterations of simplified Newton and IQN-ILS for partitioned formulation. . . . .	89
5.5	Comparison of partitioned formulation and DAE formulation using simplified Newton. . . . .	90
5.6	Comparison of number of iterations of partitioned formulation and DAE formulation using IQN-ILS method. . . . .	91
5.7	Comparison of the number of iterations of simplified Newton and IQN-ILS method for DAE formulation with mass-conservative cavitation condition. . . . .	92
5.8	Decay of time discretization error for system with SWIFT-STIEBER and JFO cavitation condition, respectively. . . . .	93
5.9	Decay of time discretization error for system with JFO cavitation condition for different time-stepping schemes. . . . .	94
5.10	Condition number for system with SWIFT-STIEBER cavitation condition. . . . .	94

6.1	Slider-crank mechanism with flexible connecting rod and lubricated joint.	96
6.2	Comparison of simulation outputs for different fluid and rod models. . . . .	97
6.3	Comparison of pressure distributions of SWIFT-STIEBER and JFO model at $t = 2.4 \text{ ms}$ . . . . .	97
6.4	Comparison of simulation outputs with pressure dependent fluid properties.	98
6.5	Influence of contact pressure on simulation outputs. . . . .	99
6.6	Contour plot of maximal contact pressure during simulation. . . . .	99
6.7	Density distribution with and without SUPG stabilization. . . . .	99
6.8	Equilibrium eccentricity $e$ in dependency of rotational speed $\Omega$ . . . . .	100
6.9	Rotor test rig with journal bearings. . . . .	101
6.10	LAVAL rotor with misalignment, preload force and fluid forces. . . . .	102
6.11	Measured and simulated curve of equilibrium positions with misalignment parameter $a = [-0.15 \text{ mm}, 0.07 \text{ mm}]$ . . . . .	104
6.12	Calculated and measured stiffness and damping coefficients for different rotational speeds. . . . .	104
6.13	Rotor orbits due to unbalance at $\Omega = 21 \text{ rps}$ . . . . .	105
6.14	Elastic half space for EHL point contact. . . . .	108
6.15	Profiles of pressure and fluid film height at $\bar{z} = 0$ for EHL point contact. . . . .	108
6.16	Pressure distribution and elastic deformation of EHL point contact. . . . .	109
6.17	Convergence of the error of the residual. . . . .	109
B.1	Dual bi-linear LAGRANGE shape functions. . . . .	117
B.2	Modified bi-quadratic serendipity shape functions. . . . .	117
B.3	Dual bi-quadratic serendipity shape functions. . . . .	118
E.1	Simulation example of journal bearing with fixed eccentricity. . . . .	125
E.2	Simulation example of grooved journal bearing with fixed eccentricity. . . . .	126
F.1	Scheme of solution strategy with IQN-ILS method and reduced Jacobian for DAE formulation for a given time step. . . . .	127

## Tables

2.1	Comparison of cavitation algorithms for SWIFT-STIEBER condition. . . . .	37
3.1	Simulation parameters for the rigid shaft in a flexible bearing. . . . .	57
3.2	Shape functions for the different fields on the fluid and structural mesh, respectively. . . . .	58
4.1	Simulation parameters for the slider crank mechanism. . . . .	70
4.2	Simulation parameters for the elastic rotor in flexible journal bearing. . . . .	73
5.1	Comparison of the number of iterations and the computational time for the partitioned formulation. . . . .	89
5.2	Comparison of the number of iterations and the computational time for the partitioned and DAE formulation with simplified Newton solution technique. . . . .	90
5.3	Comparison of the number of iterations and the computational time for partitioned formulation and DAE formulation with IQN-ILS solution technique. . . . .	91

---

5.4	Comparison of the number of iterations and the computational time for simplified Newton and IQN-ILS method for DAE formulation with mass-conservative cavitation condition. . . . .	92
6.1	Properties of the test rig. . . . .	101
6.2	Simulation time for the different rotor models. . . . .	106
6.3	Parameter for simulation example of EHL point contact. . . . .	107
E.1	Parameter for simulation example of journal bearing with fixed eccentricity.	125
E.2	Parameter for simulation example of grooved journal bearing with fixed eccentricity. . . . .	126
E.3	Parameter for simulation example of journal bearing with fixed eccentricity.	126

# Chapter 1

## Introduction

Since decades, contacts between two or multiple bodies is a demanding task in mechanical engineering research. Adequate models have to cover the fundamental contact physics and mathematical methods are needed in order to calculate the dynamic systems behavior or contact characteristics like normal and friction forces, contact stiffnesses, local deformations or stress distributions. An experimental verification with accurate measuring devices has to prove the physical principles and mathematical results. In contact mechanics, this research process is an ongoing task. [149]

In a general view, two types of contacts can be classified: the dry and the lubricated contact.

On the field of the dry contact, also known as solid-to-solid contact, differences in the modeling can be found, depending on the admittance of small penetrations of the contacting bodies or not. HERTZ was the first to develop analytical solutions for a dry contact by admitting small penetrations, by which he derived the local deformation of the surfaces and the resulting contact pressure [84]. By this, he opened a wide field of research. Usually in this modeling approach, a contact stiffness characterizes a single-valued relation between force and penetration. The use of single-valued functions was also adapted to friction force laws, even if their physics is non-smooth, e. g. looking at the COULOMB friction model. In the opposite case, when the dry contact is assumed to be ideal and no local penetration is admitted, a new field of contact mechanics arises, as now the relation between contact force and gap becomes set-valued. For example, a contact stiffness is not needed any more and non-smooth friction force laws fit well into this framework. Both approaches are motivated by a different physics and philosophy and require a different mathematical and numerical treatment. As an example, the non-smooth behavior of dynamical systems is described by methods of the convex analysis, see for instance [1, 69, 145].

The hydrodynamic lubricated contact is characterized by a thin fluid film between the contacting bodies. This contact is said to be elasto-hydrodynamic lubricated (EHL), when the pressure in the fluid film is affected by the elastic deformation of the contacting surfaces. REYNOLDS derived in 1886 a partial differential equation in order to describe the pressure distribution in the fluid film [156]. In the following years, efforts were made to derive analytical solutions for an (elasto-)hydrodynamic lubricated contact and to get relations between force and local body approach, similar to the classical HERTZ contact model. However, an analytical solution can only be found in special cases. In the general case, a numerical solution is needed.

There is a strong need for more accurate and more efficient modeling of hydrodynamic lubricated contacts, for instance to have better designs with longer lifetime and lower losses, to avoid unstable behavior leading to noise or catastrophic failures or to have optimized geometries and materials saving weight and costs. A detailed numeri-

cal calculation of the pressure distribution in an oil film can be a time-consuming task and can affect heavily the overall simulation time of a mechanical system with lubricated contacts. For instance, current modeling approaches lead to solution times of the order of days when complex hydrodynamic bearings are involved. Therefore, this thesis is aimed at the efficient numerical treatment of such systems by developing appropriate numerical methods and solution techniques. It will be seen that mathematical formulations and numerical methods from the single-valued but also from the set-valued modeling approach of dry contacts are applicable during the simulation of lubricated contacts.

In the following, the state-of-the-art techniques in modeling and simulation of EHL contacts are outlined (Section 1.1). On this basis, the aim and outline of this work is stated in Section 1.2.

## 1.1 State-of-the-art in elastohydrodynamic lubrication

This section summarizes the fundamental developments on the field of elastohydrodynamic lubrication. While Section 1.1.1 gives a general overview on developments in the simulation of EHL contacts, Section 1.1.2 addresses the specific state-of-the-art techniques in the modeling and simulation process.

### 1.1.1 General developments

Mainly, the research field of EHL contacts can be grouped into two parts: on the one hand, there is a research field focused on the classical EHL problem of a local line or point contact. It is characterized by non-conformal surface geometries, meaning that the *local* elastic deformation due to compression has a main influence on the pressure distribution. Such contacts occur e. g. in gear boxes or ball and roller bearings. On the other hand, many researchers are focused on investigations of hydrodynamic bearings, e. g. for automotive applications or rotor systems. The surface geometry of hydrodynamic bearings is conformal. It means that the *global* elastic deformation affects the pressure distribution [22]. Figure 1.1 shows a journal bearing as an example for conformal contact surfaces. Besides, a ball bearing as well as a gear wheel contact represent examples for contacts with non-conformal surfaces.

Developments on both research areas, addressing different issues of the specific problem, contributed to the current status quo in modeling and simulation of EHL contacts. In the following, a literature overview is given by highlighting the most important milestones of the history of EHL contacts. The overview is divided in a first part, addressing the developments on the field of EHL line and point contact problems and a second part focusing on the developments on the field of bearing simulation and cavitation modeling. It has to be noted that since 1886, when REYNOLDS derived the famous equation for thin film lubrication, a huge number of research articles and text books were published on the field of EHL contacts and hence, only a small amount of the existing literature can be referenced in this work.

### EHL line and point contact

For a detailed overview on the history of elastohydrodynamics and tribology, it is referred to the articles of SPIKES [177], of SCHOUTEN and LEEUWEN [168] or the textbook of DOWSON [50]. In these references, also the experimental developments are described, while here, the focus is on theoretical and numerical developments.

The work of ERTEL [126] of the year 1944 is referred as the origin of the EHL problem, see for instance [150]. He was the first to find an approximation of the minimum film height in the EHL line contact valid for heavy loads.

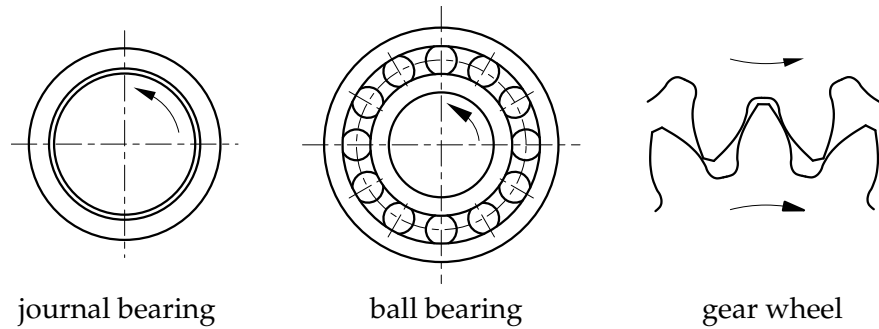


**Figure 1.1:** Different machine elements with lubricated contacts from [85].

In 1959, the first numerical solution by DOWSON and HIGGINSON [47] confirmed the results of ERTEL. Further, they derived approximative formulas for the minimum film height in the EHL line contact for different parameter sets. Later, MOES generalized these formulas by treating the dimensionless problem [125].

Investigations of ARCHARD et. al. [7] contributed to the understanding of the EHL point contact problem. In 1976, HAMROCK and DOWSON [80] published an extensive study of elliptical EHL point contacts providing a numerical solution as well as approximative formulas for the minimum film height.

As a milestone in the development of EHL contacts, the work of CHENG and STERN-LICHT [33] has to be mentioned, in which they included temperature effects into the REYNOLDS equation by solving an additional energy equation. In the same way, the articles of PATIR and CHENG [142] and CONRY et. al. [36] are regarded as origins in the treatment of surface roughness and non-NEWTONIAN fluid behavior, respectively.

In the 80s and 90s, various improvements in the numerical solution of the EHL line and point contacts were achieved. As will be seen later, the numerical solution suffers from instabilities in the high pressure regime. By the so-called inverse method developed by EVANS and SNIDLE [56] and later refined by HUGHES et. al. [90], first stable numerical solutions were achieved.

The great milestone towards a fast and stable solution was the successful application of a multi-level multi-grid discretization to the EHL problem by LUBRECHT [121] and VENNER [192]. WIJNANT [199] uses and enhances these methods for a thorough numerical and experimental study of the circular point contact.

In this context, the differential deflection method outlined by HUGHES et. al. [91] in the year 2000, has to be mentioned as a further approach towards a stable and efficient solution of the EHL problem.

The first numerical solutions were calculated by using the finite difference method (FDM). In 1972, TAYLOR and O'CALLAGHAN [186] were the first to apply the finite element method (FEM) to the EHL problem. Nowadays, the FEM is used by many researchers, see for instance ROHDE and OH [160] or HABCHI et. al. [77]. An extensive study of the FEM including stabilization techniques is shown by HABCHI et. al. [74]. Further, the discontinuous GALERKIN method is also applied to the EHL problem, see LU et. al. [120] or YANG and LAURSEN [209].

In the recent years, researchers are seeking for model-order reduction techniques for the EHL line and point contact problem. For instance, HABCHI et. al. [75] and HABCHI [73] apply "well-defined precomputed basis function" for the reduction of the elastic structure. In [76], HABCHI and ISSA apply a static condensation technique to the EHL problem. MAIER et. al. [122] treat the complete coupled problem and use techniques like a proper orthogonal decomposition to reduce the system size. In [123], the same authors apply a so-called trajectory piecewise linear method to the EHL line contact problem.

## Hydrodynamic bearings and cavitation

A wide range of relevant literature exists on the fundamentals of hydrodynamic bearings: fundamentals of fluid film bearings can be found in the text books of HAMROCK et.al. [81], SZERI [184] or BONNEAU et.al. [17]. The design and characteristics of journal bearings are addressed by the books of LANG and STEINHILPER [116] or SOMEYA [174]. Bearing design with special focus on combustion engines is the focus of the text books of BONNEAU et.al. [18] or ALLMAIER et.al. [5]. Further, the review article of BOOKER et.al. [22] gives a detailed overview on the most important literature concerning conformal EHL contacts for engine bearings. ALLMAIER and OFFNER outline in their review article [6] challenges and frontiers of EHL bearing simulation and summarize existing numerical solution methods.

Typical issues, which are analyzed in these text books, articles and their references are [22]: cavitation, thermal effects, surface roughness effects, fluid pressure-viscosity effects, fluid non-NEWTONIAN effects, fluid and structural inertia effects and experimental methods.

In the following, a short overview on the developments of the theory of hydrodynamic bearings is given, with special focus on cavitation modeling, since later in this work, this topic will be treated in more depth.

The early developments on the field of hydrodynamic (journal) bearings are closely related to the researchers TOWER [191], REYNOLDS [156], STRIBECK [180], SOMMERFELD [176], GUEMBEL [72] and VOGELPOHL [194].

In 1965, an eminent contribution on the dynamic characteristics of journal bearings was the mobility method of BOOKER [20]. Further, the works of GLIENICKE [68] and SOMEYA [175] account for bearing characteristics and studies on the stability of rotor systems with journal bearings.

In 1973, the work of OH and HUEBNER [137] marked the beginning of the detailed 3D-simulation of EHL bearings.

Since ever, the modeling and simulation of cavitation in hydrodynamic bearings was of great interest. DOWSON and TAYLOR [49] and BRAUN [25] outline detailed reviews on this topic.

The early researchers applied a cavitation condition proposed by GUEMBEL [72] by simply cutting off negative pressures in the numerical solution. A more sophisticated cavitation model, which offers mass-conservation at the cavitation boundary, was proposed by SWIFT [183] and STIEBER [179]. In 1941, CHRISTOPHERSEN [34] outlined a first numerical solution for this cavitation problem. Further, a mass-conservative cavitation condition was proposed by JACOBSSON [93], FLOBERG [59] and OLSSON [139]. In 1974, a first cavitation algorithm based on this concept was proposed by ADAMS and ELROD [55]. Its numerical implementation with a finite difference scheme resulted in the popular ELROD algorithm [54].

A further milestone in the cavitation modeling was the article of GOENKA [70]. In that, a cavitation algorithm for the cavitation model of SWIFT and STIEBER is proposed, which is based on a formulation as a linear complementarity problem, which was originally stated by KOSTREVA [99] and OH [135].

In 1991, KUMAR and BOOKER [111] proposed a mass-conservative cavitation algorithm for a finite element discretization for the formulation of ADAMS and ELROD. For its solution, they make use of the algorithm of GOENKA.

Over the years, further mass-conservative cavitation algorithms were proposed. Examples are the articles of GIACOPINI et.al. [67] or WOLOSZYNSKI et.al. [204], who both solve the linear complementarity problem of the cavitation problem in different ways. Further, there are modified formulations of the original formulation of ELROD for a more efficient solution process, see VIJAYARAGHAVAN and KEITH [193] or ALAKHRAMSING

et. al. [3]. A commonly used approach is to regularize the cavitation problem, as done for instance by NOWALD et. al. [132] or NITZKSCHE et. al. [129]

Nowadays, the full transient analysis of combustion engines with EHL journal bearings, including cavitation, surface roughness and/or thermal effects is state-of-the-art, see for instance [98, 112, 136, 157, 167, 200]. In the same way, rotor systems like turbo-charger are analyzed fully dynamically with either steady-state or mass-conservative cavitation models, see for instance [52, 53, 130, 169, 205].

### 1.1.2 Solution strategies and methods

The numerical methods, which are applied for the solution of EHL problems, are now outlined.

An important issue concerning the simulation of EHL problems is the strong nonlinearity between pressure and film height, specifically at high pressures, when the local deformation is not negligible. In literature, different solution strategies and techniques are applied during the solution process. They are reviewed in the following.

In the early simulations, the researchers used direct iteration methods and followed a partitioned solution strategy. This means that first, for a given deformation, a pressure distribution is calculated, which is then imposed via forces on the elastic structure. These steps are repeated until convergence is achieved. For instance, STAFFORD et. al. [178] and LABOUFF and BOOKER [112] use this classical approach for EHL bearing simulation. For EHL line contacts, the article of TAYLOR and O'CALLAGHAN [186] is a classical reference.

Since this original approach suffered from stability problems at high pressures [186], a full-system approach was followed for a stronger coupling. In this, pressure and deformation are updated simultaneously and therefore, it is also known as monolithic solution strategy. In 1977, this approach in combination with a Newton-Raphson scheme was first applied by OH and ROHDE [138] for EHL point contacts. Later, many researchers followed this approach, see for instance ELCOATE et. al. [51] or HUGHES et. al. [90]. In the same way, the full-system approach was applied in the EHL bearing simulation process. Again, OH [135] can be seen as the pioneer by applying the full-system approach in combination with a Newton scheme. Further, the work of MCIVOR [124] contributed to a fast convergence of the Newton-Raphson method in bearing simulation.

Nowadays, the use of the Newton method is the state-of-the-art technique to solve EHL problems. An exception is the article of PROFITO et. al [154], in which the authors apply a quasi-Newton method for the static solution of an EHL bearing problem.

A further issue in EHL simulation is the incorporation of an adequate cavitation condition in the iterative solution process of the EHL problem. It is accomplished in different ways in the literature.

The original strategy is to fulfill the stationary SWIFT-STIEBER cavitation condition during a GAUSS-SEIDEL relaxation of the pressure equation as it was proposed by CHRISTOPHERSON [34] in 1941. Examples are the articles of ROHDE and OH [160] or HUGHES et. al. [90].

With the outline of the ELROD algorithm [54], detailed solutions of transient problems with mass-conservative cavitation condition were possible, e. g. in the work of WIJNANT [199].

An often used approach for EHL line and point contacts is to use a penalization of the pressure in order to obtain positive pressure values. This penalization is usually combined with a full-system approach and a Newton method, see HABCHI et. al. [78] or AHMED et. al. [2].

A sophisticated task is the treatment of EHL contacts in a multibody simulation. Here, the dynamics of rigid and elastic bodies interacts with the hydrodynamics, while connecting links, constraints and external forces need to be considered.

The state-of-the-art technique for the incorporation of elastohydrodynamic revolute joints in multibody systems uses a nonlinear force element, in which the hydrodynamic pressure is calculated numerically [61, 189]. Hence, the solution strategy is usually partitioned. Commercial multibody simulation programs also follow this partitioned approach for the coupling of hydrodynamic and mechanical equations [115, 134].

A further partitioned approach for the coupled simulation is the use of co-simulation techniques. In [31], BUSCH and SCHWEIZER propose a semi-implicit coupling approach with a reduced computational effort for the Jacobian calculation. They treat a turbocharger system as an example and couple a commercial multibody simulation code with a commercial finite element code for the fluid film bearing calculation.

The large demand for simulation tools in research and industry becomes evident, when looking at the variety of existing commercial software tools. Nowadays, software tools like *First*, *Excite*, *Simpack* or *Madyn 2000* cover a broad spectrum of applications and services. It is noteworthy that the latter software tool was originally developed by the research association FVV and includes the former bearing calculation tool *Alp3t* [63, 165].

## 1.2 Aim and outline of this work

Despite the already existing various simulation tools for EHL problems, including sophisticated numerical methods, there are still challenges and frontiers in the EHL simulation, see ALLMAIER and OFFNER [6]. This thesis aims at a unified treatment of EHL contacts as well as the development of numerical methods contributing to a more efficient simulation. These methods are applicable to the EHL line or point contact problem in the same way as to the coupled dynamic problem of a multibody system including EHL bearings. In detail, following issues are part of this work:

**Cavitation problem** The cavitation conditions in hydrodynamics show interesting parallels to the non-penetration condition of unilateral contacts of classical contact mechanics. Following the works of WOHLMUTH [202] and POPP [151], who treat mechanical contacts in great detail, a variational consistent discretization is outlined also for the cavitation problem. Modern methods like the use of dual LAGRANGE multipliers are applied. Two classical cavitation conditions are treated, namely the SWIFT-STIEBER and the JACOBSSON-FLOBERG-OLSSON condition. For the solution of the cavitation problems, a formulation by a projection function from convex analysis is proposed. Applying a semi-smooth Newton method results in a new cavitation algorithm.

**Interface coupling** The pressure in the oil film and the elastic deformation of the surfaces can be discretized on non-conforming meshes. The reason for non-conforming meshes can be for instance, the use of different simulation codes for mechanics and hydrodynamics. This work addresses the problem of interface coupling and applies different methods from fluid-structure interaction for the transfer of surface tractions and deformations. Consistent and conservative coupling methodologies based on the work of DEBOER [42] are analyzed and compared with each other for the EHL problem.

**Interface reduction** In the simulation of EHL contacts, a large number of elastic degrees of freedom is necessary in order to cover the elastic deformation of the interface. This leads to a large number of overall degrees of freedom of a mechanical system and influences strongly the simulation time, specifically in a dynamic analysis. So far, classical reduction methods based on interface deformation are used in order to decrease the number of elastic degrees of freedom of the interface. In this work,

reduction methods also based on interface loading are outlined and their applicability is analyzed for different simulation examples. This dual approach can be well adapted to specific pressure distributions arising for instance in EHL bearings.

**Solution strategies and quasi-Newton method** The state-of-the-art solution strategy for EHL problems is partitioned. In case the problem is handled as monolithic, a penalization of the cavitation condition is usually used in order to get a nonlinear residual, which is then solved by a Newton-Raphson scheme. This work proposes a monolithic solution strategy with an exact fulfillment of the cavitation conditions. It is possible by the use of the projection function introduced for the cavitation problem. Further, a quasi-Newton method of DEGROOTE et. al. [43] is applied in modified form for the solution of the coupled dynamic problem. The benefits of using the projection formulation as well as the quasi-Newton method will be outlined.

Along these major topics, this thesis outlines a finite element discretization of the REYNOLDS equation including a consistent upwind stabilization technique for both the steady-state as well as the transient case. The developed numerical methods are applied to simulation examples. In addition, an experimental study proves the validity of the simulation program and gives insights into experimental validation.

In Fig. 1.2, a schematic overview shows the structure of a classical EHL simulation. It is characterized by a mechanical system and a fluid model, which both have to be coupled by adequate methods. Different solution methods are used to solve the coupled system. Additionally, in Fig. 1.2, the major topics and methods investigated in this thesis are highlighted for a better categorization.

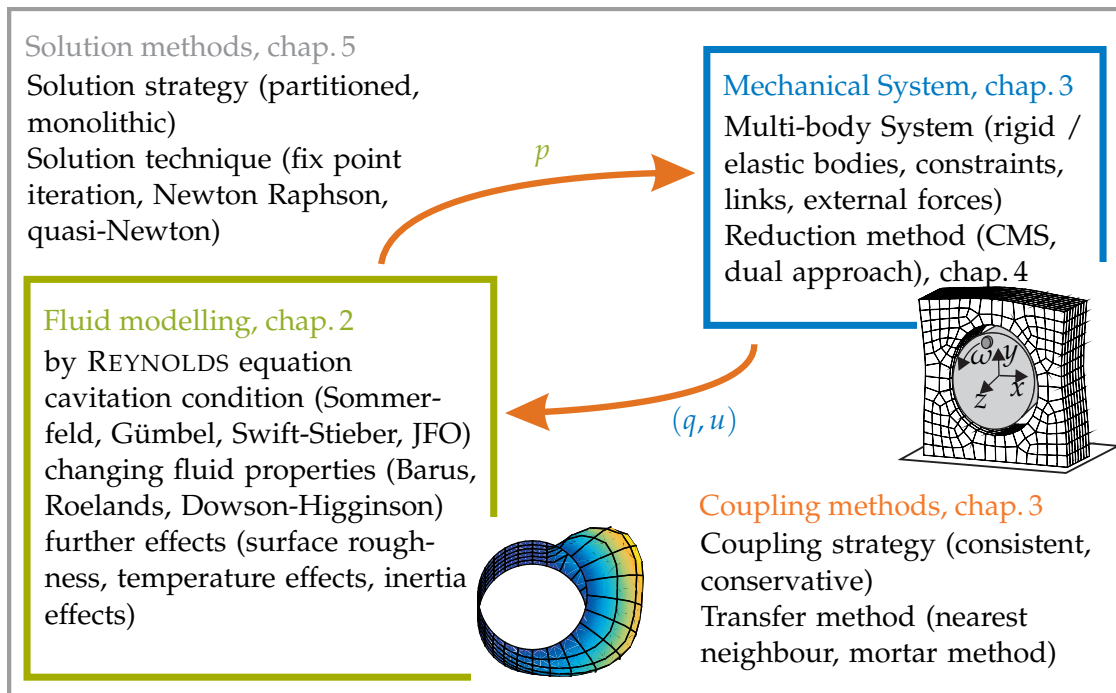


**Figure 1.2:** Schematic overview of EHL simulation and outline of topics addressed in this thesis.

### Own contributions

The important novel contributions outlined in this thesis can be summarized as follows:

- Mathematical formulation of classical cavitation conditions by a projection function.

- Novel cavitation algorithms by applying a non-smooth Newton method to the projection formulations of the cavitation problems.
- First time use of dual LAGRANGE multipliers for the discretization of the cavitation problems.
- First time application and analysis of consistent and conservative coupling methods of non-conforming meshes for EHL problems.
- Novel reduction method for reducing the elastic degrees of freedom of the interface of a revolute EHL bearing; comparison of reduction methods for classical simulation examples.
- Monolithic solution techniques for multibody systems with lubricated contacts by applying the projection formulations of the cavitation conditions.
- Adaption of a quasi-Newton method for the solution of the coupled system and development of solution algorithms for the coupled system.
- Simulation and experimental validation of a misaligned rotor in journal bearings.

### Outline of this work

The structure of this work is as follows:

Chapter 2 treats the fundamentals of the EHL contact. It introduces the REYNOLDS equation. A numerical discretization by the finite element method and an upwind stabilization provide a first numerical solution for the pressure distribution in the fluid film. Classical cavitation conditions are outlined, different mathematical formulations are given and cavitation algorithms are analyzed. The fluid film kinematics and forces are derived. Further effects in the REYNOLDS equation are discussed. Descriptive numerical examples conclude the chapter.

Chapter 3 states the governing equations of the complete coupled system. Therefore, the dynamic equations of rigid and elastic body motion are given and combined with the hydrodynamic equations of Chapter 2. The interface coupling conditions for a consistent and a conservative approach respectively, are outlined and different transfer methods are compared. A convergence study for a numerical example allows the discussion of the different coupling methodologies.

Chapter 4 addresses the reduction of elastic bodies having a lubricated interface. Two state-of-the-art reduction methods and a novel dual reduction approach are outlined for the use in a flexible multibody simulation. Their accuracy and efficiency is demonstrated for two simulation examples of multibody systems with a EHL journal bearing.

Chapter 5 treats the time integration of the coupled system and provides different solution strategies and techniques. Besides the state-of-the-art partitioned approach, a monolithic solution strategy is outlined and a quasi-Newton method is applied to the iteration process. An extensive study on a numerical example investigates the different approaches and techniques in detail.

Chapter 6 gives numerical and experimental case studies of EHL contact problems and bearing simulation. A simulation example of a flexible slider-crank mechanism is investigated due to variations in physical and numerical modeling. An experimental study of a rotor test rig is performed by the here developed simulation tools. Further, the numerical methods are tested for the simulation example of an EHL point contact.

Chapter 7 summarizes the numerical methods proposed and outlined in this work. It highlights existing challenges and outstanding topics in EHL simulation.

## Chapter 2

# The elastohydrodynamic lubricated contact

In this chapter, the fundamentals of the EHL contact are described, including the physical model as well as the mathematical treatment. Starting with the description of the REYNOLDS equation, a finite element (FE) discretization is successively derived, resulting in a stable numerical solution. The consideration of cavitation effects leads to a different physical and numerical behavior of the REYNOLDS equation. Therefore, a concise treatment of cavitation conditions is a special focus of this chapter. Further, the kinematics and the forces in the fluid film are addressed, which play an important role for the calculation of the hydrodynamic loads. Extended versions of the REYNOLDS equation and numerical examples complete the chapter.

The detailed structure of the chapter is as follows: In the first Section 2.1, the REYNOLDS equation is stated in its classical form, being the fundamental equation for the following sections.

In the second Section 2.2, a numerical discretization of the REYNOLDS equation by the FEM is given and a stabilization technique is outlined in order to avoid oscillations in the numerical solution of the REYNOLDS equation.

In Section 2.3, the most common cavitation conditions for the REYNOLDS equation are explained first and second, their numerical discretizations are given. Different mathematical formulations are outlined, resulting in different cavitation algorithms. The use of a projection function results in a novel cavitation algorithm.

Section 2.4 treats the kinematics and the forces in the fluid film. The kinematics is derived not only for the general case, but also for two classical examples – a flexible journal bearing and a EHL point contact.

Section 2.5 presents concepts for extending the REYNOLDS equation in order to capture effects, which are not covered by the classical hydrodynamic theory. In detail, these are surface roughnesses, inertia effects and temperature effects.

The last Section 2.6 shows numerical examples, which underline the theory of the previous sections. The different cavitation algorithms are compared, a solution from the literature is verified and the effect of the numerical stabilization is demonstrated.

### 2.1 REYNOLDS equation

A lubricated contact between two deformable bodies is depicted in Fig. 2.1. For the pressure distribution in the thin fluid film between the bodies, the REYNOLDS equation is valid under the following assumptions:

- The fluid behaves like a NEWTONian fluid, meaning that the shear forces linearly depend on the velocity gradient. The proportionality factor is the viscosity  $\eta$ .

- The fluid flow is slow and viscous, meaning that pressure and viscosity terms predominate, while fluid inertia and gravity effects are negligible. The flow is laminar and characterized by a small REYNOLDS number.
- The magnitude of the fluid height  $h(y, z) = h_2 - h_1$  is one order smaller than the magnitudes of the remaining two dimensions. This assumption results in a constant fluid pressure over the fluid height in local  $x$ -direction.

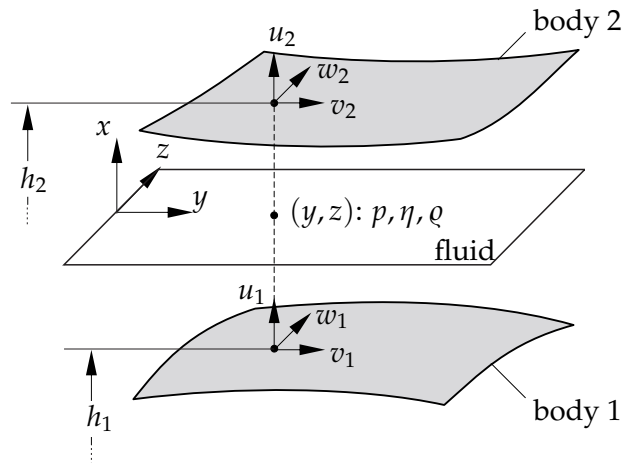


Figure 2.1: Notations in the lubricated contact.

The REYNOLDS equation can be derived from the NAVIER-STOKES equations by introducing the analytical solution of the momentum equation over the height of the fluid film into the mass conservation equation, see for instance HAMROCK et. al. [81]. A short derivation is also outlined in Appendix A. It is noted that the REYNOLDS equation is still valid for compressible fluids, meaning that the fluid properties (density  $\rho$ , viscosity  $\eta$ ) can change with the pressure or the temperature. This fact was originally neglected by REYNOLDS, but later described by HARRISON. Here in this thesis, it is assumed that the fluid properties behave isothermal. Nevertheless, Section 2.5.3 will later show the extensions to be made for the inclusion of temperature effects. The effect of shear rate on viscosity, describing a non-NEWTONian fluid behavior, is not treated here in this thesis, but may be taken into account in a generalized REYNOLDS equation, see for instance SZERI [184].

The following partial differential equation for the pressure in the two dimensional fluid domain  $\Omega \subset \mathbb{R}^2$  with descriptive coordinates  $(y, z)$  results from the REYNOLDS equation (see for instance [81] or Appendix A):

$$\underbrace{-\nabla \left( \frac{h^3 \rho}{12\eta} \nabla p \right)}_{\text{POISEUILLE}} + \underbrace{\frac{\partial}{\partial y} \left( \rho h \frac{v_1 + v_2}{2} \right) + \frac{\partial}{\partial z} \left( \rho h \frac{w_1 + w_2}{2} \right)}_{\text{COUETTE}} + \underbrace{\rho \frac{\partial h}{\partial t}}_{\text{squeeze}} + \underbrace{h \frac{\partial \rho}{\partial t}}_{\text{loc. exp.}} = 0, \quad (2.1)$$

where  $u_i$ ,  $v_i$  and  $w_i$  are the absolute velocities of body  $i$  ( $i \in \{1, 2\}$ ) in the local directions (Fig. 2.1). The first term on the left hand side of Eq. (2.1) represents the POISEUILLE term, describing the flow due to the change of the pressure gradient; the following two terms represent the COUETTE term, describing the flow due to wedge and stretch effects in the tangential plane; the fourth term represents the squeeze term, describing the mass change due to squeezing motion of the surfaces; the last term represents the local expansion term, describing the flow due to the change of density. Summarized, the REYNOLDS equation is a flux balance equation in the two-dimensional fluid domain.

For a better numerical treatment, the COUETTE flow is further split up into a flow  $q_{\text{dens}}$  describing the density wedge effect and a flow  $q_{\text{stat}}$  describing the physical wedge and stretch effects. Together with the squeeze flow  $q_{\text{squ}}$  and the flow  $q_{\text{exp}}$  for the local expansion of the density, it leads to following form:

$$-\nabla \left( \frac{h^3 \rho}{12\eta} \nabla p \right) + q_{\text{dens}} + q_{\text{stat}} + q_{\text{squ}} + q_{\text{exp}} = 0. \quad (2.2)$$

After splitting  $\frac{\partial h}{\partial t} = \frac{\partial h_2}{\partial t} - \frac{\partial h_1}{\partial t}$ , the EULERIAN derivative  $\frac{\partial h_i}{\partial t}$  can be expressed in dependence of local LAGRANGIAN velocities and height derivatives. Stating the total derivative  $\frac{dh_i}{dt} = u_i = \frac{\partial h_i}{\partial t} + v_i \frac{\partial h_i}{\partial y} + w_i \frac{\partial h_i}{\partial z}$ , it decomposes

$$\frac{\partial h_i}{\partial t} = u_i - v_i \frac{\partial h_i}{\partial y} - w_i \frac{\partial h_i}{\partial z} \quad (2.3)$$

into normal and tangential squeezing (see [81]). Now, the fluxes are defined as follows:

$$q_{\text{dens}} = \frac{h}{2} \begin{pmatrix} v_1 + v_2 \\ w_1 + w_2 \end{pmatrix}^T \nabla \rho, \quad (2.4)$$

$$q_{\text{stat}} = \rho \left[ \frac{\partial h}{\partial y} \frac{v_1 + v_2}{2} + h \frac{\partial}{\partial y} \left( \frac{v_1 + v_2}{2} \right) + \frac{\partial h}{\partial z} \frac{w_1 + w_2}{2} + h \frac{\partial}{\partial z} \left( \frac{w_1 + w_2}{2} \right) \right], \quad (2.5)$$

$$q_{\text{squ}} = \rho \frac{\partial h}{\partial t} = \rho \left[ (u_2 - u_1) - v_2 \frac{\partial h_2}{\partial y} + v_1 \frac{\partial h_1}{\partial y} - w_2 \frac{\partial h_2}{\partial z} + w_1 \frac{\partial h_1}{\partial z} \right], \quad (2.6)$$

$$q_{\text{exp}} = h \frac{\partial \rho}{\partial t}. \quad (2.7)$$

### Pressure dependent fluid properties

The effect of the pressure on the fluid parameters of the REYNOLDS equation can be in the compressibility or in the change of viscosity. The dependency of fluid density and viscosity on the pressure has to be taken into account in particular at high pressures, which usually exist in non-conformal EHL contacts.

A classical relation between viscosity and pressure is given by BARUS [10] and describes an exponential dependence:

$$\eta(p) = \eta_{p=0} e^{\xi p}, \quad (2.8)$$

with the dynamic viscosity  $\eta_{p=0}$  at zero pressure and the pressure-viscosity coefficient  $\xi$ . Experimental studies revealed that this relation is only valid at moderately high pressures. A better approximation even for high pressures gives the ROELANDS formula [159]:

$$\eta(p) = \eta_{p=0} \left( \frac{\eta_{\infty}}{\eta_{p=0}} \right)^{1 - (1 + p/c_p)^{Z_1}}, \quad (2.9)$$

with the oil specific constants  $\eta_{\infty}$  and  $c_p$  and the pressure-viscosity index  $Z_1$ . Note that  $Z_1$  is related to  $\xi$  of the BARUS formula according to  $Z_1 = c_p \xi / (\ln(\eta_{p=0}) - \ln(\eta_{\infty}))$ .

For oil, an often used relation between density and pressure is given by a formula, proposed by DOWSON and HIGGINSON [48]:

$$\rho(p) = \rho_{p=0} \left( 1 + \frac{a p}{1 + b p} \right), \quad (2.10)$$

with the density  $\rho_{p=0}$  at zero pressure and the oil specific constants  $a$  and  $b$ . In literature, a logarithmic or purely linear relation between pressure and density, based on a so-called bulk modulus, can also be found, see [54, 193].

The effect of density variation due to the pressure is usually less important than the effect of the variation of the viscosity when analyzing oil bearing forces. However, both effects have to be considered for non-conformal EHL contacts [81].

When assuming non-constant fluid parameters and inserting the formulas for the pressure dependences into REYNOLDS equation (2.2), the partial differential equation becomes nonlinear in the pressure variable  $p$ . Further, when accounting for compressibility, an effect of the time variation of the pressure through the local expansion term (2.7) becomes evident.

### Shear forces

The shear stresses  $\tau_i$  on body  $i$  ( $i \in \{1,2\}$ ) can be derived from the pressure and the kinematics as follows (see [81]):

$$\tau_{xy,1} = -\frac{h}{2} \frac{\partial p}{\partial y} - \frac{\eta(v_2 - v_1)}{h}, \quad \tau_{xy,2} = \frac{h}{2} \frac{\partial p}{\partial y} - \frac{\eta(v_2 - v_1)}{h}, \quad (2.11)$$

$$\tau_{xz,1} = -\frac{h}{2} \frac{\partial p}{\partial z} - \frac{\eta(w_2 - w_1)}{h}, \quad \tau_{xz,2} = \frac{h}{2} \frac{\partial p}{\partial z} - \frac{\eta(w_2 - w_1)}{h}. \quad (2.12)$$

They act in the local tangential  $y$ - and  $z$ -direction, respectively. Together with the pressure in the normal direction, they are responsible for the forces in the hydrodynamic contact.

## 2.2 Numerical discretization

This section treats the numerical discretization of the REYNOLDS equation. Different techniques are used in the literature. The FDM was the classical method to discretize the EHL problem of the line or the point contact, respectively, see [47, 80] for the first numerical solutions. Multigrid and multilevel methods in the solution process ensure an efficient and stable solution [121, 192, 199]. In [160, 186], the FEM is used as an alternative method and nowadays, it is applied to the EHL line and point contact problem in the same manner by using adequate stabilization techniques, see for instance [2, 77]. In the classical bearing simulation, the FDM was also used first [55], but the FEM rapidly became a widely used method [70, 111, 135].

In this section, the FEM is used for a numerical discretization of the REYNOLDS equation in its strong form (2.2). In Section 2.2.1, the FE discretization is given and in Section 2.2.2, the streamline upwind PETROV-GALERKIN (SUPG) stabilization technique is applied in order to get a stable solution of the problem. The books of DONEA and HUERTA [45] and ZIENKIEWICZ et. al. [212] serve as classical references for the FEM for fluid dynamics.

### 2.2.1 Finite element (FE) discretization

For a numerical solution of Eq. (2.2), the FEM with iso-parametric mapping is applied. It is started with the strong form of the transient problem, where the pressure  $p$  is the only unknown, as the fluid properties are either constant or pressure dependent. This means that the relations  $\rho = \rho(p)$  and  $\eta = \eta(p)$  are considered in Eq. (2.2). For the further analysis, a diffusion coefficient  $\kappa(p)$  and a convection velocity  $\mathbf{u}(p)$  are defined as follows:

$$\kappa(p) = \frac{h^3 \rho(p)}{12\eta(p)}, \quad (2.13)$$

$$\mathbf{u}(p) = \frac{h}{2} \begin{pmatrix} v_1 + v_2 \\ w_1 + w_2 \end{pmatrix} \frac{\partial \varrho}{\partial p}. \quad (2.14)$$

They arise in the POISEUILLE term of Eq. (2.2) and in the density flux (2.4), respectively. With them, the strong form can be formulated as follows: Find the pressure  $p$  such that

$$-\nabla (\kappa(p) \nabla p) + \mathbf{u}(p)^T \nabla p + h \frac{\partial \varrho}{\partial p} \dot{p} = -q_{\text{stat}} - q_{\text{squ}} \quad \text{on } \Omega \times ]0, T[, \quad (2.15)$$

$$p = \hat{p} \quad \text{on } \Gamma_p \times ]0, T[, \quad (2.16)$$

$$\kappa(p) \nabla p^T \mathbf{n} = \hat{q} \quad \text{on } \Gamma_q \times ]0, T[, \quad (2.17)$$

$$p(t = 0) = p_0 \quad \text{on } \Omega, \quad (2.18)$$

where  $\hat{p}$  is the pressure at the DIRICHLET boundary  $\Gamma_p$  and  $\hat{q}$  the flux on the NEUMANN boundary  $\Gamma_q$ <sup>1</sup>. The two boundaries do not intersect ( $\Gamma_p \cap \Gamma_q = \emptyset$ ) and together they form the boundary of the fluid domain ( $\Gamma = \partial\Omega = \Gamma_p \cup \Gamma_q$ ). The initial value at  $t = 0$  is  $p_0$  and the vector  $\mathbf{n}$  is the outpointing normal vector on  $\Gamma_q$ . For simplicity, it is assumed that  $\hat{p} = 0$ . The time interval is  $]0, T[$ .

For the weak form, weighting functions  $w(y, z) \in W$  are defined, which belong to the function space  $W$ :

$$W = \{w \in H^1(\Omega) \mid w = 0 \text{ on } \Gamma_p\}, \quad (2.19)$$

which contains functions of the SOBOLEV space  $H^1$ , which vanish at the DIRICHLET boundary  $\Gamma_p$ . The SOBOLEV space  $H^1(\Omega)$  represents the functions with square-integrable derivatives on  $\Omega$ . Then, the weak form reads as follows: Find the pressure  $p \in S$  such that

$$\begin{aligned} \int_{\Omega} \kappa(p) \nabla w^T \nabla p \, d\Omega + \int_{\Omega} w \left( \mathbf{u}(p)^T \nabla p + h \frac{\partial \varrho}{\partial p} \dot{p} \right) d\Omega = \\ - \int_{\Omega} w (q_{\text{stat}} + q_{\text{squ}}) \, d\Omega + \int_{\Gamma_q} w \hat{q} \, d\Gamma, \quad \forall w \in W. \end{aligned} \quad (2.20)$$

Here in this form, the GAUSS divergence theorem is already applied. The solution space  $S$  for the pressure is defined as:

$$S = \{p \in H^1(\Omega) \mid p = \hat{p} \text{ on } \Gamma_p\} \quad (2.21)$$

and contains all functions of the SOBOLEV space  $H^1(\Omega)$ , which fulfill the DIRICHLET boundary condition (DBC). For the discretization, the two-dimensional fluid domain  $\Omega$  is approximated by  $n_{ele}$  finite elements defining the discrete fluid domain  $\Omega_h$ :

$$\Omega \approx \Omega_h = \bigcup_{e=1}^{n_{ele}} \Omega^{(e)}.$$

Further, the space  $W$  of the weighting functions as well as the solution space  $S$  are approximated by the subspaces  $S_h \subset S$  and  $W_h \subset W$ , respectively. Following the BUBNOV-GALERKIN method, the same function space is used for the description of both subspaces. The pressure  $p(y, z)$  and the weighting function  $w(y, z)$  are approximated by the shape functions  $N(y, z)$ :

$$p(y, z) \approx p_h(y, z) = \sum_{i=1}^{n_{free}} N_i p_{free,i} + \sum_{j=1}^{n_{dbc}} N_j p_{dbc,j} \quad (2.22)$$

<sup>1</sup>Note that here, the NEUMANN boundary condition  $\hat{q}$  addresses the flux due to the pressure gradient (i. e. the POISEUILLE flow) only. Alternatively, it may address the total flux consisting of POISEUILLE and COUETTE flow. Then, also a total flux has to be prescribed on  $\Gamma_q$ .

$$\mathbf{w}(y, z) \approx \mathbf{w}_h(y, z) = \sum_{k=1}^{n_{free}} \mathbf{N}_k w_{free,k}, \quad (2.23)$$

where  $p_{free,i}$  belongs to the vector  $\mathbf{p}$  of the  $n_{free}$  unknown discrete pressure values,  $p_{dbc,j}$  belongs to the vector  $\hat{\mathbf{p}}$  of  $n_{dbc}$  known discrete pressure values at the DIRICHLET boundary and  $w_{free,k}$  belongs to the vector  $\mathbf{w}$  of the  $n_{free}$  discrete values of the weighting function. The shape functions  $\mathbf{N}_i$  are usually defined locally on the finite element ( $e$ ) and belong to one specific node of the FE mesh.

A discretization of the weak form (2.20) is obtained, when  $p_h \in S_h$  is found on  $\Omega_h$  such that the weak form is fulfilled for every  $w_h \in W_h$ . Inserting further the approximations (2.22) and (2.23) into Eq. (2.20) gives following discretized weak form:

$$\begin{aligned} \sum_{k=1}^{n_{free}} \left[ w_k \left\{ \int_{\Omega_h} \left( \kappa(p_h) \nabla \mathbf{N}_k^T + \mathbf{N}_k \mathbf{u}(p_h)^T \right) \sum_{i=1}^{n_{free}} \nabla \mathbf{N}_i p_{free,i} \, d\Omega + \right. \right. \\ \left. \left. + \int_{\Omega_h} h \frac{\partial q}{\partial p} \mathbf{N}_k \sum_{i=1}^{n_{free}} \mathbf{N}_i \dot{p}_{free,i} \, d\Omega = - \int_{\Omega_h} \mathbf{N}_k (q_{stat,h} + q_{squ,h}) \, d\Omega \right. \right. \\ \left. \left. + \int_{\Gamma_{q,h}} \mathbf{N}_k \hat{q} \, d\Gamma - \int_{\Omega_h} \left( \kappa_h \nabla \mathbf{N}_k^T + \mathbf{N}_k \mathbf{u}_h^T \right) \sum_{j=1}^{n_{dbc}} \nabla \mathbf{N}_j p_{dbc,j} \, d\Omega \right\} \right]. \quad (2.24) \end{aligned}$$

This form has to be fulfilled for each discrete value  $w_k$  and leads to a system of equations for the unknown pressure vector  $\mathbf{p}$ . The integration over the domain  $\Omega_h$  can be split up into the sum over the integrals on the finite elements  $\Omega^{(e)}$ , due to the local definition of the shape functions. After assembling the global matrices and vectors, the following nonlinear system of equations for the discretized hydrodynamic pressure  $\mathbf{p}$  results:

$$(\mathbf{A}(\mathbf{p}) + \mathbf{B}(\mathbf{p})) \mathbf{p} + \mathbf{C}(\mathbf{p}) \hat{\mathbf{p}} = \mathbf{b}(\mathbf{p}), \quad (2.25)$$

with the following FE matrices and vectors, for  $k, i \in \{1, \dots, n_{free}\}$ :

$$\begin{aligned} \mathbf{A} &= \mathbf{A}_{k,i}^{(e)}, & \mathbf{A}_{k,i}^{(e)} &= \int_{\Omega^{(e)}} \kappa(p_h) \nabla \mathbf{N}_k^T \nabla \mathbf{N}_i \, d\Omega, \\ \mathbf{B} &= \mathbf{B}_{k,i}^{(e)}, & \mathbf{B}_{k,i}^{(e)} &= \int_{\Omega^{(e)}} \mathbf{N}_k \mathbf{u}(p_h)^T \nabla \mathbf{N}_i \, d\Omega, \\ \mathbf{C} &= \mathbf{C}_{k,i}^{(e)}, & \mathbf{C}_{k,i}^{(e)} &= \int_{\Omega^{(e)}} h \frac{\partial q}{\partial p_h} \mathbf{N}_k \mathbf{N}_i \, d\Omega, \\ \mathbf{b} &= \mathbf{b}_k^{(e)}, & \mathbf{b}_k^{(e)} &= - \int_{\Omega^{(e)}} \mathbf{N}_k (q_{stat,h} + q_{squ,h}) \, d\Omega + \int_{\Gamma_q^{(e)}} \mathbf{N}_k \hat{q} \, d\Gamma \\ & & & - \int_{\Omega^{(e)}} \left( \kappa_h \nabla \mathbf{N}_k^T + \mathbf{N}_k \mathbf{u}_h^T \right) \sum_{j=1}^{n_{dbc}} \nabla \mathbf{N}_j p_{dbc,j} \, d\Omega. \end{aligned}$$

The size of the system conforms to the number  $n_{free}$  of the free nodes. Later, the complete solution vector  $\hat{\mathbf{p}}$  is needed, including the already known  $n_{dbc}$  values at the DIRICHLET boundary nodes. It is defined as  $\hat{\mathbf{p}} = (\mathbf{p}^T \ \hat{\mathbf{p}}^T)^T$  and has the length of  $n_{node} = n_{free} + n_{dbc}$  values.

### Choice of shape functions

Typically in the FEM, polynomial LAGRANGE functions are used as shape functions, as they fulfill well the differentiability requirements. Here in this work, quadrilateral ele-

ments (4 nodes) with bi-linear LAGRANGE shape functions as well as incomplete quadrilateral elements (8 nodes) with bi-quadratic serendipity shape functions are used. In the further reading, they are addressed as *Lin4* and *Quad8* elements, respectively.

### Full-SOMMERFELD solution

The first, stationary solution of the REYNOLDS equation is referred as the full-SOMMERFELD solution [176]. For that, constant fluid properties are assumed, meaning  $\rho = \rho_{p=0}$  and  $\eta = \eta_{p=0}$ , which lead to a vanishing density and expansion flux in Eq. (2.2). Looking at the discretized system of Eq. (2.25), the matrices  $\mathbf{B}$  and  $\mathbf{C}$  vanish as well as the pressure dependency of matrix  $\mathbf{A}$  and vector  $\mathbf{b}$ . In addition, the squeeze flux vanishes, when stationary conditions are considered, leading to  $\mathbf{b} = \mathbf{b}_{\text{stat}}$ . As a result, the pressure can be calculated directly by:

$$\mathbf{p} = \mathbf{A}^{-1} \mathbf{b}_{\text{stat}} \quad (2.26)$$

### 2.2.2 FE stabilization

This subsection treats the numerical stability in the discretization of the strong form (2.15) to (2.18). Equation (2.15) is a transient, convection-diffusion equation: the first term represents the diffusion term with the diffusion coefficient  $\kappa(p)$  and the second term represents the convection term with the convection velocity  $\mathbf{u}(p)$ . Typical for this class of equations are numerical oscillations, when the convective term dominates the diffusive term. The element PécLET number is a measure for the ratio between convective and diffusive transport and is defined as follows:

$$Pe^{(e)} = \frac{\|\mathbf{u}\| h^{(e)}}{2\kappa}, \quad (2.27)$$

where  $h^{(e)}$  is the characteristic length of the element ( $e$ ). In detail, the numerical FE solution becomes unstable, when the element PécLET number is larger than one. In EHL theory, this can be the case in highly loaded contacts because at high pressures, the diffusion coefficient (2.13) tends towards zero, as the viscosity increases exponentially with the pressure. Note that these oscillation do not occur in the REYNOLDS equation, when constant fluid parameters are assumed, as there is neither a convective flux  $q_{\text{dens}}$  nor the viscosity changes with the pressure.

The problem of numerical oscillations is originally known from the FDM. There, oscillations in convection-dominated flows occur, when the convective term is discretized by a central difference scheme. In the FEM, this happens in the same way, when the standard BUBNOV-GALERKIN discretization is used, since this scheme corresponds in its linear form to a central difference scheme, see BROOKS and HUGHES [29].

In the FDM, the classical approach to avoid the oscillations is the use of a pure first order upwind discretization for the convective term. It can be shown that this upwind scheme corresponds to a central difference scheme with an artificial diffusion, which damps out the oscillations, see for instance [29]. It can be further shown that there exists an optimal choice of the artificial diffusion, which ensures exact values at the element nodes for the one-dimensional case. These concepts of streamline upwind discretization and optimal artificial diffusion are also applicable in the FEM. However, the simple addition of streamline upwind/artificial diffusion terms jeopardizes the consistency of the FEM and the concept of weighted residues is not satisfied any more. A stabilization technique without this inconsistency is the SUPG method [29]. Its idea is to use streamline upwind modified weighting functions according to the PETROV-GALERKIN discretization. Thus, artificial diffusion is added in direction of the streamlines and further, the residuum is weighted by these functions, which gives a consistent formulation.

In the literature, further FE stabilization techniques can be found. These are the GALERKIN/Least-Squares (GLS) method, the Variational Multiscale Stabilized (VMS) method, the Finite Increment Calculus (FIC) method or the so-called Bubble methods, see [45] for an overview. In the context of EHL contacts, the classical methods like the artificial diffusion, the SUPG and the GLS method are applied for a stable FE solution. Examples can be found in [74].

In the following, the SUPG method is applied to stabilize the FE discretization of the strong form (2.15) to (2.18). In contrast to the standard BUBNOV-GALERKIN method of the previous subsection, the SUPG method uses following streamline upwind modified weighting functions for the discretization of the function space  $W_h$ :

$$\tilde{w}_h = w_h + v_h = w_h + \tau \mathbf{u}_h^T \nabla w_h, \quad (2.28)$$

with the stabilization parameter  $\tau$ . Using the modified weighting function  $\tilde{w}_h$  for the discretization of the weak form (2.20) gives following stabilized discrete weak form: Find  $p_h \in S_h$  such that

$$\begin{aligned} \int_{\Omega_h} \kappa(p_h) \nabla w_h^T \nabla p_h \, d\Omega + \int_{\Omega_h} w_h \left( \mathbf{u}(p_h)^T \nabla p_h + h \frac{\partial q}{\partial p_h} \dot{p}_h \right) \, d\Omega = \\ - \int_{\Omega_h} w_h (q_{\text{stat},h} + q_{\text{squ},h}) \, d\Omega + \int_{\Gamma_{q,h}} w_h \hat{q} \, d\Gamma \\ + \sum_{e=1}^{n_{ele}} \int_{\Omega_h^{(e)}} v_h^{(e)} R_h^{(e)} \, d\Omega, \quad \forall w_h \in W_h. \end{aligned} \quad (2.29)$$

The first two rows are equal to the standard BUBNOV-GALERKIN method, while the sum in the third row represents the stabilization term. The latter is added to the interior of the elements, where the discrete residuum  $R_h$  is weighted by the streamline upwind parts of the weighting functions. The discrete residuum  $R_h$  is given according to Eq. (2.15):

$$R_h = -\nabla (\kappa(p_h) \nabla p_h) + \mathbf{u}(p_h)^T \nabla p_h + h \frac{\partial q}{\partial p_h} \dot{p}_h + q_{\text{stat},h} + q_{\text{squ},h} \quad (2.30)$$

It becomes clear that the SUPG method is also residual-based.

The further proceeding is similar to the discretization with the BUBNOV-GALERKIN method. In the stabilized discrete form (2.29), the approximations (2.22) and (2.23) are inserted and the integration is performed on the finite elements. After assembling the element matrices and vectors, a system of equations for the stabilized FE discretization is obtained. It has the same form as the system of Eq. (2.25), but here the original matrices and vectors are updated by the matrices and vectors coming from the SUPG stabilization:

$$\mathbf{A} \leftarrow \mathbf{A} + \mathbf{A}_{\text{SUPG}}, \quad \mathbf{B} \leftarrow \mathbf{B} + \mathbf{B}_{\text{SUPG}}, \quad \mathbf{C} \leftarrow \mathbf{C} + \mathbf{C}_{\text{SUPG}}, \quad \mathbf{b} \leftarrow \mathbf{b} + \mathbf{b}_{\text{SUPG}}, \quad (2.31)$$

### Choice of stabilization parameter

For linear elements in 1D, an optimal choice of the stabilization parameter  $\tau$  exists for the steady-state convection-diffusion equation:

$$\tau^{(e)} = \frac{\beta^{(e)} h^{(e)}}{2 u^{(e)}}, \quad \beta^{(e)} = \coth(Pe^{(e)}) - 1/Pe^{(e)}. \quad (2.32)$$

This parameter ensures a solution with nodal exact values. For quadratic elements in 1D, an optimal parameter can be found in the same way, see [45]. Even though the concept of an optimal parameter can be generalized for bi-linear elements in 2D, the choice of

an optimal parameter, e. g. for higher order elements or for general transient problems, is still an open research field. A useful choice, which ensures that the stabilization vanishes, when the element size is small enough, gives:

$$\tau^{(e)} = \left( \left( \frac{2 \|\mathbf{u}^{(e)}\|}{h^{(e)}} \right)^2 + 9 \left( \frac{4\kappa^{(e)}}{h^{(e)2}} \right)^2 + \sigma^{(e)2} \right)^{-1/2}, \quad (2.33)$$

where  $\sigma^{(e)}$  takes into account reactive terms like the right hand side and the transient term of Eq. (2.15). For instance for the transient problem,  $\sigma^{(e)}$  may depend also on the time-step of the time discretization, see [45].

## 2.3 Cavitation conditions

So far, the REYNOLDS equation is considered in its original form (2.1) and first numerical pressure solutions, like the full-SOMMERFELD solution, can be calculated. However, these solutions could give pressures below the atmospheric pressure. This would mean physically that the fluid is exposed to tensile forces being much higher than the tensile stresses, which a fluid could eventually sustain. In reality, in this case, a rupture of the fluid film occurs and cavitation zones arise. As a consequence, an adequate cavitation model needs to be imposed on the REYNOLDS equation in order to avoid these unphysical negative pressures in the solution.

As a wide range of cavitation models exist in the literature, Section 2.3.1 gives a review on the most important models and outlines their differences in both their physical appearance and their mathematical formulation.

Based on that, the FE treatment of two widely spread models, namely the SWIFT-STIEBER and the JACOBSSON-FLOBERG-OLSSON models, are outlined in Section 2.3.2 and Section 2.3.3, respectively.

### 2.3.1 Review on cavitation models

In the literature, many cavitation models exist, which differ in their physical approach, but also in their mathematical formulation and consequently in their numerical calculation effort. In the following, the focus will be on the most popular models. For a more detailed overview, it is referred to the review papers of DOWSON [49] and BRAUN [25].

For the purpose of comparison, the left diagram of Fig. 2.2 depicts amongst others the full-SOMMERFELD solution for the pressure in the circumferential direction of an eccentric journal bearing. As can be seen, the pressure is positive in the convergent zone and has its maximum before the minimal height, which is located at  $\varphi = \pi$ . In the divergent zone, where the height increases again, the pressure becomes negative, which is only possible when no cavitation condition is imposed.

#### GUEMBEL condition

The GUEMBEL condition [72] of the year 1914 represents a first cavitation model. It is usually used for the steady-state case  $\dot{p} = 0$  and simply cuts off pressures below the cavitation pressure  $p_c$  in the full-SOMMERFELD solution, see left diagram in Fig. 2.2. Therefore, it is also known as half-SOMMERFELD solution. It assumes that the film rupture always occurs at the minimal film height, while film reformation is not considered physically. Due to the kink in the pressure at the film rupture, it is not mass-conservative at the cavitation boundary; neither is it mass-conservative inside the cavitation region. Nevertheless, it is often used due to its easy numerical treatment.

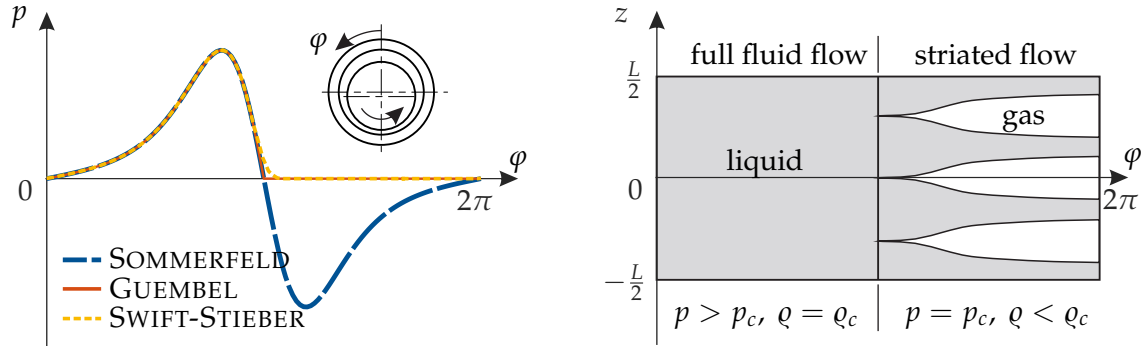


Figure 2.2: Cavitation conditions.

Using the SOMMERFELD solution (2.26), the pressure of the GUEMBEL solution is defined as:

$$\mathbf{p} - p_c = \langle \mathbf{A}^{-1} \mathbf{b}_{\text{stat}} \rangle, \quad (2.34)$$

where the  $\langle \cdot \rangle$ -operator is defined for an arbitrary vector  $\mathbf{v}$  by returning for the  $i$ -th component  $v_i$ :

$$\langle v_i \rangle = \begin{cases} v_i & \text{if } v_i \geq 0 \\ 0 & \text{else} \end{cases}. \quad (2.35)$$

### SWIFT-STIEBER condition

A more sophisticated cavitation condition was formulated by SWIFT and STIEBER [179, 183], which is also referred to as REYNOLDS boundary condition [21, 49], as it goes back to considerations made by REYNOLDS. It determines the position of the cavitation boundary by the condition that the pressure  $p = p_c$  is constant in the cavitation zone and the pressure gradient  $\nabla p$  vanishes at the film rupture. This leads to a smooth transition at the film rupture, as can be seen in the left diagram of Fig. 2.2.

This assumption holds physically very well, when a stationary striated flow is established over the complete clearance height. This flow is characterized by equally distributed gas cavities, where the liquid is transported in-between of them, see Fig. 2.2 right. Such a flow was observed in many experiments under steady-state operation and flow conditions, meaning  $q_{\text{squ}} = 0$  and  $\dot{p} = 0$ , see [49]. The SWIFT-STIEBER condition is mass-conservative at the film rupture. This fact will be shown in more depth in the next subsection, when highlighting mass-conservative models.

Mathematically, the SWIFT-STIEBER condition is formulated as a so-called free boundary problem on the fluid domain: In the full fluid zone, the pressure has to be larger than the cavitation pressure and the REYNOLDS equation has to be fulfilled such that the change of density  $\dot{q}$  vanishes. It is different in the cavitation zone: here, the pressure has to be constant and the change of density has to be negative, since the fluid cavitates. Looking at the REYNOLDS equation (2.2), the change of density correlates to the local expansion flow by  $q_{\text{exp}} = h \frac{\partial q}{\partial t}$ . By this, it can be summarized that following two zones have to be found in the fluid domain:

$$p > p_c : \quad q_{\text{exp}} = \nabla \left( \frac{h^3 q}{12\eta} \nabla p \right) - q_{\text{dens}} - q_{\text{stat}} - q_{\text{squ}} = 0 \quad (2.36)$$

$$p = p_c : \quad q_{\text{exp}} < 0, \quad (2.37)$$

with the pressure  $p$  as only unknown. This formulation assumes that the density remains constant in the cavitation zone ( $q = q_c$ ) at all time, only the time derivative of the density

has to be negative. This fact is often referred as the condition of starting cavitation [111]. Note that the GUEMBEL condition, which computes the solution of the REYNOLDS equation as usual, and then only as a post-processing, puts all the pressures below the cavitation pressure back to  $p_c$ , differs from condition (2.37), as the flux  $q_{\text{exp}}$  is at least a linear function of the pressure and not the pressure itself.

The problem of Eqs. (2.36) and (2.37) was solved by a GAUSS-SEIDEL relaxation with an if-else switching first by CHRISTOPHERSON [34]. Later, CRYER et al. formulated the SWIFT-STIEBER cavitation condition for constant fluid properties as a linear complementarity problem (LCP) [40]. In the case of pressure dependent fluid properties, this formulation becomes nonlinear and consequently a nonlinear complementarity problem (NCP) has to be solved, see [99, 135]. These complementarity problems are usually solved by a block-pivot based MURTY-algorithm [127], which was first applied by OH [135] and described by GOENKA [70].

Good experimental results for moderately loaded bearings as well as its moderate numerical implementation effort explain the broad use of the SWIFT-STIEBER condition, see for instance [22, 70, 135, 136]. However, a detailed prediction of the fluid film reformation is not possible, as mass-conservation is not fulfilled in the cavitation zone. This is due to the fact of the remaining negative flow  $q_{\text{exp}}$  in the cavitation zone.

It is worth noting that the assumptions of SWIFT and STIEBER are made originally for steady-state operation conditions. However, in practice, this cavitation condition is also applied under transient operation conditions, when the squeeze term  $q_{\text{squ}}$  is considered like in Eq. (2.36).

### Mass-conservative models

A widely spread transient and mass-conservative cavitation condition is the JACOBSSON-FLOBERG-OLSSON (JFO) condition [59, 93, 139]. Similar to the SWIFT-STIEBER condition, it assumes a striated flow in the cavitation zone like in Fig. 2.2 right. Contrarily to the previous model, it incorporates an additional condition for the fluid film reformation and ensures further mass-conservation in the cavitation zone. A typical pressure distribution based on the JFO concept is shown in Fig. 2.3 left. Further, the distribution of the density can be seen.

In order to gain deeper insight into the pressure and density distributions for the mass-conservative models, the transient flow balance is analyzed in a 1D control volume at the position of the film rupture 2, see Fig. 2.3 right. The stationary flows  $q_{\varphi}^-$  and  $q_{\varphi}^+$  in circumferential direction immediately before and after the film rupture are defined as:

$$q_{\varphi}^- = -\frac{h^3}{12\eta} \left. \frac{\partial p}{\partial \varphi} \right|_2 + h \varrho^- \frac{v_1 + v_2}{2}, \quad q_{\varphi}^+ = h \varrho^+ \frac{v_1 + v_2}{2}, \quad (2.38)$$

where  $q_{\varphi}^-$  belongs to the pressurized fluid zone with positive and  $q_{\varphi}^+$  to the cavitation zone with constant pressure. The balance of incoming and outgoing flows induces the change of mass in the control volume:

$$q_{\varphi}^- - q_{\varphi}^+ = \lim_{d\varphi \rightarrow 0} \int_{\varphi_2 - d\varphi/2}^{\varphi_2 + d\varphi/2} \frac{\partial(\varrho h)}{\partial t} d\varphi = h(\varrho^+ - \varrho^-) \dot{\varphi}_2.$$

where  $\dot{\varphi}_2$  is the velocity of the cavitation boundary. In this equation, the LEIBNIZ integral rule is already applied. Inserting the flows of Eq. (2.38), one obtains the pressure gradient immediately before the film rupture as:

$$\left. \frac{\partial p}{\partial \varphi} \right|_2 = \frac{6\eta}{h^2} (v_1 + v_2 - 2\dot{\varphi}_2) (1 - \varrho^+/\varrho^-). \quad (2.39)$$

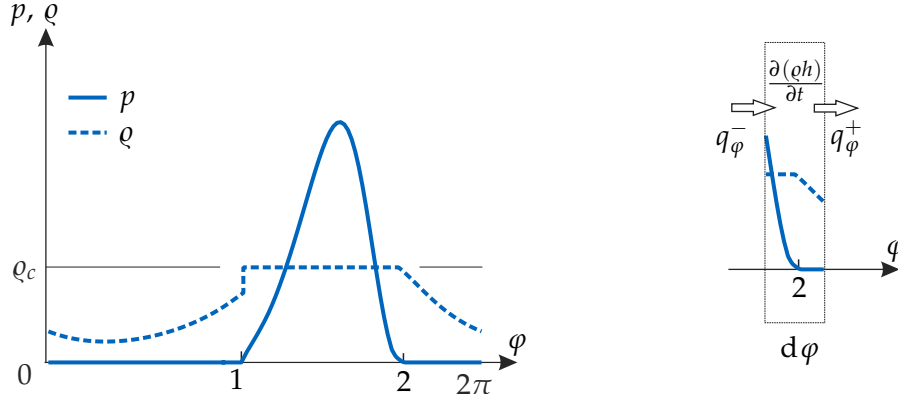


**Figure 2.3:** Pressure and density distribution in a bearing with JFO condition (assuming incompressible fluid behavior and  $p_c = 0$ )

In this equation, the velocity  $\dot{\phi}_2$  of the cavitation boundary has to be smaller than the convection velocity  $(v_1 + v_2)/2$ , otherwise the assumption for film rupture does not hold. From the condition that the pressure in the pressurized fluid zone has to be positive, it follows that the pressure gradient cannot be positive at the film rupture. Further, from the condition that the density in the cavitation zone has to be smaller or equal than the density in the pressurized zone, it follows with  $\dot{\phi}_2 < (v_1 + v_2)/2$  in Eq. (2.39) that the pressure gradient cannot be negative. As a consequence, a vanishing pressure gradient and a continuous density distribution ( $q^+ = q^-$ ) remain as the only possible solutions for the fulfillment of the mass-conservation at film rupture. With this finding, it becomes clear that the SWIFT-STIEBER condition from the previous subsection is mass-conservative at the film rupture, as there is imposed a zero pressure gradient at film rupture and a continuous density distribution in the fluid film.

A similar analysis as done for the film rupture can be done for the film reformation. Then, the transient flow balance in 1D gives the following equation for the pressure gradient at the position 1 of the film reformation:

$$\left. \frac{\partial p}{\partial \phi} \right|_1 = \frac{6\eta}{h^2} (v_1 + v_2 + 2\dot{\phi}_1) (1 - q^-/q^+).$$

Here, the upper point with density  $q^+ = q_c$  lies in the pressurized fluid zone. The velocity  $\dot{\phi}_1$  of the cavitation boundary has to be smaller than the negative convection velocity, meaning  $\dot{\phi}_1 < -(v_1 + v_2)/2$ , otherwise the assumption of film reformation does not hold any more. Due to the condition of a positive pressure in the pressurized fluid zone, the pressure gradient cannot be negative at the film reformation. As a result, either a vanishing pressure gradient with a continuous density or a positive gradient with a discontinuous density profile fulfills the mass-conservation. However, due to a discussion with RIXEN and VAN OSTAYEN [158], it comes out that a discontinuity in the density arises at the fluid film reformation with  $q^- < q_c$  and consequently, the pressure gradient has to be positive at film reformation. The reason is that the film rupture usually occurs after passing the minimal film height in the divergent zone of the film with  $\frac{\partial h}{\partial y} > 0$ . From the constant flow  $q_\phi^- = h q^- \frac{v_1 + v_2}{2}$  before the film reformation, it follows that the density can only decrease in direction of the cavitated flow. Finally, it has to jump back to the value  $q_c$  at the film reformation. This topic is also discussed by WIJNANT [199].

Mathematically, the JFO condition can be formulated also as a free-boundary problem. In order to ensure mass-conservation, the transient REYNOLDS equation (2.1) has to be valid in the full fluid zone, but also in the cavitation zone. In the cavitation zone, the POISEUILLE term vanishes due to the condition of a constant pressure  $p = p_c$  and hence, the before elliptical REYNOLDS equation (2.2) degenerates in this case to a hyperbolic

equation. In summary, following two equations have to be fulfilled on the fluid domain:

$$p > p_c, \varrho = \varrho_c : \quad -\nabla \left( \frac{h^3 \varrho}{12 \eta} \right) \nabla p + q_{\text{dens}} + q_{\text{stat}} + q_{\text{squ}} + q_{\text{exp}} = 0 \quad (2.40)$$

$$p = p_c, \varrho < \varrho_c : \quad q_{\text{dens}} + q_{\text{stat}} + q_{\text{squ}} + q_{\text{exp}} = 0. \quad (2.41)$$

These are two equations for the two unknown field variables  $p$  and  $\varrho$ . Their solution automatically fulfills the conditions for fluid film reformation and rupture.

In the literature, many mathematical formulations and algorithms based on the JFO concept exist. A first cavitation algorithm is given by ADAMS and ELROD [54, 55]. By the definition of a void coefficient  $\theta = \varrho/\varrho_c$  and a switching function  $g(\theta)$ , the problem of Eqs. (2.40) and (2.41) is solved in an iterative manner. Its numerical implementation with a finite difference scheme is the popular ELROD-algorithm [54].

A similar implementation of the JFO concept is proposed in [193], where the switching function is combined with the bulk modulus of the density-pressure relation in the cavitation zone.

KUMAR and BOOKER propose a mass-conservative cavitation algorithm for a FE discretization of the formulation of ADAMS and ELROD [111]. Unlike the ELROD algorithm, they assume incompressible fluid behavior and use the description of a mixture-flow in the cavitation zone. Further, they apply a pivot-based algorithm.

In [3], the ELROD-algorithm is modified for a better numerical efficiency by defining an optimal value of the bulk modulus. A FE discretization with iterative fixed-point solution strategy is used.

In [67], the free boundary problem is formulated as a LCP and a pivoting-based algorithm is applied during the solution process. In [14], this concept is extended to a compressible and non-NEWTONIAN fluid behavior.

In [204], the complementarity problem resulting from the stationary free boundary problem is formulated as an unconstrained problem using a FISCHER-BURMEISTER function and a FE discretization. The formulation uses the pressure  $p$  and a cavity fraction  $1 - \theta$  as unknowns and assumes incompressible fluid behavior. The system is solved by a NEWTON-RAPHSON method. A similar concept is followed in [117], while here a projection function is used for the formulation of an unconstrained problem.

In [109], in a similar way, the mass-conservative cavitation problem is formulated by a projection function, using  $p$  and  $\varrho$  as variables. As shown in [110], this formulation can be extended to compressible fluid behavior and also to a transient analysis.

The mass-conservative cavitation condition due to the JFO concept shows in many cases a very good agreement between experiments and simulation including highly loaded bearings, see [59, 181] or the review papers [25, 49]. For the transient EHL point contact, the ELROD algorithm agrees also well with experimental data, see for instance [199].

### 2.3.2 FE solution of the SWIFT-STIEBER cavitation condition

This subsection treats the numerical FE solution of the cavitation problem resulting from the SWIFT-STIEBER condition of the previous subsection. Different mathematical formulations are presented: formulations as a complementarity problem and as a variational inequality, a penalty formulation and a projection formulation. Their different weak forms, their solution spaces and the FE discretization are shown and discussed. A further focus is placed on the different solution algorithms, resulting from the different formulations.

#### Formulation as a complementarity problem

According to [99, 135], the free boundary problem of Eqs. (2.36) and (2.37) can be formulated as a NCP. By substituting  $p_{\text{ref}} = p - p_c$ , the pressure  $p_{\text{ref}}$  has to be found such that:

$$0 \leq p_{ref} \perp f(p) \geq 0, \quad f(p) = -\nabla \left( \frac{h^3 \rho}{12\eta} \nabla p \right) + q_{dens} + q_{stat} + q_{squ}, \quad (2.42)$$

where the symbol  $\perp$  stands for point-wise orthogonality ( $p_{ref} f(p) = 0$ ) and the nonlinear function  $f(p)$  represents the negative expansion flux of the REYNOLDS equation (2.2), i. e.  $f(p) = -q_{exp}$ . This NCP ensures that in the pressurized zone ( $p > p_c$ ), the REYNOLDS equation is fulfilled ( $f(p) = 0$ ), while in the cavitation zone ( $p = p_c$ ), the change of density is negative, meaning  $f(p) > 0$ . Figure 2.4(a) explains the NCP graphically.

For the FE discretization, Eq. (2.15) of the original strong form has to be replaced by Eq. (2.42). Then, the time-dependency drops and the DBC  $\hat{p}$  has to be greater or equal to  $p_c$  in order to fulfill Eq. (2.42) at the DIRICHLET boundary. By this, the weak form can be stated. Find the pressure  $p \in S^+$  such that

$$0 \leq \int_{\Omega} q p_{ref} \, d\Omega \perp \int_{\Omega} w f(p) \, d\Omega \geq 0, \quad \forall q \in Q^+, w \in W^+, \quad (2.43)$$

where  $S$  and  $W$  were defined in Eqs. (2.19) and (2.21). Due to the nonnegativity conditions, the original solution space  $S$  and the original space  $W$  of the weighting functions have to be restricted to the normal cones  $S^+$  and  $W^+$ , respectively. Further, the integrals have to be understood as a duality pairing and thus, the weighting function  $q$  is element of the dual normal cone  $Q^+$ . Obviously, the dual weighting function  $q$  corresponds to the variation of the flux  $q_{exp} = -f(p)$ , which both are the dual counterparts of the pressure  $p$  and its variation  $w$ .

For the weak formulation, adequate function spaces have to be defined. As both the pressure  $p_{ref}$  and the variation  $w$  have to be nonnegative, following normal cones  $S^+$  and  $W^+$  are defined:

$$S^+ = \{p \in S \mid \int_{\Omega} p_{ref} q \, d\Omega \geq 0, q \in Q^+\}, \quad (2.44)$$

$$W^+ = \{w \in W \mid \int_{\Omega} w q \, d\Omega \geq 0, q \in Q^+\}, \quad (2.45)$$

$$Q^+ = \{q \in H^{-1}(\Omega) \mid q = 0 \text{ on } \Gamma_p, q \geq 0\}. \quad (2.46)$$

with  $H^{-1}(\Omega)$  as the dual space of the SOBOLEV space  $H^1(\Omega)$ . Obviously, the former strong nonnegativity conditions are replaced by their weaker duality pairings.

Applying a variationally consistent discretization, meaning that adequate discrete spaces  $S_h^+$ ,  $W_h^+$  and  $Q_h^+$  are chosen, following discretized NCP can be derived for the discrete pressure  $p$ :

$$\mathbf{0} \leq N p_{ref} \perp ((A(p) + B(p)) p - b(p)) \geq \mathbf{0}. \quad (2.47)$$

The symbol  $\perp$  implies now orthogonality for each discrete node  $(y_k, z_k)$  on the FE mesh. In the same way, the inequality conditions have to be fulfilled component-wise. The matrix  $N$  corresponds to the so-called FE mass matrix and is calculated as:

$$N = \bigwedge_{e=1}^{n_{ele}} N_{k,i}^{(e)}, \quad N_{k,i}^{(e)} = \int_{\Omega^{(e)}} M_k N_i \, d\Omega, \quad (2.48)$$

with the corresponding dual shape functions  $M_k$  of the discretized weighting function  $q_h = \sum_{k=1}^{n_{free}} M_k q_k$ . This complementarity problem is valid in a weak sense on the discrete fluid domain  $\Omega_h$ . Thus, it follows that negative pressure values may occur, depending on the

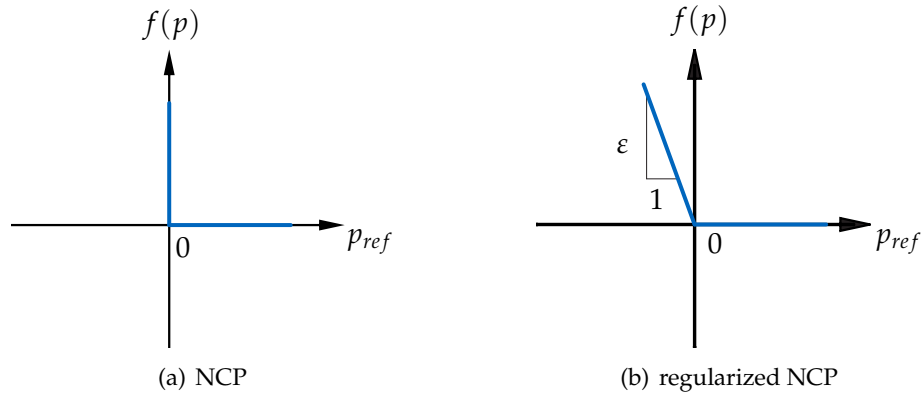


**Figure 2.4:** NCP and regularized NCP

choice of the element shape functions. The specific requirements for the shape functions are outlined in the next subsection.

In contrast to the weak formulation (2.43), the complementarity condition can also be formulated for the discrete node values, only. Then, the discrete pressure  $p_{ref}$  has to be perpendicular to the discrete negative expansion flow  $-q_{exp}$ , leading to:

$$(A(\mathbf{p}) + B(\mathbf{p})) \mathbf{p} - \mathbf{b}(\mathbf{p}) + N \mathbf{q}_{exp} = \mathbf{0}, \quad (2.49)$$

$$\mathbf{0} \leq p_{ref} \perp -q_{exp} \geq \mathbf{0}. \quad (2.50)$$

This NCP becomes linear, when constant fluid parameters are assumed. A unique solution of this NCP requires the matrix  $N^{-1}(A(\mathbf{p}) + B(\mathbf{p}))$  to be a P-matrix. In the linear case, this requirement is fulfilled, since matrices  $N$  and  $A$  are symmetric positive definite, when using standard FE shape and weighting functions.

A precise overview on solution methods for linear and nonlinear complementarity problems can be found in the text book of ACARY and BROGLIATO [1]. Splitting methods can be used to solve the LCP by a fixpoint iteration. The method, which was originally used by CHRISTOPHERSON for the solution of the LCP– a GAUSS-SEIDEL successive over-relaxation method – belongs to this group. A second group are the pivot-based methods. The MURTY algorithm, which was applied in [70] to the LCP, belongs to this group. These pivot-based methods can be further used for the solution of the NCP by solving successive LCP s and they are known as NEWTON-JOSEPHY’S or linearization methods. In [135], a linearization method is applied to the solution of the NCP. The NCP (2.42) can be linearized as follows:

$$\mathbf{0} \leq p_{ref,m+1} \perp f(p_m) + \left. \frac{\partial f}{\partial p} \right|_{p_m} (p_{m+1} - p_m) \geq \mathbf{0}. \quad (2.51)$$

This resulting LCP for the new solution  $p_{ref,m+1}$  has to be solved in each iteration  $m$ . It converges against the solution of the NCP.

It has to be noted that existence and uniqueness of the nonlinear NCP for the cavitation problem is not yet proven [135]. However, in all practical cases, a convergent solution is obtained.

### Variational inequality and function spaces

In order to discuss the solution and the weighting space of the NCP as well as its numerical solution in more detail, the cavitation problem is formulated as a variational inequality (VI). Since a VI formulation is often used for unilateral contacts, especially for

their weak formulation, equivalences between the hydrodynamic contact and the classical unilateral contact arise. The treatment of unilateral contacts as a VI can be found in the classical textbooks of PANAGIOTOPOULOS [141], KIKUCHI and ODEN [96] or WRIGGERS [206]. The treatment of the hydrodynamic contact as a VI is given by BAYADA et al. in [11, 12].

The NCP (2.42) is equivalent to the following nonlinear VI: Find  $p_{ref} \in \mathbb{R}_0^+$  such that

$$(\mathbf{w} - p_{ref}) f(p) \geq 0, \quad \forall \mathbf{w} \in \mathbb{R}_0^+. \quad (2.52)$$

The equivalence with the NCP can be verified by inserting  $\mathbf{w} = 0$ , which gives  $-p_{ref} f(p) \geq 0$ , and  $\mathbf{w} = 2p_{ref}$ , which gives  $p_{ref} f(p) \geq 0$ . Hence, since  $p_{ref} \in \mathbb{R}_0^+$ , both inequalities are fulfilled if and only if  $p_{ref} f(p) = 0$ .

For the weak formulation, the function spaces (2.44) to (2.46) are already defined.

With these function spaces, the weak formulation of the VI (2.52) is stated as follows: Find  $p \in S^+$  such that

$$\int_{\Omega} (\mathbf{w} - p_{ref}) f(p) \, d\Omega \geq 0, \quad \forall \mathbf{w} \in W^+. \quad (2.53)$$

For this weak form, a FE discretization is obtained by using consistent approximations  $S_h^+$ ,  $W_h^+$  and  $Q_h^+$  for the function spaces. A detailed discussion of a variationally consistent discretization for variational inequalities in the case of unilateral contacts is given in the work of HÜEBER [88] or WOHLMUTH [202]. These discretization techniques can be applied in a similar way to the here stated cavitation problem.

In the following, the pressure and the weighting functions are approximated by its standard shape functions, see Eqs. (2.22) and (2.23), and in the same way, the function  $q$  is approximated by  $q \approx q_h = \sum_{k=1}^{n_{free}} M_k q_k$ . These shape functions need to fulfill special requirements for a variationally consistent discretization of the function space Eqs. (2.44) to (2.46).

In [88, 202] and also in [151, 203], necessary requirements for the standard shape functions as well as the shape functions of the LAGRANGE multipliers of the unilateral contact are outlined. They can be transferred to the cavitation problem, when using the analogy that the negative expansion flow  $-q_{exp}$  is equivalent to the LAGRANGE multipliers of the unilateral contact. Then, beside the requirement that the shape functions have to fulfill the partition of unity, it can be derived that the LAGRANGE shape functions  $M_k$  ( $k \in \{1 \dots n_{node}\}$ ) have to be positive integrable on the elements, meaning  $\int_{\Omega^{(e)}} M_k \, d\Omega^{(e)} > 0$ .

Mainly, there are two different choices for the LAGRANGE shape functions  $M_k$ . The first choice is to set them equal to the standard shape functions, i. e.  $M_k = N_k$ . A second choice is obtained by constructing  $M_k$  such that bi-orthogonality is fulfilled. The latter choice was first introduced by WOHLMUTH in [201] for contact constraints and offers some nice properties<sup>2</sup>. In detail, the shape functions  $M_k$  are constructed such that

$$\int_{\Omega} M_k N_i \, d\Omega = \delta_{ki} \int_{\Omega} N_i \, d\Omega = \delta_{ki} m_k > 0, \quad k, i \in \{1 \dots n_{node}\} \quad (2.54)$$

where  $\delta_{ki}$  is the KRONECKER symbol. By using a discretization fulfilling this bi-orthogonality condition, following point-wise decoupled constraint results from Eq. (2.53):

$$0 \leq p_{ref,k} \perp -m_k q_{exp,k} \geq 0,$$

<sup>2</sup>As described by POPP [151], for an optimal convergence it is sufficient, when the dual LAGRANGE multipliers have a polynomial reproduction one order smaller than the order of the standard shape functions. It means that they are usually discontinuous.

where the derivation is similar to that of HÜEBER for unilateral contacts in [88]. Further, when using Eq. (2.49), one obtains the following NCP:

$$\mathbf{0} \leq p_{ref} \perp (A(\mathbf{p}) + B(\mathbf{p})) \mathbf{p} - \mathbf{b}(\mathbf{p}) \geq \mathbf{0}. \quad (2.55)$$

It has to be emphasized, that this NCP is derived from the duality pairing (2.53) and not from the weak formulation of Eq. (2.43). They will result in different solutions, when using for  $M_k$  the standard LAGRANGE shape functions. In contrast, when using the dual LAGRANGE shape functions, both formulations become identical. The reason is that the bi-orthogonality condition leads to a diagonal, positive definite matrix  $N$ . For the same reason, the node-wise formulation of Eq. (2.50) is then equivalent to the formulation of Eq. (2.55) and thus, also to the formulation of Eq. (2.50).

As already mentioned, the LAGRANGE shape functions  $M_k$  have to be positive integrable on the elements. The same requirement results for the standard shape functions  $N_k$ , independently of using standard or dual LAGRANGE shape functions, see for instance [202]. While this requirement is valid for the already introduced *Lin4* element shape functions, it is not fulfilled for the *Quad8* element shape functions. One possibility for remedy is to define modified *Quad8Mod* element shape functions, which fulfill the requirement of positive integrability, see the work of POPP [151, 153]. Figure B.2 of Appendix B.2 shows such *Quad8Mod* element shape functions. Another possibility is to use a node-based integration scheme like the LOBATTO-GAUSS integration for the numerical evaluation of the element matrices, see LAMICHHANE et al. [113]. With such a node-based integration, in some cases also the bi-orthogonality condition is fulfilled, when using standard shape functions for  $M_k$ . Figure B.1 of Appendix B.1 shows dual bi-linear and Fig. B.3 of Appendix B.3 dual bi-quadratic element shape functions, respectively. For the further literature on the construction of bi-orthogonal shape functions, it is referred to [58, 82, 88, 113, 114, 153, 202].

### Penalty formulation

A penalty formulation is a convenient approach for solving a complementarity problem. For the steady-state cavitation problem, it is applied in many cases, see for instance [74, 209]. The penalty formulation of NCP (2.42) reads:

$$f(\mathbf{p}) - \varepsilon \langle -p_{ref} \rangle = 0, \quad (2.56)$$

where the second term is the penalty term. It consists of the penalty parameter  $\varepsilon > 0$  and the expression  $\langle -p_{ref} \rangle$ , which is defined like in Eq. (2.35) and returns the negative pressure or zero else, meaning  $\langle -p_{ref} \rangle = \min(p_{ref}, 0)$ . The penalty formulation can be understood as a regularized NCP as depicted in Fig. 2.4(b). It converges for  $\varepsilon \rightarrow \infty$  against the original NCP.

For the FE solution, the weak form of the residual (2.56) has to be used. It gives: Find the pressure  $p \in S$  such that

$$\int_{\Omega} \mathbf{w} (f(\mathbf{p}) - \varepsilon \langle -p_{ref} \rangle) \, d\Omega = 0, \quad \forall \mathbf{w} \in W. \quad (2.57)$$

It is noted that, when following the penalty approach, the solution space  $S$  and the weighting space  $W$  do not have to be restricted to their normal cones, as claimed for the complementarity formulations. The nonnegativity is ensured by the penalization.

After the discretization, following discrete residuum is obtained:

$$(A(\mathbf{p}) + B(\mathbf{p})) \mathbf{p} - \mathbf{b}(\mathbf{p}) - \mathbf{b}_{\varepsilon}(p_{ref}) = \mathbf{0} \quad (2.58)$$

with equivalent matrices and vectors like in Eq. (2.25) and the additional nonlinear vector  $\mathbf{b}_\varepsilon(\mathbf{p}_{ref})$  due to the regularization. When the numerical integration on the finite elements is performed by quadrature rules like the GAUSS integration, that need values in the element interior, the integration and assembly of  $\mathbf{b}_\varepsilon(\mathbf{p}_{ref})$  has to be done in every iteration step. In contrast, when using quadrature rules like the LOBATTO integration, that need values at the nodes only, the  $\langle \cdot \rangle$ -operator can be shifted on the discrete vector  $\mathbf{p}_{ref}$ , meaning  $\mathbf{b}_\varepsilon(\mathbf{p}_{ref}) = \varepsilon \mathbf{N} \langle -\mathbf{p}_{ref} \rangle$ . In the same way, the  $\langle \cdot \rangle$ -operator can be shifted, when the FE shape functions  $N_k > 0$  are strictly positive.

As far, the penalty formulation is applied to the strong form (2.56), which results in the weak discrete form of Eq. (2.58). Differently, the penalty formulation is now applied to the already discretized NCP (2.47), yielding following nonlinear residual:

$$(\mathbf{A}(\mathbf{p}) + \mathbf{B}(\mathbf{p})) \mathbf{p} - \mathbf{b}(\mathbf{p}) - \varepsilon \langle -\mathbf{N} \mathbf{p}_{ref} \rangle = \mathbf{0}. \quad (2.59)$$

Similarly, the discretized NCP (2.50) can be regularized as follows:

$$\mathbf{N}^{-1} ((\mathbf{A}(\mathbf{p}) + \mathbf{B}(\mathbf{p})) \mathbf{p} - \mathbf{b}(\mathbf{p})) - \varepsilon \langle -\mathbf{p}_{ref} \rangle = \mathbf{0}. \quad (2.60)$$

The system of Eqs. (2.59) and (2.60) differ from the discrete Eq. (2.58) in the sense that the underlying weak forms and solution spaces are different. Further, as already mentioned, the system of Eq. (2.60) is different to that of Eq. (2.59), except, when dual LAGRANGE shape functions are used.

However, all the nonlinear systems of Eqs. (2.58) to (2.60) have in common that they can be solved iteratively, e. g. with a NEWTON-RAPHSON method.

### Projection formulation

The stationary cavitation problem of Eqs. (2.36) and (2.37) can also be formulated by a projection function, see [109, 110]. The use of such a function was initially proposed for plasticity problems and later for contact and friction problems in multi-body dynamics [4, 89, 164]. It is based on an augmented LAGRANGIAN approach and gives an equivalent formulation of a NCP. For the NCP (2.42) in its strong form, it reads:

$$p_{ref} = \text{proj}_{\mathbb{R}_0^+} (p_{ref} - r f(p)) = \begin{cases} p_{ref} - r f(p), & \text{for } p_{ref} - r f(p) > 0 \\ 0 & \text{else} \end{cases}, \quad r > 0. \quad (2.61)$$

The projection operator is explained by Fig. 2.5: For an argument  $x$  belonging to the convex set  $\mathcal{C}$ , the projection operator  $\text{proj}_{\mathcal{C}}(x)$  returns the argument itself. Otherwise, the function returns the projection of the value onto the convex set  $\mathcal{C}$ . The projection parameter  $r$  can be chosen arbitrarily greater than zero. For frictional contacts, this projection formulation was first outlined in [4]. In nowadays multi-body dynamics, it is common practice to consider non-smooth events like unilateral contacts by a projection formulation [1, 211]. As an unconstrained problem results, it gives the opportunity to solve the contact problem in a monolithic manner [166]. Nevertheless, partitioned strategies still can be used, see [62, 164]

For the FE discretization, again the weak form of Eq. (2.61) has to be stated. It reads: Find  $p \in S$  such that

$$\int_{\Omega} \mathbf{w} \left( p_{ref} - \text{proj}_{\mathbb{R}_0^+} (p_{ref} - r f(p)) \right) d\Omega = 0, \quad \forall \mathbf{w} \in W. \quad (2.62)$$

Similarly to the penalty formulation, the solution space  $S$  and the weighting space  $W$  do not have to be restricted to the normal cones, as this is already accomplished by the projection operator.

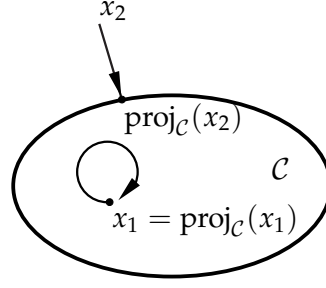


**Figure 2.5:** Projection function.

After discretization, a nonlinear residual results. During the solution process, it has to be evaluated in the interior of the finite elements, when an integration method like the GAUSS integration is used. In contrast, when using a node based integration method, the projection operator can be shifted to the discrete values in a similar way as done for the penalty formulation.

Instead of formulating a weighted residual with the projection function, the projection formulation can also be applied to the already discretized NCP (2.47). Then, the following nonlinear residual results:

$$\mathbf{N} \mathbf{p}_{ref} - \mathbf{proj}_{\mathbb{R}_0^+} \left( \mathbf{N} \mathbf{p}_{ref} - r \left( (\mathbf{A}(\mathbf{p}) + \mathbf{B}(\mathbf{p})) \mathbf{p} - \mathbf{b}(\mathbf{p}) \right) \right) = \mathbf{0}, \quad r > 0. \quad (2.63)$$

with equivalent matrices and vectors like in Eq. (2.25). Similarly, it can be applied to the discretized NCP (2.50), leading:

$$\mathbf{p}_{ref} - \mathbf{proj}_{\mathbb{R}_0^+} \left( \mathbf{p}_{ref} - r \mathbf{N}^{-1} \left( (\mathbf{A}(\mathbf{p}) + \mathbf{B}(\mathbf{p})) \mathbf{p} - \mathbf{b}(\mathbf{p}) \right) \right) = \mathbf{0}, \quad r > 0. \quad (2.64)$$

As mentioned in a similar fashion for the penalty approach, the systems of Eqs. (2.63) and (2.64) differ from the discrete form obtained from the weak form (2.62). Again, the reason is that different weak formulations and solution spaces are underlying. Besides, the formulations (2.63) and (2.64) are only identical, when dual LAGRANGE shape functions are used.

For all nonlinear projection formulation, the solution can be found by an iterative scheme like a fix-point iteration or a semi-smooth NEWTON-RAPHSON method.

### 2.3.3 FE solution of the mass-conservative JFO cavitation condition

In this subsection, the FE solution of the mass-conservative free boundary cavitation problem of Eqs. (2.40) and (2.41) is derived. In difference to the REYNOLDS equation with its numerical treatment in Sections 2.2.1 and 2.2.2, the density  $\varrho$  has to be considered as a further unknown variable. Hence, a new strong form for the pressure-density problem needs to be stated. Again, the free boundary problem is formulated as a complementarity problem. In addition, a density-dependent diffusion coefficient  $\kappa_\varrho$  and a different, now constant convection velocity  $\mathbf{u}_\varrho$  arise. They are defined as

$$\kappa_\varrho(p, \varrho) = \frac{h^3 \varrho}{12 \eta(p)}, \quad (2.65)$$

$$\mathbf{u}_\varrho = \frac{h}{2} \begin{pmatrix} v_1 + v_2 \\ w_1 + w_2 \end{pmatrix}. \quad (2.66)$$

With them, the pressure  $p$  and the density  $\varrho$  have to be found such that

$$-\nabla \cdot (\kappa_\varrho(p, \varrho) \nabla p) + \mathbf{u}_\varrho^T \nabla \varrho + h \dot{\varrho} = -q_{stat} - q_{squ} \quad \text{on } \Omega \times ]0, T[, \quad (2.67)$$

$$0 \leq p - p_c \perp f_\varrho(p) - \varrho \geq 0 \quad \text{on } \Omega \times ]0, T[, \quad (2.68)$$

$$p = \hat{p}, \quad \varrho = \hat{\varrho} \quad \text{on } \Gamma_p \times ]0, T[, \quad (2.69)$$

$$0 \leq \hat{p} - p_c \perp f_\varrho(\hat{p}) - \hat{\varrho} \geq 0 \quad \text{on } \Gamma_p \times ]0, T[, \quad (2.70)$$

$$\kappa_\varrho(p, \varrho) \nabla p^T \mathbf{n} = \hat{\varrho} \quad \text{on } \Gamma_q \times ]0, T[, \quad (2.71)$$

$$p(t=0) = p_0, \quad \varrho(t=0) = \varrho_0 \quad \text{on } \Omega, \quad (2.72)$$

$$0 \leq p_0 - p_c \perp f_\varrho(p_0) - \varrho_0 \geq 0 \quad \text{on } \Omega. \quad (2.73)$$

The first equation is the original REYNOLDS equation (2.1), while the second equation states a complementarity condition between pressure and density. They both fulfill equivalently Eqs. (2.40) and (2.41) and even consider compressible fluid behavior: In the pressurized zone ( $p > p_c$ ), the density becomes a function of the pressure  $\varrho = f_\varrho(p)$  and the full compressible REYNOLDS equation is valid. Note that the function  $f_\varrho(p)$  may represent a compressibility relation as stated by the DOWSON-HIGGINSON formula (2.10), but may also be a constant value  $\varrho_0$  when no compressibility is assumed. In the cavitation zone, the pressure is constant ( $p = p_c$ ) and the density is smaller than the density at cavitation pressure ( $\varrho < \varrho_c$  with  $\varrho_c = f_\varrho(p_c)$ ). Note that in the cavitation zone, the POISEUILLE term drops in the REYNOLDS equation. The pressure  $\hat{p}$  and the density  $\hat{\varrho}$ , respectively represent the DBC at the DIRICHLET boundary  $\Gamma_p$ . Equation (2.71) represents the NEUMANN boundary condition (NBC) for the pressure and Eq. (2.72) represents the initial time conditions for both, the pressure and the density, respectively. Equations (2.70) and (2.73) ensure the complementarity condition for the DBCs and the initial conditions, respectively.

Appendix C.1 derives the FE discretization of the strong form described by Eqs. (2.67) to (2.73) by using the standard GALERKIN method. Therefore, the complementarity problem is treated as a VI, similar to Eq. (2.53). Then, following nonlinear system of equations for the discrete vectors of the unknown pressure  $\mathbf{p}$  and density  $\varrho$  results:

$$A_\varrho(\mathbf{p}, \varrho) \mathbf{p} + B_\varrho \varrho + C_\varrho \dot{\varrho} = \mathbf{b}_\varrho(\mathbf{p}, \varrho) \quad (2.74)$$

$$\mathbf{0} \leq \mathbf{p}_{ref} \perp N \left( f_\varrho(\mathbf{p}) - \varrho \right) \geq \mathbf{0}. \quad (2.75)$$

It is noted that, instead of using a VI formulation, the complementarity condition can also be treated in a weak formulation, similar to Eq. (2.43), or formulated for the discrete nodes only, similar to Eq. (2.50). Then a different discretization would be obtained. Further, the application of the dual LAGRANGE multiplier used in this work is not valid anymore for the here stated problem. The reason is that the density variable requires a  $C^0$  continuous solution space, which can not be guaranteed by the dual LAGRANGE multiplier spaces used in this work.

Similar to the FE solution of the SWIFT-STIEBER condition of Section 2.3.2, the discrete NCP (2.75) can be reformulated by using a penalty term or a projection function. The penalty formulation gives:

$$N \left( f_\varrho(\mathbf{p}) - \varrho \right) - \varepsilon \langle -\mathbf{p}_{ref} \rangle = 0, \quad (2.76)$$

and the projection formulation gives:

$$\mathbf{p}_{ref} = \mathbf{proj}_{\mathbb{R}_0^+}(\mathbf{p}_{ref} - r N \left( f_\varrho(\mathbf{p}) - \varrho \right)), \quad r > 0. \quad (2.77)$$

Here, both formulations (2.76) and (2.77) are given for the already discretized complementarity problem (2.75). They could also be applied to Eq. (2.68) of the strong form. Then, in combination with a GAUSS quadrature, the  $\langle \cdot \rangle$ -operator and the projection function would have to be evaluated each time in the interior of the elements, see also [117].

It was already stated that the POISSEUILLE term vanishes in the cavitation zone and, therefore, the partial differential equation changes its character. While the REYNOLDS equation is elliptical in the pressurized zone, it becomes hyperbolic in the cavitation zone, meaning a remaining pure convection-dominated flow for the density. Therefore, similar as described in Section 2.2.2, numerical oscillations can occur in the solution of the standard-GALERKIN discretization. They can be avoided by using again a SUPG stabilized FE discretization. For the strong form, it is similar to Section 2.2.2 and is given in Appendix C.2. The stabilization parameter  $\tau_\rho$  for the *Lin4* and *Quad8* elements, respectively, is chosen as follows (compare also Eq. (2.32)):

$$\tau_\rho^{(e)} = \left( \left( \frac{2 \|\mathbf{u}_\rho^{(e)}\|}{h^{(e)}} \right)^2 + \frac{1}{\varepsilon_\rho} \left( \frac{1}{g^{(e)}} \right)^2 + \sigma^{(e)2} \right)^{-1/2}, \quad (2.78)$$

with  $g^{(e)} = (\mathbf{f}_\rho(\mathbf{p}) - \rho)/\rho_{p=0}$ . This choice ensures with  $\varepsilon_\rho \gg 1$  that the stabilization is active only in the cavitation zone, where the flow is purely convection dominated. In the pressurized zone, the stabilization is inactive since  $g^{(e)}$  – and thus  $\tau_\rho^{(e)}$  – tends towards zero. By this a smooth activation of the stabilization in the cavitation zone only is guaranteed<sup>3 4</sup>.

It has to be noted that both, the standard-GALERKIN as well as the BUBNOV-GALERKIN method use interpolation functions, which are continuous in the solution space. These functions are not suitable to capture discontinuities, like the jump of the density at the fluid reformation boundary. Due to the weak formulation and the continuous function spaces, such jumps are smeared in the solution process. An adequate method to dissolve discontinuities is the discontinuous-GALERKIN method as proposed in [118].

## 2.4 Kinematics and forces in the fluid film

The previous Sections 2.1 to 2.3 treat the constitutive equations and the numerical solution of the pressure in the EHL contact. This section now deals with the analytical and numerical derivation of the kinematics and forces in the fluid film. While the kinematics is needed for the pressure calculation, the forces can be computed, when the pressure distribution is known.

Section 2.4.1 starts with an general introduction to the fluid film kinematics and gives then the specific kinematic relations for two classical EHL contacts – for a cylindrical journal bearing and an EHL point contact.

Section 2.4.2 shows the calculation of the forces in normal and tangential direction due to the pressure and shear forces in the EHL contact.

### 2.4.1 Fluid film kinematics

In this section, the kinematic quantities, which are needed in the REYNOLDS equation, are derived. These are the local heights, the local absolute velocities and their derivatives with respect to (wrt.)  $y$  and  $z$ , as needed in Eqs. (2.4) to (2.7).

Figure 2.6 depicts the general notation for the kinematics in a lubricated contact. The inertia frame is denoted by  $I$ . The fluid domain is characterized by the fixed coordinate system  $F$  with the descriptive coordinates  $(y, z)$ . The two bodies are characterized each by a body-fixed coordinate system  $B_i$  ( $i \in \{1, 2\}$ ).

<sup>3</sup>By this choice of  $\tau_\rho^{(e)}$ , if-else conditions in order to check if an element is cavitated or not are avoided and due to the experience of the author, no cycling occurs in the solution process.

<sup>4</sup>During the practical examples of this work, the author made the experience that the best choice of the parameter  $\sigma^{(e)}$ , which accounts for reactive and/or time-depending terms, is to set it to zero for an efficient stabilization.

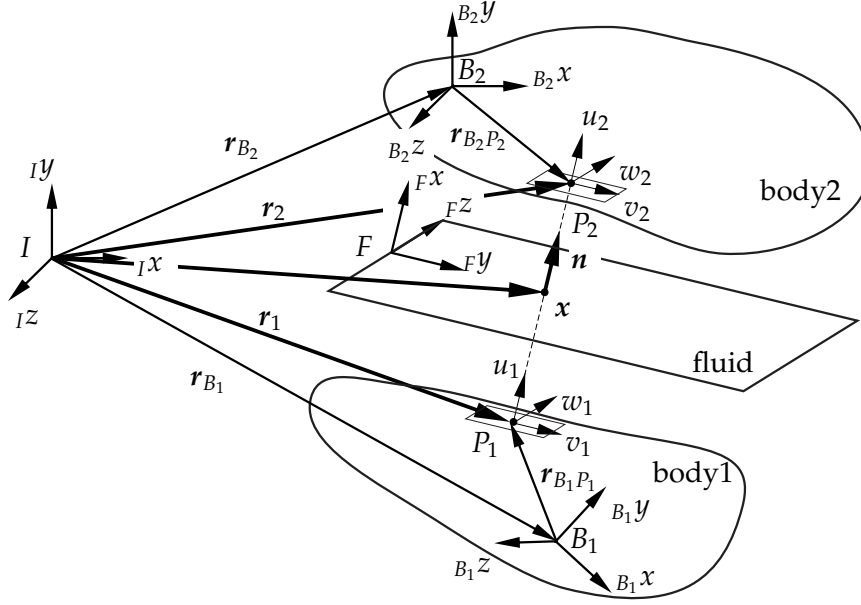


**Figure 2.6:** Notations in the lubricated contact.

At each position  $(y, z)$  of the fluid domain, the local height  $h(y, z)$  needs to be derived. The position of the fluid point in the inertia frame is denoted by  ${}_I\mathbf{x} = {}_I\mathbf{x}(x_F, y, z)$ , where  ${}_I\mathbf{x}_F$  is the absolute position of the fluid frame  $F$ . It is assumed that the surfaces of the bodies are parametrized by respective surface parameters  $(\xi_i, \eta_i)$ . Then, the position  $P_i$ , which defines the distance between the surface of body  $i$  and the fluid point  $x$  in local normal direction  $\mathbf{n}$ , can be determined. For a given local position  $(y, z)$ , the following condition has to be fulfilled:

$${}_I\mathbf{n}(y, z) \times {}_I\mathbf{g}_i \stackrel{!}{=} \mathbf{0}, \quad {}_I\mathbf{g}_i = {}_I\mathbf{r}_{B_i} + {}_I\mathbf{r}_{B_i P_i}(\xi_i, \eta_i) - {}_I\mathbf{x}(x_F, y, z), \quad i \in \{1, 2\}. \quad (2.79)$$

It ensures that the distance vector  $\mathbf{g}_i$  is collinear to the normal vector  $\mathbf{n}$ . With that, the surface parameters  $(\xi_i(y, z), \eta_i(y, z))$  can be determined. With them, the local heights can be defined as the following projection onto the normal vector:

$$h_i(y, z) = {}_I(\mathbf{r}_{B_i} + \mathbf{r}_{B_i P_i}(\xi_i, \eta_i) - \mathbf{x}_F)^T {}_I\mathbf{n}(y, z). \quad (2.80)$$

At the end, the local height is given by  $h(y, z) = h_2 - h_1$ .

When knowing the surface parameter  $(\xi_i(y, z), \eta_i(y, z))$  for a given position  $(y, z)$  in the fluid domain, the absolute local velocities can be determined. They are defined by the absolute surface velocity of point  $P_i$  transformed into the local normal and tangential directions, yielding:

$$u_i = {}_I\dot{\mathbf{r}}_{P_i}^T {}_I\mathbf{n}(y, z), \quad v_i = {}_I\dot{\mathbf{r}}_{P_i}^T {}_I\mathbf{t}_y(y, z), \quad w_i = {}_I\dot{\mathbf{r}}_{P_i}^T {}_I\mathbf{t}_z(y, z), \quad (2.81)$$

where  ${}_I\mathbf{t}_y$  and  ${}_I\mathbf{t}_z$  are the tangents in local  $y$ - and  $z$ -direction, respectively. In most cases, it is useful to decompose the absolute velocity into  ${}_I\dot{\mathbf{r}}_{P_i} = {}_I\dot{\mathbf{r}}_{B_i} + {}_I\dot{\mathbf{r}}_{B_i P_i}$ .

Having the local heights and velocities, their derivations wrt.  $y$  and  $z$  can be calculated.

In the following, the specific kinematics for a cylindrical journal bearing and a lubricated point contact are given. They can be classified as a cylinder-hollow/cylinder and a plane/sphere contact pairing, respectively. It becomes clear that the film kinematics has to be stated anew for each specific contact geometry.

### Kinematics for cylindrical journal bearing

The geometric and kinematic relations for a cylindrical joint with flexible bearing are derived according to Fig. 2.7. For simplicity the procedure is explained for a 2-dimensional problem with a rigid shaft, but it can without difficulty be extended to the 3-dimensional case and to the case when both bodies are flexible. A similar but slightly different derivation of the kinematics is given in [110].

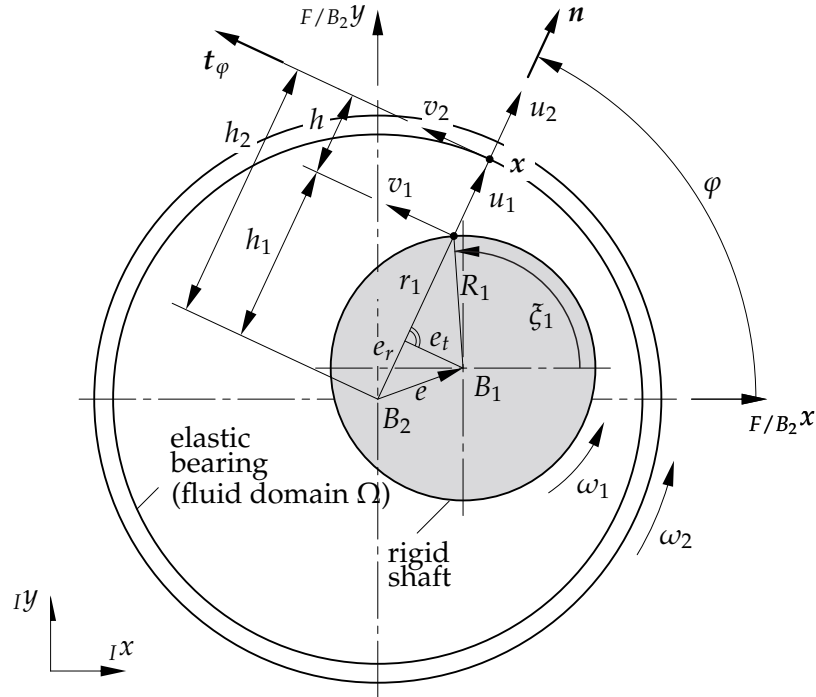


**Figure 2.7:** Kinematics in cylindrical journal bearing.

The fluid frame  $F$  is located in the center of the undeformed bearing and coincides with its body-fixed frame  $B_2$ , leading to  $\mathbf{x}_F = \mathbf{r}_{B_2}$ . Further, the cylindrical fluid domain is described by the coordinates  $(\varphi, z)$  and is attached to the undeformed bearing. Following relation between the new coordinate  $\varphi$  and the original coordinate  $y$  holds:

$$y = R_2 \varphi, \quad dy = R_2 d\varphi. \quad (2.82)$$

This transformation corresponds to an unwrapping of the cylindrical fluid domain into a plane, which is valid for a thin fluid film with  $h \ll R_2$ . Then, it follows for a point  $\mathbf{x}$  in the fluid domain and its normal and tangential vectors  $\mathbf{n}$  and  $\mathbf{t}_\varphi$ , respectively:

$${}^I\mathbf{x} = \begin{pmatrix} x_{B_2} \\ y_{B_2} \\ 0 \end{pmatrix} + \begin{pmatrix} R_2 \cos(\varphi) \\ R_2 \sin(\varphi) \\ z \end{pmatrix}, \quad {}^I\mathbf{n} = \begin{pmatrix} \cos(\varphi) \\ \sin(\varphi) \\ 0 \end{pmatrix}, \quad {}^I\mathbf{t}_\varphi = \begin{pmatrix} -\sin(\varphi) \\ \cos(\varphi) \\ 0 \end{pmatrix}.$$

Next, the position  $P_2$  of the deformable bearing house is described by the coordinates  $(\varphi, z)$  in the following way:

$${}^I\mathbf{r}_{P_2} = {}^I\mathbf{r}_{B_2} + {}^I\mathbf{r}_{B_2 P_2} = \begin{pmatrix} x_{B_2} \\ y_{B_2} \\ 0 \end{pmatrix} + \begin{pmatrix} (R_2 + \delta_r(\varphi, z)) \cos(\varphi) \\ (R_2 + \delta_r(\varphi, z)) \sin(\varphi) \\ z \end{pmatrix},$$

with the deformation  $\delta_r(\varphi, z)$  in radial direction. This vector  $\mathbf{r}_{P_2}$  always fulfills condition (2.79) and hence, the local height is given due to Eq. (2.80) as  $h_2(\varphi, z) = R_2 + \delta_r(\varphi, z)$ .

A position  $P_1$  on the surface of the rigid shaft is described by the surface parameters  $(\xi_1, \eta_1)$  as:

$${}^I\mathbf{r}_{P_1} = {}^I\mathbf{r}_{B_1} + {}^I\mathbf{r}_{B_1P_1} = \begin{pmatrix} x_{B_1} \\ y_{B_1} \\ 0 \end{pmatrix} + \begin{pmatrix} R_1 \cos(\xi_1) \\ R_1 \sin(\xi_1) \\ \eta_1 \end{pmatrix}.$$

Inserting this relation into condition (2.79), it results analytical expressions  $\xi_1(\varphi, z)$  and  $\eta_1(\varphi, z)$ : for  $\xi_1$ , it results  $\sin(\xi_1 - \varphi) = e_t/R_1$  and for  $\eta_1$ , it results  $\eta_1 = z$ . By defining the eccentricity  $e$  with its radial and tangential components  $e_r$  and  $e_t$ , respectively:

$${}^I\mathbf{e} = {}^I\mathbf{r}_{B_1} - {}^I\mathbf{r}_{B_2}, \quad e_r = {}^I\mathbf{e}^T {}^I\mathbf{n} = e_x \cos \varphi + e_y \sin \varphi, \quad e_t = {}^I\mathbf{e}^T {}^I\mathbf{t}_\varphi = -e_x \sin \varphi + e_y \cos \varphi,$$

the heights  $h_1$  and  $h$  can be calculated. Equation (2.80) yields:

$$h_1(\varphi, z) = e_r + r_1 = e_r + R_1 \sqrt{1 - (e_t/R_1)^2} \approx e_r + R_1$$

$$h(\varphi, z) = h_2 - h_1 = R_2 + \delta_r - e_r - r_1 \approx h_0 + \delta_r - e_x \cos \varphi - e_y \sin \varphi.$$

Here, an approximation for  $e_t \ll R_1$  is used and the radial clearance  $h_0$  is defined as  $h_0 = R_2 - R_1$ .

For the local velocities, the absolute velocities  ${}^I\dot{\mathbf{r}}_{P_i}$  of each body  $i \in \{1, 2\}$  are needed. Considering the rotation to be described by the rotational vector  ${}^I\boldsymbol{\omega}_i$ , they are given by:

$${}^I\dot{\mathbf{r}}_{P_i} = {}^I\dot{\mathbf{r}}_{B_i} + {}^I\boldsymbol{\omega}_i \times {}^I\mathbf{r}_{B_iP_i} + {}^I\mathbf{v}_{B_iP_i}, \quad i \in \{1, 2\},$$

with the relative velocity  ${}^I\mathbf{v}_{B_iP_i}$  in the inertia frame. Neglecting tilting rotational velocities and assuming the shaft to be rigid, the rotational vectors and the relative velocities for each body are given by:

$${}^I\boldsymbol{\omega}_1 = \begin{pmatrix} 0 \\ 0 \\ \omega_1 \end{pmatrix}, \quad {}^I\boldsymbol{\omega}_2 = \begin{pmatrix} 0 \\ 0 \\ \omega_2 \end{pmatrix}, \quad {}^I\mathbf{v}_{B_1P_1} = \begin{pmatrix} 0 \\ 0 \\ 0 \end{pmatrix}, \quad {}^I\mathbf{v}_{B_2P_2} = \begin{pmatrix} \delta_x \\ \delta_y \\ \delta_z \end{pmatrix}.$$

Here, the quantities  $\delta_x$ ,  $\delta_y$  and  $\delta_z$  are the velocities due to the elastic deformation in the inertia frame. From here, the local velocities  $u_i$ ,  $v_i$  and  $w_i$  can be calculated by using Eq. (2.81). The results for the velocities as well as the derivatives wrt. to  $y$  and  $z$  of all quantities can be found in Appendix D. There is also an order analysis given, where all second order terms due to  $h \ll R_2$  are neglected.

### Kinematics for the EHL point contact

An EHL point contact is depicted in Fig. 2.8 left. It consists of two rolling ellipsoids separated by a thin lubricating fluid film. Its numerical solution is topic of many articles in the literature, see [47, 48, 56, 77, 119, 121, 160, 192, 199] for an overview.

Under the assumption of a small contact zone compared to the curvature radii of the elements, the surface can be approximated by local paraboloids. The latter are described by the curvature radii  $R_{i,y}$  and  $R_{i,z}$  ( $i \in 1, 2$ ) in the local  $y$ - and  $z$ -direction, respectively. Further, this contact problem can be transformed into a contact problem of an elastic half-space and a paraboloid with the reduced curvature radii  $R_y$  and  $R_z$ , see Fig. 2.8 right. The elastic half-space takes into account the elastic deformation of both rolling elements. Its deformation in  $x$ -direction is denoted by  $\delta_x$ .

In the following, the fluid domain is attached to the undeformed surface of the half-space and the position  $x_F$  of the fluid frame  $F$  coincides with the position of both, the

inertia frame  $I$  as well as the body-fixed frame  $B_1$ . By using Eqs. (2.79) and (2.80), the local heights can be derived as follows:

$$\begin{aligned} h_1(y, z) &= \delta_x(y, z), \\ h_2(y, z) &= g_N + \frac{y^2}{2R_y} + \frac{z^2}{2R_z}, \\ \rightarrow h(y, z) &= g_N + \frac{y^2}{2R_y} + \frac{z^2}{2R_z} - \delta_x(y, z). \end{aligned}$$

Usually, in the EHL point contact, constant velocities in only one direction of the  $(y, z)$ -plane are analyzed. In the example of Fig. 2.8, the velocities  $w_1$  and  $w_2$  are set to zero, while  $v_1 = \text{const.}$  and  $v_2 = \text{const.}$ . The velocities in normal direction effect the squeezing motion by  $u_1 = \dot{\delta}_x$  and  $u_2 = \dot{g}_N$ . Note that in many cases of the literature, the squeeze effect is not considered, since stationary operation conditions are analyzed.

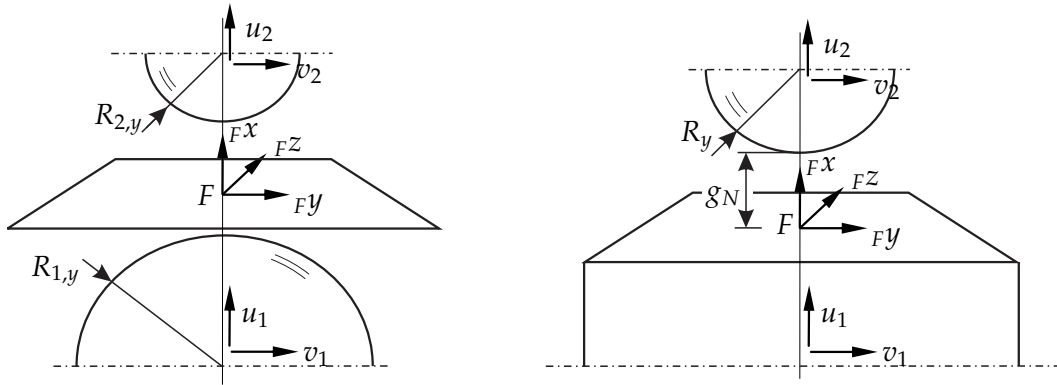


**Figure 2.8:** Kinematics in the EHL point contact.

#### 2.4.2 Fluid film forces

It is outlined, how the acting forces can be calculated from the pressure and the shear stresses in the lubricated contact. Section 2.1 already reveals the dependency of the shear stresses from the pressure and the kinematics, respectively.

Integrating over the body surface of the pressure in normal direction and of the shear stresses in tangential directions, respectively, gives the acting forces. They are defined on body  $i$  ( $i \in \{1, 2\}$ ) in the inertia frame  $I$  as follows:

$$\mathbf{F}_i = \int_{\Gamma_{f,i}} - (p \mathbf{n}_i + \tau_{xy,i} \mathbf{t}_{y,i} + \tau_{xz,i} \mathbf{t}_{z,i}) \, dA =: \int_{\partial B_i} \bar{\mathbf{t}}_i \, dA \quad (2.83)$$

with the outpointing normal vector  $\mathbf{n}_i$  of the lubricated surface  $\Gamma_{f,i}$  of body  $i$  and the tangential vectors  $\mathbf{t}_{y,i}$  and  $\mathbf{t}_{z,i}$ , respectively. The integration needs to be performed on each surface individually, each described by the respective parameters  $(\xi_i, \eta_i)$ .

However, due to the fact that the fluid film is thin, the assumption  $\mathbf{n} \approx \mathbf{n}_1 \approx -\mathbf{n}_2$  is often made. When further neglecting the influence of the shear stresses, which are different on both surfaces, then, the integration has to be done only once on the fluid domain  $\Omega$ , yielding:

$$\mathbf{F}_1 \approx -\mathbf{F}_2 \approx - \int_{\Omega} p(y, z) \mathbf{n}(y, z) \, d\Omega. \quad (2.84)$$

As far, only the resulting force is calculated. Its acting position is still unknown. In order to resolve this problem, the moment effect of the pressure has to be considered. The

moment  $M_i^{B_i}$  on body  $i$  wrt. the position of the point  $B_i$  can be calculated as follows:

$$M_{B_i} = - \int_{\Gamma_{f,i}} \mathbf{r}_{B_i P_i} \times (p \mathbf{n}_i + \tau_{xy,i} \mathbf{t}_{y,i} + \tau_{xz,i} \mathbf{t}_{z,i}) \, dA. \quad (2.85)$$

By considering this moment, the resulting force  $F_i$  is shifted to the point  $B_i$ .

In summary, Eqs. (2.83) and (2.85) give the force  $F_i$  at position  $B_i$  and the moment  $M_{B_i}$  wrt. the position of  $B_i$ , respectively. Looking at the example of the journal bearing of 2.4.1, the pressure in the bearing does not induce a moment, as the normal vector  $n_i$  always points into the direction of the vector  $\mathbf{r}_{B_i P_i}$ . However, the shear stresses induce a (friction) moment around the  $z$ -axis of the inertia frame.

Numerically, the resultant forces and moments are calculated by the FEM. By using the discrete values  $\tilde{\mathbf{p}}$  of the complete solution including the values at the DIRICHLET boundaries, following equations can be stated:

$$F_i = W_{p,i} \tilde{\mathbf{p}} + W_{sy,i} \tilde{\mathbf{s}}_{y,i} + W_{sz,i} \tilde{\mathbf{s}}_{z,i} \quad (2.86)$$

$$M_{B_i} = V_{p,i} \tilde{\mathbf{p}} + V_{sy,i} \tilde{\mathbf{s}}_{y,i} + V_{sz,i} \tilde{\mathbf{s}}_{z,i}, \quad (2.87)$$

where  $\tilde{\mathbf{s}}_{x,i}$  and  $\tilde{\mathbf{s}}_{y,i}$  denote the discrete values of the shear stresses at body  $i$  in  $y$ - and  $z$ -direction, respectively. The force and moment matrices can be calculated element-wise as follows, with  $k \in \{1, \dots, n_{node}\}$ :

$$\begin{aligned} W_{p,i} &= \mathbf{A}_{e=1}^{n_{ele}} \mathbf{w}_1(:,k), & \mathbf{w}_1(:,k) &= \int_{\Omega^{(e)}} \mathbf{n}_i N_k \, dA_i(\Omega), \\ W_{sy,i} &= \mathbf{A}_{e=1}^{n_{ele}} \mathbf{w}_2(:,k), & \mathbf{w}_2(:,k) &= \int_{\Omega^{(e)}} \mathbf{t}_{y,i} N_k \, dA_i(\Omega), \\ W_{sz,i} &= \mathbf{A}_{e=1}^{n_{ele}} \mathbf{w}_3(:,k), & \mathbf{w}_3(:,k) &= \int_{\Omega^{(e)}} \mathbf{t}_{z,i} N_k \, dA_i(\Omega), \\ V_{p,i} &= \mathbf{A}_{e=1}^{n_{ele}} \mathbf{v}_1(:,k), & \mathbf{v}_1(:,k) &= \int_{\Omega^{(e)}} (\mathbf{r}_{B_i P_i} \times \mathbf{n}_i) N_k \, dA_i(\Omega), \\ V_{sy,i} &= \mathbf{A}_{e=1}^{n_{ele}} \mathbf{v}_2(:,k), & \mathbf{v}_2(:,k) &= \int_{\Omega^{(e)}} (\mathbf{r}_{B_i P_i} \times \mathbf{t}_{y,i}) N_k \, dA_i(\Omega), \\ V_{sz,i} &= \mathbf{A}_{e=1}^{n_{ele}} \mathbf{v}_3(:,k), & \mathbf{v}_3(:,k) &= \int_{\Omega^{(e)}} (\mathbf{r}_{B_i P_i} \times \mathbf{t}_{z,i}) N_k \, dA_i(\Omega). \end{aligned}$$

The integration of the element matrices has to be performed on the fluid domain by using the surface parameters  $(\xi_i(y, z), \eta_i(y, z))$  in dependency of  $(y, z)$ . Attaching the fluid domain to one of both surfaces (for instance to surface 1) and using the simplification made in Eq. (2.84) circumvents this issue, as then  $\xi_1 = y$  and  $\eta_1 = z$ .

It is noted that here, in this section, only the resultant fluid forces and moments are calculated. For the case of an elastic surface with an additional FE mesh on the structure, methods from fluid-structure interaction have to be applied. This is treated in Sections 3.1.3 and 3.2.

## 2.5 Extended REYNOLDS equation and mixed lubrication

This section focuses on further physical effects in lubricated contacts. Here in this work, influences of surface roughness, fluid inertia and temperature effects are treated exemplary and their main concepts are explained. The book of SZERI [184] gives a good overview on the most common extensions based on the classical lubrication theory.

Section 2.5.1 deals with the mixed lubrication regime, where surface roughnesses on the one hand effect the pressure distribution and on the other hand can lead locally to a rigid body contact. Sections 2.5.2 and 2.5.3 show the main concepts of considering inertia and temperature effects in the EHL contacts, respectively

### 2.5.1 Mixed lubrication

The mixed lubrication theory takes into account the effects of surface roughness, see [19] for an overview. Methods from statistics allow a convenient description of asperities. Instead of modeling each singular asperity, they define average values and variances by using probability functions.

A very often used model, is the flow averaged REYNOLDS equation from PATIR and CHENG [142]. They use flow factors in order to adjust the flow between rough surfaces (height  $h_t$ ) to the flow between smooth surfaces (height  $h$ ). They derive following modified REYNOLDS equation:

$$-\nabla \cdot \left( \frac{h^3 \varrho}{12\eta} \begin{pmatrix} \Phi_y & 0 \\ 0 & \Phi_z \end{pmatrix} \nabla p \right) + \frac{\partial}{\partial y} \left( \varrho \bar{h}_t \frac{v_1 + v_2}{2} + \varrho \sigma \Phi_{sy} \frac{v_1 - v_2}{2} \right) + \frac{\partial(\bar{h}_t \varrho)}{\partial t} = 0. \quad (2.88)$$

For simplicity, the COUETTE flow in  $z$ -direction is neglected here. The pressure flow factors are  $\Phi_y$  and  $\Phi_z$  and the shear flow factor is  $\Phi_{sy}$ . Further,  $\bar{h}_t$  is defined as an averaged fluid height of the local film height  $h_t$ , which describes the rough surface. The variance  $\sigma$  corresponds to the mean roughness of the surface. In [142], analytical equations for the flow factors are given in dependence on the orientation of the roughness by assuming a GAUSSIAN distribution of the asperities. The concepts of PATIR and CHENG is adopted and enhanced by many researchers, see for instance [101, 157] or for an overview [19].

The surface roughnesses influence not only the flow between the surfaces, but they can also lead to very local rigid body contact situation. The latter effect can be treated by the same statistical methods as already mentioned.

For instance, GREENWOOD and TRIPP [71] approximate a contact pressure for isotropic and GAUSS-distributed rough surfaces under the assumption of an elastic deformation.

A further, often used model is proposed by BOWDEN and TABOR [24]. They take into account plastic deformation and state following formula for the contact pressure  $p_c$  in dependence of the height  $h$ :

$$p_c = \frac{H}{2} \left( 1 - \operatorname{erf} \left( \frac{h}{\sqrt{2}\sigma} \right) \right), \quad (2.89)$$

with the error-function  $\operatorname{erf}$  and the surface hardness  $H$ . The contact pressure, when described by such an analytical formula, needs to be added to the fluid pressure. It can be understood as a further force element with a high and nonlinear stiffness.

In summary, the concept of the modified REYNOLDS equation in combination with an analytical formula for the contact pressure can be included very well in the numerical framework described in the previous sections. For instance, it is shown in [133], where also a detailed analysis of the physical and numerical influence of mixed lubrication in the bearing simulation is given.

### 2.5.2 Inertia effects

The original REYNOLDS equation completely neglects inertia effects and assumes laminar flow conditions. However, these assumptions may not hold any more, when the fluid flow becomes turbulent, for example due to high rotational speeds, or when rapid

squeezing motion is present. For this reason, OSTERLE and SAIBEL [140] as well as PINKUS and STERNLICHT [147] follow the concept of an inertia extended REYNOLDS equation. The idea is to use averaged flow velocities in the fluid domain, which take into account the inertia effects. The resulting equations are often referred to as bulk flow equations.

This concept is adopted by many researchers: for example in [190], inertia is considered in bearings with large squeezing motion; or in [37], the REYNOLDS equation is extended to turbulent flow. Recently in [46], DOUSTI et al. give a review on the existing inertia averaged REYNOLDS equations and propose a unified extended REYNOLDS equation, capturing all inertia effects for both laminar and turbulent flow conditions. By neglecting the COUETTE flow in  $z$ -direction for simplicity, it reads as follows:

$$-\frac{\partial}{\partial y} \left( \frac{h^3 \varrho}{k_y \eta} \frac{\partial p}{\partial y} \right) - \frac{\partial}{\partial z} \left( \frac{h^3 \varrho}{k_z \eta} \frac{\partial p}{\partial z} \right) + \frac{\partial}{\partial y} \left( \varrho h \frac{v_1 + v_2}{2} \right) + \frac{\partial(h \varrho)}{\partial t} + I_t + I_c + \Gamma_c = 0,$$

where  $k_y$  and  $k_z$  are the turbulence coefficients as proposed in [37],  $\Gamma_c$  is the convective inertia term from [37] and  $I_t$  and  $I_c$  are a temporal and an additional convective inertia term, respectively. All three inertia terms depend on the pressure through the pressure driven average flow velocities. Thus, the equation can be solved in an iterative way, starting with the pressure solution of the REYNOLDS equation without inertia effects. In the temporal inertia term, the accelerations of the surfaces appear, ending up in a lubricate added mass, e. g. like in [163].

The concept of an averaged REYNOLDS equation can also be used for textured bearing surfaces, see [100], where a texture averaged REYNOLDS equation is developed.

In conclusion, the inertia effects can be included in the REYNOLDS equation by additional inertia terms in combination with flow factors. Their numerical treatment agrees with the use of the FEM, as proposed in the previous sections.

### 2.5.3 Temperature effects

The fluid properties, mainly the viscosity, do not only depend on the pressure, but also on the temperature. The theory of so-called thermal hydrodynamic lubricated (THL) and thermal elastohydrodynamic lubricated (TEHL) contacts considers such temperature effects. Here, only a short insight into the existing concepts is given. The interested reader is referred to the corresponding chapters of HAMROCK [81] or SZERI [184] or to the book of PINKUS [148] with their references inside.

In general, a 3-dimensional transient temperature field  $T(x, y, z, t)$  has to be solved in the fluid film in order to capture all heat sources and heat transfer paths. By this, the REYNOLDS equation has to be modified for temperature averaged fluid properties. Effects like heat convection in the fluid film or heat conduction in the contacting bodies can be fully considered by this approach. Usually, the temperature field in the surrounding bodies has to be solved additionally.

A simplification is often made by neglecting the heat conduction in the solid bodies and considering the convective heat transfer in the fluid film only. Then, the heat equation can be solved in the fluid domain  $(y, z)$  for the 2-dimensional temperature field  $T(y, z, t)$ . This temperature profile can be considered in the REYNOLDS equation by adding a temperature dependency to the fluid properties, especially to the viscosity.

In [53], ELING makes an even more severe simplification by applying a thermal network model to a rotor bearing system and considering one average temperature for the fluid film. Measurement data and comparisons to more detailed thermal models underline the potential of this method.

In conclusion, when considering temperature effects, an additional heat equation has to be solved for the temperature distribution and the REYNOLDS equation has to be modified for the consideration of thermal fluid properties.

## 2.6 Numerical examples

Different simulation examples demonstrate the physical solution of the REYNOLDS equation, but also the numerical behavior of the FE discretization and the cavitation algorithms.

The first example compares the different cavitation algorithms for the SWIFT-STIEBER condition and analyses the convergence in space. The second example validates the FEM solution of the mass-conservative cavitation condition by a reference solution from the literature. The third example demonstrates the effect of the SUPG stabilization in the FEM solution.

### 2.6.1 SWIFT-STIEBER condition: comparison of cavitation algorithms

The pressure solution of a journal bearing with a fixed eccentricity is analyzed. The SWIFT-STIEBER cavitation condition is imposed on the REYNOLDS equation and the numerical solution is calculated by using the different formulations and algorithms of Section 2.3.2. In detail, the SWIFT-STIEBER cavitation condition is imposed on the node values of the discretized REYNOLDS equation, meaning NCP (2.50) is solved.

First, the NEWTON-JOSEPHY algorithm explained by Eq. (2.51) is used for the solution of the NCP (2.50). Second, the penalty formulation (2.60) and third, the projection formulation (2.64) are applied. The latter two are solved by a NEWTON-RAPHSON method.

The rigid shaft has a fixed eccentricity of  $0.5 h_0$  in negative  $y$ -direction. Compressible fluid behavior is assumed by using the BARUS formula (2.8) for the viscosity and the formula (2.10) of DOWSON-HIGGINSON for the density. The detailed simulation parameters are listed in Table E.1 and can be found in Appendix E.1, where also a picture of the simulation example is given.

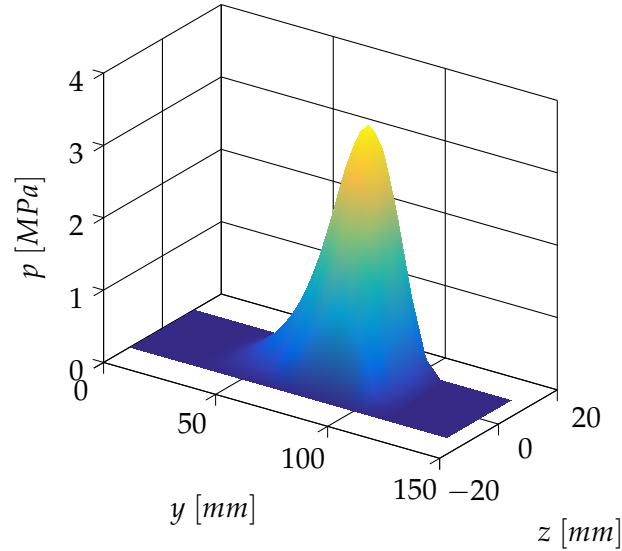
Figure 2.9 shows the numerical pressure distribution in the fluid domain  $(y, z)$ . For the FE solution, the *Quad8*-elements are used with 20 elements in  $y$ -direction and 5 elements in  $z$ -direction, respectively.

Table 2.1 left shows the number of global iterations, which are needed for each cavitation algorithm. It can be stated that the NEWTON-JOSEPHY method needs the smallest number of iterations, while the penalty-algorithm needs the largest number.

Looking at the norm of difference of the solutions in Table 2.1 right, reveals that the NEWTON-JOSEPHY algorithm and the one based on the projection formulation give the same solution. They both solve the NCP exactly. In contrast, the solution of the penalty formulation slightly differs. The reason is the regularization of the NCP by the penalty formulation.

**Table 2.1:** Comparison of cavitation algorithms for SWIFT-STIEBER condition.

algorithm	nb. of iterations	comparison	norm of difference
NEWTON-JOSEPHY	4	NEW.-JOS. – penalty	$1.68e-5 Pa$
penalty ( $\epsilon = 1e7$ )	7	NEW.-JOS. – projection	$4.21e-8 Pa$
projection ( $r = 1$ )	6	projection – penalty	$1.68e-5 Pa$



**Figure 2.9:** Pressure distribution for eccentric journal bearing.

### Convergence study

Here, the convergence of the finite element solution of the complementarity problem and its regularization by the penalty method are analyzed. In detail, the convergence of the discretization error is studied for the NCP (2.55) and the penalty formulation (2.57) using quadratic finite elements of the type *Quad8Mod*. For that purpose, a structured mesh is refined by selecting  $(n_{ele,y} \times n_{ele,z}) \in \{(20 \times 4), (40 \times 8), (60 \times 12), (80 \times 16), (120 \times 20)\}$ . The discretization error is measured in the  $L_2$ -norm, while a solution calculated on a very fine mesh serves as a reference solution.

Figure 2.10 summarizes the convergence of the discretization error for both formulations. While for the NCP, an  $O(h^{5/2})$  convergence is recognized, the error of the penalty formulation converges with  $O(h^3)$ . The  $O(h^{5/2})$  convergence of the NCP solution is in accordance with theoretical a priori error estimates given for unilateral contacts by WOHLMUTH et.al. [203]. In addition, the  $O(h^3)$  convergence of the penalty solution agrees well with the a priori error estimate for the regularized EHL problem given by WU and ODEN [208].

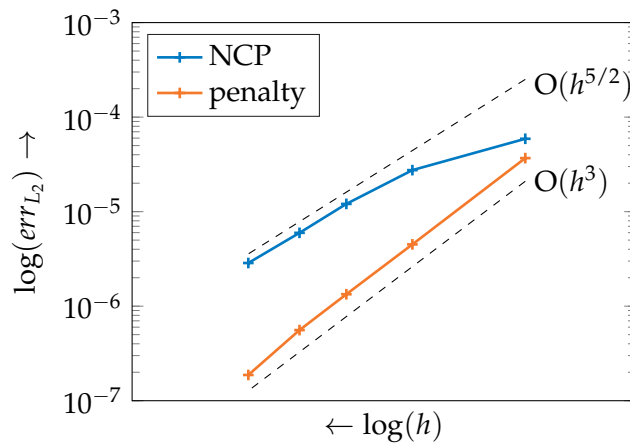


**Figure 2.10:** Convergence of the discretization error for NCP and penalty formulation using quadratic finite elements.

### 2.6.2 JFO condition: validation with solution from the literature

The stationary FEM solution of the JFO cavitation problem is compared with the numerical solution of an example from the literature. As reference solution serves the pressure and density distribution of a finite grooved journal bearing as calculated in [193, 210].

The journal bearing has a fixed eccentricity of  $0.6 h_0$ . It is flooded at an inlet at the position of the maximal height ( $\varphi = 0^\circ$ ) by setting the void coefficient  $\theta = \rho/\rho_c$  to 1.0001 at this inlet. The pressure is set to zero at the inlet as well as at the two boundaries in axial direction. A linear density-pressure relation and a constant viscosity are assumed. By defining the normalized pressure  $\bar{p} = (p h_0^2)/(R_2 v_1 \eta_{p=0})$ , the JFO problem can be formulated dimensionless. In Appendix E.2, the dimensionless simulation parameters as well as a figure of the simulation example are given.

Equation (2.74) is solved in combination with the projection formulation (2.77) for stationary flow conditions ( $\dot{q} = \mathbf{0}$ ). The SUPG stabilization with the parameter (2.78) is absolutely necessary for a stable solution. The nonlinear set of equations is solved by the NEWTON-RAPHSON method.

Figure 2.11 shows the distributions of the pressure and the void coefficient. It is the same result as in [193, 210]. The smooth transition of the density at the film rupture as well as the jump at the film reformation can be seen clearly. As mentioned, the jump is smeared due to the continuous shape functions.

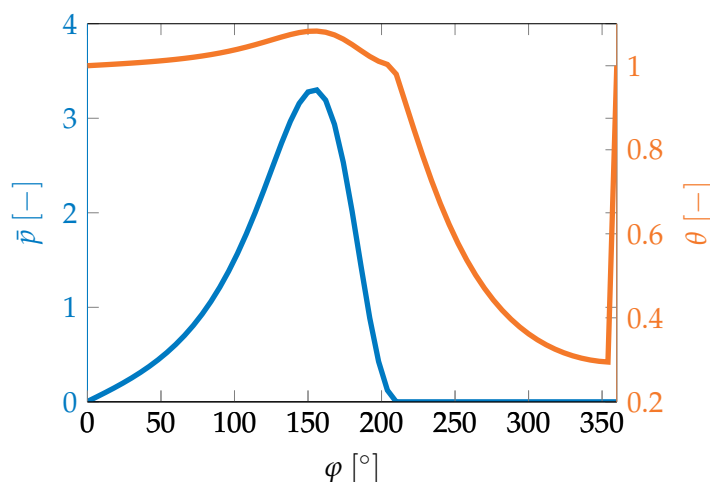


**Figure 2.11:** Distributions of pressure and film content in angular direction of a grooved journal bearing.

### 2.6.3 SWIFT-STIEBER condition: SUPG stabilization

Similar to Section 2.6.1, the pressure solution of a journal bearing with a fixed eccentricity is analyzed. Again, the SWIFT-STIEBER cavitation condition is imposed on the REYNOLDS equation. However, in this example, a highly viscous oil is used, which leads to such high pressure values that the SUPG stabilization of Section 2.2.2 has to be applied to the numerical solution. This example is similar to that of HOFER in [85].

The rigid shaft has a fixed eccentricity of  $0.245 h_0$  in negative  $y$ -direction. The density and the viscosity are chosen to depend on the pressure by the DOWSON-HIGGINSON formula (2.10) and the ROELANDS formula (2.9), respectively. The detailed simulation parameters are listed in Table E.3 and can be found in Appendix E.3.

For the FE solution, linear finite elements are used with 30 elements in  $y$ -direction and 5 elements in  $z$ -direction, respectively. While the pressure is discretized by the stan-

standard *Lin4* elements, the expansion flow is discretized by dual *Lin4* elements, fulfilling the bi-orthogonality condition (2.54). Thus, the NCP (2.55) is solved.

The numerical solution of the pressure distribution in angular direction in the middle of the bearing width is depicted in Fig. 2.12. The first solution is calculated without SUPG stabilization and therefore, numerical oscillations occur due to the dominating convective term at high pressure values. In contrast, when adding SUPG stabilization terms, the oscillations vanish in the numerical solution. The stabilization parameter is chosen according to Eq. (2.32).

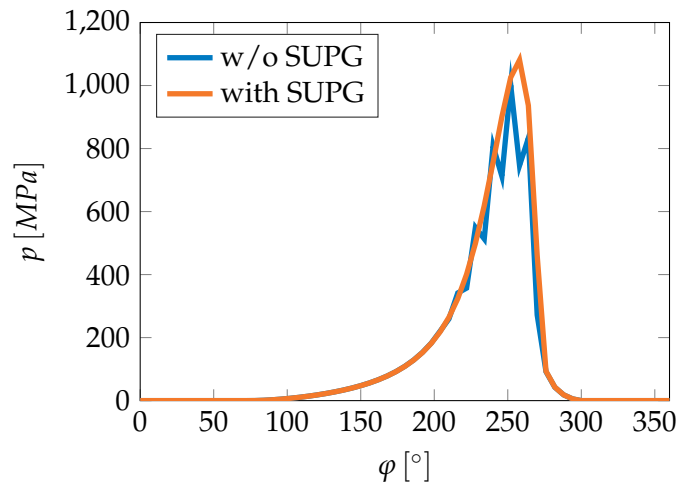


**Figure 2.12:** Numerical pressure solution with and without SUPG stabilization in angular direction of a journal bearing.

## Chapter 3

### Coupled system

The EHL contact represents a coupled system of hydrodynamic equations for the fluid and solid equations of the mechanical system, respectively. The focus of this thesis is an efficient coupling of both subsystems. Thus, after having introduced the hydrodynamic equations in Chapter 2, this chapter outlines now the governing equations of a mechanical multibody system (MBS) and realizes the numerical coupling of both subsystems.

Adequate interface coupling methodologies are important when the subsystems are discretized differently, e. g. by the use of different partitioned solvers for each subsystem. There can be differences in the discretization technique, in the mesh type or in the interpolation scheme. As a consequence, one has to deal with nonconforming fluid and structural meshes. Therefore, methods from fluid structure interaction (FSI) are applied for the interface coupling in the EHL contact.

The structure of this chapter is as follows: in Section 3.1, the governing equations of a rigid MBS are derived and the description of an elastic body by a floating frame of reference (FFR) formulation is given. On these basic formulations, the weak form of the coupled system is stated. Section 3.2 outlines a consistent and a conservative interface coupling strategy, which are both combined with different FSI transfer methods. With the described coupling conditions and methods, the discretized form of the coupled system is stated in Section 3.3. The numerical behavior and differences of the different coupling techniques are discussed in Section 3.4 for an academic example. A convergence analysis of the errors for the different methods is given.

#### 3.1 Multi-body system dynamics with lubricated contacts

In this section, the governing equations for a MBS including lubricated contacts are derived. The procedure is as follows: in Section 3.1.1, the dynamic equations of motion of a rigid MBS are derived from the principle of virtual work. Section 3.1.2 shows the treatment of elastic bodies in a MBS by using the FFR formulation. It is derived from the principle of virtual work as well. In Section 3.1.3, this principle of virtual work is extended by adding the weighted residuum of the pressure in the fluid film. The result is the weak form of the coupled system. For the following derivations, it is sufficient to treat only two bodies, as the equations can be easily extended to many bodies.

LAGRANGE'S principle of virtual work is used for the derivation of the mechanical equations. According to BREMER [27], it is stated for two bodies as follows:

$$\sum_{i=1}^2 \left[ \int_{B_i} \delta \mathbf{r}_{P_i}^T \ddot{\mathbf{r}}_{P_i} \, dm_i - \delta W_i \right] + \delta V_c = 0. \quad (3.1)$$

The first integral represents the variation of the kinetic energy of body  $B_i$  and  $\delta W_i$  represents the virtual work due to external and internal forces on body  $B_i$ . Similar to the text

book of WRIGGERS [206], the variation of the potential  $V_c$  of the contact forces is added in order to deal with constrained motion as well.

### 3.1.1 Rigid body motion

In this section, the dynamic equations of two rigid bodies with holonomic constraints are derived. The aim is to demonstrate the concept of virtual work, as it is later used for the coupled system as well. For detailed derivations and explanations, it is referred to the text books of BREMER [26], BREMER and PFEIFFER [28] and PFEIFFER and SCHINDLER [146].

The position of a point  $P_i$  on the rigid body  $i$  is denoted by the vector  $\mathbf{r}_{P_i}$ . It can be split up into a position of a body reference point  $\mathbf{r}_{C_i}$  and a relative position  ${}_{C_i}\mathbf{r}_{C_i P_i}$  denoted in the body fixed frame  $C_i$ . Here, the center of gravity  $C_i$  is chosen as body fixed reference point. It is noted that the left index of a vector signifies the referring coordinate system. If there is no left index, it implicitly means that the inertia frame is considered. Then, the vector  $\mathbf{r}_{P_i}$  and its variation  $\delta\mathbf{r}_{P_i}$  are given in the inertia frame, see for instance [26]:

$$\mathbf{r}_{P_i} = \mathbf{r}_{C_i} + {}_I\mathbf{A}_{C_i}(\boldsymbol{\theta}_i) {}_{C_i}\mathbf{r}_{C_i P_i}, \quad (3.2)$$

$$\delta\mathbf{r}_{P_i} = \delta\mathbf{r}_{C_i} - {}_I\mathbf{A}_{C_i} {}_{C_i}\tilde{\mathbf{r}}_{C_i P_i} \delta\boldsymbol{\Theta}_i, \quad (3.3)$$

with the rotation matrix  ${}_I\mathbf{A}_{C_i}(\boldsymbol{\theta}_i)$ , which transforms a vector from the body fixed frame  $C_i$  into the inertia frame  $I$ . The rotation is described by the vector  $\boldsymbol{\theta}_i$  of rotational pseudo parameters such that  $\delta\boldsymbol{\Theta}_i$  represents an infinitesimal virtual rotation. Together with the vector  $\mathbf{r}_{C_i}$ , it forms the vector of generalized pseudo coordinates  $\mathbf{q}_i = \left( \mathbf{r}_{C_i}^T \quad \boldsymbol{\theta}_i^T \right)^T$  of body  $i$ . The  $\sim$ -operator gives the skew-symmetric matrix corresponding to a matrix vector representation  $\tilde{\mathbf{a}}\mathbf{b}$  of the vector cross product  $\mathbf{a} \times \mathbf{b}$ .

Next, the absolute velocity and acceleration of  $P_i$  are given as:

$$\dot{\mathbf{r}}_{P_i} = \mathbf{v}_{C_i} + {}_I\mathbf{A}_{C_i}(\boldsymbol{\theta}_i) ({}_{C_i}\boldsymbol{\omega}_i \times {}_{C_i}\mathbf{r}_{C_i P_i}), \quad (3.4)$$

$$\ddot{\mathbf{r}}_{P_i} = \dot{\mathbf{v}}_{C_i} + {}_I\mathbf{A}_{C_i}(\boldsymbol{\theta}_i) ({}_{C_i}\dot{\boldsymbol{\omega}}_i \times {}_{C_i}\mathbf{r}_{C_i P_i} + {}_{C_i}\boldsymbol{\omega}_i \times {}_{C_i}\boldsymbol{\omega}_i \times {}_{C_i}\mathbf{r}_{C_i P_i}). \quad (3.5)$$

Here,  $\mathbf{v}_{C_i}$  is the absolute velocity of the center of gravity and  ${}_{C_i}\boldsymbol{\omega}_i$  is the rotational vector of body  $i$ . They are summarized as generalized velocities  $\dot{\mathbf{z}}_i = \left( \mathbf{v}_{C_i}^T \quad {}_{C_i}\boldsymbol{\omega}_i^T \right)^T$  and related to the generalized pseudo coordinates by  $\dot{\mathbf{z}}_i = \mathbf{H}(\mathbf{q}_i)\dot{\mathbf{q}}_i$  by the transformation matrix  $\mathbf{H}$ .

Further, the virtual work  $\delta W_i$  and the variation of the contact potential  $\delta V_c$  are needed. For  $\delta W_i$ , the virtual work  $\delta W_i^e$  of external forces  $\mathbf{F}_{C_i}$  and moments  ${}_{C_i}\mathbf{M}_{C_i}$  is considered only, without loss of generality. For  $\delta V_c$ , the vector  $\boldsymbol{\lambda}$  of LAGRANGE multipliers corresponding to a vector  $\boldsymbol{\Phi}(\mathbf{r}(\mathbf{q}), t)$  of constraint functions is introduced. It follows:

$$\delta W_i = \delta W_i^e = \delta\mathbf{r}_{C_i}^T \mathbf{F}_{C_i} + \delta\boldsymbol{\Theta}_i^T {}_{C_i}\mathbf{M}_{C_i}, \quad (3.6)$$

$$\delta V_c = \delta(-\boldsymbol{\lambda}^T \boldsymbol{\Phi}) = -\delta\boldsymbol{\lambda}^T \boldsymbol{\Phi} - \delta\boldsymbol{\Phi}^T \boldsymbol{\lambda}. \quad (3.7)$$

Inserting Eqs. (3.3) and (3.5) to (3.7) into the principle of virtual work (3.1) and integrating over each body  $i$ , ends up with following system of equations for the constrained motion of two rigid bodies:

$$\begin{bmatrix} m_1 \mathbf{I} & & & \\ & {}_{C_1}J_{C_1} & & \\ & & m_2 \mathbf{I} & \\ & & & {}_{C_2}J_{C_2} \end{bmatrix} \begin{pmatrix} \dot{\mathbf{v}}_{C_1} \\ {}_{C_1}\dot{\boldsymbol{\omega}}_1 \\ \dot{\mathbf{v}}_{C_2} \\ {}_{C_2}\dot{\boldsymbol{\omega}}_2 \end{pmatrix} = \begin{pmatrix} \mathbf{F}_{C_1} \\ {}_{C_1}\mathbf{M}_{C_1} \\ \mathbf{F}_{C_2} \\ {}_{C_2}\mathbf{M}_{C_2} \end{pmatrix} - \begin{pmatrix} \mathbf{0} \\ {}_{C_1}\tilde{\boldsymbol{\omega}}_1 {}_{C_1}J_{C_1} {}_{C_1}\boldsymbol{\omega}_1 \\ \mathbf{0} \\ {}_{C_2}\tilde{\boldsymbol{\omega}}_2 {}_{C_2}J_{C_2} {}_{C_2}\boldsymbol{\omega}_2 \end{pmatrix} + \mathbf{W}\boldsymbol{\lambda}, \quad (3.8)$$

$$\boldsymbol{\Phi}(\mathbf{r}(\mathbf{q}), t) = \mathbf{0}. \quad (3.9)$$

The matrix  ${}_{C_i}J_{C_i}$  represents the inertia tensor wrt. the center of gravity of body  $i$  and the matrix  $W = \frac{\partial \Phi}{\partial q}^T$  is the direction matrix of the LAGRANGE multiplier. The vectors  $F_{C_i}$  and  ${}_{C_i}M_{C_i}$  include all external forces and moments wrt. the center of gravity of each body, respectively. For instance, the force of Eq. (2.83) and the moment of Eq. (2.85) of the lubricated contact can be considered herein.

The system of Eqs. (3.8) and (3.9) represents the well known translational and rotational momentum equations with LAGRANGE multipliers enforcing the holonomic constraints of  $\Phi(r(q), t)$ . They are referred to as LAGRANGE's equations of the first kind, see [26, 146].

### 3.1.2 Flexible multibody dynamics

Flexible bodies in a MBS can be treated in different ways. Classical methods are the FFR, the absolute nodal coordinate (ANCF) or the co-rotated formulation, see for a review [172, 198]. Nevertheless, the description of flexible bodies is still a topic of research, as the generalized component mode synthesis approach in [143] shows for instance.

Here, the description of the FFR is used as a state-of-the-art formulation, since the coupling procedure would be similar for all other descriptions. The FFR formulation of one single elastic body is given in the following. As references serve the corresponding text books [27, 28, 170, 172, 173].

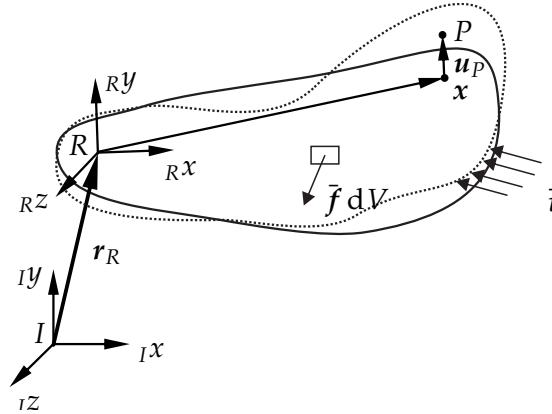


**Figure 3.1:** Kinematics and external forces in floating frame of reference formulation.

The kinematics of a body in the FFR formulation is depicted in Fig. 3.1. It is decomposed in a motion of the undeformed configuration wrt. the floating frame  $R$  and an overlaying elastic deformation. For an elastic continuum, one obtains for the position  $r_P$  of an arbitrary point  $P$  on the body and its variation  $\delta r_P$ , see for instance [173]:

$$r_P = r_R + {}_I A_R(\theta) {}_R(x + u_P) \quad (3.10)$$

$$\delta r_P = \delta r_R - {}_I A_R(\theta) {}_R(x + u_P) \delta \Theta + {}_I A_R(\theta) \delta_R u_P \quad (3.11)$$

where  $r_R$  is the position of the FFR,  ${}_I A_R(\theta)$  is the rotation matrix depending on the vector  $\theta$  of the rotational parameters of the FFR,  $x$  is the position of  $P$  in the undeformed configuration and  $u_P$  is the elastic deformation of  $P$ .

For the dynamics in the FFR, the velocity  $\dot{r}_P$  and the acceleration  $\ddot{r}_P$  are needed. They are given by:

$$\begin{aligned} \dot{r}_P &= \dot{v}_R + {}_I A_R(\theta) ({}_R \omega \times {}_R(x + u_P) + {}_R \dot{u}_P), \\ \ddot{r}_P &= \ddot{v}_R + {}_I A_R(\theta) ({}_R \dot{\omega} \times {}_R(x + u_P) + {}_R \ddot{u}_P) + \end{aligned} \quad (3.12)$$

$$\underbrace{{}_I A_R(\boldsymbol{\theta}) ({}_R \boldsymbol{\omega} \times {}_R \boldsymbol{\omega} \times {}_R (\mathbf{x} + \mathbf{u}_P) + 2 {}_R \boldsymbol{\omega} \times {}_R \dot{\mathbf{u}}_P)}_{\boldsymbol{\xi}}. \quad (3.13)$$

Further, the virtual work  $\delta W$  is needed. It is split up into the variation of the inner potential  $V_{int}$  of elastic deformation and the virtual work  $\delta W^e$  of external forces. Assuming isotropic linear elastic material behavior and small deformations, HOOKE'S law holds for the elastic deformation. With the vectors  $\bar{\mathbf{f}}$  and  $\bar{\mathbf{t}}$  of external body forces and surface tractions respectively (see Fig. 3.1), the virtual work yields:

$$\begin{aligned} \delta W &= -\delta V_{int} + \delta W^e \\ &= -\int_B \delta \boldsymbol{\varepsilon}(\mathbf{u})^T \mathbf{G} \boldsymbol{\varepsilon}(\mathbf{u}) \, dV + \int_B \delta \mathbf{r}_P^T \bar{\mathbf{f}} \, dV + \int_{\Gamma_t} \delta \mathbf{r}_P^T \bar{\mathbf{t}} \, dA, \end{aligned} \quad (3.14)$$

with the vector  $\boldsymbol{\varepsilon}$  collecting the elastic strain components and the material matrix  $\mathbf{G}$ , describing a linear relation between stress and strain. The NEUMANN boundary, where the surface tractions act, is denoted by  $\Gamma_t$ .

In the following, the deformation field  ${}_R \mathbf{u}(\mathbf{x}, t)$  is approximated by the RITZ approach. The RITZ approach claims linearly independent shape functions, which fulfill the geometric boundary conditions of the elastic deformation field. The standard FEM is a special form of the RITZ approach, using locally defined shape functions, see [28]. Hence, following approximation is used:

$${}_R \mathbf{u}_P = {}_R \mathbf{u}(\mathbf{x}, t) \approx \mathbf{N}(\mathbf{x}) \mathbf{d}(t) = \mathbf{N}(\mathbf{x}) \mathbf{P} \mathbf{q}_{el}(t), \quad \text{with } \mathbf{d}(t) = \mathbf{P} \mathbf{q}_{el}(t) \quad (3.15)$$

with the matrix  $\mathbf{N}(\mathbf{x})$  of the shape functions and the time-dependent vector  $\mathbf{d}$  of the discrete displacements. It is related to a vector  $\mathbf{q}_{el}$  of generalized elastic coordinates by a transformation matrix  $\mathbf{P}$ , which will be specified more below. By this, the vector  $\mathbf{q} = (\mathbf{r}_R^T \quad \boldsymbol{\theta}^T \quad \mathbf{q}_{el}^T)^T$  of generalized pseudo coordinates of the body can be defined as well as the generalized velocities  $\dot{\mathbf{z}} = (\mathbf{v}_R^T \quad {}_R \boldsymbol{\omega}^T \quad \dot{\mathbf{q}}_{el}^T)^T$ . The relation between generalized velocities and coordinates is given by  $\dot{\mathbf{z}} = \mathbf{H}(\mathbf{q}) \dot{\mathbf{q}}$ . With them, one obtains the velocity and the acceleration of a point  $P$  on the body as:

$$\dot{\mathbf{r}}_P = \left( \mathbf{I} \quad -{}_I A_R(\boldsymbol{\theta}) {}_R (\mathbf{x} + \widetilde{\mathbf{N}}(\mathbf{x}) \mathbf{P} \mathbf{q}_{el}) \quad {}_I A_R(\boldsymbol{\theta}) \mathbf{N}(\mathbf{x}) \mathbf{P} \right) \dot{\mathbf{z}} = \mathbf{T}(\mathbf{q}) \dot{\mathbf{z}}, \quad (3.16)$$

$$\ddot{\mathbf{r}}_P = \mathbf{T}(\mathbf{q}) \ddot{\mathbf{z}} + \boldsymbol{\xi}, \quad (3.17)$$

with the state-dependent matrix  $\mathbf{T}$  and the abbreviation  $\boldsymbol{\xi}$  of Eq. (3.13). In the same way, the approximation of Eq. (3.15) can be used for the variation in Eq. (3.11) and the virtual work of Eq. (3.14). Then, all these quantities can be inserted in the principle of virtual work (3.1) and its discretized form is obtained. The first integral gives the mass matrix  $\mathbf{M}$  and the vector  $\mathbf{h}_\omega$  of nonlinear inertia forces. For the mass matrix  $\mathbf{M}$  follows:

$$\mathbf{M} = \int \mathbf{T}^T \mathbf{T} \, dm = \begin{bmatrix} m\mathbf{I} & \text{sym.} \\ m_R \tilde{\mathbf{c}} \mathbf{A}^T & \mathbf{J} \\ \mathbf{C}_t \mathbf{A}^T & \mathbf{C}_r \quad \mathbf{M}_{el} \end{bmatrix}, \quad (3.18)$$

with

$$m = \int dm,$$

$$m_R \tilde{\mathbf{c}} = \int {}_R (\mathbf{x} + \widetilde{\mathbf{N}}(\mathbf{x}) \mathbf{P} \mathbf{q}_{el}) \, dm = m_R \tilde{\mathbf{c}}_0 + (\mathbf{C}_t^T \mathbf{q}_{el}),$$

$$\mathbf{J} = \int {}_R (\mathbf{x} + \widetilde{\mathbf{N}}(\mathbf{x}) \mathbf{P} \mathbf{q}_{el})^T {}_R (\mathbf{x} + \widetilde{\mathbf{N}}(\mathbf{x}) \mathbf{P} \mathbf{q}_{el}) \, dm = \mathbf{J}_0 + \mathbf{J}_1 + \mathbf{J}_2,$$

$$\begin{aligned}
\mathbf{C}_t &= \int \mathbf{P}^T \mathbf{N}(\mathbf{x})^T \, dm, \\
\mathbf{M}_{el} &= \int \mathbf{P}^T \mathbf{N}(\mathbf{x})^T \mathbf{N}(\mathbf{x}) \mathbf{P} \, dm = \mathbf{P}^T \mathbf{M}_{FE} \mathbf{P}, \\
\mathbf{C}_r &= - \int \mathbf{P}^T \mathbf{N}(\mathbf{x})^T \mathbf{R}(\mathbf{x} + \widetilde{\mathbf{N}}(\mathbf{x}) \mathbf{P} \mathbf{q}_{el}) \, dm = \mathbf{C}_{r,0} + \mathbf{C}_{r,1}.
\end{aligned}$$

Here,  $m$  is the mass of the body,  $\mathbf{c}$  is the position of the center of mass in the deformed configuration,  $\mathbf{J}$  is the inertia tensor in the deformed configuration and  $\mathbf{M}_{el}$  is the mass matrix of the generalized elastic coordinates  $\mathbf{q}_{el}$ . The mass matrix  $\mathbf{M}_{FE}$  belongs to the displacement vector  $\mathbf{d}$  of the original FE system. The terms  $\mathbf{C}_t$  and  $\mathbf{C}_r$  couple the inertia of the elastic degrees of freedom (DOFs) with the inertia of the translational and rotational DOFs, respectively. As can be seen, the terms  $m\tilde{\mathbf{c}}$ ,  $\mathbf{J}$  and  $\mathbf{C}_r$  can be developed in zero, first and second order terms (indicated by index 0, 1 and 2), while the zero order terms correspond to the undeformed configuration. Usually, the second order term  $J_2$  of the rotational inertia is neglected. A detailed description of the computation of the different integrals of the generalized mass matrix (3.18) for a linear finite element model is given in [170]. In addition, a standardization of the input data needed for flexible multibody dynamics is outlined in [197].

According to [170], the vector  $\mathbf{h}_\omega$  of inertia forces is derived as follows:

$$\mathbf{h}_\omega = - \int \mathbf{T}^T \boldsymbol{\xi} \, dm = \begin{pmatrix} - \int \mathbf{A}_R \tilde{\boldsymbol{\omega}} ({}_R \tilde{\boldsymbol{\omega}} \mathbf{R}(\mathbf{x} + \mathbf{N}(\mathbf{x}) \mathbf{d}) + 2 \mathbf{N}(\mathbf{x}) \dot{\mathbf{d}}) \, dm \\ - \int {}_R(\mathbf{x} + \widetilde{\mathbf{N}}(\mathbf{x}) \mathbf{d}) \tilde{\boldsymbol{\omega}} ({}_R \tilde{\boldsymbol{\omega}} \mathbf{R}(\mathbf{x} + \mathbf{N}(\mathbf{x}) \mathbf{d}) + 2 \mathbf{N}(\mathbf{x}) \dot{\mathbf{d}}) \, dm \\ - \int \mathbf{P}^T \mathbf{N}(\mathbf{x})^T \tilde{\boldsymbol{\omega}} ({}_R \tilde{\boldsymbol{\omega}} \mathbf{R}(\mathbf{x} + \mathbf{N}(\mathbf{x}) \mathbf{d}) + 2 \mathbf{N}(\mathbf{x}) \dot{\mathbf{d}}) \, dm \end{pmatrix}.$$

For the computation of the integrals, following form can be stated:

$$\mathbf{h}_\omega = \begin{pmatrix} -2 \mathbf{A}_R \tilde{\boldsymbol{\omega}} \mathbf{C}_t^T \dot{\mathbf{q}}_{el} - m \mathbf{A}_R \tilde{\boldsymbol{\omega}} \mathbf{R} \tilde{\boldsymbol{\omega}} \mathbf{c} \\ -{}_R \tilde{\boldsymbol{\omega}} \mathbf{J} \mathbf{R} \boldsymbol{\omega} - \mathbf{G}_r \mathbf{R} \boldsymbol{\omega} \\ -\mathbf{R} \boldsymbol{\omega}^T \mathbf{O}_e \mathbf{R} \boldsymbol{\omega} - \mathbf{G}_e \mathbf{R} \boldsymbol{\omega} \end{pmatrix},$$

where some of the terms already appear in the mass matrix (3.18) and therefore, only the remaining three integrals have to be solved:

$$\begin{aligned}
\mathbf{G}_r &= -2 \int {}_R(\mathbf{x} + \widetilde{\mathbf{N}}(\mathbf{x}) \mathbf{P} \mathbf{q}_{el}) (\mathbf{N}(\mathbf{x}) \mathbf{P} \mathbf{q}_{el}) \, dm = \mathbf{G}_{r,0} + \mathbf{G}_{r,1}, \\
\mathbf{G}_e &= -2 \int \mathbf{P}^T \mathbf{N}(\mathbf{x})^T (\mathbf{N}(\mathbf{x}) \mathbf{P} \mathbf{q}_{el}) \, dm, \\
\mathbf{O}_e &= \int \widetilde{\mathbf{N}}(\mathbf{x}) \mathbf{P} \mathbf{R}(\mathbf{x} + \widetilde{\mathbf{N}}(\mathbf{x}) \mathbf{P} \mathbf{q}_{el}) \, dm.
\end{aligned}$$

For the detailed computation of these terms with the input data of a linear finite element model, it is referred again to [170].

Next, the evaluation of the virtual work (3.14) leads to the vector  $\mathbf{h}_{el}$  of elastic forces and the vector  $\mathbf{h}_{ext}$  of external forces. Further, the vector  $\mathbf{h}_g$  of the gravity force can be computed by considering the constant gravity acceleration  $\mathbf{g}$ . They are calculated as follows:

$$\begin{aligned}
\mathbf{h}_{el} &= \begin{pmatrix} \mathbf{0} \\ \mathbf{0} \\ -\mathbf{K}_{el} \mathbf{q}_{el} - \mathbf{D}_{el} \dot{\mathbf{q}}_{el} \end{pmatrix}, \quad \mathbf{h}_{ext} = \int_B \mathbf{T}^T \bar{\mathbf{f}} \, dV + \int_{\Gamma_t} \mathbf{T}^T \bar{\mathbf{t}} \, dA, \\
\mathbf{h}_g &= \int \mathbf{T}^T \mathbf{g} \, dm = \begin{pmatrix} m \mathbf{I} \\ m \mathbf{R} \tilde{\mathbf{c}} \mathbf{A}^T \\ \mathbf{C}_t \mathbf{A}^T \end{pmatrix} \mathbf{g}.
\end{aligned}$$

Here, the internal potential leads to the linear stiffness matrix  $K_{el}$ . A damping matrix  $D_{el}$  is added and can be chosen proportional to the stiffness and/or mass matrix or modal damping can be used.

Summarized, following system of equations for the dynamics of a flexible body can be written:

$$H(\mathbf{q}) \dot{\mathbf{q}} = \dot{\mathbf{z}}, \quad (3.19)$$

$$M(\mathbf{q}) \ddot{\mathbf{z}} = \mathbf{h}_\omega + \mathbf{h}_g + \mathbf{h}_{el} + \mathbf{h}_{ext}. \quad (3.20)$$

### Definition of the reference frame

In the FFR formulation, the rigid body motion is described by the motion of the reference frame  $R$ . Thus, for a unique description, the elastic deformation field  ${}_R \mathbf{u}(\mathbf{x}, t)$  is not allowed to exhibit additional rigid body motion. In the following, the transformation matrix  $P$  introduced in Eq. (3.15) is used to remove the rigid body motion from the discrete displacement field  $\mathbf{d}$ . There are different ways on how to restrict the rigid body motion, leading to different definitions of the reference frame, see for instance [171].

A first definition is given by restricting the deformation of different nodes of the elastic body, such that the three translational and the three rotational DOFs of the rigid body motion are omitted. One example would be to attach the floating frame to one single node of the elastic body by clamping the six DOFs of this node. It means that the deformation of the reference point  $R$  must vanish, i. e.  ${}_R \mathbf{u}_R = \mathbf{0}$ . However, this choice requires that the reference node has three translational and three rotational DOFs, which is for instance not the case for a linear FE system with translational deformation degrees only. Therefore, another choice would be to restrict six translational DOFs of three points on the body, which do not lie on a line, such that no rigid body motion is possible. In all cases, the matrix  $P$  can be constructed as a transformation matrix between the restricted and unrestricted coordinates vectors  $\mathbf{q}_{el}$  and  $\mathbf{d}$ , respectively.

Another definition of the reference frame is given by choosing it such that the linear and angular momentum of the elastic deformation field are vanishing. Then, the following two conditions have to hold, see for instance [171]:

$$C_t^T \dot{\mathbf{q}}_{el} = \mathbf{0}, \quad C_r^T \dot{\mathbf{q}}_{el} = \mathbf{0}.$$

This condition leads to a vanishing center of gravity  $c$  at every time and thereby, the floating frame is attached to the center of gravity of the deformed configuration, meaning  $R \rightarrow C$ . Such a frame is referred as TISSERANT frame or mean-axis frame, which has the nice property of a block-diagonal mass matrix or of a minimum kinetic energy due to elastic deformation. When fulfilling the linearized condition  $C_{r,0} \dot{\mathbf{d}} = \mathbf{0}$  only, the frame is referred to as BUCKEN's frame, which has the property of leading the smallest deformations in the linearized configuration. It can be shown that the condition of the BUCKEN's frame holds, when the matrix  $P$  contains in its columns a set of vibration modes – and no rigid body modes – of the free floating structure, see for instance [170].

### 3.1.3 Coupled system equations

This section outlines the weak form of the coupled system with the main focus on the lubricated interfaces. The weak form of the previous section is extended for the constrained motion of two elastic bodies having a lubricated interface. For the sake of clearness, in the following, only bilateral constraints in normal directions are considered. However, the treatment of unilateral and/or frictional contacts can be included as well into the formulations.

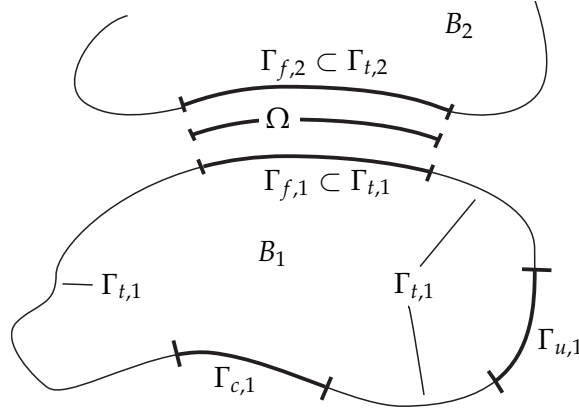


**Figure 3.2:** Computational domains for the coupled system.

The different computational domains of the coupled system are depicted in Fig. 3.2. The surface  $\partial B_i$  of body  $B_i$  consists of the DIRICHLET boundary  $\Gamma_{u,i}$ , the NEUMANN boundary  $\Gamma_{t,i}$  and the contact surface  $\Gamma_{c,i}$ , yielding:

$$\partial B_i = \Gamma_{u,i} \cup \Gamma_{t,i} \cup \Gamma_{c,i} \quad \text{with} \quad \Gamma_{u,i} \cap \Gamma_{t,i} \cap \Gamma_{c,i} = \emptyset.$$

On the contact surface  $\Gamma_{c,i}$ , holonomic constraints given by the vector  $\Phi$  of constraint functions are taken into account. The contact potential is defined by  $V_c = \lambda \Phi$ . Its variation is given as

$$\delta V_c = - \int_{\Gamma_c} \delta \Phi^T \lambda \, dA - \int_{\Gamma_c} \delta \lambda^T \Phi \, dA = - \int_{\Gamma_c} \delta r_p^T \frac{\partial \Phi^T}{\partial r_p} \lambda \, dA - \int_{\Gamma_c} \delta \lambda^T \Phi \, dA.$$

This variation together with the virtual work (3.14) of an elastic body can be inserted in the principle of virtual work (3.1). It gives the following weak form for the constrained motion of two elastic bodies:

$$\begin{aligned} \sum_{i=1}^2 \left[ \int_{B_i} \delta r_{p_i}^T \ddot{r}_{p_i} \, dm_i + \int_{B_i} \delta \varepsilon(\mathbf{u}_{p_i})^T \mathbf{H} \varepsilon(\mathbf{u}_{p_i}) \, dV - \int_{B_i} \delta r_{p_i}^T \bar{f}_i \, dV \right. \\ \left. - \int_{\Gamma_{t,i}} \delta r_{p_i}^T \bar{t}_i \, dA - \int_{\Gamma_c} \delta r_{p_i}^T \mathbf{W}_i \lambda \, dA \right] = 0, \\ \int_{\Gamma_c} \delta \lambda^T \Phi \, dA = 0, \end{aligned}$$

which must hold for all admissible  $\delta r_{p_i}$  and  $\delta \lambda$ .

Next, this weak form is extended by the weak form of the hydrodynamic equations. For simplicity, it is assumed that the surface tractions from the hydrodynamics are the only acting forces.

By adding the weak form (2.53) of the REYNOLDS equation with the SWIFT-STIEBER cavitation condition, one obtains the following weak form for the constrained motion of two deformable bodies with a lubricated contact:

$$\sum_{i=1}^2 \left[ \int_{B_i} \delta r_{p_i}^T \ddot{r}_{p_i} \, dm_i + \int_{B_i} \delta \varepsilon(\mathbf{u}_{p_i})^T \mathbf{H} \varepsilon(\mathbf{u}_{p_i}) \, dV - \int_{B_i} \delta r_{p_i}^T \bar{f}_i \, dV \right. \\ \left. - \int_{\Gamma_{f,i}} \delta r_{p_i}^T \bar{t}_i(p_i, \mathbf{r}_{p_i}, \dot{\mathbf{r}}_{p_i}) \, dA - \int_{\Gamma_c} \delta r_{p_i}^T \mathbf{W}_i \lambda \, dA \right] = 0, \quad (3.21)$$

$$\int_{\Gamma_c} \delta \lambda^T \Phi \, dA = 0, \quad (3.22)$$

$$\int_{\Omega} (\delta p - p_{ref}) f(p, \mathbf{r}_{p_1}, \mathbf{r}_{p_2}, \dot{\mathbf{r}}_{p_1}, \dot{\mathbf{r}}_{p_2}) \, dA \geq 0. \quad (3.23)$$

Here, the weighting function  $w$  of Eq. (2.62) is replaced by  $\delta p$ , clearly indicating that  $\delta p$  is the variation of  $p$ . This form must hold for all admissible  $\delta \mathbf{r}_{P_i}$ ,  $\delta \lambda$  and  $\delta p$ . The coupling between the mechanical system and the hydrodynamics is indicated by the surface traction  $\bar{\mathbf{t}}_i(p_i, \mathbf{r}_{P_i}, \dot{\mathbf{r}}_{P_i})$  and the nonlinear function  $f$  of the REYNOLDS equation. They are both depending on the pressure and the kinematics due to Eq. (2.83) and Eq. (2.42), respectively. It is noted that all other weak formulations of Eqs. (2.43), (2.57) and (2.62) could have been added instead of Eq. (2.53).

Also the mass conservative cavitation model can be added to the mechanical virtual work. Then, instead of Eq. (3.23), the following two equations have to be considered, see Section 2.3.3 and Appendix C.1:

$$\int_{\Omega} \delta p (h(\mathbf{r}_{P_1}, \mathbf{r}_{P_2}) \dot{q} + f(p, q, \mathbf{r}_{P_1}, \mathbf{r}_{P_2}, \dot{\mathbf{r}}_{P_1}, \dot{\mathbf{r}}_{P_2})) \, dA = 0,$$

$$\int_{\Omega} (\delta q - (f_q(p) - q)) p_{ref} \, dA \geq 0,$$

with now the density as further state variable. The weighting function  $q$  of Eq. (C.3) is replaced by  $\delta q$ . Again, this form must hold for all admissible  $\delta \mathbf{r}_{P_i}$ ,  $\delta \lambda$ ,  $\delta p$  and  $\delta q$ . The solution and weighting spaces are analyzed in more detail in Section 3.3.

## 3.2 Interface coupling methodologies

This section addresses the numerical coupling of the lubricated interfaces. During the discretization of the solid and the fluid domain, non-conforming meshes may occur for different reasons: For example, the elastic body may be discretized by a commercial FE tool using an unstructured mesh, while the fluid domain is discretized on a structured mesh. The use of different interpolation functions for deformation and pressure may also lead to dissimilar meshes. These aspects require adequate coupling conditions between the subdomains as well as properly defined transfer methods.

The problem of non-conforming meshes in FSI is treated by many researchers, see [41, 57, 87, 97, 152, 161]. YANG and LAURSEN [209] and POPP [151] treat the FSI problem in EHL contacts by using the mortar method. However, a detailed study of the interface problem for EHL contacts does not exist yet. Therefore, in this thesis, the most common methods are analyzed for the EHL contact problem. These are the methods described in the work of DEBOER [42] and the work of POPP [151].

First, this section outlines a consistent and a conservative coupling strategy. On their basis, adequate transfer methods for the discrete surface fields are given in a second step.

### 3.2.1 Consistent and conservative coupling strategy

At the interface between fluid and structure, surface tractions as well as deformations are exchanged; their numerical compatibility has to be enforced. In the following, the surface tractions on the fluid domain are denoted by  $\boldsymbol{\mu}_i^F$ , with the index  $F$  denoting the fluid domain and the index  $i$  denoting the interface to body  $i$  ( $i \in \{1, 2\}$ ). According to Eq. (2.83), the relation  $\boldsymbol{\mu}_i^F = \bar{\mathbf{t}}_i$  on  $\Gamma_{f,i}^F$  holds and from now on, it is used in the EHL interface problem described by Eqs. (3.21) to (3.23). The interface  $\Gamma_{f,i}^F$  is the projection of the fluid domain  $\Omega$  onto the surface of body  $i$ .

For the continuous system, the following three conditions hold for the surface tractions and the deformation field on the interface  $\Gamma_{f,i}$  with  $i \in \{1, 2\}$ :

$$\mathbf{u}_i^F = \mathbf{u}_i^S \quad \text{on } \Gamma_{f,i}, \quad (3.24)$$

$$\boldsymbol{\mu}_i^F = \boldsymbol{\mu}_i^S \quad \text{on } \Gamma_{f,i}, \quad (3.25)$$

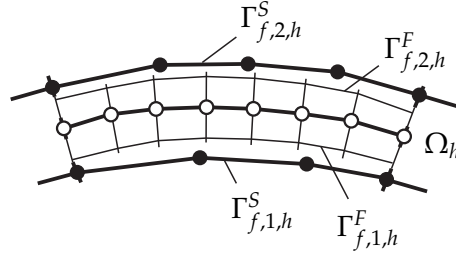


**Figure 3.3:** Discretized surfaces and computational domain for the coupled system.

$$\int_{\Gamma_{f,i}^F} (\boldsymbol{\mu}_i^F)^T \mathbf{u}_i^F \, dA = \int_{\Gamma_{f,i}^S} (\boldsymbol{\mu}_i^S)^T \mathbf{u}_i^S \, dA. \quad (3.26)$$

The index  $S$  denotes a surface field that belongs to the interface  $\Gamma_{f,i}^S$  of the elastic body  $i$ . While the first two Eqs. (3.24) and (3.25) represent conditions for the individual interface fields, the third condition ensures the conservation of the interface energy. For the continuous system, it follows that, if two of the three above stated conditions are fulfilled, the third one is fulfilled automatically. The reason is that in the continuous system, the lubricated interfaces are identical, meaning  $\Gamma_{f,i} = \Gamma_{f,i}^F = \Gamma_{f,i}^S$ .

This relation is not valid anymore, when the surfaces are discretized and thereby non-matching meshes are used; the discretized surfaces – indicated in the following by the subscript  $h$  – are not identical any more, see Fig. 3.3. Further, the three conditions of Eqs. (3.24) to (3.26) in their discretized form can not be fulfilled all at once any more. Depending on which two of the three conditions are maintained in the discrete setting, denoted as a consistent or a conservative coupling approach. Both are described in the following in more detail. As a reference serves the work of DE BOER [42].

### Consistent coupling approach

The consistent coupling approach ensures compatibility such that constant distributions of both deformations and surface tractions remain constant over the interfaces. Consistency follows, when the first two conditions (3.24) and (3.25) hold. Besides the already stated strong formulation, these conditions can also be given in a weak form. Then, it is referred as mortar method, which is originally proposed by BERNARDI [13]. The weak form of the strong conditions Eqs. (3.24) and (3.25) reads as:

$$\int_{\Gamma_{f,i}} (\delta \boldsymbol{\mu}_i^F)^T (\mathbf{u}_i^F - \mathbf{u}_i^S) \, dA = 0, \quad (3.27)$$

$$\int_{\Gamma_{f,i}} (\delta \mathbf{u}_i^S)^T (\boldsymbol{\mu}_i^F - \boldsymbol{\mu}_i^S) \, dA = 0, \quad (3.28)$$

with  $\delta \boldsymbol{\mu}_i^F$  and  $\delta \mathbf{u}_i^S$  being variations of the corresponding surface traction  $\boldsymbol{\mu}_i^F$  and deformation field  $\mathbf{u}_i^S$ , respectively. This form must be valid for all admissible  $\delta \boldsymbol{\mu}_i^F$  and  $\delta \mathbf{u}_i^S$ . Later in Section 3.2.2, consistent transfer methods on the basis of both the strong and the weak form will be presented.

Consistency of this coupling approach can also be interpreted as the preservation of the linear momentum over the interface. However, the interface energy is not conserved.

### Conservative coupling approach

The conservative coupling approach ensures compatibility of the total work at the fluid-structure interface [57]. It follows that condition (3.26) must hold for the transfer of the interface quantities. Condition (3.24) is chosen as a second condition, claiming that the

deformation field is transferred consistently over the interface. This ensures that a deformation field which contains a rigid body motion still contains the rigid body motion, when it is transferred to the other surface. The following two conditions have to be fulfilled for all admissible  $\delta \boldsymbol{\mu}_i^F$ :

$$\int_{\Gamma_{f,i}} (\delta \boldsymbol{\mu}_i^F)^T (\mathbf{u}_i^F - \mathbf{u}_i^S) \, dA = 0, \quad (3.29)$$

$$\int_{\Gamma_{f,i}^F} (\boldsymbol{\mu}_i^F)^T \mathbf{u}_i^F \, dA = \int_{\Gamma_{f,i}^S} (\boldsymbol{\mu}_i^S)^T \mathbf{u}_i^S \, dA. \quad (3.30)$$

Again, the consistent condition for the deformation field is stated in its weak form, while the conservation of the interface energy represents a strong condition. Adequate coupling methods are presented in the next section.

While by this approach, the interface energy is conserved and the deformation is transferred consistently, the consistency of the surface tractions over the interface is given up when dealing with non-matching meshes.

### 3.2.2 Transfer methods

In practice, different transfer methods exist for the realization of the above stated coupling conditions. It is emphasized that they all address the transfer of discrete values from one mesh to another. From these transferred values, one obtains a smooth field on each mesh by an adequate interpolation rule.

For the EHL interface, the path of transfer is always as follows: the surface tractions are calculated on the fluid domain and need to be transferred to the structural domain. It is contrary for the displacements, as they are solved on each structural domain and serve as inputs for the pressure calculation on the fluid domain. Hence, the displacements need to be transferred from the fluid to the structural domain.

For the discrete values, the transfer process can be expressed by the following matrix vector multiplication with  $i \in \{1, 2\}$ :

$$\mathbf{d}_{f,i}^F = \mathbf{H}_i^{FS} \mathbf{d}_{f,i}^S, \quad (3.31)$$

$$\boldsymbol{\mu}_i^S = \mathbf{H}_i^{SF} \boldsymbol{\mu}_i^F, \quad (3.32)$$

with the still unknown transfer matrices  $\mathbf{H}_i^{FS}$  and  $\mathbf{H}_i^{SF}$ . The vector  $\mathbf{d}_f$  is a subset of vector  $\mathbf{d}$  and contains the discrete displacements belonging to the lubricated interface  $\Gamma_{f,h,i}$ . The vector  $\boldsymbol{\mu}$  is the vector of the discrete surface tractions.

For sake of clearness, in the following studies, the index  $i$  is suppressed, as the transfer process is identical for each surface of body  $i$ ,  $i \in \{1, 2\}$ .

In the case, when following a conservative coupling strategy, condition (3.30) gives a dependency between the transfer matrices  $\mathbf{H}^{FS}$  and  $\mathbf{H}^{SF}$  for all the transfer methods. Its derivation is given in the following. Therefore, the two integrals of Eq. (3.30) need to be discretized by introducing interpolation functions for each vector field. Using  $\boldsymbol{\mu}_h^F = \mathbf{M}^F(\mathbf{x}) \boldsymbol{\mu}^F$  and  $\mathbf{u}_h^F|_{\Gamma_{f,h}} = \mathbf{N}_f^F(\mathbf{x}) \mathbf{d}_f^F$  for the interpolation of quantities on the fluid mesh, the left integral in its discretized form gives:

$$\int_{\Gamma_{f,h}^F} (\boldsymbol{\mu}_h^F)^T \mathbf{u}_h^F \, dA = \int_{\Gamma_{f,h}^F} (\mathbf{M}^F(\mathbf{x}) \boldsymbol{\mu}^F)^T (\mathbf{N}_f^F(\mathbf{x}) \mathbf{d}_f^F) \, dA = (\boldsymbol{\mu}^F)^T (\mathbf{M}^{FF})^T \mathbf{d}_f^F.$$

Using further  $\boldsymbol{\mu}_h^S = \mathbf{M}^S(\mathbf{x}) \boldsymbol{\mu}^S$  and  $\mathbf{u}_h^S|_{\Gamma_{f,h}} = \mathbf{N}_f^S(\mathbf{x}) \mathbf{d}_f^S$  for the interpolation of the quantities on the structural mesh, the right integral of Eq. (3.30) in its discretized form gives:

$$\int_{\Gamma_{f,h}^S} (\boldsymbol{\mu}_h^S)^T \mathbf{u}_h^S \, dA = \int_{\Gamma_{f,h}^S} (\mathbf{M}^S(\mathbf{x}) \boldsymbol{\mu}^S)^T (\mathbf{N}_f^S(\mathbf{x}) \mathbf{d}_f^S) \, dA = (\boldsymbol{\mu}^S)^T (\mathbf{M}^{SS})^T \mathbf{d}_f^S. \quad (3.33)$$

The equality of these two integrals in combination with the discrete condition (3.31) gives the definition of  $\mathbf{H}^{SF}$ . It follows:

$$\mathbf{H}^{SF} = (\mathbf{M}^{SS})^{-1} (\mathbf{H}^{FS})^T \mathbf{M}^{FF}, \quad (3.34)$$

which is always valid for the conservative coupling strategy. A closer look identifies the discrete forces  $\mathbf{F}^F = \mathbf{M}^{FF} \boldsymbol{\mu}^F$  and  $\mathbf{F}^S = \mathbf{M}^{SS} \boldsymbol{\mu}^S$  on the fluid and structural mesh, respectively. Thus, it holds the relation  $\mathbf{F}^S = (\mathbf{H}^{FS})^T \mathbf{F}^F$  for the force transfer by the conservative coupling approach.

In the following, three different transfer methods are outlined with the aim of determining  $\mathbf{H}^{FS}$  and also  $\mathbf{H}^{SF}$  in the case of a consistent coupling strategy. These are a nearest neighbor (NN) method, a nearest neighbor projected (NNPro) method and a weighted residual (WR) approach. The first two are based on the strong form of the coupling conditions and therefore, are often referred as direct force motion transfer methods, see [161]. In contrast, the third method is based on the weak form of the coupling conditions, requiring the definition of additional LAGRANGE multiplier  $\lambda_u$  and  $\lambda_\mu$ .

### Nearest neighbor

The NN approach approximates unknown values by known values of the nearest neighbor.

First, the discretization of the continuous condition (3.24) by the NN approach is demonstrated for the deformation field. The discrete value  $\mathbf{u}_h^F(\mathbf{x}_{h,k}^F)$  of the deformation field at the discrete position  $\mathbf{x}_{h,k}^F$  at each node  $k \in \{1 \dots n_{node}^F\}$  of the fluid mesh is approximated as:

$$\mathbf{u}_h^F(\mathbf{x}_{h,k}^F) \approx \mathbf{u}_h^S(\mathbf{x}_{NN}^S), \quad \mathbf{x}_{NN}^S = \arg\left\{ \min_{l \in \{1 \dots n_{node}^S\}} (\|\mathbf{x}_{h,l}^S - \mathbf{x}_{h,k}^F\|) \right\},$$

where  $\mathbf{x}_{NN}^S$  is the node on the structural mesh, which discrete position has the closest distance to the given position  $\mathbf{x}_{h,k}^F$ . Since the deformation field is known on the structural side, the transfer matrix  $\mathbf{H}^{FS}$  for the discrete values in Eq. (3.31) can be determined; it results in a BOOLEAN matrix.

In the case of a consistent coupling strategy, in a similar way, the NN approach can be used for the transfer of the surface tractions from the fluid mesh to the structural mesh. By discretizing the condition (3.25), the transfer matrix  $\mathbf{H}^{SF}$  of Eq. (3.32) is again a BOOLEAN matrix and a consistent transmitting also for the surface traction is realized.

In the contrary case, when following a conservative coupling strategy, condition (3.30) has to be fulfilled instead of condition (3.28). Then, as already shown, Eq. (3.34) states the definition of  $\mathbf{H}^{SF}$ .

### Nearest neighbor projected

The NNPro approach determines unknown values by the direct projection of known values.

Like for the NN approach, the projection procedure is outlined for the deformation field. The discrete value  $\mathbf{u}_h^F(\mathbf{x}_{h,k}^F)$  of the deformation field at the discrete position  $\mathbf{x}_{h,k}^F$  at each node  $k \in \{1 \dots n_{node}^F\}$  of the fluid mesh is obtained by

$$\mathbf{u}_h^F(\mathbf{x}_{h,k}^F) = \mathbf{u}_h^S(\mathbf{x}_{NNP}^S), \quad \mathbf{x}_{NNP}^S = \arg\left\{ \min_{\mathbf{x}_h^S \in \Gamma_{f,h}^S} (\|\mathbf{x}_h^S - \mathbf{x}_{h,k}^F\|) \right\} \quad (3.35)$$

where  $\mathbf{x}_{NNP}^S$  is the projection of the point  $\mathbf{x}_{h,k}^F$  of the fluid mesh onto the structural mesh. In the following, let the fluid domain be parametrized by the coordinates  $(y, z)$  and

the surface of the body by the coordinates  $(\xi, \eta)$ . Then, at each discrete position  $\mathbf{x}_{h,k}^F$ ,  $k \in \{1 \dots n_{node}^F\}$ , of the fluid mesh, a nonlinear equation has to be solved for the surface parameters, which describe the projected point  $\mathbf{x}_{NNP}^S$ . The solution of Eq. (2.79) exactly defines the projection<sup>1</sup>. As a result, when evaluating Eq. (3.35) at the nodes of the fluid mesh, the transfer matrix  $\mathbf{H}^{FS}$  for the discrete values is determined.

In the case of a consistent coupling strategy, this procedure can be applied in the same manner to the transfer of the surface tractions from the fluid to the structural mesh. Then, the transfer matrix  $\mathbf{H}^{SF}$  is obtained.

Otherwise, in the case of a conservative coupling strategy, Eq. (3.34) gives already the definition of the transfer matrix  $\mathbf{H}^{SF}$ .

### Weighted residual approach

By the mortar method, the interface conditions are fulfilled in a weak sense, see for instance Eqs. (3.27) and (3.28). The respective variations  $\delta\boldsymbol{\mu}^F$  and  $\delta\mathbf{u}^S$  serve as weighting functions and are used to enforce the coupling conditions.

In the following, the transfer matrix  $\mathbf{H}^{FS}$  for the discrete deformation values is derived from the condition of Eq. (3.27). A discretization of the weak form is obtained by using the approximations  $\delta\boldsymbol{\mu}_h^F$ ,  $\mathbf{u}_h^F$  and  $\mathbf{u}_h^S$ . Further, the discrete surface  $\Gamma_{f,h}^F$  of the fluid mesh serves as a slave surface, meaning that  $\delta\boldsymbol{\mu}_h^F$  is defined on the fluid mesh and the integration is performed on the fluid mesh. The field values are interpolated by using  $\delta\boldsymbol{\mu}_h^F = \mathbf{M}^F(\mathbf{x}) \boldsymbol{\mu}^F$ ,  $\mathbf{u}_h^F|_{\Gamma_{f,h}^F} = \mathbf{N}_f^F(\mathbf{x}) \mathbf{d}_f^F$  and  $\mathbf{u}_h^S|_{\Gamma_{f,h}^F} = \mathbf{N}_f^S(\mathbf{x}) \mathbf{d}_f^S$ , where  $\boldsymbol{\mu}^F$ ,  $\mathbf{d}_f^F$  and  $\mathbf{d}_f^S$  are the vectors of discrete values of the surface traction and the deformation fields on each mesh, respectively. Then, the following discretized condition results for Eq. (3.27):

$$\int_{\Gamma_{f,h}^F} (\delta\boldsymbol{\mu}_h^F)^T (\mathbf{u}_h^F - \mathbf{u}_h^S) \, dA = \int_{\Gamma_{f,h}^F} (\delta\boldsymbol{\mu}_h^F)^T (\mathbf{M}^F(\mathbf{x}))^T (\mathbf{N}_f^F(\mathbf{x}) \mathbf{d}_f^F - \mathbf{N}_f^S(\bar{\mathbf{y}}) \mathbf{d}_f^S) \, dA = 0. \quad (3.36)$$

The first summand can be evaluated on the fluid mesh without difficulties, as all entities are defined on it. It yields:

$$(\delta\boldsymbol{\mu}^F)^T \left( \int_{\Gamma_{f,h}^F} (\mathbf{M}^F(\mathbf{x}))^T \mathbf{N}_f^F(\mathbf{x}) \mathbf{d}_f^F \, dA \right) = (\delta\boldsymbol{\mu}^F)^T \mathbf{C}^{FF} \mathbf{d}_f^F. \quad (3.37)$$

The second summand is defined as

$$(\delta\boldsymbol{\mu}^F)^T \left( \int_{\Gamma_{f,h}^F} (\mathbf{M}^F(\mathbf{x}))^T \mathbf{N}_f^S(\bar{\mathbf{y}}) \mathbf{d}_f^S \, dA \right) = (\delta\boldsymbol{\mu}^F)^T \mathbf{C}^{FS} \mathbf{d}_f^S. \quad (3.38)$$

During the evaluation, one has to deal with the mapping  $\bar{\mathbf{y}}$ , which projects points of the structural mesh onto the fluid mesh. It is required here, as the matrix  $\mathbf{N}_f^S$  of shape functions is originally defined on the structural mesh, but the integration is performed on the fluid mesh. Due to the discretization of the surfaces, they do not coincide any more, when non-matching meshes are used. The mapping is defined by solving the same nonlinear equation, as already used for the coupling by the NNPro method:

$$\bar{\mathbf{y}} : \mathbf{x}_h^F \rightarrow \mathbf{x}_h^S \quad \text{such, that} \quad \mathbf{n}_h^F(\mathbf{x}_h^F) \times (\mathbf{x}_h^S(\bar{\xi}, \bar{\eta}) - \mathbf{x}_h^F) = \mathbf{0}.$$

<sup>1</sup>Usually in the FEM, an iso-parametric concept is applied during discretization, meaning that the geometry is approximated by the same shape functions as the solution space. This may lead to surface gradients not being continuous over the elements. Therefore, often mean surface gradients  $\hat{\mathbf{n}}_h^F$  and  $\hat{\mathbf{n}}_h^S$ , respectively, are used in order to avoid numerical inconsistencies during the projection, see for instance [151].

In conclusion, the discretization (3.36) of the weak condition gives the definition of the transfer matrix  $\mathbf{H}^{FS}$  by

$$\mathbf{H}^{FS} = (\mathbf{C}^{FF})^{-1} \mathbf{C}^{FS}. \quad (3.39)$$

In the case of a consistent coupling strategy, the procedure has to be performed for the weak condition (3.28) as well. Then, the structural mesh is chosen as a slave surface, as the variation  $\delta \mathbf{u}^S$  is defined on the structural mesh. By using approximations similar as for the coupling of the deformation field, one obtains following discretized condition:

$$\int_{\Gamma_{f,h}^S} (\delta \mathbf{u}_h^S)^T (\boldsymbol{\mu}_h^F - \boldsymbol{\mu}_h^S) \, dA = \int_{\Gamma_{f,h}^S} (\delta \mathbf{d}_f^S)^T (\mathbf{N}_f^S(\mathbf{x}))^T (M^F(\bar{\mathbf{z}}) \boldsymbol{\mu}^F - M^S(\mathbf{x}) \boldsymbol{\mu}^S) \, dA = 0,$$

with the discretized surface tractions  $\boldsymbol{\mu}_h^F = M^F(\mathbf{x}) \boldsymbol{\mu}^F$  and  $\boldsymbol{\mu}_h^S = M^S(\mathbf{x}) \boldsymbol{\mu}^S$  on the fluid and structural mesh, respectively. The nonlinear mapping  $\bar{\mathbf{z}}$  is now defined as:

$$\bar{\mathbf{z}} : \mathbf{x}_h^S \rightarrow \mathbf{x}_h^F \quad \text{such, that} \quad \mathbf{n}_h^S(\mathbf{x}_h^S) \times (\mathbf{x}_h^F(y, z) - \mathbf{x}_h^S) = \mathbf{0}.$$

With this mapping, the integral can be solved, yielding following two matrices:

$$\mathbf{C}^{SF} = \int_{\Gamma_{f,h}^S} (\mathbf{N}_f^S(\mathbf{x}))^T M^F(\bar{\mathbf{z}}) \, dA, \quad (3.40)$$

$$\mathbf{C}^{SS} = \int_{\Gamma_{f,h}^S} (\mathbf{N}_f^S(\mathbf{x}))^T M^S(\mathbf{x}) \, dA, \quad (3.41)$$

defining the transfer matrix  $\mathbf{H}^{SF}$  as:

$$\mathbf{H}^{SF} = (\mathbf{C}^{SS})^{-1} \mathbf{C}^{SF}. \quad (3.42)$$

It is noted that consistency and thus preserving of the linear momentum for the discretized weak forms of the mortar method, only hold, when choosing one discrete interface as slave side and using a consistent integration scheme, as verified e. g. in [42, 151, 155].

In the case of a conservative coupling strategy, this transfer matrix  $\mathbf{H}^{SF}$  is again already defined by the relation (3.34).

### 3.3 Discretized form

The previous section highlights different coupling conditions with their numerical discretization for non-matching meshes. By considering them, a full discretization of the coupled system of equations for two flexible bodies with lubricated contacts can be given.

In the following, the weak form of Eqs. (3.21) to (3.23) of the coupled system of equations is extended for the case of non-matching meshes. It is outlined for a consistent coupling approach using the mortar method. This approach is chosen, since it requires appropriate weighting and solution spaces also for the LAGRANGE multiplier, which are explained in more detail. Nevertheless, the other coupling methods of Section 3.2.2 are applicable as well without any difficulties. A detailed discussion of function spaces for flexible MBS including LAGRANGE multiplier for bilateral constraints is outlined by SIMEON in [173]. As further references for the LAGRANGE multiplier spaces also for unilateral contact problems serve the text book of KIKUCHI and ODEN [96] and the work of WOHLMUTH [201, 202].

Adding the coupling conditions (3.27) and (3.28) to the weak form of Eqs. (3.21) to (3.23) results in following weak form for the coupled system with non-matching interfaces: Find  $\mathbf{u}_i^S \in U_i$ ,  $p \in S^+$ ,  $\lambda \in M_c$  such that

$$\sum_{i=1}^2 \left[ \int_{B_i} (\delta \mathbf{r}_{P_i}^S)^T \ddot{\mathbf{r}}_{P_i}^S \, dm_i + \int_{B_i} \delta \boldsymbol{\varepsilon}(\mathbf{u}_{P_i}^S)^T \mathbf{H} \boldsymbol{\varepsilon}(\mathbf{u}_{P_i}^S) \, dV - \int_{B_i} (\delta \mathbf{r}_{P_i}^S)^T \tilde{\mathbf{f}}_i \, dV - \int_{\Gamma_{f,i}^S} (\delta \mathbf{r}_{P_i}^S)^T \boldsymbol{\mu}_i^S \, dA - \int_{\Gamma_c} \delta \mathbf{r}_{P_i}^T \mathbf{W}_i \boldsymbol{\lambda} \, dA \right] = 0, \quad \forall \delta \mathbf{u}_i^S \in V_i, \quad (3.43)$$

$$\int_{\Gamma_c} \delta \boldsymbol{\lambda}^T \boldsymbol{\Phi} \, dA = 0, \quad \forall \delta \boldsymbol{\lambda} \in M_c, \quad (3.44)$$

$$\int_{\Omega} (\delta p - p_{ref}) f(p, \mathbf{r}_{P_1}, \mathbf{r}_{P_2}, \dot{\mathbf{r}}_{P_2}, \dot{\mathbf{r}}_{P_2}) \, dA \geq 0, \quad \forall \delta p \in W^+, \quad (3.45)$$

$$\int_{\Gamma_{f,i}^F} (\delta \boldsymbol{\mu}_i^F)^T (\mathbf{u}_i^F - \mathbf{u}_i^S) \, dA = 0, \quad \forall \delta \boldsymbol{\mu}_i^F \in M_t, \quad (3.46)$$

$$\int_{\Gamma_{f,i}^S} (\delta \mathbf{u}_i^S)^T (\boldsymbol{\mu}_i^F - \boldsymbol{\mu}_i^S) \, dA = 0, \quad \forall \delta \mathbf{u}_i^S \in V_i. \quad (3.47)$$

As already mentioned, the weak form requires the definition of adequate spaces for both the solution and the weighting functions.

Standard FE solution and weighting spaces  $U_i$  and  $V_i$  respectively, are applicable for the elastic deformation field  $\mathbf{u}_i^S$  of each body  $i$ . They are defined as:

$$U_i = \{ \mathbf{u}_i^S \in H^1(B_i) \mid \mathbf{u}_i^S = \hat{\mathbf{u}}_i \text{ on } \Gamma_{u,i} \}, \quad (3.48)$$

$$V_i = \{ \delta \mathbf{u}_i^S \in H^1(B_i) \mid \delta \mathbf{u}_i^S = \mathbf{0} \text{ on } \Gamma_{u,i} \}. \quad (3.49)$$

These two spaces can be discretized by using classical shape functions like LAGRANGE polynomials. Here in this thesis, the elastic structure is always discretized by 3-dimensional incomplete quadrilateral *Hex20* elements (20 nodes) with serendipity shape functions. On the facets, they degenerate to the already introduced *Quad8* elements. The number of nodes on each structural mesh of body  $i$  is denoted by  $m_{i,node}$ . On the fluid mesh, the deformation field is interpolated by the already existing shape functions of the pressure discretization, meaning  $N_{f,k}^F = N_k$  with  $k \in \{1 \dots n_{node}\}$ , see Section 2.2.1.

The solution and weighting spaces  $S^+$  and  $W^+$ , respectively for the pressure solution  $p$  with its variation  $\delta p$  are already defined in Eqs. (2.44) to (2.46). For the definition of  $S$  and  $W$ , see also Section 2.2.1 or Section 2.2.2, when using stabilization techniques. For the sake of comprehension, they are repeated here:

$$S^+ = \{ p \in S \mid \int_{\Omega} (p - p_c) q \, d\Omega \geq 0, \, q \in Q^+ \},$$

$$W^+ = \{ \delta p \in W \mid \int_{\Omega} \delta p q \, d\Omega \geq 0, \, q \in Q^+ \}.$$

The surface tractions  $\boldsymbol{\mu}_i^F$  on the fluid mesh are approximated by the same shape functions as used for the pressure interpolation, meaning  $M_k^F = N_k$  with  $k \in \{1 \dots n_{node}^F\}$ . The surface tractions  $\boldsymbol{\mu}_i^S$  on each structural mesh are approximated by the same shape functions as used for the interpolation of the deformation field, i. e.  $M_k^S = N_k^S$  with  $k \in \{1 \dots n_{i,node}^S\}$ .

The spaces  $M_c$  for the LAGRANGE multiplier  $\boldsymbol{\lambda}$  and  $M_t$  for the variation  $\delta \boldsymbol{\mu}_i^F$  respectively, are defined as:

$$M_c = H^{-1/2}(\Gamma_c), \quad (3.50)$$

$$M_t = H^{-1/2}(\Gamma_{f,i}), \quad (3.51)$$

which are the dual trace spaces of  $U_i$  on the corresponding interfaces, see for instance [173]. Thus, the integrals in Eqs. (3.44), (3.46) and (3.47) have to be understood as duality pairings. Note that the surface tractions  $\mu_i^S$  and  $\mu_i^F$  can be understood as further LAGRANGE multiplier. In this thesis, their shape functions are chosen equal to the existing shape functions of the deformation field on the corresponding mesh. However, they could be also constructed bi-orthogonal to these shape functions, similar as already discussed in Section 2.3.2. When using these dual LAGRANGE multiplier shape functions, the matrices, defined in Eqs. (3.37) and (3.41), become diagonal matrices.

With the defined solution spaces and shape functions, the overall discrete form of the dynamic equations of the coupled system can be stated. It yields for the constraint motion of two flexible bodies with lubricated contacts and non-conforming meshes:

$$\mathbf{H}(\mathbf{q}) \dot{\mathbf{q}} = \dot{\mathbf{z}}, \quad (3.52)$$

$$\mathbf{M}(\mathbf{q}) \ddot{\mathbf{z}} = \mathbf{h}_\omega + \mathbf{h}_g + \mathbf{h}_{el} + \mathbf{h}_{ext} + \mathbf{W}(\mathbf{q}) \boldsymbol{\lambda} + \mathbf{C}(\mathbf{q}) \boldsymbol{\mu}^S, \quad (3.53)$$

$$\mathbf{g}(\mathbf{q}, \dot{\mathbf{z}}) = \mathbf{0}, \quad (3.54)$$

$$\mathbf{p}_{ref} = \mathbf{proj}_{\mathbb{R}_0^+} \left( \mathbf{p}_{ref} - r \left( (\mathbf{A}(\mathbf{p}, \mathbf{q}^F) + \mathbf{B}(\mathbf{p}, \mathbf{q}^F)) \mathbf{p} + \mathbf{b}(\mathbf{p}, \mathbf{q}^F, \dot{\mathbf{z}}^F) \right) \right), \quad r > 0, \quad (3.55)$$

$$\mathbf{d}_f^F = \mathbf{H}^{FS} \mathbf{d}_f^S, \quad (3.56)$$

$$\boldsymbol{\mu}^S = \mathbf{H}^{SF} \boldsymbol{\mu}^F(\tilde{\mathbf{p}}, \mathbf{q}^F, \dot{\mathbf{z}}^F). \quad (3.57)$$

The state vector  $\mathbf{q} = (\mathbf{q}_1^T \ \mathbf{q}_2^T)^T$  as well as the vector of generalized velocities  $\dot{\mathbf{z}} = (\dot{\mathbf{z}}_1^T \ \dot{\mathbf{z}}_2^T)^T$  assemble the vector  $\mathbf{q}_i$  and  $\dot{\mathbf{z}}_i$  of each body  $i \in \{1, 2\}$ , respectively. They are defined as  $\mathbf{q}_i = (\mathbf{r}_i^T \ \boldsymbol{\theta}_i^T \ (\mathbf{d}_i^S)^T)^T$  and  $\dot{\mathbf{z}}_i = (\mathbf{v}_i^T \ \boldsymbol{\omega}_i^T \ (\mathbf{d}_i^S)^T)^T$ , respectively, and describe the kinematics of each flexible body in the FFR formulation, see Section 3.1.2. The system of the first two Eqs. (3.52) and (3.53) represents the dynamic equation of the two flexible bodies, see Eq. (3.20). The vector  $\boldsymbol{\lambda}$  of discrete LAGRANGE multipliers enforces the discretized holonomic constraints  $\mathbf{g}(\mathbf{q}, \dot{\mathbf{z}})$  of Eq. (3.54). Equation (3.55) represents the discretized SWIFT-STIEBER cavitation condition, formulated by the projection function, see Section 2.3.2. As the pressure is calculated on the fluid mesh, the deformation field has to be transferred, which is indicated by the superscript  $F$  in the vectors  $\mathbf{q}^F$  and  $\dot{\mathbf{z}}^F$ . The transformation of the deformation field is given by Eq. (3.56). With Eq. (3.57), the discrete surface tractions  $\boldsymbol{\mu}^F$ , which depend on the pressure and the kinematics on the fluid mesh, can be transferred to the structural mesh. The state dependent matrix  $\mathbf{C}(\mathbf{q})$  in Eq. (3.53) performs the numerical calculation of the forces due to the surface tractions in the proper reference system.

Note that here in this thesis, the transfer matrices  $\mathbf{H}^{FS}$  and  $\mathbf{H}^{SF}$  are denoted as constant matrices, since in the later examples, it is only considered the case where the fluid mesh is attached to the deformable side and the other side is assumed to be non-deformable. However, the matrices become state-dependent when dealing with two deformable surfaces which are rotating against each other or when treating large deformations, see [151, 206]

Instead of considering the SWIFT-STIEBER cavitation model for the hydrodynamic pressure, the mass conservative cavitation model of Section 2.3 can also be used. Then, the density is a further state variable and Eq. (3.54) has to be replaced by the discrete Eqs. (2.74) and (2.75). It yields, when using the projection function:

$$\mathbf{A}_\rho(\mathbf{p}, \boldsymbol{\rho}, \mathbf{q}^F) \mathbf{p} + \mathbf{B}_\rho(\mathbf{q}^F) \boldsymbol{\rho} + \mathbf{C}_\rho(\mathbf{q}^F) \dot{\boldsymbol{\rho}} = \mathbf{b}_\rho(\mathbf{p}, \boldsymbol{\rho}, \mathbf{q}^F, \dot{\mathbf{z}}^F)$$

$$\mathbf{p}_{ref} = \mathbf{proj}_{\mathbb{R}_0^+} \left( \mathbf{p}_{ref} - r \mathbf{N} \left( \mathbf{f}_\rho(\mathbf{p}) - \boldsymbol{\rho} \right) \right), \quad r > 0.$$

Again, the dependency of the hydrodynamic equations on the state vectors  $\mathbf{q}^F$  and  $\dot{\mathbf{z}}^F$  are indicated by the superscript  $F$ .

### 3.4 Numerical example

The described coupling strategies and methods of Sections 3.2.1 and 3.2.2 are analyzed and compared for a simulation example of a rigid shaft in a flexible cylindrical bearing housing. In contrast to the results published in [103], only the static solution is calculated without performing a dynamic time integration. This has the benefit of analyzing the space discretization only and thus, avoiding errors due to the time discretization.

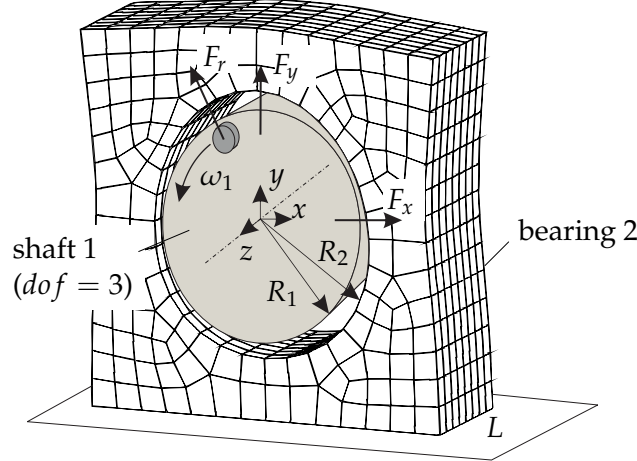


**Figure 3.4:** Simulation example of a rigid shaft in a flexible bearing.

The simulation example is depicted in Fig. 3.4. The rigid shaft 1 rotates with a constant angular velocity about the  $z$ -direction and has two degrees of freedom for the translation in the  $x$ -/ $y$ -plane of the inertial frame. It is represented by the generalized coordinates  $\mathbf{q}_1 = (x_{C1} \ y_{C1} \ \varphi_1)^T$  and the generalized velocities  $\dot{\mathbf{z}}_1 = \dot{\mathbf{q}}_1 = (\dot{x}_{C1} \ \dot{y}_{C1} \ \omega_1)^T$ . The shaft has the mass  $m_1$  and the inertia  $J_1$ , which gives the mass matrix  $\mathbf{M}_1$  of the rigid shaft.

The flexible bearing 2 is represented by a linear flexible structure, which is fixed at the bottom and has only elastic DOFs. The CRAIG-BAMPTON method is applied in order to reduce the inner elastic DOFs and consequently the size of the matrices [9, 66]. As a result, the interface DOFs  $\mathbf{d}_f^S$  are maintained, as they are needed for a detailed calculation of the pressure, and the inner DOFs are replaced by a small number of normal modes described by the modal coordinates  $\mathbf{q}_n$ . It yields for the vector of generalized coordinates  $\mathbf{q}_2 = (\mathbf{q}_n^T \ (\mathbf{d}_f^S)^T)^T$  and the vector of generalized velocities  $\dot{\mathbf{z}}_2 = (\dot{\mathbf{q}}_n^T \ (\dot{\mathbf{d}}_f^S)^T)^T$ . The CRAIG-BAMPTON method gives the reduced mass matrix  $\mathbf{M}_2$  and the reduced stiffness matrix  $\mathbf{K}_2$  for the flexible structure.

On the shaft, the gravity force, an external constant force and a radial force, representing an unbalance, are acting. They yield:

$$\mathbf{h}_{g,1} + \mathbf{h}_{ext,1} = \begin{pmatrix} 0 \\ -m g \\ 0 \end{pmatrix} + \begin{pmatrix} F_x + F_r \cos(\varphi_1) \\ F_y + F_r \sin(\varphi_1) \\ 0 \end{pmatrix}.$$

For the bearing housing, the elastic forces  $\mathbf{h}_{el,2} = -\mathbf{K}_2 \mathbf{q}_2$  are considered. The hydrodynamic forces are acting on both the shaft and the bearing housing. For this simulation example, the forces due to shear stresses are neglected.

As a result, the following dynamic equations of motion of the simulation example are assembled:

$$\begin{pmatrix} \mathbf{M}_1 & 0 \\ 0 & \mathbf{M}_2 \end{pmatrix} \begin{pmatrix} \ddot{\mathbf{q}}_1 \\ \ddot{\mathbf{q}}_2 \end{pmatrix} = \begin{pmatrix} \mathbf{h}_{g,1} + \mathbf{h}_{ext,1} \\ \mathbf{h}_{el,2} \end{pmatrix} + \begin{pmatrix} \mathbf{C}_1 & 0 \\ 0 & \mathbf{C}_2 \end{pmatrix} \begin{pmatrix} \mathbf{H}_1^{SF} \boldsymbol{\mu}_1^F(\tilde{\mathbf{p}}, \mathbf{q}^F, \dot{\mathbf{q}}^F) \\ \mathbf{H}_2^{SF} \boldsymbol{\mu}_2^F(\tilde{\mathbf{p}}, \mathbf{q}^F, \dot{\mathbf{q}}^F) \end{pmatrix},$$

**Table 3.1:** Simulation parameters for the rigid shaft in a flexible bearing.

parameter	value	parameter	value
angular velocity $\omega_1$	500 $rad/s$	fluid density $\rho_{p=0}$	800 $kg/m^3$
clearance $R_2 - R_1$	17.0 $\mu m$	dyn. viscosity $\eta_{p=0}$	0.005 $kg/ms$
radius bearing $R_2$	2.25 $cm$	cavitation pressure $p_c$	0 $N/m^2$
bearing width $L$	2.20 $cm$	Young's modulus $E$	2e11 $N/m^2$
mass shaft $m$	1.0 $kg$	force $F_x$	2.5 $kN$
		forces $F_y, F_r$	0 $kN$

$$\mathbf{p}_{ref} = \mathbf{proj}_{\mathbb{R}_0^+} \left( \mathbf{p}_{ref} - r \left( (\mathbf{A}(\mathbf{p}, \mathbf{q}^F) + \mathbf{B}(\mathbf{p}, \mathbf{q}^F)) \mathbf{p} + \mathbf{b}(\mathbf{p}, \mathbf{q}^F, \dot{\mathbf{q}}^F) \right) \right), \quad r > 0.$$

Here, the pressure is calculated by the SWIFT-STIEBER cavitation condition. The matrices  $\mathbf{H}_1^{SF}$  and  $\mathbf{H}_2^{SF}$  ensure the transfer of the surface tractions from the fluid to the structural mesh. Due to the assumption of a rigid shaft, for the first body, only the resultant fluid force and moment are needed. Using Eqs. (2.86) and (2.87) they are calculated on the fluid mesh and therefore, no transfer operation is necessary, meaning  $\mathbf{H}_1^{SF} = \mathbf{I}$ . For the pressure calculation, the vector  $\mathbf{d}_f^S$  of the interface DOFs needs to be transferred from the structural to the fluid mesh, which is performed by the matrix  $\mathbf{H}_2^{SF}$ .

For the following study, the static equilibrium position  $(x_{C1,0} \ y_{C1,0})^T$  of the system is computed, when no radial force is acting. Therefore, constant velocities are considered; they are set to zero, except the rotational velocity  $\omega_1$ , which is set to 500  $rad/s$ . The horizontal force  $F_x$  is set to 2500  $N$  and the vertical force  $F_y$  is zero. Further simulation parameters of the system are listed in Table 3.1.

In the following, the convergence of the discretization error for the different coupling methodologies is analyzed. Both the fluid and the structural interface are discretized by a structured mesh using incomplete quadratic finite elements. While the modified *Quad8Mod* elements are used for the pressure on the fluid mesh in order to fulfill the requirement of positive integrability due to the cavitation condition, the standard *Quad8* elements are used for deformation on the structural mesh. Consequently, the surface tractions on the structural mesh are interpolated also by the shape functions of the *Quad8Mod* element and the deformation field on the fluid mesh is interpolated by the shape functions of the *Quad8* element, respectively. The shape functions of the different interface fields are summarized in Table 3.2.

A reference solution is created by using very fine and matching meshes with 40 elements in circumferential and 10 elements in z-direction. For the subsequent convergence analysis, the fluid and the structural mesh are refined simultaneously in circumferential and z-direction. The discretization error is measured in the  $L_2$ -norm and normalized by the maximal value of the corresponding interface field. For instance, the error in the deformation on the structural mesh is calculated by

$$err_{L_2} = \frac{1}{u_{h,ref,max}^S} \sqrt{\int_{\Gamma_f^S} \left( \mathbf{u}_h^S - \mathbf{u}_{h,ref}^S \right)^T \left( \mathbf{u}_h^S - \mathbf{u}_{h,ref}^S \right) dA}.$$

In a similar manner, the discretization error in the pressure on both the fluid and structural mesh is calculated. It is noted that finite elements with shape functions of polynomial degree  $n$  converge in the  $L_2$ -norm with order  $O(h^{n+1})$ , when considering classical problems of structural mechanics [92]. Herein,  $h$  is the characteristic element length.

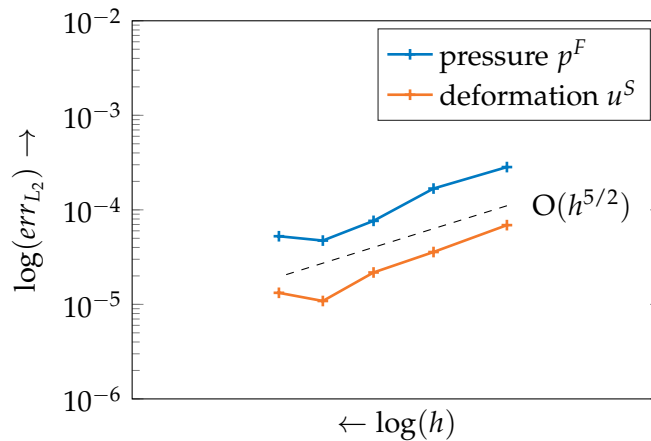
First, the convergence of the discretization error of the coupled system is considered, when using matching meshes. Therefore, the elements on both meshes are refined by selecting  $(n_{ele,y}^F \times n_{ele,z}^F) = (n_{ele,y}^S \times n_{ele,z}^S) \in \{(16 \times 4), (20 \times 5), (24 \times 6), (28 \times 7), (32 \times$

**Table 3.2:** Shape functions for the different fields on the fluid and structural mesh, respectively.

fluid		structure	
field	element	field	element
$\mu_{i,h}^F$	<i>Quad8Mod</i>	$\mu_{i,h}^S$	<i>Quad8Mod</i>
$u_{i,h}^F$	<i>Quad8</i>	$u_{i,h}^S$	<i>Quad8</i>

8)}. In the case of matching meshes, all coupling methodologies become identical and the transfer of discrete values is both conservative and consistent, as the values can be transferred directly from one mesh to the other.

In Fig. 3.5, the discretization errors in the pressure on the fluid mesh and the deformation on the structural mesh respectively, are shown. It can be seen that the discretization error converges with  $O(h^{5/2})$  for both solution fields. As already mentioned in Section 2.6.1, the cavitation condition deteriorates the  $O(h^3)$  convergence of the bi-quadratic finite elements by an  $O(h^{1/2})$ . As a consequence, this loss of convergence in the pressure solution is also present in the  $O(h^{5/2})$  convergence of the error in the deformation field. Due to the matching meshes, there is no coupling error, which could affect the convergence of the discretization error.

**Figure 3.5:** Convergence of discretization error for pressure on fluid and deformation on structural mesh respectively, using matching meshes.

In the following, the convergence of the discretization error is analyzed, when using non-matching meshes. Therefore, the elements on the structural mesh are still refined by selecting  $(n_{ele,y}^S \times n_{ele,z}^S) \in \{(16 \times 4), (20 \times 5), (24 \times 6), (28 \times 7), (32 \times 8)\}$ , whereas the elements on the fluid mesh are refined such that the number of elements in each direction is always one larger than the number of elements in the respective direction of the structural mesh, i. e.  $n_{ele,y}^F = n_{ele,y}^S + 1$  and  $n_{ele,z}^F = n_{ele,z}^S + 1$ . In this way, there is always a small non-conformance between the meshes, while both meshes can be refined simultaneously.

The different coupling strategies (consistent, conservative) and transfer methods (NN, NNPro, WR) are compared by analyzing the discretization error for the system with now non-matching meshes.

**Consistent coupling** Figures 3.6(a) and 3.6(b) show the discretization error in the pressure on the fluid mesh and in the deformation on the structural mesh respectively, for the different transfer methods, when following the consistent coupling approach.

It can be seen that, when using both the consistent WR and the NNPro transfer

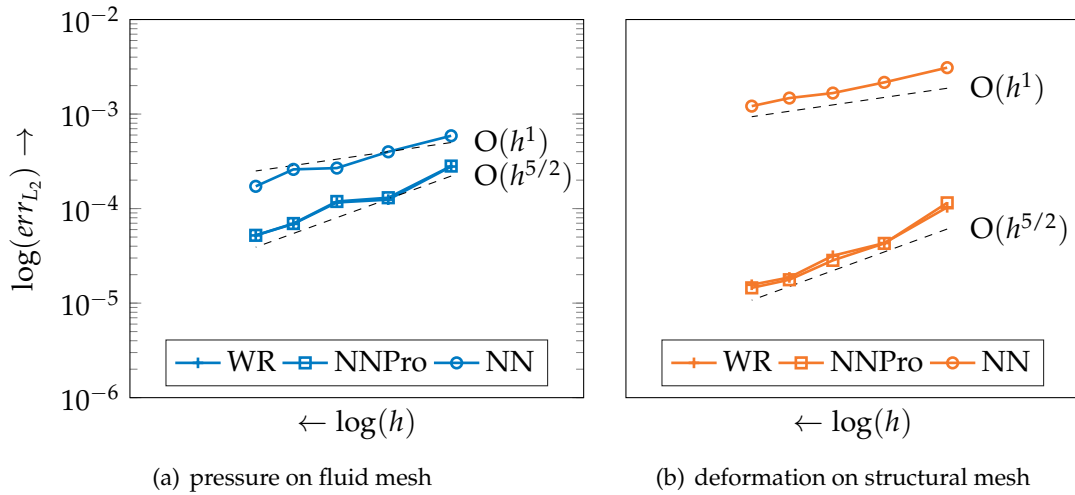


**Figure 3.6:** Convergence of the discretization error of the pressure on the fluid and the deformation on the structural mesh respectively, for non-matching meshes with **consistent** coupling technique.

methods, the discretization errors converge with the same order as the errors in the case of matching meshes of Fig. 3.5. This means that the coupling error introduced by these two coupling methods does not affect the discretization error, neither in its convergence order nor in its magnitude.

In contrast, when using the NN transfer method, the convergence of the discretization error in both the pressure on the fluid mesh and the deformation on the structural mesh reduces to the  $O(h^1)$ . The reason is that the NN method can approximate only constant distributions exactly and hence, is only  $O(h^1)$  convergent in the  $L_2$ -norm. In summary, the error of the NN coupling method dominates the convergence of the coupled system significantly.

**Conservative coupling** Figures 3.7(a) and 3.7(b) show the discretization error in the pressure field on the fluid mesh and in the deformation field on the structural mesh respectively, for the different transfer methods, when following the conservative coupling approach.

Looking at the discretization error, when using the WR transfer method, the convergences and the magnitudes of the errors are identical to that of the system with matching meshes. It can be deduced that the coupling error influences neither the convergence nor the magnitude of the discretization error.

When using the NNPro transfer method, it can be recognized that the discretization error of the pressure on the fluid mesh has still an  $O(h^{5/2})$  convergence and the same magnitude as the error of the system with matching meshes. This is due to the fact, that the deformations are transferred consistently from the structural to the fluid mesh, whereby the coupling error is not influencing the discretization error of the pressure at all. The discretization error of the deformation on the structural mesh converges with  $O(h^2)$ . Obviously, the conservative coupling technique yields a coupling error, which deteriorates the convergence of the discretization error compared to the convergence of the error of the system with matching meshes.

When using the NN transfer method, both discretization errors converge with order  $O(h^1)$ . The reason is similar to the above mentioned for the consistent approach that the NN method is originally only first order accurate. This low convergence of the coupling method becomes evident in the convergence of the overall discretization error.

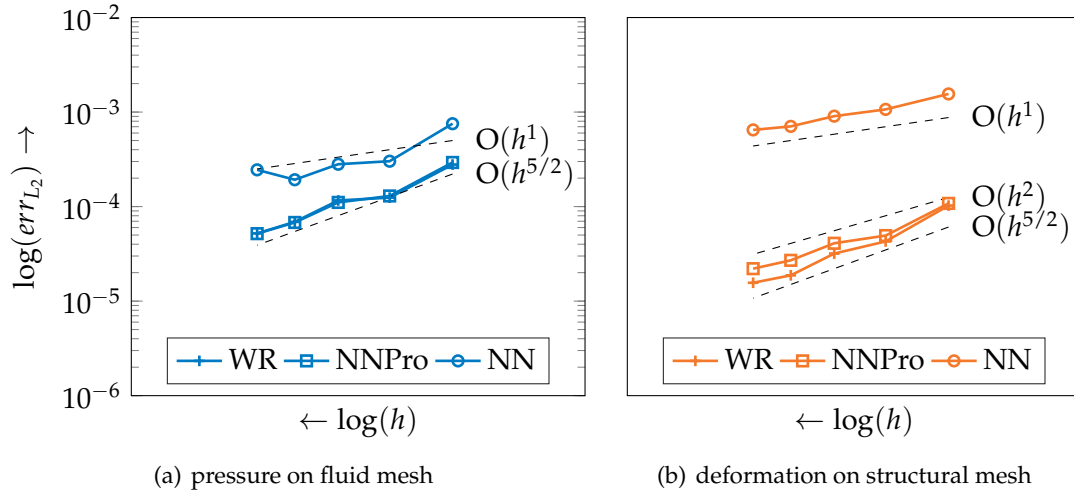


**Figure 3.7:** Convergence of the discretization error of the pressure on the fluid and the deformation on the structural mesh respectively, for non-matching meshes with **conservative** coupling technique.

From the convergence study of the coupled system with non-matching meshes, following conclusions are derived:

- The consistent transfer with the NNPro and the WR as well as the conservative transfer with the WR method maintain the  $O(h^{5/2})$  convergence of the errors of the conforming coupled system in both the pressure on the fluid mesh and the deformation on the structural mesh.
- The conservative NNPro transfer method leads to an  $O(h^2)$  convergence of the error in the deformation on the structural mesh, while it maintains the  $O(h^{5/2})$  convergence of the error in the pressure on the fluid mesh of the conforming coupled system.
- Both the consistent and the conservative transfer by the NN method lead to an  $O(h^1)$  convergence of the discretization errors.

Further, it can be concluded that the conservative transfer with the WR method would be the favorite transfer method, when being interested in long-time simulations, where no artificial energy shall be created nor annihilated.

It is worth analyzing the difference between the consistent and the conservative coupling technique in more detail: In Fig. 3.8, the convergence of the discretization error of the pressure, which is received by the structural mesh, is depicted. Figure 3.8(a) shows the error for the consistent and Fig. 3.8(b) for the conservative coupling technique, respectively.

In Fig. 3.8, it can be seen that the discretization error in the pressure, which is transferred consistently by the WR and the NNPro as well as conservatively by the WR method, shows an  $O(h^{5/2})$  convergence. In fact, for these three methods, the coupling error converges with an  $O(h^3)$  and hence, does not affect the convergence of the discretization error.

In contrast, when transferring the pressure consistently by the NN method, the convergence is only of  $O(h^1)$ . The reason is the natural low convergence of the NN method.

Further, Fig. 3.8(b) reveals that the error in the pressure received by the structure is not convergent, when using the conservative NNPro or NN transfer method. At a first glance, this is surprising, since the error in the deformation on the structural mesh is still convergent. However, the explanation for this apparent contradiction is given by

the definition of the conservative coupling technique of Eq. (3.34). Due to its construction, discrete interface forces – and not discrete surface tractions – are transferred from the fluid to the structural mesh. The matrix  $(\mathbf{H}^{FS})^T$  serves as transformation matrix for the discrete forces. It means that the surface tractions on the structural mesh do not have to be necessarily convergent, as long as the surface forces are. This is the case for the conservative coupling by the NNPro and the NN method, respectively. It follows further that the convergence of the error in the deformation on the structural mesh also depends on the transfer matrix  $(\mathbf{H}^{FS})^T$ . Obviously, for the NNPro transfer method, this transformation has only an  $O(h^2)$  convergence, when comparing the convergence of the error in the pressure on the fluid mesh with that in the deformation on the structural mesh, see Fig. 3.7. The fact that the error in the pressure distribution on the structural mesh for the conservative coupling technique is only convergent for the WR method, can be explained by the smoothing character of the weighting functions of the WR method. The non-convergence of the error for the NNPro and NN method is also shown in detail by DEBOER in [42].

For the different coupling methodologies, the pressure distributions, which are received by the structural mesh in the case of non-matching meshes, are shown in Fig. 3.9. It can be seen that the pressure distributions are smooth, when using a consistent transfer method. The low accuracy of the consistent NN transfer method becomes also visible. When using a conservative transfer method, only the WR method gives a smooth pressure distribution. The NNPro and the NN method lead to very jagged pressure distributions on the structural mesh. This observation agrees with the results obtained by the error analysis of Fig. 3.8.

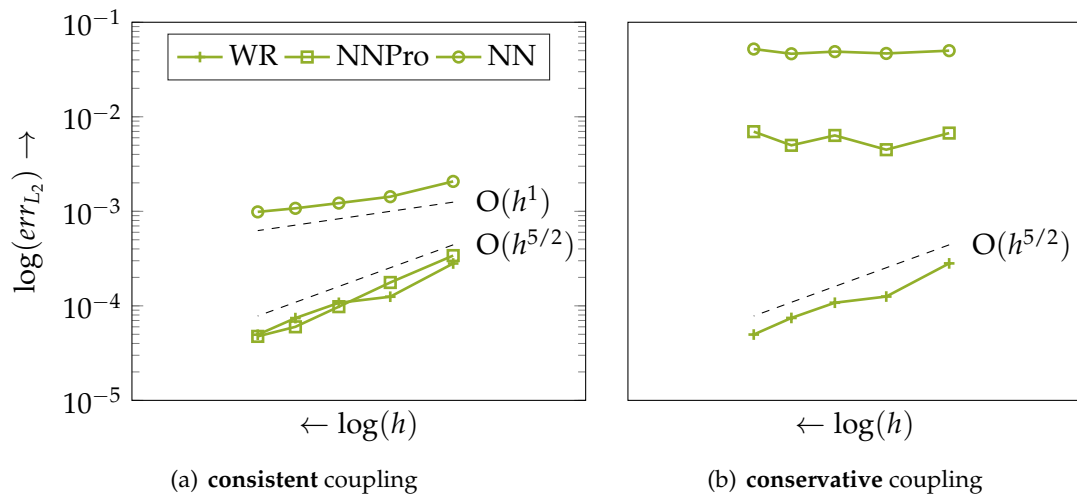


**Figure 3.8:** Convergence of the discretization error in the pressure on the structural mesh for non-matching meshes with different coupling techniques.

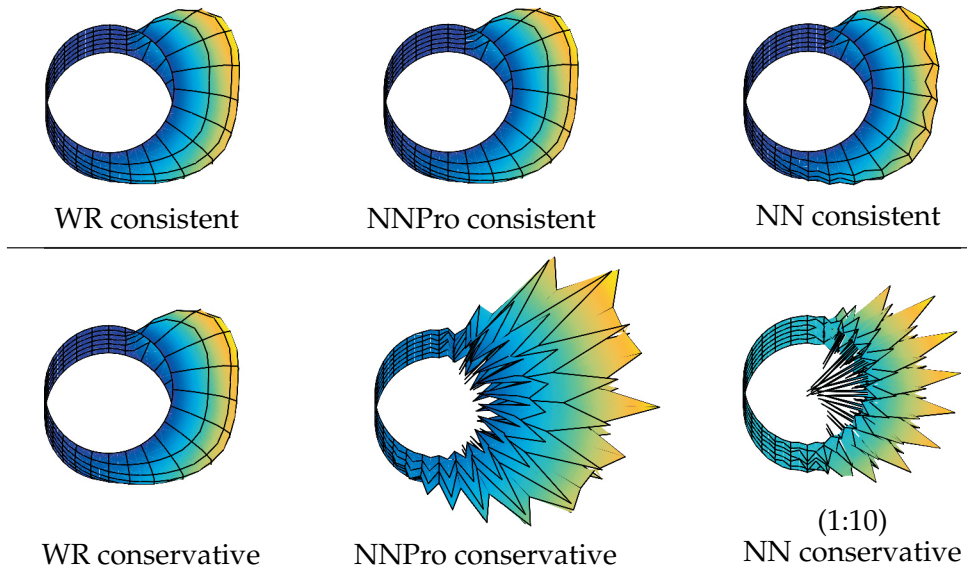


**Figure 3.9:** Pressure distributions on the structural mesh for different coupling techniques.

## Chapter 4

# Interface reduction methods

The numerical example of the previous chapter reveals that a large number of interface DOFs is necessary for an accurate calculation of the pressure distribution. In practice, when performing a simulation of a mechanical systems with lubricated joints or contacts, the total number of DOFs is usually strongly dominated by the DOFs, which are required for the lubricated interfaces. Therefore, adequate methods for reducing the DOFs of an elastic structure having a lubricated interface are a further focus of this thesis. Of special interest is their use in a flexible multibody simulation in the FFR formulation. Note that the following essay is published in great detail also in [102, 107] and [108]

### Review of existing methods

As mentioned, for further simulation purposes like a flexible multibody simulation, a reduction of the elastic structure with the large coupling interface is inevitable. In the context of component mode synthesis (CMS) [39], the classical approaches are based on a static or a modal interface reduction, as described by CRAIG and CHANG [38]. On the basis of CMS, interface reduction methods for systems with fluid-structure interaction are outlined in [83, 95]. However, dual approaches can also be used, which account for interface loads by the use of attachment modes. Following this approach, a time dependent parametric model order reduction scheme for systems with varying loads is given by TAMAROZZI et. al. [185]. In the context of EHL lubrication, a dual approach is followed by HABCHI et. al. [75] and HABCHI [73], where a set of basis vectors coming from a static analysis at different load regimes is applied for the interface reduction of line and circular point contacts, respectively. MAIER et. al. [122] use a proper orthogonal decomposition of training sets at different load regimes for the reduction of the full nonlinear system of the EHL line and point contact, respectively.

### Outline of this chapter

In this chapter, three different reduction schemes for structures with lubricated interfaces are applied and their numerical and computational efficiency are discussed in the context of a multibody simulation by using a FFR formulation. The first method represents a classical CRAIG BAMPTON [9] reduction of the structure without considering the lubricated interface in particular. In the second method, which is applied by NOVOTNY [131], first, a CRAIG BAMPTON reduction is applied to the elastic structure in order to maintain the degrees of freedom of the lubricated interface. In a second step, the already reduced structure is further reduced by a second CRAIG BAMPTON step. The third method, proposed in [107], makes use of a dual reduction strategy as outlined by GERADIN and RIXEN [65]. Within this concept, load dependent interface modes are used to represent the elastic deformation of the interface due to pressure forces.

All the methods are described for a linear finite element model ( $N$  degrees of freedom) governed by the equation

$$\mathbf{M}_{\text{FE}} \ddot{\mathbf{d}} + \mathbf{K}_{\text{FE}} \mathbf{d} = \mathbf{f}(t) \quad (4.1)$$

with mass matrix  $\mathbf{M}_{\text{FE}}$ , stiffness matrix  $\mathbf{K}_{\text{FE}}$  and a vector  $\mathbf{f}(t)$  of external forces. For further considerations, the displacement vector  $\mathbf{d}$  of the finite element model (4.1) is partitioned into  $n_i$  DOFs of inner nodes,  $n_f$  DOFs of nodes of the lubricated interface and  $n_b$  boundary DOFs, yielding:

$$\mathbf{d} = \begin{pmatrix} \mathbf{d}_i^T & \mathbf{d}_f^T & \mathbf{d}_b^T \end{pmatrix}^T.$$

In Section 4.1, a CRAIG BAMPTON procedure is applied, which does not particularly take care of the lubricated interface. In Section 4.2, the CRAIG BAMPTON method is applied twice in sequence, in order to cover the deformation of the lubricated interface in a better way. In contrast to the first two methods, which are based on fixed interface modes, the third method in Section 4.3 describes a dual reduction scheme using vibration modes of the free floating structure, attachment modes and additionally load dependent static modes for the lubricated interface. In Section 4.4, the described reduction methods are compared for two classical simulation examples – for a one-sided EHL joint of a slider-crank mechanism in FFR formulation as well as for an elastic rotor in a flexible journal bearing.

#### 4.1 CRAIG BAMPTON reduction method

The first method is a classical CRAIG BAMPTON reduction [9] without considering the lubricated interface in particular. Hence, the nodes  $\mathbf{d}_f$  of the lubricated interface are treated like inner nodes, which leads to the following partitioned finite element system:

$$\begin{bmatrix} \mathbf{M}_{\bar{f}\bar{f}} & \mathbf{M}_{\bar{f}b} \\ \mathbf{M}_{b\bar{f}} & \mathbf{M}_{bb} \end{bmatrix} \begin{pmatrix} \ddot{\mathbf{d}}_{\bar{f}} \\ \ddot{\mathbf{d}}_b \end{pmatrix} + \begin{bmatrix} \mathbf{K}_{\bar{f}\bar{f}} & \mathbf{K}_{\bar{f}b} \\ \mathbf{K}_{b\bar{f}} & \mathbf{K}_{bb} \end{bmatrix} \begin{pmatrix} \mathbf{d}_{\bar{f}} \\ \mathbf{d}_b \end{pmatrix} = \begin{pmatrix} \mathbf{f}_{\bar{f}} \\ \mathbf{f}_b \end{pmatrix},$$

with the partitioned displacement vector  $\mathbf{d}_{\bar{f}} = \begin{pmatrix} \mathbf{d}_i^T & \mathbf{d}_f^T \end{pmatrix}^T$ . The CRAIG BAMPTON procedure gives the following reduction of the displacement vector:

$$\mathbf{d} = \begin{bmatrix} \Phi_{\bar{f}\bar{v}} & -\mathbf{K}_{\bar{f}\bar{f}}^{-1} \mathbf{K}_{\bar{f}b} \\ \mathbf{0}_{b\bar{v}} & \mathbf{I}_{bb} \end{bmatrix} \begin{pmatrix} \mathbf{q}_{\bar{v}} \\ \mathbf{d}_b \end{pmatrix} = \bar{\mathbf{V}} \begin{pmatrix} \mathbf{q}_{\bar{v}} \\ \mathbf{d}_b \end{pmatrix}, \quad (4.2)$$

where  $\mathbf{q}_{\bar{v}}$  is the vector of the reduced modal coordinates,  $\mathbf{I}_{bb}$  is the identity matrix and the matrix  $\Phi_{\bar{f}\bar{v}}$  contains a subset of the first  $\bar{n}_v < n_i + n_f$  fixed-boundary vibration modes. They correspond to the solution of the eigenvalue problem for the DOFs  $\mathbf{d}_{\bar{f}}$ :

$$(-\omega_i^2 \mathbf{M}_{\bar{f}\bar{f}} + \mathbf{K}_{\bar{f}\bar{f}}) \boldsymbol{\phi}_i = \mathbf{0}, \quad i = 1 \dots (n_i + n_f)$$

with eigenvalues  $\omega_i^2$  and eigenvectors  $\boldsymbol{\phi}_i$ . The CRAIG BAMPTON reduction matrix is denoted by  $\bar{\mathbf{V}}$ , see Eq. (4.2). For its use in the FFR formulation, the rigid body motion has still to be removed. It can be ensured by fixing specific boundary DOFs by the use of the transformation matrix  $\bar{\mathbf{P}}$ . Then, the vector  $\mathbf{d}_b$  of boundary DOFs is restricted to a reduced vector  $\mathbf{q}_{b,el}$  and the overall reduction is given by

$$\mathbf{d} = \bar{\mathbf{P}} \bar{\mathbf{V}} \begin{pmatrix} \mathbf{q}_{\bar{f}} \\ \mathbf{q}_{b,el} \end{pmatrix} = \mathbf{V} \boldsymbol{\eta}_{el}, \quad (4.3)$$

with the overall reduction matrix  $\mathbf{V}$  and the vector  $\boldsymbol{\eta}_{el}$  of reduced coordinates. This relation for  $\mathbf{d}$  can now be used in the approximation (3.15) of the FFR formulation.

## 4.2 Two-step CRAIG BAMPTON method

The second method, which is already used for mechanical systems with lubricated contacts [131], is decomposed into two steps.

In the first step, the nodes of the lubricated interface of system (4.1) are treated like boundary nodes and the CRAIG BAMPTON procedure is applied, leading to the following transformation:

$$\mathbf{d} = \begin{bmatrix} \hat{\Phi}_{i\hat{v}} & -\mathbf{K}_{ii}^{-1} \mathbf{K}_{if} & -\mathbf{K}_{ii}^{-1} \mathbf{K}_{ib} \\ \mathbf{0}_{f\hat{v}} & \mathbf{I}_{ff} & \mathbf{0}_{fb} \\ \mathbf{0}_{b\hat{v}} & \mathbf{0}_{bf} & \mathbf{I}_{bb} \end{bmatrix} \begin{pmatrix} \mathbf{q}_{\hat{v}} \\ \mathbf{d}_f \\ \mathbf{d}_b \end{pmatrix} = \hat{\mathbf{V}}_1 \hat{\mathbf{d}}, \quad (4.4)$$

where the matrix  $\hat{\Phi}_{i\hat{v}}$  contains a subset of the first  $\hat{n}_v < n_i$  fixed-interface vibration modes corresponding to the eigenvalue problem for the inner nodes  $\mathbf{d}_i$ . Assuming the vibration modes to be  $\mathbf{M}_{ii}$ -orthogonal, this first reduction step gives the reduced system matrices:

$$\hat{\mathbf{V}}_1^T \mathbf{M}_{\text{FE}} \hat{\mathbf{V}}_1 = \begin{bmatrix} \mathbf{I}_{\hat{v}\hat{v}} & \hat{\mathbf{M}}_{\hat{v}f} & \hat{\mathbf{M}}_{\hat{v}b} \\ \hat{\mathbf{M}}_{f\hat{v}} & \hat{\mathbf{M}}_{ff} & \hat{\mathbf{M}}_{fb} \\ \hat{\mathbf{M}}_{b\hat{v}} & \hat{\mathbf{M}}_{bf} & \hat{\mathbf{M}}_{bb} \end{bmatrix}, \quad \hat{\mathbf{V}}_1^T \mathbf{K}_{\text{FE}} \hat{\mathbf{V}}_1 = \begin{bmatrix} \Omega_{\hat{v}}^2 & \mathbf{0}_{\hat{v}f} & \mathbf{0}_{\hat{v}b} \\ \mathbf{0}_{f\hat{v}} & \hat{\mathbf{K}}_{ff} & \hat{\mathbf{K}}_{fb} \\ \mathbf{0}_{b\hat{v}} & \hat{\mathbf{K}}_{bf} & \hat{\mathbf{K}}_{bb} \end{bmatrix}. \quad (4.5)$$

Due to the CRAIG-BAMPTON step, the matrix  $\Omega_{\hat{v}}^2$  is diagonal with the  $\hat{n}_v$  eigenvalues on its diagonal.

In a second step, the already reduced system is reduced by a further CRAIG BAMPTON reduction step for the new coordinate vector  $\hat{\mathbf{d}} = \left( \mathbf{q}_{\hat{v}}^T \quad \mathbf{d}_f^T \quad \mathbf{d}_b^T \right)^T$ . Maintaining the boundary nodes  $\mathbf{d}_b$ , the second transformation is given by

$$\hat{\mathbf{d}} = \begin{bmatrix} \Phi_{\hat{v}\hat{v}} & \mathbf{0}_{\hat{v}b} \\ \Phi_{f\hat{v}} & -\hat{\mathbf{K}}_{ff}^{-1} \hat{\mathbf{K}}_{fb} \\ \mathbf{0}_{b\hat{v}} & \mathbf{I}_{bb} \end{bmatrix} \begin{pmatrix} \mathbf{q}_{\hat{v}} \\ \mathbf{d}_b \end{pmatrix} = \hat{\mathbf{V}}_2 \begin{pmatrix} \mathbf{q}_{\hat{v}} \\ \mathbf{d}_b \end{pmatrix}. \quad (4.6)$$

The matrix  $\left[ \Phi_{\hat{v}\hat{v}}^T \quad \Phi_{f\hat{v}}^T \right]^T$  contains a subset of the first  $\tilde{n}_v < \hat{n}_v + n_f$  fixed-boundary vibration modes computed from the reduced system (4.5), where the boundary degrees of freedom are fixed, namely

$$\left( -\omega_i^2 \begin{bmatrix} \mathbf{I}_{\hat{v}\hat{v}} & \hat{\mathbf{M}}_{\hat{v}f} \\ \hat{\mathbf{M}}_{f\hat{v}} & \hat{\mathbf{M}}_{ff} \end{bmatrix} + \begin{bmatrix} \Omega_{\hat{v}}^2 & \mathbf{0}_{\hat{v}f} \\ \mathbf{0}_{f\hat{v}} & \hat{\mathbf{K}}_{ff} \end{bmatrix} \right) \phi_i = \mathbf{0} \quad i = 1 \dots (\hat{n}_v + n_f).$$

This second reduction step couples the static interface modes with the fixed-interface vibration modes of the first step. In conclusion, the complete procedure of the second method is expressed by the reduction basis  $\hat{\mathbf{V}}$ , see Eqs. (4.4) and (4.6):

$$\mathbf{d} = \hat{\mathbf{V}} \begin{pmatrix} \mathbf{q}_{\hat{v}} \\ \mathbf{d}_b \end{pmatrix}, \quad \hat{\mathbf{V}} = \hat{\mathbf{V}}_1 \hat{\mathbf{V}}_2.$$

In order to use the reduced coordinates in the FFR formulation, rigid body modes need still to be removed. This is ensured by restricting the vector  $\mathbf{d}_b$  of boundary nodes by the transformation matrix  $\hat{\mathbf{P}}$ . Then, similar to Eq. (4.3), the overall reduction is obtained by

$$\mathbf{d} = \hat{\mathbf{P}} \hat{\mathbf{V}} \begin{pmatrix} \mathbf{q}_{\hat{v}} \\ \mathbf{q}_{b,el} \end{pmatrix} = \mathbf{V} \boldsymbol{\eta}_{el}. \quad (4.7)$$

### 4.3 Dual reduction approach

In this section, a load dependent reduction strategy is proposed. The general framework of the procedure is based on a dual superelement formulation of GERADIN and RIXEN [65]. Therefore, for a more detailed description of the surrounding framework, it is referred to [65] and here, only the main steps of the procedure and its specification for lubricated interfaces are given.

#### General framework

In [65], for the finite element system (4.1), a reduction basis

$$\tilde{\mathbf{V}} = [\mathbf{U} \quad \Phi_v \quad \mathbf{G}_a \quad \mathbf{G}_r] = [\mathbf{U} \quad \mathbf{V}] \quad (4.8)$$

is proposed. The matrix  $\mathbf{U}$  collects the  $n_u$  rigid body modes of the floating structure, the matrix  $\Phi_v$  collects the  $n_v$  vibration modes of the free floating structure (usually  $n_v \ll (N - n_u)$ ), the matrix  $\mathbf{G}_a$  collects the  $n_a$  attachment modes obtained by the static responses of a unit loading at the attachment nodes and the matrix  $\mathbf{G}_r$  collects  $n_r$  residual modes, which can be chosen in different ways in order to enrich the reduction basis, e. g. in the case of nonlinear external forces like contact forces. In this work, the set of residual modes will be created by static responses due to pressure forces.

In the following, the main steps of the mode computation and preparation are outlined according to [65]:

- The eigenvalue problem of system (4.1)

$$\begin{aligned} (-\omega_i^2 \mathbf{M}_{\text{FE}} + \mathbf{K}_{\text{FE}}) \phi_i &= \mathbf{0} \quad i = 1 \dots N \\ \rightarrow \text{rigid body modes: } \mathbf{U} &= [\phi_1 \dots \phi_{n_u}] \quad \text{for } \omega_i^2 = 0, \\ \rightarrow \text{vibration modes: } \Phi_v &= [\phi_{n_u+1} \dots \phi_{n_u+n_v}] \quad \text{for } \omega_i^2 \neq 0, \end{aligned}$$

gives the  $n_u$  rigid body modes belonging to the zero eigenvalues and the  $(N - n_u)$  vibration modes belonging to the remaining eigenvalues. A modal reduction is obtained, when only a reduced set of  $n_v < (N - n_u)$  vibration modes is used. The vibration modes can be mass normalized in such a way that

$$\Phi_v^T \mathbf{K}_{\text{FE}} \Phi_v = \Omega_v^2, \quad \Phi_v^T \mathbf{M}_{\text{FE}} \Phi_v = \mathbf{I}_{vv}.$$

- For the  $n_a$  attachment modes, a loading matrix  $\mathbf{J}_a$  is constructed, in which each column belongs to a unit force vector at a single attachment node. In a similar way, for the residual modes, a loading set  $\mathbf{J}_c$  is constructed, which contains  $n_c$  arbitrary load cases not necessarily being unit force vectors or belonging to an attachment node. The static responses  $\mathbf{G}_a$  and  $\mathbf{G}_c$  are calculated by solving:

$$\begin{bmatrix} \mathbf{K}_{\text{FE}} & \mathbf{M}_{\text{FE}} \mathbf{U} \\ \mathbf{U}^T \mathbf{M}_{\text{FE}} & \mathbf{0} \end{bmatrix} \begin{bmatrix} \mathbf{G}_a & \mathbf{G}_c \\ \lambda_a & \lambda_c \end{bmatrix} = \begin{bmatrix} \mathbf{J}_a & \mathbf{J}_c \\ \mathbf{0} & \mathbf{0} \end{bmatrix}, \quad (4.9)$$

where the LAGRANGE multiplier  $\lambda_a$  and  $\lambda_c$  ensure mass orthogonality of the static mode sets with respect to the rigid body modes.

- The directions of the static mode set  $[\mathbf{G}_a \quad \mathbf{G}_c]$ , which are already covered by the vibration modes  $\Phi_v$ , are filtered out by the following transformation:

$$[\mathbf{G}_a \quad \mathbf{G}_c] \leftarrow [\mathbf{G}_a \quad \mathbf{G}_c] - \Phi_v \Omega_v^{-2} \Phi_v^T [\mathbf{J}_a \quad \mathbf{J}_c].$$

- For the mass normalization of the static modes, the following Cholesky factorization is outlined:

$$[\mathbf{G}_a \ \mathbf{G}_c]^T \mathbf{M}_{\text{FE}} [\mathbf{G}_a \ \mathbf{G}_c] = \mathbf{C}^T \mathbf{C}, \quad [\mathbf{G}_a \ \mathbf{G}_c] \leftarrow [\mathbf{G}_a \ \mathbf{G}_c] \mathbf{C}^{-1},$$

which gives a fully diagonal mass matrix, meaning  $\mathbf{G}_a^T \mathbf{M}_{\text{FE}} \mathbf{G}_a = \mathbf{I}_{aa}$ ,  $\mathbf{G}_c^T \mathbf{M}_{\text{FE}} \mathbf{G}_c = \mathbf{I}_{cc}$  and  $\mathbf{G}_a^T \mathbf{M}_{\text{FE}} \mathbf{G}_c = \mathbf{0}$ .

- For the attachment modes, the previous step yields  $\mathbf{G}_a^T \mathbf{M}_{\text{FE}} \mathbf{G}_a = \mathbf{I}_{aa}$  and  $\mathbf{G}_a^T \mathbf{K}_{\text{FE}} \mathbf{G}_a = \mathbf{K}_{aa}$ . For a further diagonalization of the stiffness matrix  $\mathbf{K}_{aa}$ , the eigenvalue problem

$$\mathbf{K}_{aa} \mathbf{Z} = \mathbf{Z} \mathbf{\Omega}_a^2$$

has to be solved, yielding a transformation for a diagonal stiffness matrix

$$\mathbf{G}_a \leftarrow \mathbf{G}_a \mathbf{Z}_a, \quad \mathbf{\Omega}_a^2 \leftarrow \mathbf{K}_{aa}.$$

- A reduced set  $\mathbf{G}_r$  of residual modes can be obtained from the static set  $\mathbf{G}_c$  by different approaches, e. g. by selecting these modes, which contribute the most to the strain energy. In this contribution, they are computed by an eigenvalue problem for the reduced stiffness matrix  $\mathbf{K}_{cc} = \mathbf{G}_c^T \mathbf{K}_{\text{FE}} \mathbf{G}_c$ :

$$(-\omega_i^2 \mathbf{I}_{cc} + \mathbf{K}_{cc}) \mathbf{Z}_i = \mathbf{0}, \quad i = 1 \dots n_c,$$

and choosing the set of eigenvectors  $\mathbf{Z}_r$  belonging to the first  $n_r$  smallest eigenvalues  $\omega_i^2$ . Then, a reduction of the static modes  $\mathbf{G}_c$  is achieved by following transformation:

$$n_r \leftarrow n_c, \quad \mathbf{G}_r \leftarrow \mathbf{G}_c \mathbf{Z}_r, \quad \mathbf{\Omega}_r^2 \leftarrow \mathbf{K}_{cc}. \quad (4.10)$$

- To obtain a fully diagonal stiffness matrix, a further eigenvalue calculation for the static stiffness matrix  $\mathbf{K}_s = [\mathbf{G}_a \ \mathbf{G}_r]^T \mathbf{K}_{\text{FE}} [\mathbf{G}_a \ \mathbf{G}_r]$ , namely

$$\begin{bmatrix} \mathbf{\Omega}_a^2 & \mathbf{K}_{ar} \\ \mathbf{K}_{ra} & \mathbf{\Omega}_r^2 \end{bmatrix} \mathbf{Z} = \mathbf{Z} \mathbf{\Omega}_s^2,$$

can be solved, yielding the transformation:

$$\mathbf{G}_s \leftarrow [\mathbf{G}_a \ \mathbf{G}_r] \mathbf{Z}_s, \quad \mathbf{\Omega}_s^2 \leftarrow \mathbf{K}_s.$$

At the end of this procedure, a reduction of the mass matrix  $\mathbf{M}_{\text{FE}}$  and the stiffness matrix  $\mathbf{K}_{\text{FE}}$  with the reduction matrix  $\mathbf{V}$  gives fully diagonal superelement matrices  $\mathbf{M}_{el}$  and  $\mathbf{K}_{el}$ :

$$\mathbf{M}_{el} = \mathbf{V}^T \mathbf{M}_{\text{FE}} \mathbf{V} = \begin{bmatrix} \mathbf{I}_{vv} & \mathbf{0} \\ \mathbf{0} & \mathbf{I}_{ss} \end{bmatrix}, \quad \mathbf{K}_{el} = \mathbf{V}^T \mathbf{K}_{\text{FE}} \mathbf{V} = \begin{bmatrix} \mathbf{\Omega}_v^2 & \mathbf{0} \\ \mathbf{0} & \mathbf{\Omega}_s^2 \end{bmatrix},$$

which can be used directly in the FFR formulation. Since in the reduction  $\mathbf{d} = \mathbf{V} \boldsymbol{\eta}_{el}$ , the rigid body modes are already projected out, see Eq. (4.8), no further transformation like in Eqs. (4.3) and (4.7) is needed. As a result, this reduction fulfills the condition of the BUCKEN's frame, see Section 3.1.2.

### Construction of interface modes

The set  $G_r$  of the static residual modes is a subset of the static set  $G_c$ , which is defined by an arbitrary load set  $J_c$ , see Eqs. (4.9) and (4.10). In the following, the load set  $J_c$  is specified for pressure forces coming from the surface tractions of the hydrodynamic equations, see Sections 3.2 and 3.3. By Eq. (3.33), which defines the forces on the structural domain, the load set  $J_c$  can be defined generally as:

$$J_c = M^{SS} (N^{SS} P_c^S),$$

where  $P_c^S$  is a set of discrete pressure distributions and the matrix  $N^{SS}$  contains in its columns the discrete normal vectors of each structural interface node and hence transforms each discrete pressure distribution to a discrete surface traction in normal direction. The surface tractions in tangential directions are not considered here, as the shear forces are usually negligible compared to the pressure forces. Setting

$$P_{c,1}^S = I_{cc} \quad (4.11)$$

to the identity matrix, gives an overall definition of the pressure set, as unit pressure values are applied at the interface nodes. This choice already reduces the  $3 n_{node}^S$  DOFs of the interface to  $n_{node}^S$  DOFs, since only pressure forces in normal direction are considered.

As the number  $n_{node}^S$  still can be large, it is proposed to build a set of pressure distributions, which is applicable for lubricated revolute joints, where the relative rotation occurs about the  $FZ$ -direction only (no tilting), like in Fig. 2.7. In this case, analytical solutions for the pressure distribution in  $FZ$ -direction exist for an infinite long and an infinite short bearing respectively, see Fig. 4.1. The solution  $p_l(z)$  of an infinite long bearing gives a constant pressure distribution and the solution  $p_s(z)$  of an infinite short bearing a quadratic distribution:

$$p_l(z) = p_m, \quad p_s(z) = \frac{4 p_0}{L^2} \left( \frac{L^2}{4} - z^2 \right),$$

where  $L$  is the bearing width. The respective mean pressure  $p_m$  of the long and the maximal pressure  $p_0$  of the short bearing solution still have to be specified in circumferential direction. Next, it is proposed to build a set of pressure distributions by assuming the analytical axial distribution at several circumferential positions:

$$P_{c,2}^S = \left[ P_{l,1} \quad \dots \quad P_{l,n_{node,y}^S}, \quad P_{s,1} \quad \dots \quad P_{s,n_{node,y}^S} \right]. \quad (4.12)$$

With this pressure set  $P_{c,2}$ , the  $3 n_{node}^S$  interface DOFs are reduced to  $2 n_{node,y}^S$  from the beginning.

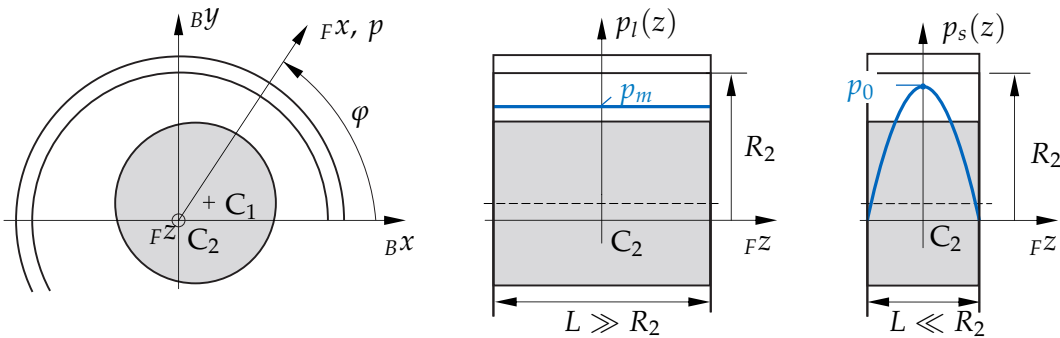


**Figure 4.1:** Pressure distributions for infinitely long (middle) and infinitely short bearing (right), computed in a discrete  $(F_x, F_z)$ -plane (left).

## 4.4 Numerical applications

In the following two sections, the introduced reduction methods are analyzed and compared for two different simulation examples. Therefore, the three reduction methods of Sections 4.1 to 4.3 are abbreviated by M1, M2 and M3, respectively.

### 4.4.1 Simulation example 1: flexible slider-crank mechanism

Here, the described reduction methods are compared for a simulation example of a slider-crank mechanism with an elastic connecting rod between a rigid crank shaft and a rigid piston. Hence, the connecting rod is the only body with flexible behavior. This simplification is made in order to better demonstrate and compare the different reduction methods. Note that the elastic structure deforms three-dimensionally, while the main rigid body motion of the rod takes place in the  $IX/IY$ -plane. Due to the rotation about the  $IZ$ -axis only, the concept of combining the short and long bearing solutions in the third reduction scheme is well applicable. The more general case will be considered in Section 4.4.2.

#### Flexible slider-crank mechanism

The flexible slider-crank mechanism is shown in Fig. 4.2. A hydrodynamic revolute cylindrical joint links the rigid shaft with the flexible connecting rod. A constant rotation speed  $\omega_1 = 500 \text{ rad/s}$  is enforced. At the beginning of the simulation, the slider is positioned at  $IX = l_1 + l_2$ , i. e. the relative eccentricity in the bearing is zero.

The mass and stiffness matrix of the flexible rod come from a finite element software tool. They are embedded in the multibody simulation by the FFR formulation as described in Section 3.1.2. For the first two CMS-based reduction methods, the floating frame is attached to the center  $C_2$  of the hydrodynamic bearing by constraining the rigid body translation and rotation of point  $C_2$ . Note that the point  $C_2$  accounts for the mean deformation of the interface DOFs, which is ensured by adequate constraint definitions in the FE model. For the third reduction method, where the dual approach is followed and free-interface normal modes are used, the floating frame is automatically located in the deformed configuration of the center of mass.

The cylindrical interface for the bearing is meshed with  $20 \times 5$  bi-quadratic elements in circumferential and  $z$ -direction respectively, which results in  $n_{node}^S = 340$  interface

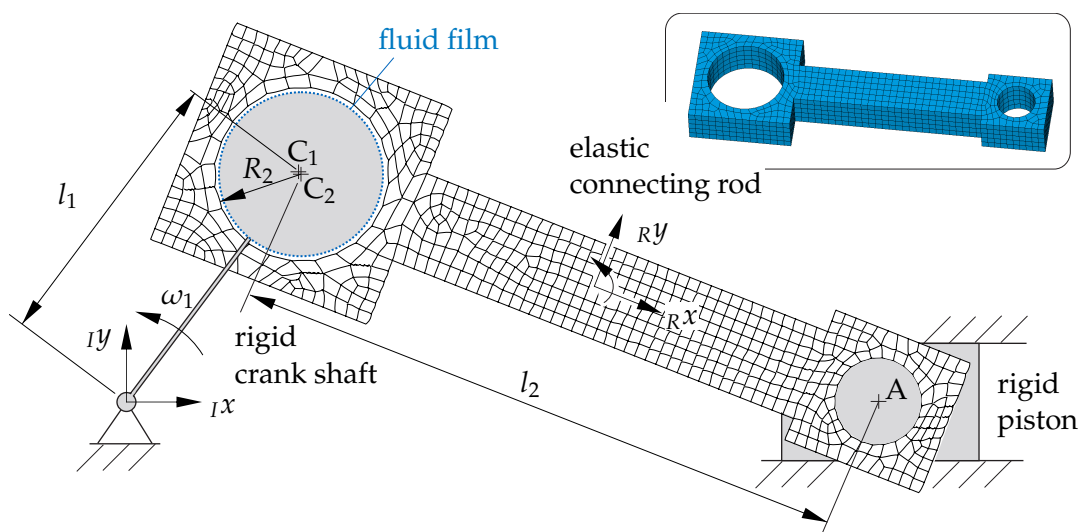


Figure 4.2: Slider-crank mechanism with flexible connecting rod and lubricated joint.

**Table 4.1:** Simulation parameters for the slider crank mechanism.

parameter	value	parameter	value
angular velocity $\omega_1$	500 $rad/s$	dyn. viscosity $\eta$	0.01 $kg/ms$
radius bearing $R_2$	2.25 $cm$	fluid density $\rho$	800 $kg/m^3$
clearance $h_0 = R_2 - R_1$	17.0 $\mu m$	nb. fluid nodes $n_{node}^F$	340
bearing width $L$	2.20 $cm$	nb. interface nodes $n_{node}^S$	340
crank length $l_1$	0.048 $m$	damping factor $\zeta$	0.001
rod length $l_2$	0.160 $m$	E-Modul $E$	210e9 $N/m^2$
rod center of mass $c_{2,x}$	0.0677 $m$	tolerances $tol_{Abs}, tol_{Rel}$	1e-7
crank mass $m_1$	1.00 $kg$	crank inertia $J_{1,zz}$	1e-3 $kg m^2$
rod mass $m_2$	0.973 $kg$	rod inertia $J_{2,zz}$	4e-3 $kg m^2$
piston mass $m_3$	0.500 $kg$		

nodes on the structure with  $n_{node,y}^S = 40$  equally distributed circumferential positions. Structural damping is applied by choosing the reduced damping matrix  $D_{el} = \zeta K_{el}$  proportional to the reduced stiffness matrix with damping factor  $\zeta$ . For the fluid mesh, a structured mesh with  $20 \times 5$  bi-quadratic elements in circumferential and z-direction respectively is used, leading to  $n_{node}^F = 340$  fluid nodes. The fluid mesh is assumed to be attached to the housing, meaning it is always conforming with the structural mesh. Further simulation parameters and fluid properties are listed in Table 4.1.

### Comparison of the three reduction methods

Global simulation outputs of the flexible slider-crank mechanism are compared for the three reduction methods of Sections 4.1 to 4.3. In detail, the maximal pressure and the minimal height during one rotation are analyzed, meaning the simulation time  $T$  is  $2\pi/\omega_1$ .

A reference solution is created with the third reduction method (M3) by applying the general choice  $P_{c,1}^S = I_{cc}$  for the pressure set. A large number of  $n_r = 60$  residual modes is used ensuring a reduction basis, which is rich enough to cover the interface behavior. The maximal pressure and minimal height over time are shown in Fig. 4.3(a) and Fig. 4.3(b), respectively. The number of vibration modes is  $n_v = 6$ .

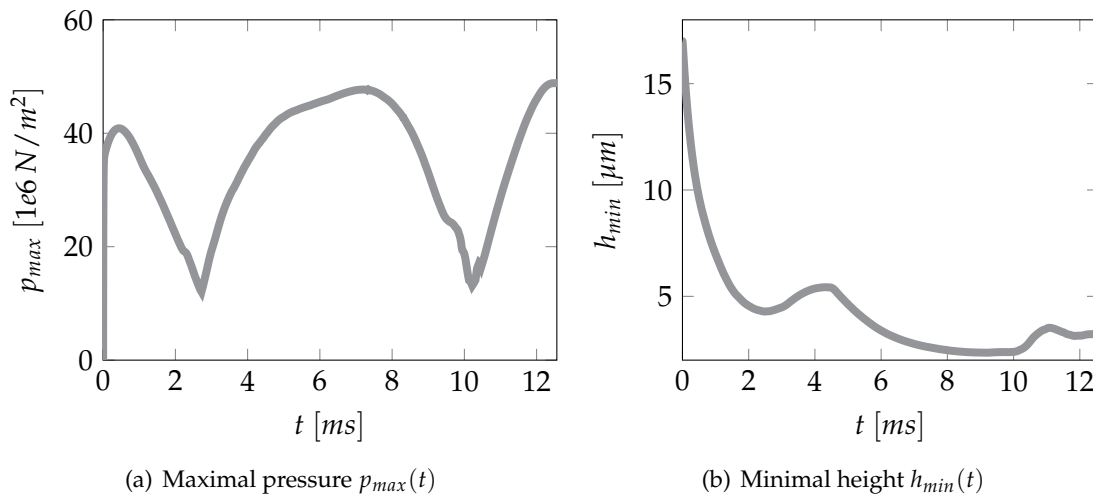


**Figure 4.3:** Reference solution with (M3) by using  $P_{c,1} = I_{cc}$ ,  $n_r = 60$  residual modes and  $n_v = 6$  vibration modes.

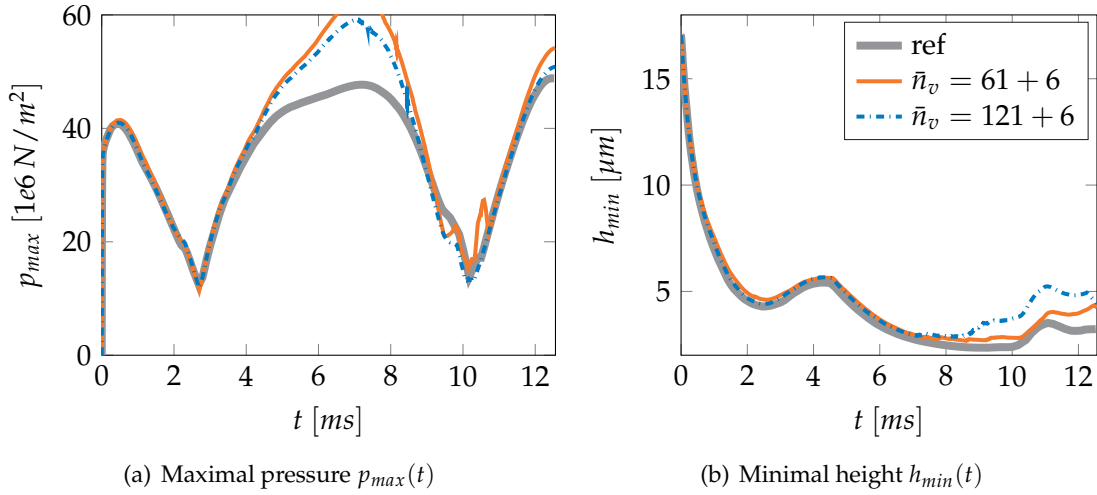


Figure 4.4: CRAIG BAMPTON scheme (M1).

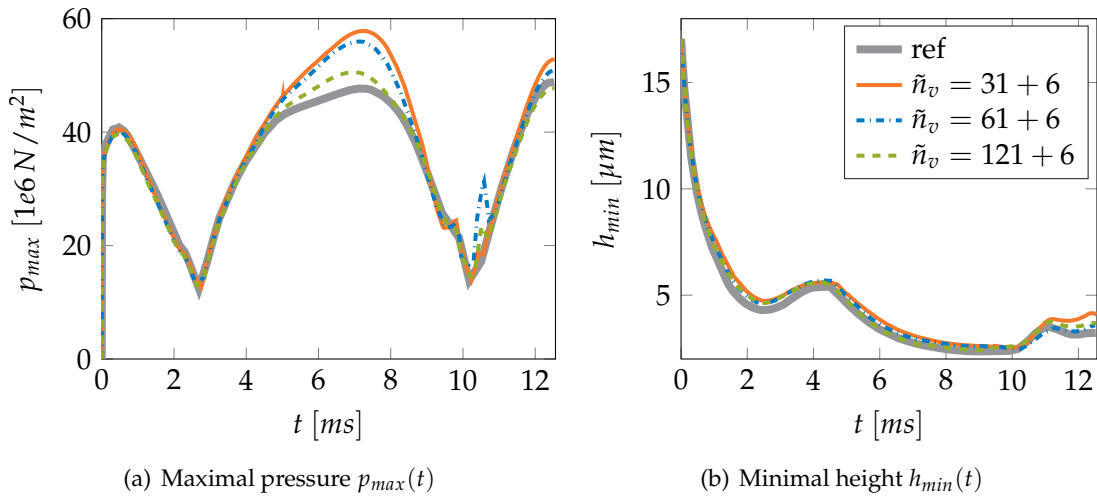


Figure 4.5: Two-step CRAIG BAMPTON scheme (M2).

In order to compare the three methods, the results of the maximal pressure and the minimal height are analyzed for a comparable number of modes. Point *A* of the flexible rod is considered as a boundary node in the reduction methods M1 and M2 and as an attachment mode in method M3, respectively. In the first two methods,  $n_b = 2$  static deformation modes and in the third method,  $n_a = 2$  attachment modes, respectively are used by applying unit displacements and unit forces in  $Rx/Ry$ -direction, respectively. For the load dependent reduction method (M3), it can be well distinguished between vibration modes and residual modes, which allows one to use a fixed number of 6 vibration modes ( $n_v = 6$ ) and vary the number  $n_r$  of residual modes. For the two-step CRAIG BAMPTON method (M2), the number of overall vibration modes is varied in dependence of  $n_r$  by  $\tilde{n}_v = n_r + 6$  and  $\hat{n}_v = 6$  vibration modes are used in the first CRAIG BAMPTON step. Making the CRAIG BAMPTON method (M1) comparable as well, the number  $\tilde{n}_v$  of vibration modes is varied in the same way, yielding  $\tilde{n}_v = n_r + 6$ .

In Fig. 4.4, the results for the first reduction method (M1) are shown. Compared to the reference solution, it is obvious that a large number of modes is required to cover the interface deformation. In particular, in the segments of high loads of Fig. 4.4(a), the pressure is overestimated, as the reduction basis is too poor.

Figure 4.5 shows the maximal pressure and minimal height obtained by the second reduction method (M2). Compared to M1, for similar results, less modes are required. However, the number  $\tilde{n}_v$  of modes has still to be large, when the reference solution should

be well approximated. As can be seen in Fig. 4.5(a), the elastic structure with  $\tilde{n}_v = 127$  modes behaves still too stiff in the high pressure segments.

The maximal pressure and minimal height for the load dependent reduction scheme (M3) with  $P_{c,2}^S$  are depicted in Fig. 4.6. The analytical pressure distributions in  $FZ$ -direction of the bearing width are normalized by setting  $p_m = 1$  and  $p_0 = 1.5$ . It becomes clear that the reference solution is well approximated when using  $n_r = 31$  residual modes only. Compared to M2, for similar results, less than a quarter of the number of modes are required. It is noteworthy that the combination of short and long bearing solution in Eq. (4.12) is mainly necessary in order to account properly for the bending deformation of the bearing in  $FZ$ -direction. The application of only one of the two analytical solutions would not converge to the reference solution.

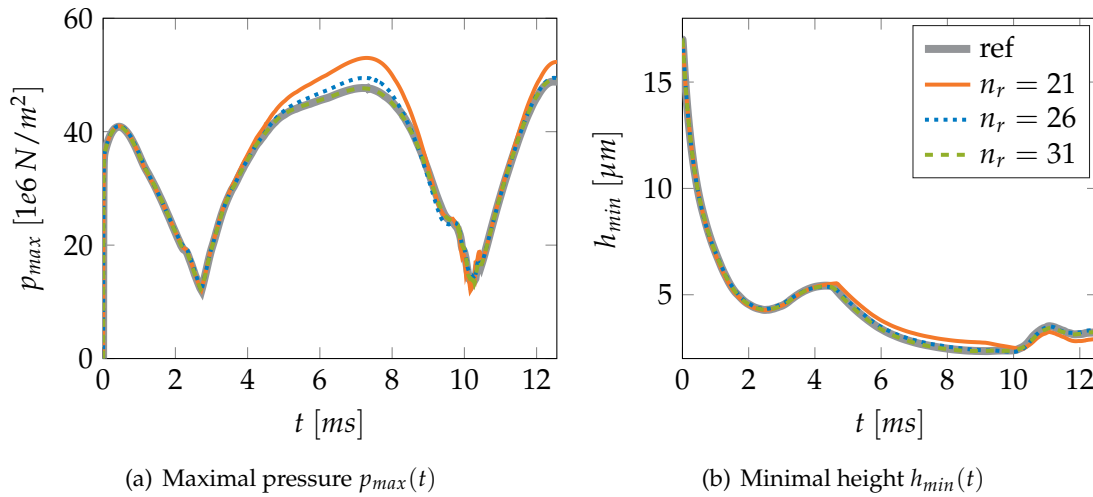


**Figure 4.6:** Load dependent reduction scheme (M3) with  $P_{c,2}^S$  ( $p_m = 1$  and  $p_0 = 1.5$ ).

#### 4.4.2 Simulation example 2: elastic rotor in flexible journal bearing

Here, the second simulation example of an elastic rotor in a flexible journal bearing is analyzed. In contrast to the simulation example of the previous section, unsymmetrical pressure distributions occur now along the axial direction in the journal bearing. Again, the three reduction methods are compared with each other.

##### Elastic rotor in flexible journal bearing

The simulation model of the elastic rotor in the flexible journal bearing is depicted in Fig. 4.7.

The elastic rotor consist of an elastic shaft with a rigidly attached disk in the middle. The shaft is modeled by 20 BERNOULLI beam elements, each with two nodes and 4 DOFs per node for the bending deformation in  $x$ - and  $y$ -direction respectively. A modal reduction gives 20 modes for the elastic deformation of the rotor, leading together with the shaft rotation to 21 overall DOFs. Gyroscopic effects are considered, see for instance [27, 162]. The rotor with the length  $l$  is supported at both ends elastically by a stiffness  $c$  and at half length by a flexible journal bearing. Modal damping with the damping ratio  $\zeta$  for each mode is considered. The rotor rotates with a constant rotation speed  $\omega_1 = 600 \text{ rad/s}$  and at three quarter length of the rotor an unbalance force  $F_r$  acts in radial direction.

The flexible bearing house is modeled as a linear finite element system ( $N = 8931$ ) with mass and stiffness matrix coming from a finite element software tool. Damping in the bearing house is not considered. The cylindrical interface of the bearing consists of  $20 \times 5$  bi-quadratic elements in circumferential and  $z$ -direction respectively, leading to

$n_{node}^S = 340$  interface nodes on the structure with  $n_{node,y}^S = 40$  circumferential positions. A conformal mesh is applied to the fluid zone, resulting in  $n_{node}^S = 340$  fluid nodes.

In summary, the elastic structure deforms three-dimensionally and the rotor performs a bending motion in the  $x/y$ -plane while rotating about the initial  $z$ -axis. This motion results in unsymmetrical 3D pressure distributions in the journal bearing.

Further simulation parameters of the rotor model and the fluid properties are listed in Table 4.2.

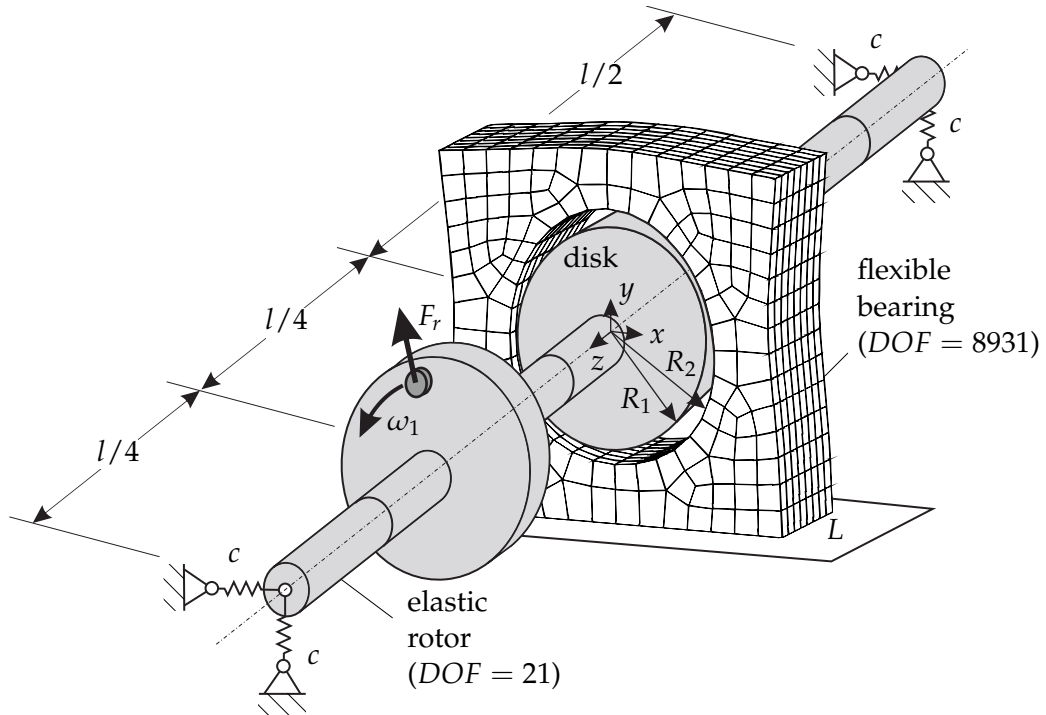


**Figure 4.7:** Elastic rotor with unbalance in flexible journal bearing.

**Table 4.2:** Simulation parameters for the elastic rotor in flexible journal bearing.

parameter	value	parameter	value
angular velocity $\omega_1$	$600 \text{ rad/s}$	dyn. viscosity $\eta$	$0.01 \text{ kg/ms}$
radius bearing $R_2$	$2.25 \text{ cm}$	fluid density $\rho$	$800 \text{ kg/m}^3$
clearance $h_0 = R_2 - R_1$	$17.0 \text{ }\mu\text{m}$	nb. fluid nodes $n_{node}^F$	340
bearing width $L$	$2.20 \text{ cm}$	nb. interface nodes $n_{node}^S$	340
rotor length $l$	$1.00 \text{ m}$	damping factor $\zeta$	0.001
rotor diameter $d_r$	$2.25 \text{ cm}$	E-Modul $E$	$210\text{e}9 \text{ N/m}^2$
steel density $\rho_r$	$7446 \text{ kg/m}^3$	simulation time $T$	$2\pi/\omega_1$
rotor inertia $J_{r,zz}$	$1\text{e-}3 \text{ kg m}^2$	tolerances $tol_{Abs}, tol_{Rel}$	$1\text{e-}8$
stiffness $c$	$1.58\text{e}8 \text{ N/m}$	radial force $F_r$	$3.60 \text{ kN}$

### Comparison of the three reduction methods

For the simulation example, the maximal pressure and minimal height are compared for the three reduction methods. The simulation time  $T$  is  $2\pi/\omega_1$ , meaning that one rotation is analyzed. In contrast to the simulation example of the slider-crank mechanism, un-

symmetrical pressure distributions in axial direction now occur due to the small tilting of the rotor shaft about the  $x$ - and  $y$ -directions, respectively. Therefore, the load dependent method (M3) is applied with the more general choice  $P_{c,1}^S$ , see Eq. (4.11).

Similar to Section 4.4.1, the three reduction methods are compared for a comparable number of modes. For the load dependent method (M3),  $n_v = 10$  vibration modes are used and the number  $n_r$  of residual modes is varied. For the two-step CRAIG BAMPTON method (M2), the number  $\tilde{n}_v$  of overall modes is chosen in dependence of  $n_r$  by  $\tilde{n}_v = n_r + 10$ . In a similar way, the number  $\tilde{n}_v$  of overall modes of the CRAIG BAMPTON method (M1) is chosen by  $\tilde{n}_v = n_r + 10$ .

A reference solution is created by M2, using  $\hat{n}_v = 10$  vibration modes and maintaining all interface DOFs. In Fig. 4.8, the error in the maximal pressure and minimal height are shown for all the three methods by using for each method 30 modes, which for the third method, are decomposed into  $n_r = 20$  residual and  $n_v = 10$  vibration modes. It can be seen that the error in the maximal pressure is large, especially in time intervals, which belong to high pressure situations. However, it becomes also clear that the load dependent method M3 comes closer to the reference solution than the two CMS-based methods. The classical CRAIG-BAMPTON method (M1) shows the largest deviations. In Fig. 4.9, the number of residual modes  $n_r$  in method M3 is increased to 40, leading to 50 overall modes. While the first two methods still behave too stiff, the error by the third method is relatively small.

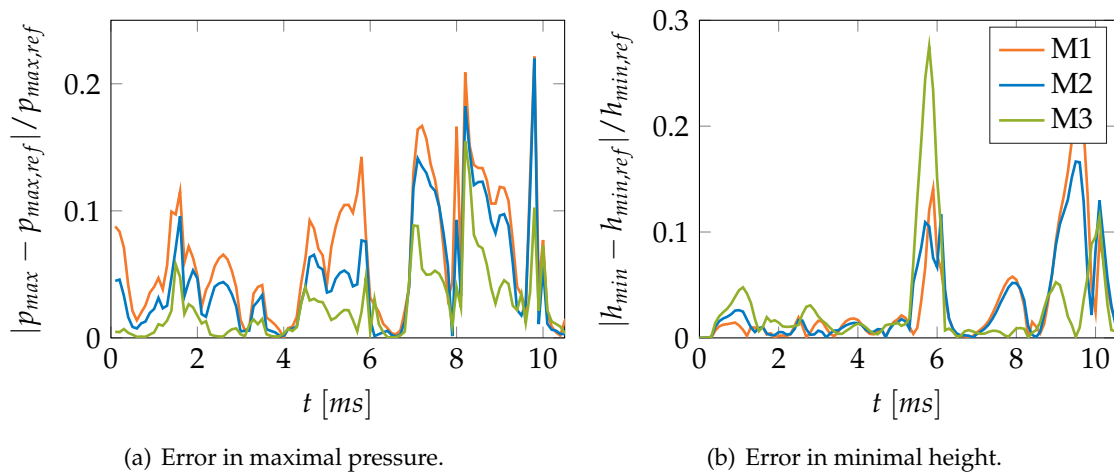


**Figure 4.8:** Comparison of the three reduction methods, each with 30 overall modes.

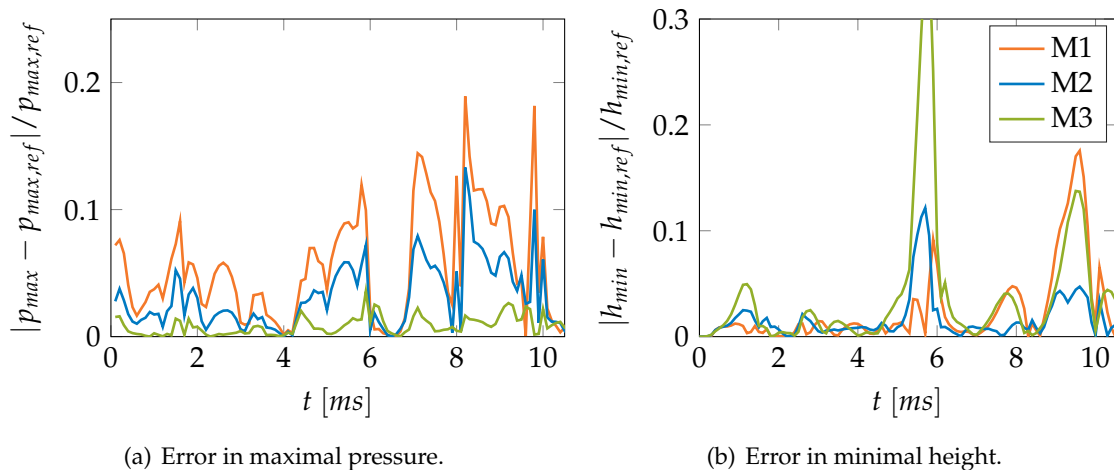


**Figure 4.9:** Comparison of the three reduction methods, each with 50 overall modes.

When analyzing the errors in the minimal height, it can be seen that there are situations with high errors at  $t \approx 5.9$  ms and  $t \approx 9.8$  ms. In these situations, the tilting of the rotor shaft causes sharp pressure distributions close to the bearing edges. The reduction basis of all the three methods is still too poor to cover the very local deformation of such load situations.

#### 4.4.3 Concluding remarks

Different reduction schemes for structures with lubricated interfaces are presented and compared for classical simulation examples.

The first two reduction methods are based on classical component mode synthesis. The first method does not take into account the lubricated interface in particular. The second method – a two-step CRAIG BAMPTON scheme – gives a reduced set of modes by combining static interface deformation and the vibration modes of a interface-fixed structure. By this, the interface deformation is covered in a better way, but still a large number of modes is required.

The best results are obtained by a load dependent reduction strategy, where the interface modes are computed as static responses due to pressure forces. Within this dual approach, it is possible to use analytical pressure distributions like the infinitely short and long bearing solution. These analytical solutions are well applicable during the reduction process for 3D elastic revolute joints with a shaft rotating about one axis only, as the example of the slider crank mechanism demonstrates. A more general choice is required, when unsymmetrical pressure distributions occur, like in the example of a flexible rotor in a flexible bearing housing.

As a further advantage, this load dependent reduction strategy allows a clear decomposition of vibration modes of the free floating structure and static modes belonging to attachment points and interface nodes. As a consequence, the number of modes for the lubricated interface can be adjusted independently of the vibration modes.



## Chapter 5

# Time integration and solution techniques

This chapter is dedicated to the time discretization of mechanical systems with EHL contacts. A special focus is placed on the solution of the dynamic equilibrium between pressure and deformation. Since the elastic deformation enters the REYNOLDS equation by the height in the third power, the relation between pressure and elastic deformation is highly nonlinear and thus, iterative solution techniques need to be applied during time integration.

The state-of-the-art technique to solve the coupled equations of EHL problems in MBS, is a partitioned approach, where the hydrodynamic pressure is considered inside a nonlinear force element, see for instance [61, 136, 189]. Further, in static as well as dynamic simulations of systems with EHL joints, the Newton-Raphson method is the favored solution technique for the nonlinear equations, see for instance [124, 135, 136].

In this chapter, alternative solution approaches and techniques are outlined and compared with the existing ones.

Besides the partitioned solution approach, this chapter also outlines a monolithic solution approach. It is achieved by coupling the hydrodynamic equations to the MBS by an additional algebraic equation using the projection formulation, which leads to a differential algebraic equation (DAE) of index 1.

As an alternative to the Newton-Raphson method, quasi-Newton algorithms are proposed for the solution of the nonlinear equations coming from the time-discretization. It will be shown that the Newton-Raphson method has the drawback of a time-consuming calculation of the Jacobian – especially in the case of a numeric differentiation, since a large number of elastic DOFs at the interface is considered. Therefore, partitioned quasi-Newton methods from FSI are applied to find the pressure-deformation equilibrium. A method with an inverse approximation of the Jacobian from a least-squares model, named interface quasi Newton - inverse least squares (IQN-ILS) method, is stated by DEGROOTE et al. [43]. Further quasi-Newton methods are described by DEGROOTE et al. [44] and BOGAERS et al. [16], where comparisons of the different methods are also given. For EHL joints, the partitioned IQN-ILS method is applied amongst others to the static solution by PROFITO et al. [154]. Here in this chapter, the IQN-ILS method of DEGROOTE is applied in modified form to the dynamic solution of the EHL problem.

Section 5.1 outlines the partitioned and the DAE formulation for the incorporation of the hydrodynamic equations into a MBS. Solution strategies by the simplified Newton and the IQN-ILS method are proposed.

Section 5.2 compares and discusses the different solution approaches and techniques for a numerical example.

It is noted that main parts of the following sections are published in the article of KRINNER et al. [110].

## 5.1 Formulations and time discretization

In this section, two different formulations for the incorporation of the pressure distribution into an arbitrary mechanical system are presented. The first one is a partitioned formulation, in which the hydrodynamic pressure is considered inside a nonlinear force element, which implies a staggered solution strategy for the dynamic equilibrium and the cavitation problem (Section 5.1.1). The second formulation is a DAE formulation and accounts for the cavitation problem in a monolithic manner using the projection formulation. This is possible since with the projection formulation of the cavitation problem the iterations can be computed with a tangent matrix. It will be shown, that the DAE formulation is well applicable for both the steady-state (Section 5.1.2) and the mass-conservative cavitation condition (Section 5.1.3).

The dynamic equations of motion are discretized in time by a generalized- $\alpha$  method [8, 35]. This integration scheme, which belongs to the class of NEWMARK integrators, is chosen because it introduces damping for the parasitic high frequencies in the solution while affecting only marginally the important lower frequencies.

For each of the formulations, an adequate solution technique is proposed: For the partitioned incorporation, a simplified Newton method as well as a quasi-Newton method are adapted to the solution of the nonlinear system of equations resulting from time discretization. In detail, it is shown, how the quasi-Newton algorithm of DEGROOTE [43] can be used in order to avoid calculation of the most time-consuming parts of the Jacobian during time integration.

For the DAE formulation with the projection function, the simplified Newton method is presented first. Second, it is shown, how the quasi-Newton algorithm can also be applied to the DAE formulation.

For the further analysis, the coupled system of Eqs. (3.52) to (3.57) is written in the following more compact and simplified form:

$$\mathbf{M}(\mathbf{q}) \ddot{\mathbf{q}} = \mathbf{h}_r(\mathbf{q}, \dot{\mathbf{q}}, t) + \mathbf{W}_p(\mathbf{q}) \mathbf{p}, \quad (5.1)$$

$$\mathbf{0} \leq \mathbf{p} \perp ((\mathbf{A}(\mathbf{p}, \mathbf{q}) + \mathbf{B}(\mathbf{p}, \mathbf{q})) \mathbf{p} + \mathbf{b}(\mathbf{p}, \mathbf{q}, \dot{\mathbf{q}})) \geq \mathbf{0}, \quad (5.2)$$

where, for simplicity,  $\dot{\mathbf{q}} = \dot{\mathbf{z}}$  is assumed, although considering a transformation matrix  $\mathbf{H}(\mathbf{q})$  would be straightforward. For the same reason, constraint equations are not considered. Further, only hydrodynamic forces due to the pressure in the normal direction are considered and viscous forces neglected. However, their consideration would be straightforward. The force direction matrix of the pressure is denoted by  $\mathbf{W}_p(\mathbf{q})$ . The vector  $\mathbf{h}_r$  summarizes all remaining non-hydrodynamic forces.

Again, when considering the mass-conservative cavitation condition, the following two equations are considered instead of Eq. (5.2):

$$\mathbf{C}_\varrho(\mathbf{q}) \dot{\mathbf{q}} = \mathbf{b}_\varrho(\mathbf{p}, \varrho, \mathbf{q}, \dot{\mathbf{q}}) - \mathbf{A}_\varrho(\mathbf{p}, \varrho, \mathbf{q}) \mathbf{p} - \mathbf{B}_\varrho(\mathbf{q}) \varrho \quad (5.3)$$

$$\mathbf{0} \leq \mathbf{p} \perp (\mathbf{f}_\varrho(\mathbf{p}) - \varrho) \geq \mathbf{0}. \quad (5.4)$$

Note that the complementarity condition is formulated for the node values only, without loss of generality.

For the further analysis in this chapter, the vector  $\mathbf{q}$  of generalized coordinates is decomposed into a vector of generalized coordinates of the global DOFs (subscript  $r$ ) describing the global motion of the bodies and a vector of the elastic DOFs (subscript  $el$ ) describing the deformation of the bodies:

$$\mathbf{q} = \begin{pmatrix} \mathbf{q}_r \\ \mathbf{q}_{el} \end{pmatrix}.$$

Compared to the coordinates of the FFR formulation of Section 3.1.2, the vector  $\mathbf{q}_r$  contains the vectors  $\mathbf{r}_R$  and  $\boldsymbol{\theta}$  of the motion of the reference frame, while  $\mathbf{q}_{el}$  represents the generalized coordinates of the overlaid small deformations.

### 5.1.1 Partitioned formulation

In the first formulation, the hydrodynamic pressure is considered inside a nonlinear force element. By defining the vector  $\mathbf{h}_{HD}(\mathbf{q}, \dot{\mathbf{q}}) = \mathbf{W}_p(\mathbf{q}) \mathbf{p}(\mathbf{q}, \dot{\mathbf{q}})$  of hydrodynamic forces, the pressure  $\mathbf{p}$  is regarded as an internal algebraic state. It is computed in each call of the vector  $\mathbf{h}_{HD}$  by solving the complementarity problem (5.2) for given position and velocity states by one of the outlined algorithms of Section 2.3.2.

A time discretization of Eq. (5.1) with the generalized- $\alpha$  scheme [8, 35] can be summarized as follows:

$$\mathbf{M}_{i+1} \ddot{\mathbf{q}}_{i+1} = \mathbf{h}_{r,i+1} + \mathbf{h}_{HD,i+1}, \quad (5.5)$$

$$(1 - \alpha_m) \mathbf{a}_{i+1} + \alpha_m \mathbf{a}_i = (1 - \alpha_f) \ddot{\mathbf{q}}_{i+1} + \alpha_f \ddot{\mathbf{q}}_i, \quad (5.6)$$

$$\mathbf{q}_{i+1} = \mathbf{q}_i + \Delta t \dot{\mathbf{q}}_i + \Delta t^2 [(0.5 - \beta) \mathbf{a}_i + \beta \mathbf{a}_{i+1}], \quad (5.7)$$

$$\dot{\mathbf{q}}_{i+1} = \dot{\mathbf{q}}_i + \Delta t [(1 - \gamma) \mathbf{a}_i + \gamma \mathbf{a}_{i+1}], \quad (5.8)$$

$$\mathbf{q}_0 = \mathbf{q}(0), \quad \dot{\mathbf{q}}_0 = \dot{\mathbf{q}}(0), \quad (5.9)$$

$$\ddot{\mathbf{q}}_0 = \mathbf{M}_0^{-1}(\mathbf{h}_{r,0} + \mathbf{h}_{HD,0}), \quad \mathbf{a}_0 = \ddot{\mathbf{q}}_0. \quad (5.10)$$

Here,  $\mathbf{q}_i$  is the vector of generalized coordinates at time-step  $t_i$ ,  $\dot{\mathbf{q}}_i$  is the vector of generalized velocities,  $\ddot{\mathbf{q}}_i$  is the vector of generalized accelerations,  $\mathbf{a}_i$  is the vector of acceleration-like auxiliary variables and  $\Delta t$  is the time-step size. Equations (5.5) to (5.8) have to be solved in each time-step by considering the starting conditions Eqs. (5.9) and (5.10) at  $t = 0$ .

By eliminating  $\dot{\mathbf{q}}_{i+1}$ ,  $\ddot{\mathbf{q}}_{i+1}$  and  $\mathbf{a}_{i+1}$ , the four Eqs. (5.5) to (5.8) can be reduced to one equation for the unknown discretized generalized coordinates  $\mathbf{q}_{i+1}$ . This leads to the following nonlinear residual equation for  $\mathbf{q}_{i+1}$  at the new time-step  $t_{i+1}$ :

$$\mathbf{R}_1(\mathbf{q}_{i+1}) = \mathbf{M}_{i+1} \ddot{\mathbf{q}}_{i+1}(\mathbf{q}_{i+1}) - \mathbf{h}_{r,i+1} - \mathbf{h}_{HD,i+1} = 0, \quad (5.11)$$

where  $\mathbf{a}_{i+1}$ ,  $\dot{\mathbf{q}}_{i+1}$  and  $\ddot{\mathbf{q}}_{i+1}$  are functions of  $\mathbf{q}_{i+1}$ :

$$\mathbf{a}_{i+1} = \mathbf{f}_a(\mathbf{q}_{i+1}) = \frac{1}{\Delta t^2 \beta} [\mathbf{q}_{i+1} - \mathbf{q}_i - \Delta t \dot{\mathbf{q}}_i - \Delta t^2 (0.5 - \beta) \mathbf{a}_i], \quad (5.12)$$

$$\dot{\mathbf{q}}_{i+1} = \mathbf{f}_{\dot{q}}(\mathbf{q}_{i+1}) = \dot{\mathbf{q}}_i + \Delta t [(1 - \gamma) \mathbf{a}_i + \gamma \mathbf{a}_{i+1}], \quad (5.13)$$

$$\ddot{\mathbf{q}}_{i+1} = \mathbf{f}_{\ddot{q}}(\mathbf{q}_{i+1}) = \frac{1}{1 - \alpha_f} [(1 - \alpha_m) \mathbf{a}_{i+1} + \alpha_m \mathbf{a}_i - \alpha_f \ddot{\mathbf{q}}_i]. \quad (5.14)$$

The generalized- $\alpha$  scheme offers second order behavior by defining the coefficients

$$\alpha_m = \frac{2\rho_\infty - 1}{\rho_\infty + 1}, \quad \alpha_f = \frac{\rho_\infty}{\rho_\infty + 1},$$

$$\gamma = \frac{1}{2} - \alpha_m + \alpha_f, \quad \beta = \frac{1}{4}(1 - \alpha_m + \alpha_f)^2,$$

where the numerical dissipation can be controlled by the spectral radius  $\rho_\infty \in [0, 1]$  at the high frequency limit.

For the residual (5.11), the Jacobian  $\mathbf{S}_1$  (also known as iteration matrix) is calculated as follows:

$$\mathbf{S}_1 = \frac{\partial \mathbf{R}_1}{\partial \mathbf{q}} = \mathbf{M} \frac{1 - \alpha_m}{(1 - \alpha_f) \Delta t^2 \beta} + \mathbf{C}_t \frac{\gamma}{\Delta t \beta} + \mathbf{K}_t, \quad (5.15)$$

where  $\mathbf{K}_t = \frac{\partial(M\ddot{\mathbf{q}} - \mathbf{h}_r - \mathbf{h}_{HD})}{\partial \mathbf{q}}$  is the tangent stiffness matrix and  $\mathbf{C}_t = \frac{\partial(-\mathbf{h}_r - \mathbf{h}_{HD})}{\partial \dot{\mathbf{q}}}$  is the tangent damping matrix. With the iteration matrix, the nonlinear residual Eq. (5.11) can be solved by Newton-Raphson iterations with iteration index  $k$ :

$$\begin{aligned} \mathbf{S}_{1,i+1}^k \Delta \mathbf{q}_{i+1}^k &= -\mathbf{R}_{1,i+1}^k \\ \mathbf{q}_{i+1}^{k+1} &= \mathbf{q}_{i+1}^k + \Delta \mathbf{q}_{i+1}^k. \end{aligned}$$

According to [8, 23], a scaled form  $\bar{\mathbf{S}}_1 \Delta \bar{\mathbf{q}} = -\bar{\mathbf{R}}_1$  with  $\bar{\mathbf{S}}_1 = \mathbf{D}_{L1} \mathbf{S}_1 \mathbf{D}_{R1}$ ,  $\Delta \bar{\mathbf{q}} = \mathbf{D}_{R1}^{-1} \Delta \mathbf{q}$  and  $\bar{\mathbf{R}}_1 = \mathbf{D}_{L1} \mathbf{R}_1$  can be used, where the preconditioning matrices

$$\mathbf{D}_{L1} = \beta \Delta t^2 \mathbf{I}, \quad \mathbf{D}_{R1} = \mathbf{I}$$

with the identity matrix  $\mathbf{I}$  ensuring optimal conditioning of the Jacobian and avoiding sensitivity to perturbations of the solution. For this formulation without algebraic equations, this scaling has no effect, but an extension of it will be outlined in Section 5.1.2.

Note that this formulation is called partitioned because the pressure is always calculated for given position and velocity states  $\mathbf{q}_{i+1}^k$  and  $\dot{\mathbf{q}}_{i+1}^k$ , respectively, by solving the complementarity problem. There is no strong coupling between the dynamic equations of motion and the cavitation problem in a way that the change of position and velocity states would affect the change of pressure. Due to this partitioned formulation, all the solution techniques have in common that there is an outer global iteration loop for fulfilling the dynamic equilibrium and an inner iteration loop for the solution of the steady-state cavitation problem.

In the next two subsections, two alternative solution techniques beside the Newton-Raphson method are presented in order to find the discretized dynamic equilibrium in each time-step more efficiently. The first one is the well-known simplified Newton method, the second one is a quasi Newton method.

### Simplified Newton method

The simplified Newton method does not update the Jacobian in each iteration, meaning  $\mathbf{S}_{i+1}^k = \mathbf{S}_{i+1}^0$ . Compared to the Newton-Raphson method, it has the benefit of calculating the Jacobian only once per time-step. However, since for EHL problems a large number of elastic DOFs at the interface is required, the calculation of the derivatives  $\frac{\partial \mathbf{h}_{HD}}{\partial \mathbf{q}_{el}}$  and  $\frac{\partial \mathbf{h}_{HD}}{\partial \dot{\mathbf{q}}_{el}}$  of the hydrodynamic forces in Eq. (5.15) can be either cumbersome, if it is done analytically, or time-consuming, if it is done numerically.

In the next subsection, a quasi-Newton method is applied in order to completely avoid the calculation of derivatives wrt. the elastic degrees of freedom.

### IQN-ILS method

In [43] a quasi-Newton method is proposed, which approximates the inverse Jacobian from a least-squares model during the iteration and is therefore called IQN-ILS method. Its application to the static solution of EHL contacts is shown in [154]. Here, it is applied in a different form to the dynamic solution process. A matrix-free implementation is described for the following form of the residual with its linearization:

$$\mathbf{R}(\mathbf{q}) = \mathbf{0} \quad \rightarrow \quad \mathbf{S}^k \Delta \mathbf{q}^k + \mathbf{R}(\mathbf{q}^k) = \mathbf{0}. \quad (5.16)$$

From here on, the subscript  $i + 1$  of the time step number is dropped to avoid lengthy notations. In short, the IQN-ILS method can be described by the following steps:

1. Estimate  $\tilde{\mathbf{q}}^k = \mathbf{q}^k - \mathbf{R}(\mathbf{q}^k)$  from the residual, i. e. by a steepest descent step.

2. Set up matrices (by abbreviating  $\mathbf{R}^k = \mathbf{R}(\mathbf{q}^k)$ )

$$\begin{aligned} \mathbf{V}^k &= [\Delta \mathbf{R}^{k-1} \quad \Delta \mathbf{R}^{k-2} \quad \dots \quad \Delta \mathbf{R}^1 \quad \Delta \mathbf{R}^0], & \text{where } \Delta \mathbf{R}^i &= \mathbf{R}^i - \mathbf{R}^k \\ \mathbf{W}^k &= [\Delta \tilde{\mathbf{q}}^{k-1} \quad \Delta \tilde{\mathbf{q}}^{k-2} \quad \dots \quad \Delta \tilde{\mathbf{q}}^1 \quad \Delta \tilde{\mathbf{q}}^0], & \text{where } \Delta \tilde{\mathbf{q}}^i &= \tilde{\mathbf{q}}^i - \tilde{\mathbf{q}}^k \end{aligned}$$

3. Calculate new direction  $\Delta \mathbf{q}^k = \mathbf{W}^k \alpha^k - \mathbf{R}^k$  with

$$\alpha^k = (\mathbf{V}^{kT} \mathbf{V}^k)^{-1} \mathbf{V}^{kT} (-\mathbf{R}^k)$$

corresponding to a least-square approximation. Note that this calculation is more stable when using a QR-decomposition of  $\mathbf{V}^k$ .

4. Update  $\mathbf{q}^{k+1} = \mathbf{q}^k + \Delta \mathbf{q}^k$  and  $k = k + 1$ .

Note that without calculating  $\alpha^k$  in step 3 (i. e.  $\alpha^k = 0$ ), the IQN-ILS method would result in a steepest descent method. Hence, the original method of DEGROOTE enriches the search direction of the steepest descent with search directions of previous iteration steps, which are optimal in a least-squares sense.

In this work the author proposes to modify the original IQN-ILS method by considering a preconditioned or scaled residual and defines

$$\mathbf{R}_{scal}^k = \left( \tilde{\mathbf{S}}^0 \right)^{-1} \mathbf{R}(\mathbf{q}^k) \quad (5.17)$$

to include information used in the simplified Newton. For that, the initial guess  $\tilde{\mathbf{q}}^k$  of each IQL-ILS iteration is computed from the simplified Newton (and not from a steepest descent estimate) using the form:

$$\tilde{\mathbf{q}}^k = \mathbf{q}^k - \mathbf{R}_{scal}^k. \quad (5.18)$$

For the residual (5.17), the incomplete Jacobian  $\tilde{\mathbf{S}}_1$  contains all entries except the derivatives  $\frac{\partial h_{HD}}{\partial q_{el}}$  and  $\frac{\partial h_{HD}}{\partial \tilde{q}_{el}}$ :

$$\tilde{\mathbf{S}}_1 = \mathbf{M} \frac{1 - \alpha_m}{(1 - \alpha_f) \Delta t^2 \beta} + \tilde{\mathbf{C}}_t \frac{\gamma}{\Delta t \beta} + \tilde{\mathbf{K}}_t, \quad (5.19)$$

with the incomplete tangential stiffness matrix  $\tilde{\mathbf{K}}_t = \frac{\partial(\mathbf{M}\tilde{\mathbf{q}} - \mathbf{h}_r)}{\partial \mathbf{q}} + \frac{\partial(-\mathbf{h}_{HD})}{\partial \mathbf{q}_r}$  and the incomplete tangential damping matrix  $\tilde{\mathbf{C}}_t = \frac{\partial(-\mathbf{h}_r)}{\partial \dot{\mathbf{q}}} + \frac{\partial(-\mathbf{h}_{HD})}{\partial \dot{\mathbf{q}}_r}$ . This means that *only the hydrodynamic stiffness and damping coefficients related to the global rigid motion of the components are considered*. Due to the preconditioned residual (5.17), the convergence properties of the quasi-Newton method are increased. A scheme of the quasi-Newton algorithm is proposed in Algorithm 1. For the first quasi-Newton step a relaxation with factor  $\omega$  for the state vector  $\mathbf{q}$  is used, as the matrices  $\mathbf{V}^k$  and  $\mathbf{W}^k$  need at least one column. If the global tolerances cannot be fulfilled within  $k_{max}$  iterations, the algorithm is restarted with a relaxation factor  $\omega/2$ . The prediction step of the original IQN-ILS method [43] is replaced by the prediction step of the generalized- $\alpha$  scheme on position level [8], leading:

$$\begin{aligned} \mathbf{a}_i^0 &= \frac{1}{1 - \alpha_m} (\alpha_f \ddot{\mathbf{q}}_{i-1} - \alpha_m \mathbf{a}_{i-1}), \\ \mathbf{q}_i^0 &= \mathbf{q}_{i-1} + \Delta t \dot{\mathbf{q}}_{i-1} + \Delta t^2 [(0.5 - \beta) \mathbf{a}_{i-1} + \beta \mathbf{a}_i^0]. \end{aligned}$$

With Algorithm 1, the calculation of the derivatives of the hydrodynamic forces with respect to the elastic degrees of freedom at the interface is completely circumvented.

**Algorithm 1** IQN-ILS method for partitioned formulation

---

```

1:  $\mathbf{q}_0 = \mathbf{q}(0), \dot{\mathbf{q}}_0 = \dot{\mathbf{q}}(0)$ 
2:  $\mathbf{a}_0 = \ddot{\mathbf{q}}_0 = \mathbf{M}_0^{-1}(\mathbf{h}_{r,0} + \mathbf{h}_{HD,0})$ 
3:  $k = 0$ 
4: for  $i = 1$  to number time-steps do
5:    $\mathbf{a}_i^0 = \frac{1}{1-\alpha_m}(\alpha_f \ddot{\mathbf{q}}_{i-1} - \alpha_m \mathbf{a}_{i-1})$ 
6:    $\mathbf{q}_i^0 = \mathbf{q}_{i-1} + \Delta t \dot{\mathbf{q}}_{i-1} + \Delta t^2 [(0.5 - \beta) \mathbf{a}_{i-1} + \beta \mathbf{a}_i^0]$ 
7:   Calculate Jacobian  $\tilde{\mathbf{S}}_i^0$  by Eq. (5.19) and Residual  $\mathbf{R}_i^0$  by Eq. (5.11)
8:   Calculate  $\mathbf{R}_{scal,i}^0$  by Eq. (5.17)
9:   Estimate  $\tilde{\mathbf{q}}_i^0$  by Eq. (5.18)
10:   $\omega = 1$ 
11:  while  $\omega \geq \omega_{min}$  do
12:     $\mathbf{q}_i^1 = \mathbf{q}_i^0 - \omega \mathbf{R}_{scal,i}^0$ 
13:     $k = 1$ 
14:    while  $|\mathbf{R}^{k-1}| > tol$  and  $k \leq k_{max}$  do
15:      Calculate Residual  $\mathbf{R}_i^k$  by Eq. (5.11) and scaled Residual  $\mathbf{R}_{scal,i}^k$  by Eq. (5.17)
16:      Estimate  $\tilde{\mathbf{q}}_i^k$  by Eq. (5.18)
17:      Update  $\mathbf{V}^k$  with  $\mathbf{R}_{scal,i}^k$  and  $\mathbf{W}^k$  with  $\tilde{\mathbf{q}}_i^k$ 
18:      Solve  $\mathbf{V}^k \alpha^k = -\mathbf{R}_{scal,i}^k$  using QR-decomposition
19:       $\Delta \mathbf{q}_i^k = \mathbf{W}^k \alpha^k - \mathbf{R}_{scal,i}^k$ 
20:       $\mathbf{q}_i^{k+1} = \mathbf{q}_i^k + \Delta \mathbf{q}_i^k$ 
21:       $k = k + 1$ 
22:    end while
23:     $\omega = \omega/2$ 
24:    if  $|\mathbf{R}^{k-1}| \leq tol$  and  $k \leq k_{max}$  then
25:       $\mathbf{q}_i = \mathbf{q}_i^k$ 
26:      Update  $\mathbf{a}_i, \dot{\mathbf{q}}_i, \ddot{\mathbf{q}}_i$  by Eqs. (5.12) to (5.14)
27:      break
28:    end if
29:  end while
30: end for

```

---

**5.1.2 DAE formulation by projection function**

For a monolithic solution strategy, the projection formulation (2.64) of the steady-state cavitation problem is used to couple the pressure by an additional algebraic equation to the dynamic equations of motion. In contrast to the state-of-the-art formulation, the pressure  $\mathbf{p}$  is now an explicit system variable:

$$\mathbf{M}(\mathbf{q}) \ddot{\mathbf{q}} = \mathbf{h}_r(\mathbf{q}, \dot{\mathbf{q}}, t) + \mathbf{W}_p(\mathbf{q}) \mathbf{p}, \quad (5.20)$$

$$\mathbf{p} = \text{proj}_{\mathbb{R}_0^+}[\mathbf{p} - r ((\mathbf{A}(\mathbf{p}, \mathbf{q}) + \mathbf{B}(\mathbf{p}, \mathbf{q})) \mathbf{p} - \mathbf{b}(\mathbf{p}, \mathbf{q}, \dot{\mathbf{q}}))], r > 0. \quad (5.21)$$

The resulting DAE is of index 1. With this formulation, the dynamic equilibrium of forces and displacements and the solution of the cavitation problem can be found simultaneously in a monolithic iteration procedure. Applying the generalized- $\alpha$  scheme for time integration leads to the following discretized system:

$$\mathbf{M}_{i+1} \ddot{\mathbf{q}}_{i+1} = \mathbf{h}_{r,i+1} + \mathbf{W}_{p,i+1} \mathbf{p}_{i+1}, \quad (5.22)$$

$$(1 - \alpha_m) \mathbf{a}_{i+1} + \alpha_m \mathbf{a}_i = (1 - \alpha_f) \ddot{\mathbf{q}}_{i+1} + \alpha_f \ddot{\mathbf{q}}_i, \quad (5.23)$$

$$\mathbf{q}_{i+1} = \mathbf{q}_i + \Delta t \dot{\mathbf{q}}_i + \Delta t^2 [(0.5 - \beta) \mathbf{a}_i + \beta \mathbf{a}_{i+1}], \quad (5.24)$$

$$\dot{\mathbf{q}}_{i+1} = \dot{\mathbf{q}}_i + \Delta t [(1 - \gamma) \mathbf{a}_i + \gamma \mathbf{a}_{i+1}], \quad (5.25)$$

$$\mathbf{p}_{i+1} = \text{proj}_{\mathbb{R}_0^+} [\mathbf{p}_{i+1} - r ((\mathbf{A}_{i+1} + \mathbf{B}_{i+1}) \mathbf{p}_{i+1} - \mathbf{b}_{i+1})], r > 0, \quad (5.26)$$

with similar starting conditions (5.9) and (5.10) and a consistent pressure starting condition  $\mathbf{p}(0) = \mathbf{p}_0$ . In contrast to Eqs. (5.5) to (5.8), the pressure  $\mathbf{p}_{i+1}$  and the algebraic Eq. (5.26) are now added explicitly.  $\mathbf{W}_{p,i+1}$  is the direction matrix of the pressure. By using Eqs. (5.12) to (5.14) for eliminating  $\dot{\mathbf{q}}_{i+1}$ ,  $\ddot{\mathbf{q}}_{i+1}$  and  $\mathbf{a}_{i+1}$ , the following residual for  $\mathbf{q}_{i+1}$  and  $\mathbf{p}_{i+1}$  has to be solved for a time-step  $t_{i+1}$ :

$$\mathbf{R}_2(\mathbf{q}_{i+1}, \mathbf{p}_{i+1}) = \begin{pmatrix} \mathbf{R}_q \\ \mathbf{R}_p \end{pmatrix} = \begin{pmatrix} \mathbf{M} \ddot{\mathbf{q}}_{i+1}(\mathbf{q}_{i+1}) - \mathbf{h}_{r,i+1} - \mathbf{W}_{p,i+1} \mathbf{p}_{i+1} \\ \mathbf{p}_{i+1} - \text{proj}_{\mathbb{R}_0^+} [\mathbf{p}_{i+1} - r ((\mathbf{A} + \mathbf{B}) \mathbf{p} - \mathbf{b})_{i+1}] \end{pmatrix} \stackrel{!}{=} \mathbf{0}, \quad (5.27)$$

with following row-wise evaluation of  $\mathbf{R}_p$  (suppressing the index  $i + 1$ ):

$$\mathbf{R}_p \Big|_{\text{row } j} = \begin{cases} r ((\mathbf{A} + \mathbf{B}) \mathbf{p} - \mathbf{b}) \Big|_{\text{row } j} & \text{if } [\mathbf{p} - r ((\mathbf{A} + \mathbf{B}) \mathbf{p} - \mathbf{b})] \Big|_{\text{row } j} > 0, \\ \mathbf{p} \Big|_{\text{row } j} & \text{else} \end{cases}.$$

The Jacobian  $\mathbf{S}_2$  of the residual (5.16) can be derived as follows:

$$\mathbf{S}_2 = \frac{\partial \mathbf{R}_2}{\partial (\mathbf{q}, \mathbf{p})} = \begin{bmatrix} \mathbf{M} \frac{(1-\alpha_m)}{(1-\alpha_f) \Delta t^2 \beta} + \mathbf{C}_t \frac{\gamma}{\Delta t \beta} + \mathbf{K}_t & -\mathbf{W}_{p,i+1} \\ \frac{\partial \mathbf{R}_p}{\partial \dot{\mathbf{q}}} \frac{\gamma}{\Delta t \beta} + \frac{\partial \mathbf{R}_p}{\partial \mathbf{q}} & \frac{\partial \mathbf{R}_p}{\partial \mathbf{p}} \end{bmatrix}, \quad (5.28)$$

where  $\mathbf{K}_t = \frac{\partial (\mathbf{M} \ddot{\mathbf{q}} - \mathbf{h}_r - \mathbf{W}_p \mathbf{p})}{\partial \mathbf{q}}$  is the tangent stiffness matrix and  $\mathbf{C}_t = \frac{\partial (-\mathbf{h}_r)}{\partial \dot{\mathbf{q}}}$  is the tangent damping matrix. The derivations of  $\mathbf{R}_p$  have to be evaluated row-by-row and are given in detail by:

$$\frac{\partial \mathbf{R}_p}{\partial \mathbf{q}} \Big|_{\text{row } j} = \begin{cases} r \left( \frac{\partial ((\mathbf{A} + \mathbf{B}) \mathbf{p} - \mathbf{b})}{\partial \mathbf{q}} \right) \Big|_{\text{row } j} & \text{if } [\mathbf{p} - r ((\mathbf{A} + \mathbf{B}) \mathbf{p} - \mathbf{b})] \Big|_{\text{row } j} > 0, \\ 0 & \text{else} \end{cases}, \quad (5.29)$$

$$\frac{\partial \mathbf{R}_p}{\partial \dot{\mathbf{q}}} \Big|_{\text{row } j} = \begin{cases} r \left( -\frac{\partial \mathbf{b}}{\partial \dot{\mathbf{q}}} \right) \Big|_{\text{row } j} & \text{if } [\mathbf{p} - r ((\mathbf{A} + \mathbf{B}) \mathbf{p} - \mathbf{b})] \Big|_{\text{row } j} > 0, \\ 0 & \text{else} \end{cases}, \quad (5.30)$$

$$\frac{\partial \mathbf{R}_p}{\partial \mathbf{p}} \Big|_{\text{row } j} = \begin{cases} r \left( \frac{\partial ((\mathbf{A} + \mathbf{B}) \mathbf{p})}{\partial \mathbf{p}} \right) \Big|_{\text{row } j} & \text{if } [\mathbf{p} - r ((\mathbf{A} + \mathbf{B}) \mathbf{p} - \mathbf{b})] \Big|_{\text{row } j} > 0, \\ \mathbf{I} \Big|_{\text{row } j} & \text{else} \end{cases}. \quad (5.31)$$

Motivated by [23], for the DAE formulation, following preconditioning matrices are proposed:

$$\mathbf{D}_{L2} = \begin{bmatrix} \beta \Delta t^2 \mathbf{I} & \mathbf{0} \\ \mathbf{0} & \beta \Delta t^2 \mathbf{I} \end{bmatrix}, \quad \mathbf{D}_{R2} = \begin{bmatrix} \mathbf{I} & \mathbf{0} \\ \mathbf{0} & \frac{1}{\beta \Delta t^2} \mathbf{I} \end{bmatrix}.$$

This rescaling is necessary, since the generalized displacements are chosen as the active variables in the generalized- $\alpha$  scheme. If the generalized accelerations were to be chosen as active variables, this rescaling would not be necessary, as both, the dynamic and pressure equations would be on acceleration level. Further, for an optimal scaling of the residual  $\mathbf{R}_p$ , it is proposed to choose the projection parameter  $r = 1/\sigma_{max}$ , with  $\sigma_{max}$  being the largest eigenvalue of matrix  $\mathbf{A}$ .

In the following two subsections, two monolithic solution techniques are presented for the DAE formulation: The simplified Newton method has again the drawback, that the derivations of the pressure equation with respect to the elastic displacement and velocity variables are computationally expensive. Therefore, a new solution technique is proposed by applying the IQN-ILS method for the updating of the state increment.

### Simplified Newton method for DAE formulation

The iteration matrix is given by Eq. (5.28). For the simplified Newton method, following iteration matrix is recommended at iteration step  $k$ :

$$\mathbf{S}_2^k = \begin{bmatrix} \mathbf{S}_{qq}^0 & \mathbf{S}_{qp}^0 \\ \mathbf{S}_{pq}^{0k} & \mathbf{S}_{pp}^k \end{bmatrix}, \quad (5.32)$$

where the entries  $\mathbf{S}_{qq}^0$  and  $\mathbf{S}_{qp}^0$  as well as the derivatives  $\left(\frac{\partial \mathbf{b}}{\partial \mathbf{q}_{el}}\right)^0$ ,  $\left(\frac{\partial((\mathbf{A}+\mathbf{B})\mathbf{p})}{\partial \mathbf{q}_{el}}\right)^0$  and  $\left(\frac{\partial \mathbf{b}}{\partial \dot{\mathbf{q}}_{el}}\right)^0$  in the derivatives (5.29) and (5.30) of  $\mathbf{S}_{pq}^{0k}$  are calculated only once per time-step and only the entries  $\mathbf{S}_{pq}^{0k}$  and  $\mathbf{S}_{pp}^k$  (Eq. (5.31)) are updated in each iteration due to the change of the if-else condition of the projection function.

The computationally expensive part is still the calculation of the derivatives  $\frac{\partial \mathbf{b}}{\partial \mathbf{q}_{el}}$ ,  $\frac{\partial((\mathbf{A}+\mathbf{B})\mathbf{p})}{\partial \mathbf{q}_{el}}$  and  $\frac{\partial \mathbf{b}}{\partial \dot{\mathbf{q}}_{el}}$ , as vector  $\mathbf{b}$  and square matrices  $\mathbf{A}$  and  $\mathbf{B}$  are calculated on the fluid mesh and  $\mathbf{q}_{el}$  and  $\dot{\mathbf{q}}_{el}$  include the large number of elastic DOFs at the interface.

### IQN-ILS method for DAE formulation

An alternative monolithic solution technique using the IQN-ILS method is presented in order to avoid the calculation of the derivations with respect to the elastic DOFs.

Similar to Eq. (5.18) of Algorithm 1, a linearization of the residual (5.16) with an incomplete Jacobian is used for the estimation of  $(\tilde{\mathbf{q}}^k, \tilde{\mathbf{p}}^k)$ :

$$\begin{pmatrix} \mathbf{R}_q \\ \mathbf{R}_p \end{pmatrix} \stackrel{!}{=} \mathbf{0} \quad \rightarrow \quad \begin{pmatrix} \tilde{\mathbf{q}}^k \\ \tilde{\mathbf{p}}^k \end{pmatrix} = \begin{pmatrix} \mathbf{q}^k \\ \mathbf{p}^k \end{pmatrix} - \underbrace{\left(\tilde{\mathbf{S}}_2^k\right)^{-1} \mathbf{R}_2^k}_{\mathbf{R}_{2,scal}}. \quad (5.33)$$

The author proposes the following incomplete Jacobian for the IQN-ILS method:

$$\tilde{\mathbf{S}}_2^k = \begin{bmatrix} \mathbf{S}_{qq}^0 & \mathbf{S}_{qp}^0 \\ \tilde{\mathbf{S}}_{pq}^{0k} & \mathbf{S}_{pp}^k \end{bmatrix}, \quad (5.34)$$

where again information of the simplified Newton is included. In contrast to the iteration matrix of Eq. (5.32), only the derivatives  $\left(\frac{\partial \mathbf{b}}{\partial \mathbf{q}_r}\right)^0$ ,  $\left(\frac{\partial((\mathbf{A}+\mathbf{B})\mathbf{p})}{\partial \mathbf{q}_r}\right)^0$  and  $\left(\frac{\partial \mathbf{b}}{\partial \dot{\mathbf{q}}_r}\right)^0$  wrt. the global generalized coordinates  $(\mathbf{q}_r, \dot{\mathbf{q}}_r)$  are used in the derivatives of Eqs. (5.29) and (5.30) of  $\tilde{\mathbf{S}}_{pq}^{0k}$ .

Using the incomplete iteration matrix (5.34), an algorithm for the DAE formulation with the IQN-ILS method is outlined, see Algorithm 2. The scheme of the algorithm is shown in Fig. F.1 of Appendix F.1 and has a framework similar to that of Algorithm 1. During the iterations, only the parts  $\tilde{\mathbf{S}}_{pq}^{0k}$  and  $\mathbf{S}_{pp}^k$  of the incomplete Jacobian are updated due to the change of the if-else condition of the projection function. Once, a new estimate  $\tilde{\mathbf{q}}^k$  is calculated, the state vector is updated by the IQN-ILS method. The pressure is advanced simply by  $\mathbf{p}^{k+1} = \tilde{\mathbf{p}}^k$ .

#### 5.1.3 DAE formulation for mass-conservative cavitation condition

In the previous two subsections, only a steady-state cavitation condition is considered, which is not mass-conservative in the cavitation region. In this subsection, the DAE formulation of Section 5.1.2 is extended for the mass-conservative cavitation condition. As shown in Sections 2.3.1 and 2.3.3, a mass-conservative formulation is achieved by integrating the density and modifying the system of Eqs. (5.20) and (5.21) as follows:

$$\mathbf{M}(\mathbf{q}) \ddot{\mathbf{q}} = \mathbf{h}_r(\mathbf{q}, \dot{\mathbf{q}}, t) + \mathbf{W}_p(\mathbf{q}) \mathbf{p}, \quad (5.35)$$

**Algorithm 2** IQN-ILS method for DAE formulation

---

```

1:  $\mathbf{q}_0 = \mathbf{q}(0), \dot{\mathbf{q}}_0 = \dot{\mathbf{q}}(0), \mathbf{p}_0 = \mathbf{p}_0$ 
2:  $\mathbf{a}_0 = \ddot{\mathbf{q}}_0 = \mathbf{M}_0^{-1} \mathbf{h}_{r,0}$ 
3:  $k = 0$ 
4: for  $i = 1$  to number time-steps do
5:    $\mathbf{a}_i^0 = \frac{1}{1-\alpha_m} (\alpha_f \ddot{\mathbf{q}}_{i-1} - \alpha_m \mathbf{a}_{i-1})$ 
6:    $\mathbf{q}_i^0 = \mathbf{q}_{i-1} + \Delta t \dot{\mathbf{q}}_{i-1} + \Delta t^2 [(0.5 - \beta) \mathbf{a}_{i-1} + \beta \mathbf{a}_i^0]$ 
7:    $\mathbf{p}_i^0 = \mathbf{p}_{i-1}$ 
8:   Calculate Jacobian  $\tilde{\mathbf{S}}_i^0$  by Eq. (5.34) and Residual  $\mathbf{R}_i^0$  by Eq. (5.27)
9:   Calculate  $\mathbf{R}_{scal,i}^0$  by Eq. (5.33)
10:  Estimate  $\tilde{\mathbf{q}}_i^0$  and  $\tilde{\mathbf{p}}_i^0$  by Eq. (5.33)
11:   $\omega = 1$ 
12:  while  $\omega \geq \omega_{min}$  do
13:     $\mathbf{q}_i^1 = \mathbf{q}_i^0 - \omega \mathbf{R}_{scal,i}^0$ 
14:     $\mathbf{p}_i^1 = \tilde{\mathbf{p}}_i^0$ 
15:     $k = 1$ 
16:    while ( $|\mathbf{R}_q^{k-1}| > tol_q$  or  $|\mathbf{R}_p^{k-1}| > tol_p$ ) and  $k \leq k_{max}$  do
17:      Calculate Residual  $\mathbf{R}_i^k$  by Eq. (5.27)
18:      Update terms  $\tilde{\mathbf{S}}_{pq}^{0k}$  and  $\tilde{\mathbf{S}}_{pp}^k$  of Jacobian  $\tilde{\mathbf{S}}_i^k$  by Eq. (5.34)
19:      Calculate scaled Residual  $\mathbf{R}_{scal,i}^k = (\tilde{\mathbf{S}}_i^k)^{-1} \mathbf{R}_i^k$  by Eq. (5.33)
20:      Estimate  $\tilde{\mathbf{q}}_i^k$  and  $\tilde{\mathbf{p}}_i^k$  by Eq. (5.33)
21:      Update  $\mathbf{V}^k$  with  $\mathbf{R}_{scal,i}^k$  and  $\mathbf{W}^k$  with  $\tilde{\mathbf{q}}_i^k$ 
22:      Solve  $\mathbf{V}^k \alpha^k = -\mathbf{R}_{scal,i}^k$  using QR-decomposition
23:       $\Delta \mathbf{q}_i^k = \mathbf{W}^k \alpha^k - \mathbf{R}_{scal,i}^k$ 
24:       $\mathbf{q}_i^{k+1} = \mathbf{q}_i^k + \Delta \mathbf{q}_i^k$ 
25:       $\mathbf{p}_i^{k+1} = \tilde{\mathbf{p}}_i^k$ 
26:       $k = k + 1$ 
27:    end while
28:     $\omega = \omega / 2$ 
29:    if  $|\mathbf{R}_q^{k-1}| \leq tol_q$  and  $|\mathbf{R}_p^{k-1}| \leq tol_p$  and  $k \leq k_{max}$  then
30:       $\mathbf{q}_i = \mathbf{q}_i^k$  and  $\mathbf{p}_i = \mathbf{p}_i^k$ 
31:      Update  $\mathbf{a}_i, \dot{\mathbf{q}}_i, \ddot{\mathbf{q}}_i$  by Eqs. (5.12) to (5.14)
32:      break
33:    end if
34:  end while
35: end for

```

---

$$\dot{\mathbf{q}} = -\mathbf{C}_q(\mathbf{q})^{-1} [\mathbf{A}_q(\mathbf{q}, \boldsymbol{\varrho}) \mathbf{p} + \mathbf{B}_q(\mathbf{q}) \boldsymbol{\varrho} - \mathbf{b}_q(\mathbf{q}, \dot{\mathbf{q}}, \boldsymbol{\varrho})], \quad (5.36)$$

$$\mathbf{p} = \text{proj}_{\mathbb{R}_0^+} [\mathbf{p} - r (\mathbf{f}_q(\mathbf{p}) - \boldsymbol{\varrho})], \quad r > 0, \quad (5.37)$$

where now the density  $\boldsymbol{\varrho}$  is a further state variable and the additional algebraic equation for the pressure is formulated by the condition (5.4). The set of dynamic equations of motion (5.35) is discretized by the generalized- $\alpha$  scheme and leads to similar Eqs. (5.22) to (5.25). For the density, a time-discretization by the  $\theta$ -rule is applied, where the pressure is considered fully implicit. This leads to following two equations, which have to replace Eq. (5.26) for a mass-conservative representation:

$$\begin{aligned} \boldsymbol{\varrho}_{i+1} = \boldsymbol{\varrho}_i + \Delta t ((1 - \theta) \mathbf{C}_{\boldsymbol{\varrho},i+1}^{-1} (\mathbf{b}_{\boldsymbol{\varrho},i+1} - \mathbf{B}_{\boldsymbol{\varrho},i+1} \boldsymbol{\varrho}_{i+1}) + \theta \mathbf{C}_{\boldsymbol{\varrho},i}^{-1} (\mathbf{b}_{\boldsymbol{\varrho},i} - \mathbf{B}_{\boldsymbol{\varrho},i} \boldsymbol{\varrho}_i)) \\ - \Delta t \mathbf{C}_{\boldsymbol{\varrho},i+1}^{-1} \mathbf{A}_{\boldsymbol{\varrho},i+1} \mathbf{p}_{i+1}, \end{aligned} \quad (5.38)$$

$$\mathbf{p}_{i+1} = \text{proj}_{\mathbb{R}_0^+} [\mathbf{p}_{i+1} - r (\mathbf{f}_\rho(\mathbf{p}_{i+1}) - \mathbf{q}_{i+1})], \quad r > 0. \quad (5.39)$$

This scheme can maintain the second order behavior of the generalized- $\alpha$  scheme for the density by setting  $\theta = 1/2$ . In order to ensure the non-smooth algebraic Eq. (5.39), the pressure has to be considered fully implicit. This leads to a first order convergence of the pressure<sup>12</sup>.

The discretized system with the unknown state vector  $\mathbf{q}_{i+1}$ , pressure  $\mathbf{p}_{i+1}$  and density  $\mathbf{q}_{i+1}$  can be solved efficiently when inserting Eq. (5.38) in Eq. (5.39), leading to the following pressure residual  $\hat{\mathbf{R}}_p$ :

$$\hat{\mathbf{R}}_p = \mathbf{p}_{i+1} - \text{proj}_{\mathbb{R}_0^+} [\mathbf{p}_{i+1} - r (\hat{\mathbf{A}}_{i+1} \mathbf{p}_{i+1} - \hat{\mathbf{b}}_{i+1})], \quad r > 0, \quad (5.40)$$

with the abbreviations

$$\begin{aligned} \hat{\mathbf{b}}_{i+1} &= -[\mathbf{f}_\rho(\mathbf{p}_{i+1}) - \mathbf{q}_i - \Delta t (1 - \theta) \mathbf{C}_{\rho,i+1}^{-1} (\mathbf{b}_{\rho,i+1} - \mathbf{B}_{\rho,i+1} \mathbf{q}_{i+1}) \\ &\quad + \Delta t \theta \mathbf{C}_{\rho,i}^{-1} (\mathbf{b}_{\rho,i} - \mathbf{B}_{\rho,i} \mathbf{q}_i)], \\ \hat{\mathbf{A}}_{i+1} &= \Delta t (\mathbf{C}_{\rho,i+1}^{-1} \mathbf{A}_{\rho,i+1}). \end{aligned}$$

Further, the following density residual  $\mathbf{R}_\rho$  has to be solved:

$$\begin{aligned} \mathbf{R}_\rho &= \mathbf{q}_{i+1} - \mathbf{q}_i - \Delta t (1 - \theta) \mathbf{C}_{\rho,i+1}^{-1} (\mathbf{b}_{\rho,i+1} - \mathbf{B}_{\rho,i+1} \mathbf{q}_{i+1}) \\ &\quad - \Delta t \theta \mathbf{C}_{\rho,i}^{-1} (\mathbf{b}_{\rho,i} - \mathbf{B}_{\rho,i} \mathbf{q}_i) + \Delta t \mathbf{C}_{\rho,i+1}^{-1} \mathbf{A}_{\rho,i+1} \mathbf{p}_{i+1}. \end{aligned}$$

During the solution process, the derivation  $\frac{\partial \hat{\mathbf{R}}_p}{\partial \mathbf{q}}$  can be neglected due to its small sensitivity and an iteration matrix  $\mathbf{S}_3$  similar to (5.28) can be used during the iterative solution process, yielding:

$$\mathbf{S}_3 = \frac{\partial \mathbf{R}_3}{\partial (\mathbf{q}, \mathbf{p})} = \begin{bmatrix} \mathbf{M} \frac{(1-\alpha_m)}{(1-\alpha_f) \Delta t^2 \beta} + \mathbf{C}_t \frac{\gamma}{\Delta t \beta} + \mathbf{K}_t & -\mathbf{W}_{p,i+1} \\ \frac{\partial \hat{\mathbf{R}}_p}{\partial \mathbf{q}} \frac{\gamma}{\Delta t \beta} + \frac{\partial \hat{\mathbf{R}}_p}{\partial \mathbf{q}} & \frac{\partial \hat{\mathbf{R}}_p}{\partial \mathbf{p}} \end{bmatrix}.$$

As a result, the solution techniques presented in Sections 5.1.2 and 5.1.2 can be well applied, when the residual (5.40) instead of (5.26) is used. According to Eq. (5.38), the density has to be updated hand-in-hand with the pressure:

$$\mathbf{q}_{i+1}^{k+1} = \mathbf{q}_{i+1}^k + \Delta \mathbf{q}_{i+1}^k,$$

with the density increment

$$\Delta \mathbf{q}_{i+1}^k = \left( \frac{\partial \mathbf{R}_\rho^k}{\partial \mathbf{q}} \right)^{-1} \left( -\mathbf{R}_{\rho,i+1}^k - \left( \frac{\partial \mathbf{R}_\rho^k}{\partial \mathbf{p}} \right) \Delta \mathbf{p}_{i+1}^k - \left( \frac{\partial \mathbf{R}_\rho}{\partial \mathbf{q}} \frac{\gamma}{\Delta t \beta} + \frac{\partial \mathbf{R}_\rho}{\partial \mathbf{q}} \right) \Delta \mathbf{q}_{i+1}^k \right)$$

being obtained from the linearization of the density residual in the Newton method.

Note that the scaling method of the previous subsection is still valid for the Jacobian  $\mathbf{S}_3$  and the residual  $\mathbf{R}_3$ . The only difference is that now the projection parameter has to be chosen by  $r = 1/(\Delta t \hat{\sigma}_{max})$  with  $\hat{\sigma}_{max}$  being the largest eigenvalue of the matrix  $(\mathbf{C}^{-1} \mathbf{A})$ .

<sup>1</sup>It is noted that besides the time discretization by the  $\theta$ -method, also the generalized- $\alpha$  scheme for first order systems as described by JANSEN et. al. [94] and BRUELS et. al. [30] or a RUNGE-KUTTA scheme for DAE systems as described by HAIRER and WANNER [79] could be applied to the hydrodynamic equations.

<sup>2</sup>The effect of the time discretization by the  $\theta$ -scheme can be considered in the stabilization parameter of Eq. (2.78) by setting  $\sigma^{(e)} = h/(\theta \Delta t)$  with the fluid height  $h$ . However, practical examples showed that  $\tau_q^{(e)}$  becomes too small for an effective stabilization, when considering the time-step size in  $\sigma^{(e)}$ , see Footnote 4 on page 29.

## 5.2 Numerical Example

In this section, the two different cavitation models as well as the different formulations (partitioned, DAE) with different solution techniques (simplified Newton, IQN-ILS) are compared for the same simulation model of Section 3.4. However, now a dynamic analysis is performed by considering the radial force of  $F_r = 2.5 \text{ kN}$  instead of the static force  $F_x$ . Further, the shaft mass is set now to  $10 \text{ kg}$  and a compressibility of the density by a factor  $a = 1e-8 \text{ m}^2/\text{N}$  is added. Global outputs like the maximal pressure and the orbit of the rotor are used to analyze the physical difference between the steady-state and the mass-conservative cavitation model. For the numerical analysis of the different formulations and solution strategies, the number of global iterations, the number of pressure iterations and the simulation time are compared with each other.

At the beginning of the simulation, the rotor is situated in the center of the bearing and rotates with constant angular velocity ( $\omega_1 = 500 \text{ rad/s}$ ). Due to its weight, the radial force and the pressure force, the rotor reaches a constant orbit in the bearing after a few rotations. The simulation time is  $T = 1.4^2\pi/\omega_1$ , a constant time-step size  $\Delta t = 1e-4 \text{ s}$  is used. All the simulations are performed with Matlab on a i3-3220 CPU (3,3 GHz, 8 GB RAM).

In Fig. 5.1, the maximal pressure over time and the orbit of the rotor are plotted for the steady-state as well as the mass-conservative cavitation model. It can be seen, that mass conservation does not change the maximal pressure or the orbit significantly as the change of density is small. However, a tendency to a weaker elasticity in the mass-conservative cavitation model can be recognized in the orbit of Fig. 5.1 right. The reason is, that the density wedge term (2.4) influences the mass-flow at the cavitation boundary and as a consequence the maximal pressure differs slightly from the steady-state cavitation model. In Fig. 5.1 left, it becomes evident, that the maximal pressure of the mass-conservative model is less smooth. This could be avoided by a finer mesh for this cavitation model, but it is not realized in order to allow a better comparison of the numerical behavior. For the comparison at one time-step, the pressure distribution of the steady-state cavitation model is shown in Fig. 5.2, whereas in Fig. 5.3, the pressure and density distribution of the mass-conservative model are shown.

In the following subsections, the numerical behavior of the formulations and solution methods are compared. For all the methods, both the complete and the incomplete Jacobian are calculated once by an analytical, element-wise differentiation and once by a numerical differentiation with a finite difference scheme. It is noted that, in the analytical case, the calculation of the complete Jacobian is as time-consuming as the calculation of the incomplete Jacobian.

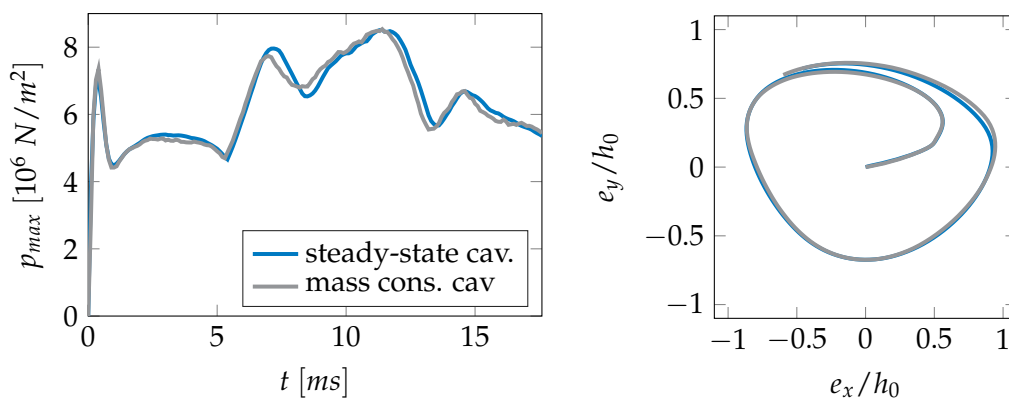


**Figure 5.1:** Maximal pressure (left) and orbit (right) for steady-state and mass-conservative cavitation model.

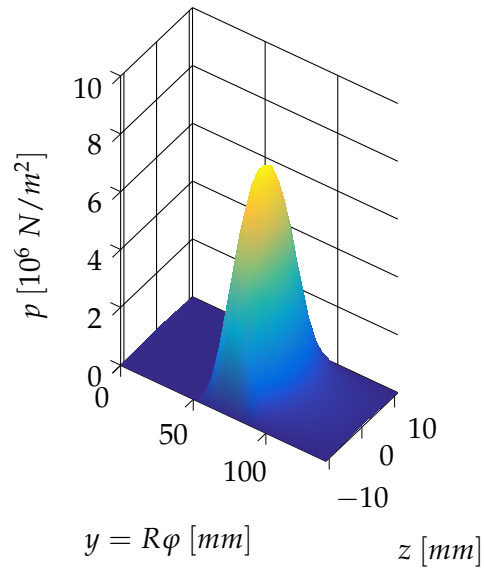


**Figure 5.2:** Pressure distribution for steady-state cavitation model at  $t = 0.0067$  s.

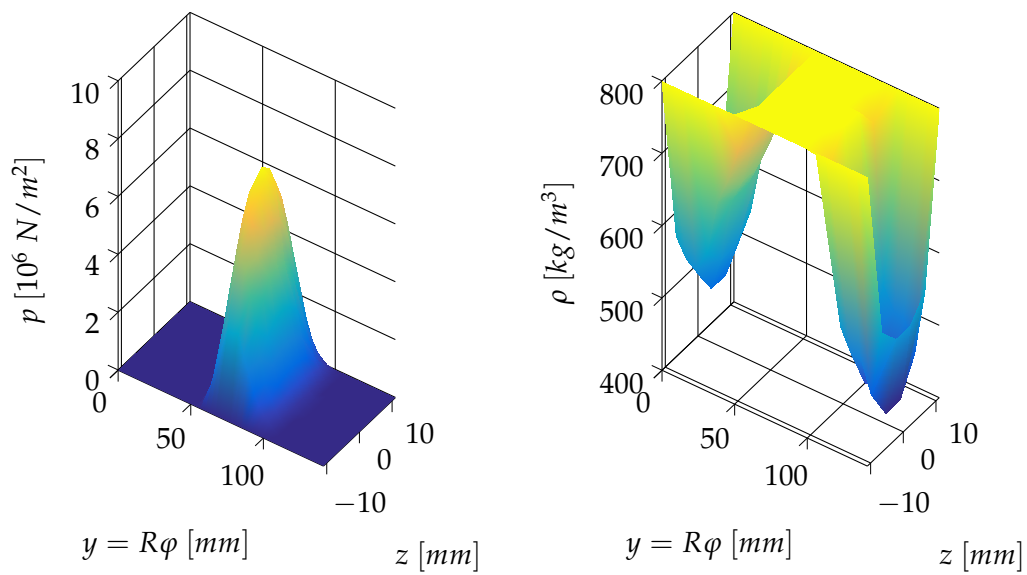


**Figure 5.3:** Pressure (left) and density (right) distribution for mass-conservative cavitation model at  $t = 0.0067$  s.

### 5.2.1 Comparison of IQN-ILS and simplified Newton: partitioned formulation

According to Section 5.1.1, the partitioned formulation of a system with an EHL revolute joint is used. The IQN-ILS method is compared with a simplified Newton method for the solution of the nonlinearity between deformation and pressure. The steady-state cavitation model is applied.

Figure 5.4 shows the number of iterations of the IQN-ILS and SN method (blue and gray solid lines) as well as the iterations, which are needed to solve the cavitation problem of the pressure in the hydrodynamic force element (blue and gray dotted lines). In Table 5.1, the statistics of the iterations as well as the simulation time are listed.

Comparing both iteration loops, the simplified Newton method needs fewer iterations than the IQN-ILS method. In the case of an analytical calculation of the Jacobian, the simplified Newton method needs also less simulation time, as the number of evaluations of the pressure force is smaller and there is no difference in the time needed for the calculation of the Jacobian. Indeed, even though the IQN-ILS uses the approximate Jacobian (5.19), where only rigid body motion is considered for the hydrodynamic forces, all elements need to be parsed before computing the tangent matrix for the rigid motion. However, in the case of a numerical calculation of the Jacobian, the IQN-ILS needs much less simulation time, as the time-consuming calculation of the derivatives wrt. the elastic DOFs is avoided and only a finite difference with a rigid motion perturbation is required.

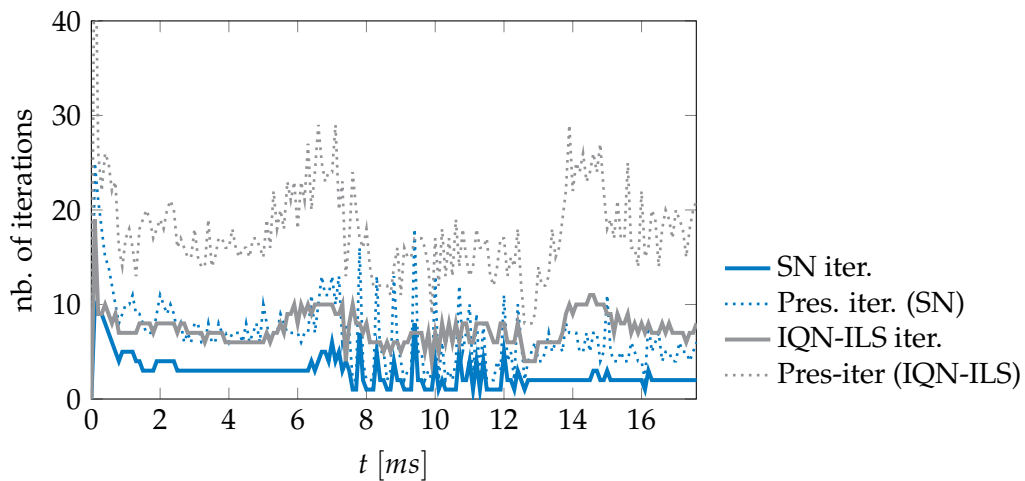


**Figure 5.4:** Comparison of number of iterations of simplified Newton and IQN-ILS for partitioned formulation.

	number of SN/IQN-ILS iter.				number of pressure iter.				Sim. time	
	Sum	Mean	Min	Max	Sum	Mean	Min	Max	ana. J	num. J
SN	498	2.8	1	10	1222	6.9	2	32	651 s	4786 s
IQN-ILS	1315	7.4	4	18	3176	17.9	8	54	1138 s	1350 s

**Table 5.1:** Comparison of the number of iterations and the computational time for the partitioned formulation.

### 5.2.2 Comparison partitioned formulation and DAE formulation: simplified Newton

In this subsection, the partitioned formulation and the DAE formulation of Sections 5.1.1 and 5.1.2 are compared, respectively. The steady-state cavitation condition is applied. For both formulations, the simplified Newton method is used as solution technique.

Figure 5.5 shows the number of global iterations for the two formulations (blue and gray solid lines). For the partitioned formulation, also the iterations, which are needed to solve the cavitation problem in the hydrodynamic force element, are plotted with blue dotted lines. For the DAE formulation exists only one iteration loop, in which the dynamic equations as well as the cavitation problem are solved. In Table 5.2, the statistics of the iterations as well as the simulation times are listed.

The results show that the DAE formulation needs approximatively the same number of iterations in the global loop than the partitioned formulation. As no inner iteration loop for the cavitation problem is necessary, the simulation time is smaller than for the partitioned formulation, see Table 5.2. The avoidance of an inner iteration loop also outweighs the fact, that the system size of the DAE formulation is higher than the size of the partitioned formulation.

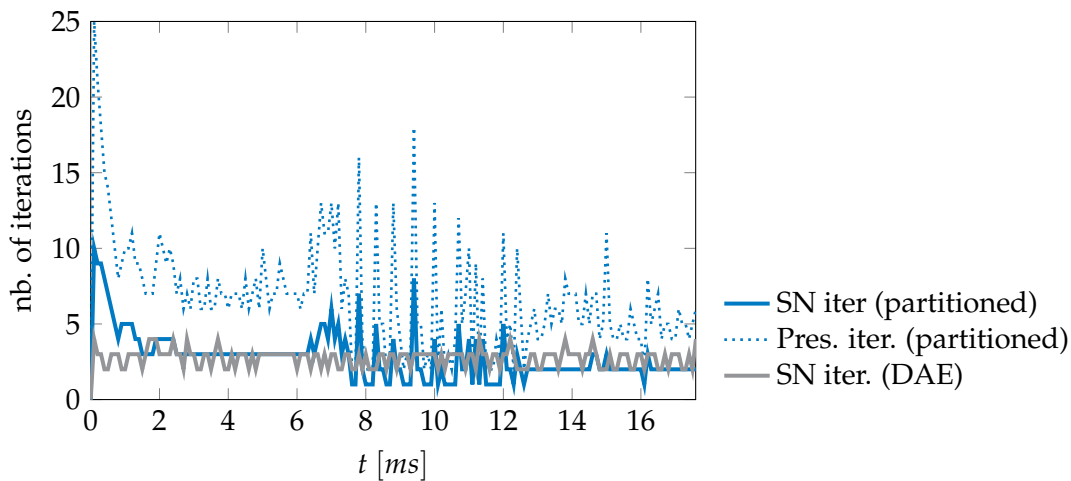


**Figure 5.5:** Comparison of partitioned formulation and DAE formulation using simplified Newton.

	number of SN iter.				number of pressure iter.				Sim. time	
	Sum	Mean	Min	Max	Sum	Mean	Min	Max	ana. J	num. J
part.	498	2.8	1	10	1222	6.9	2	32	651 s	4786 s
DAE	488	2.8	2	4	-	-	-	-	516 s	4688 s

**Table 5.2:** Comparison of the number of iterations and the computational time for the partitioned and DAE formulation with simplified Newton solution technique.

### 5.2.3 Comparison partitioned formulation and DAE formulation: IQN-ILS

The previous Section 5.2.2 shows that a solution strategy, which solves the dynamic equilibrium and the cavitation problem simultaneously, needs less simulation time. Besides, Section 5.2.1 reveals that the application of the IQN-ILS method instead a simplified Newton method works without needing the complete Jacobian. The presented solution strategy for the DAE formulation of Section 5.1.2 combines these two aspects.

In the following, the IQN-ILS method for the partitioned formulation of Section 5.1.1 is compared with the IQN-ILS algorithm for the DAE formulation with steady-state cavitation condition.

Figure 5.6 shows the number of iterations of the IQN-ILS method for the two formulations (blue and gray solid lines) as well as the number of pressure iterations for the partitioned formulation (blue dotted line). In Table 5.3, the statistics of the iterations as well as the simulation times are listed.

The results show that the DAE formulation needs a smaller number of global iterations as the partitioned formulation. Further, by the DAE formulation, the pressure is updated hand in hand with the deformation and needs no inner iteration loop like in the partitioned formulation. These two effects lead to the smaller simulation time for the DAE formulation.

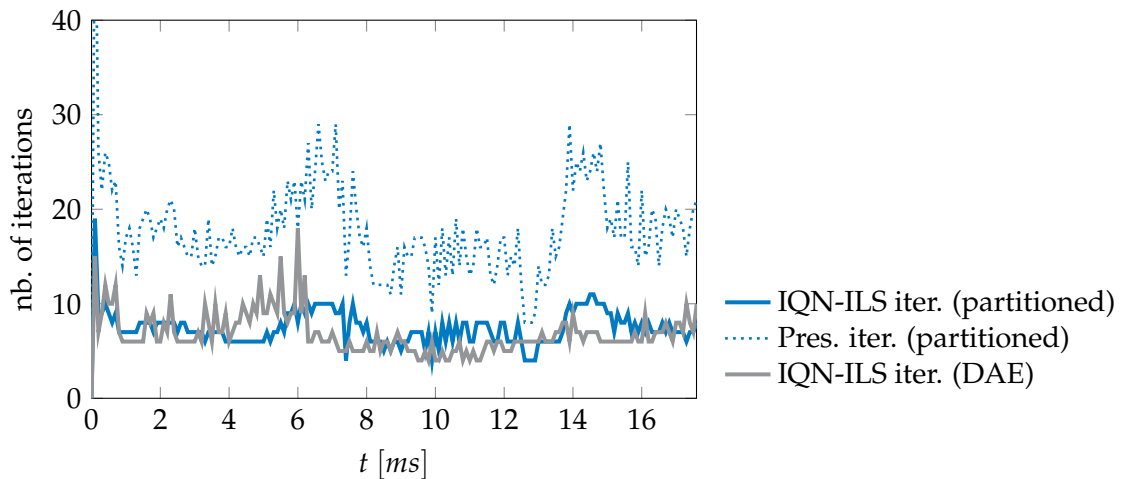


**Figure 5.6:** Comparison of number of iterations of partitioned formulation and DAE formulation using IQN-ILS method.

	number of IQN-ILS iter.				number of pressure iter.				Sim. time	
	Sum	Mean	Min	Max	Sum	Mean	Min	Max	ana. J	num. J
part.	1315	7.4	4	18	3176	17.9	8	54	1138 s	1350 s
DAE	1211	6.8	4	18	-	-	-	-	870 s	4688 s

**Table 5.3:** Comparison of the number of iterations and the computational time for partitioned formulation and DAE formulation with IQN-ILS solution technique.

### 5.2.4 DAE formulation with mass-conservative cavitation

The solution strategy with the IQN-ILS method for the DAE formulation of Section 5.1.2 is also applicable for the mass-conservative cavitation problem. In the following it is compared with the simplified Newton method.

Figure 5.7 shows the numbers of global iterations for the two methods and Table 5.4 contains the statistics of the comparison.

As the simplified Newton method uses the complete Jacobian, it needs less global iterations. When the Jacobian is calculated analytically, the simulation time of the simplified Newton method is smaller, as the number of evaluations of the pressure calculations is smaller and there is no difference in the time needed for the calculation of the Jacobian. The advantage of the IQN-ILS method becomes evident, when the Jacobian is calculated numerically. Then, with the IQN-ILS method, the simulation time is reduced by more than 80%.

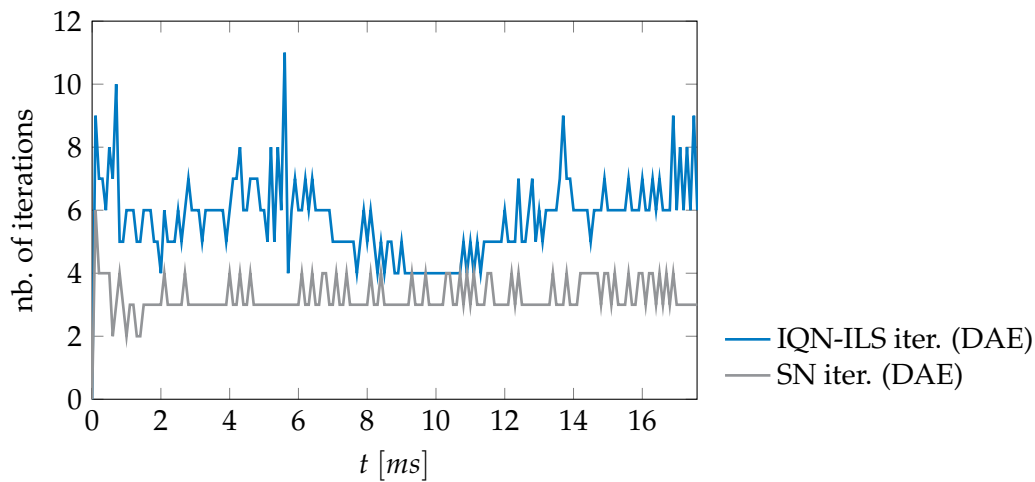


**Figure 5.7:** Comparison of the number of iterations of simplified Newton and IQN-ILS method for DAE formulation with mass-conservative cavitation condition.

	number of SN/IQN-ILS iter.				Sim. time	
	Sum	Mean	Min	Max	ana. J	num. J
SN	581	3.3	2	6	598 s	5621 s
IQN-ILS	1013	5.7	4	10	864 s	1101 s

**Table 5.4:** Comparison of the number of iterations and the computational time for simplified Newton and IQN-ILS method for DAE formulation with mass-conservative cavitation condition.

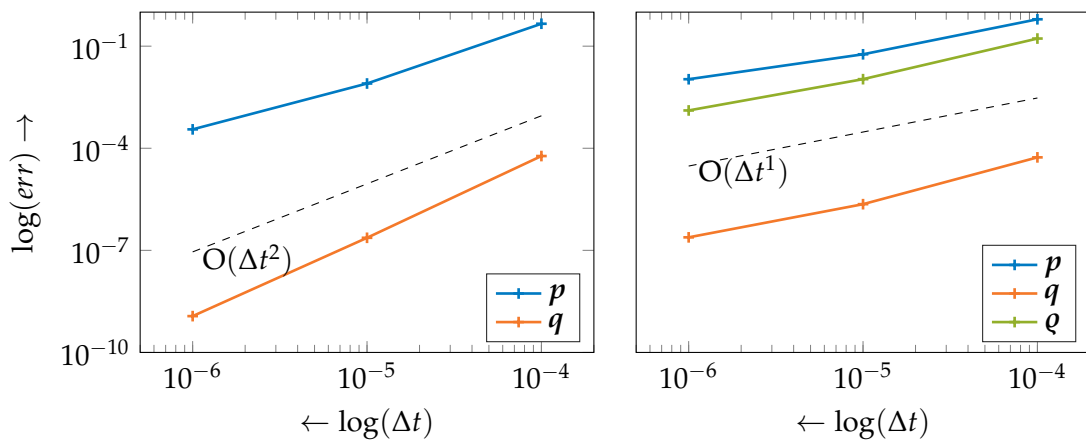
### 5.2.5 Time convergence and scaling

This section analyzes the convergence of the error of the time discretization schemes as well as the effect of the scaling of the matrices during the solution process.

For the mechanical system with the steady-state SWIFT-STIEBER cavitation condition, the generalized- $\alpha$  scheme is applied to the resulting DAE of index 1, see Section 5.1.2. Due to the generalized- $\alpha$  scheme, a second order time-convergence of the system variables is expected. Figure 5.8(a) shows the convergence of the error of the time discretization for this simulation example. A solution, which is calculated with a very small time-step size, serves as a reference solution. Clearly, the  $O(\Delta t^2)$  convergence of both the generalized coordinates and the pressure variable can be recognized.

For the mechanical system with the transient JFO cavitation condition, the generalized- $\alpha$  scheme for the mechanical system is combined with an additional time-discretization of the REYNOLDS equation, see Section 5.1.3. In detail, a  $\theta$ -scheme is applied to the density equation, where the pressure is considered always purely implicit. In Figs. 5.8(b) and 5.9(a), the convergence of the errors in the state variables are analyzed for  $\theta = 0.5$  and  $\theta = 1$ , respectively. In addition, a time-discretization of the density by a purely second order generalized- $\alpha$  scheme for first order systems, as described by BRUELS et. al. [30], is analyzed and its error decays can be seen in Fig. 5.9(b). It becomes clear that independently of using a first or a second order time-discretization scheme for the density equation, the convergence of the density and the pressure variable is always  $O(\Delta t)$ . The reason for that is the complementarity condition between density and pressure, which can be interpreted as a non-smooth right-hand-side of the density differential equation and leads to jumps in the density variable. For such systems, the convergence order is always one, independently of the order of the time stepping scheme, as outlined by ACARY and BROGLIATO [1]. Further, it becomes obvious that the  $O(\Delta t)$  convergence of the error in the density and pressure variable respectively, affects also the convergence of the error in the generalized coordinates.

The effect of the scaling of the matrices is demonstrated for this simulation example by Fig. 5.10. For the system with the SWIFT-STIEBER cavitation condition, the condition number of the Jacobian  $S_2$  is evaluated at a certain time point of the simulation, which is reached by using different time-step sizes. Figure 5.10 shows that without scaling, the condition number is high and increases with decreasing time-step size. In contrast, when using the scaling method, the condition number remains constant with decreasing time-step size and is much smaller than the condition number of the unscaled Jacobian.



(a) system with SWIFT-STIEBER condition

(b) system with JFO condition,  $\theta = 0.5$

**Figure 5.8:** Decay of time discretization error for system with SWIFT-STIEBER and JFO cavitation condition, respectively .

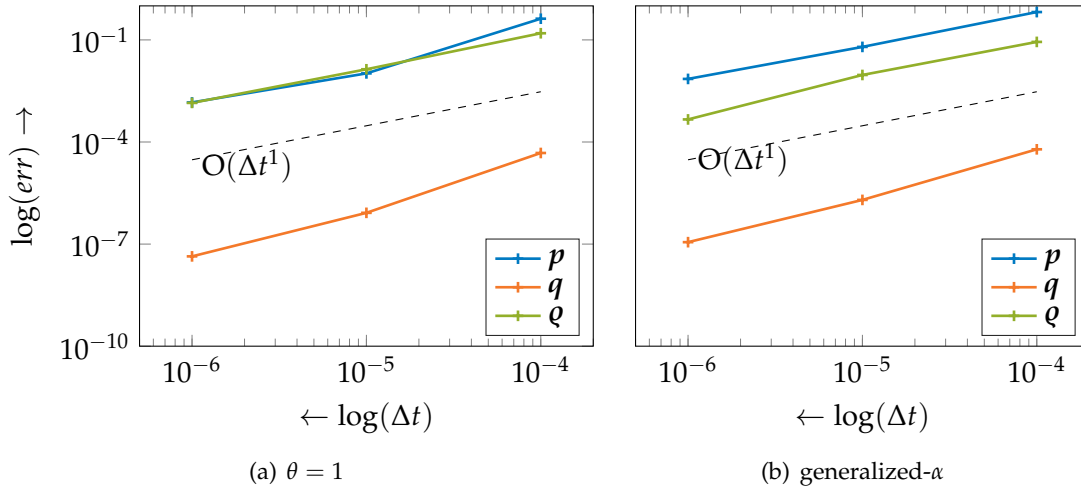


**Figure 5.9:** Decay of time discretization error for system with JFO cavitation condition for different time-stepping schemes.

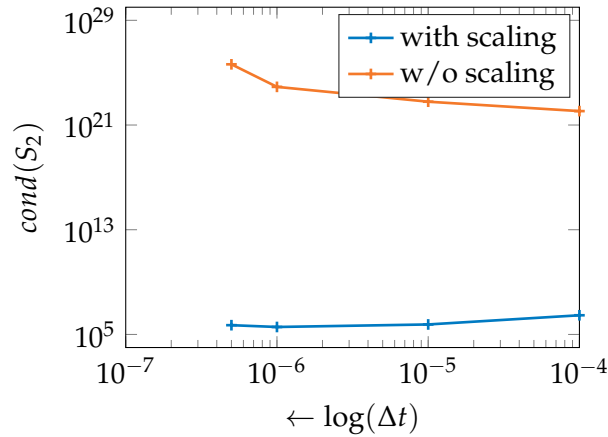


**Figure 5.10:** Condition number for system with SWIFT-STIEBER cavitation condition.

### 5.2.6 Concluding remarks

In this chapter, the projection function is used to couple different cavitation conditions of the hydrodynamic pressure to a MBS by a set of algebraic equations, leading to a DAE of index 1. This new formulations enable a monolithic solution strategy for dynamic equilibrium and cavitation zones and need no inner iteration loop for the pressure calculation like a partitioned formulation. By avoiding this inner iteration loop a reduction of simulation time can be reached (Section 5.2.2).

Further, it is demonstrated how the calculation of the complete Jacobian of a simplified Newton method can be avoided by the use of a quasi-Newton method with a partial linearized residual. As a consequence, in contrast to the simplified Newton method, the quasi-Newton method is still efficient, when a numeric differentiation formula for the (incomplete) Jacobian is used. Algorithms for the partitioned formulation as well as for the DAE formulation with the projection function are proposed.

In conclusion, the projection formulation combined with the quasi-Newton method (Section 5.1.2) is the most efficient solution strategy for the time-integration of the here presented system with EHL revolute joint, when the Jacobian is calculated numerically.

## Chapter 6

### Numerical-experimental case studies

This chapter presents different case studies of mechanical systems with (elasto-)hydrodynamic lubricated contacts and is aimed at the discussion of differences in the physical modeling but also in the numerical treatment of the systems. The outlined methods of the previous chapters are applied during the simulation process and their capabilities are highlighted.

In Section 6.1, a slider-crank mechanism is investigated as a first case study. Different lubrication models, the influence of the flexibility of the structure or the effect of friction and contact pressure are analyzed amongst other effects.

In Section 6.2, an experimental study of a rotor test rig with a journal bearing component is presented. A special focus is placed on the identification of the misalignment of the rotor axes by an adequate simulation model.

Section 6.3 treats the classical EHL point contact. A comparison with a reference solution is given and the application of the quasi-Newton method is investigated.

#### 6.1 Slider-crank mechanism revised

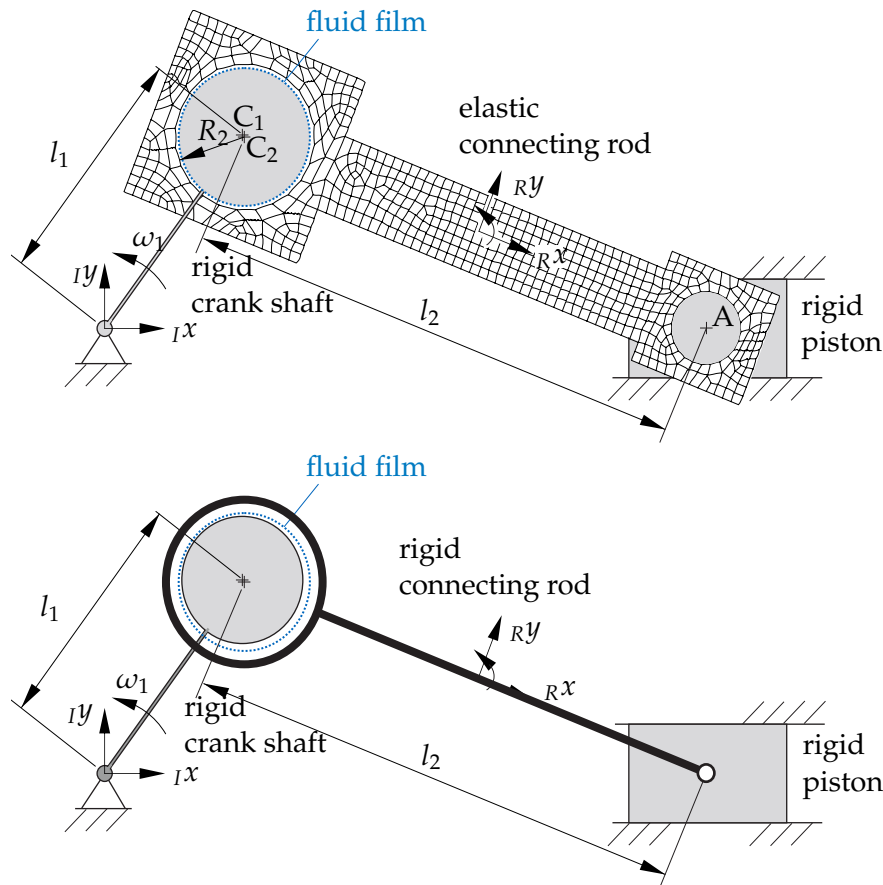
This section focuses on physical and numerical aspects of the slider-crank mechanism simulation example, which is already introduced in Section 4.4.1. The aim is to show the main differences in the fluid modeling and to give an understanding overview of the effects, which influence the dynamics of the mechanical system. Further, the stabilization technique of the FE discretization is demonstrated.

Figure 6.1 shows in the upper half the already described simulation model of the slider-crank mechanism with the 3D elastic connecting rod, while it shows on the lower half the same mechanism, but now with a rigid connecting rod. The parameters of the simulation model are identical to those of Table 4.1, as far as they are not specified differently.

In the following, comparisons are given for the mechanical model with either an elastic or a rigid connecting rod, for the fluid model with either the SWIFT-STIEBER or the JFO cavitation condition as well as for the fluid model with either constant or pressure dependent fluid properties. Further, the physical effect of the contact pressure and the numerical effect of the SUPG stabilization for the JFO cavitation condition are demonstrated.

#### SWIFT-STIEBER and JFO cavitation condition with rigid or elastic connecting rod

This section outlines the difference between the steady-state SWIFT-STIEBER (Section 2.3.2) and the mass conservative JFO (Section 2.3.3) cavitation condition for the slider-crank mechanism for both cases of a rigid and an elastic connecting rod.



**Figure 6.1:** Slider-crank mechanism with flexible connecting rod and lubricated joint.

In Fig. 6.2, the maximal pressure and the minimal height over the time for the first rotation are shown for both cavitation and rod models. In Fig. 6.2(a), it can be seen that a rigidly modeled connecting rod leads to higher pressures than an elastically modeled rod does. The reason is that the flexibility of the surface has a smoothing effect on the local pressure distribution, leading to smaller but wider pressure profiles than a rigid surface does. Further, the minimal height is smaller in the case of the flexible rod than in the case of the rigid rod, see Fig. 6.2(b). The reason is that due to the flexibility, the surface deforms parabolically in axial direction, which leads to a small distance between crank shaft and rod surface at the axial ends of the bearing.

The physical difference between the two cavitation models becomes also clear in Fig. 6.2(a). For the model with the rigid rod, the JFO cavitation model gives at the high pressure phase between  $t = 6 \text{ ms}$  to  $t = 8 \text{ ms}$  a higher maximum pressure value than the SWIFT-STIEBER model. The reason is that in contrast to the SWIFT-STIEBER condition, the JFO condition fulfills mass-conservation at the fluid film reformation boundary. This leads to a higher pressure gradient at the reformation boundary and consequently to the higher pressure value in the highly loaded zone. This observation agrees with the disadvantage of the SWIFT-STIEBER model of not modeling the reformation boundary properly, as stated in Section 2.3.1.

A further difference between the two cavitation models arises in the low pressure zone between  $t = 2 \text{ ms}$  to  $t = 4 \text{ ms}$  in Fig. 6.2(a). Figure 6.3 depicts the corresponding pressure profiles of the two cavitation models at the middle of the unwrapped bearing shell at  $t = 2.4 \text{ ms}$ , correlating to a crank angle of about  $68^\circ$ . For the JFO model, the density profile is also shown in Fig. 6.3(b). The JFO cavitation model shows two separated cavitation zones. In contrast, the SWIFT-STIEBER model assumes the larger cavitation

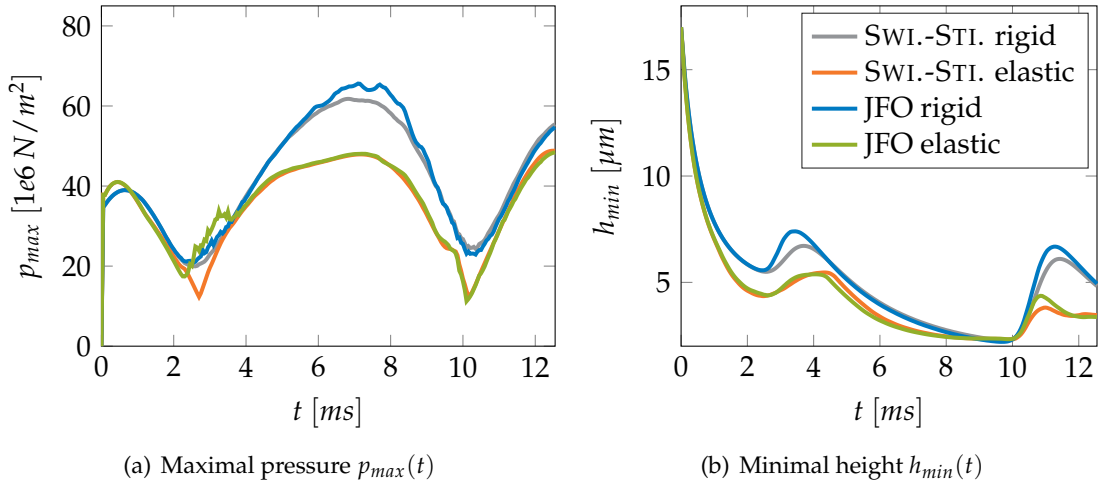


**Figure 6.2:** Comparison of simulation outputs for different fluid and rod models.

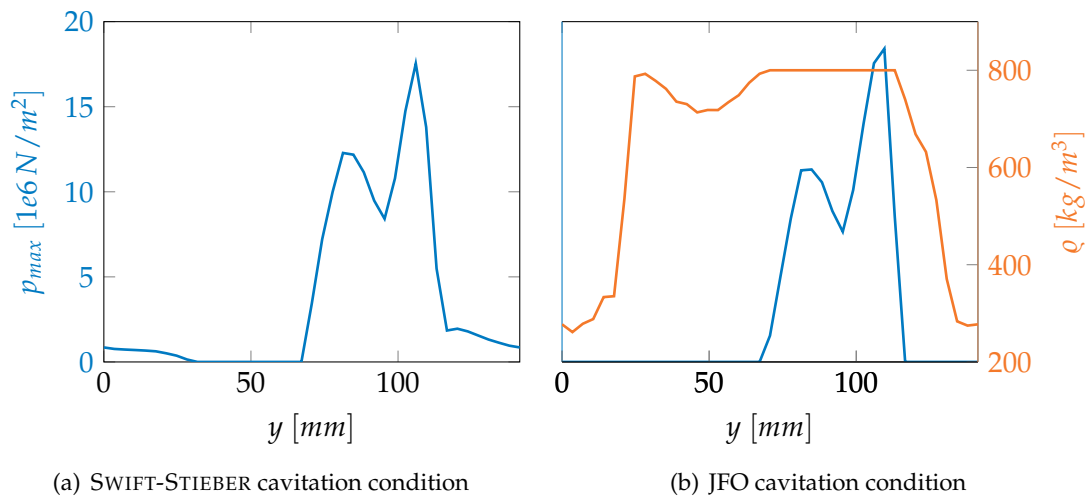


**Figure 6.3:** Comparison of pressure distributions of SWIFT-STIEBER and JFO model at  $t = 2.4$  ms.

zone already to be vanished, as can be recognized due to the positive pressure zone in Fig. 6.3(a). As a consequence, the pressure profile in the JFO model has less space for its development in angular direction than the profile of the SWIFT-STIEBER model and hence, larger pressure values arise for the JFO model.

### SWIFT-STIEBER and JFO cavitation condition with pressure dependent fluid properties with rigid or elastic connecting rod

In the previous section, constant fluid properties are assumed. Now, the effect of pressure dependent density and viscosity is investigated. Therefore, it is assumed that the density depends on the pressure by the DOWSON-HIGGINSON formula (2.10) with coefficients  $a = 0.6e - 9 \text{ m}^2/\text{N}$  and  $b = 1.7e - 9 \text{ m}^2/\text{N}$  and the viscosity depends on the pressure by the ROELANDS formula (2.9) with coefficients  $Z_1 = 0.39$ ,  $c_p = 1.03e8 \text{ N/m}^2$  and  $\eta_\infty = 6.31e - 5 \text{ kgm/s}$ . The coefficient of both formulas are taken from the work of WIJNANT [199].

In Fig. 6.4, the maximal pressure and the minimal height for the two cavitation and rod models respectively, are depicted for pressure dependent fluid properties. Figure 6.4(a) shows the maximal pressure for the first rotation; its difference to the maximal pressure of Fig. 6.2(a) is the largest when the pressure level is highest. Similarly, Fig. 6.4(b) shows the minimal height for the first rotation; its difference to the minimal height of Fig. 6.2(b) is the largest when the pressure level is highest. The explanation is as follows: Since, the viscosity increases stronger with the pressure than the density, the diffusion coefficient  $\kappa$

of Eq. (2.13) of the POISEUILLE flow in Eq. (2.1) decreases with rising pressure. By means of flow conservation it follows that the pressure gradient has to increase faster with rising pressure as it does for constant fluid properties, since  $\kappa$  decreases. As a consequence, the local pressure distributions are sharper for the pressure dependent fluid properties leading to higher pressure values. Further, since  $\kappa$  is in average smaller than it is for constant fluid properties, the minimal height is usually larger.

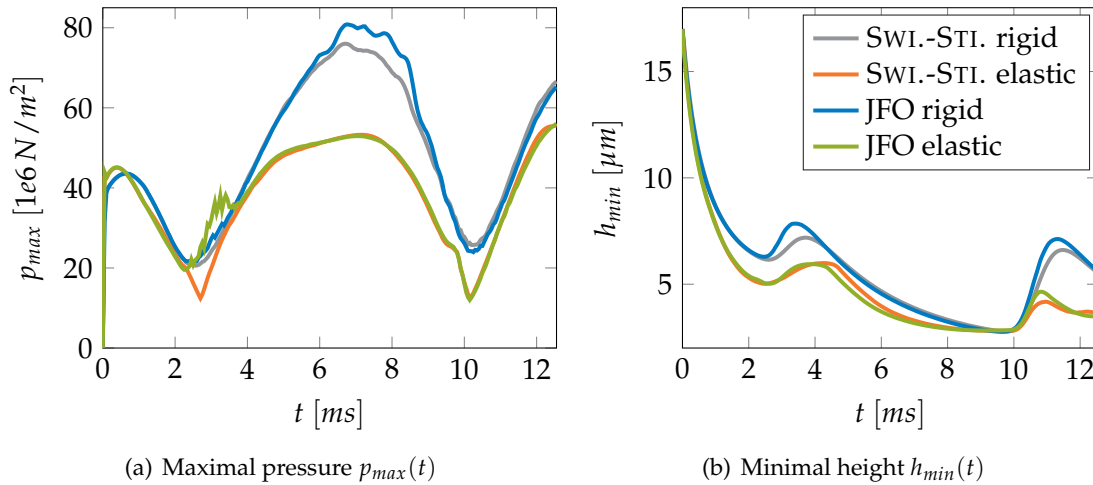


**Figure 6.4:** Comparison of simulation outputs with pressure dependent fluid properties.

### SWIFT-STIEBER cavitation condition with and without contact pressure with elastic connecting rod

In this section, the effect of mixed lubrication, described in Section 2.5.1, is analyzed for the slider-crank mechanism with elastic rod and SWIFT-STIEBER cavitation condition.

In the following, the contact pressure according to Eq. (2.89) is added to the fluid pressure, which is solved by the modified REYNOLDS equation (2.88). The average fluid height  $\bar{h}_t$  is described by a model of WU et. al. [207] by

$$\bar{h}_t = \frac{h}{2} \left( 1 + \operatorname{erf} \left( \frac{h}{\sqrt{2}\sigma} \right) \right) + \frac{h}{\sqrt{2\pi}} \exp \left( -\frac{1}{2} (h/\sigma)^2 \right),$$

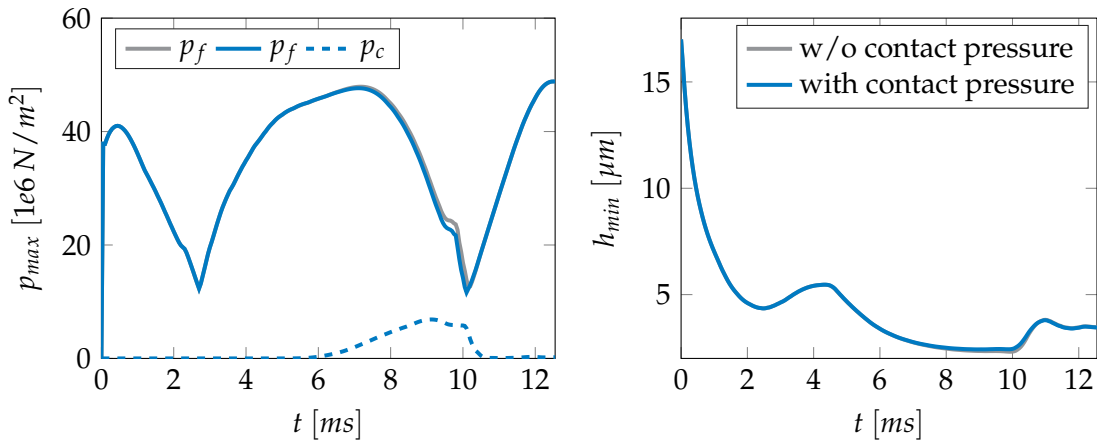
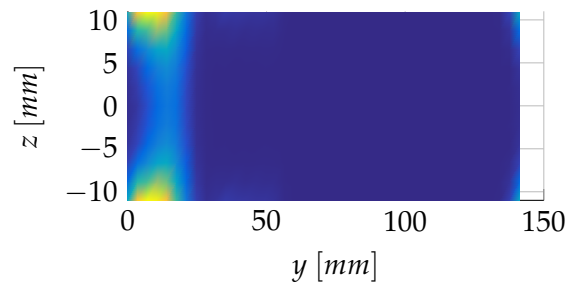
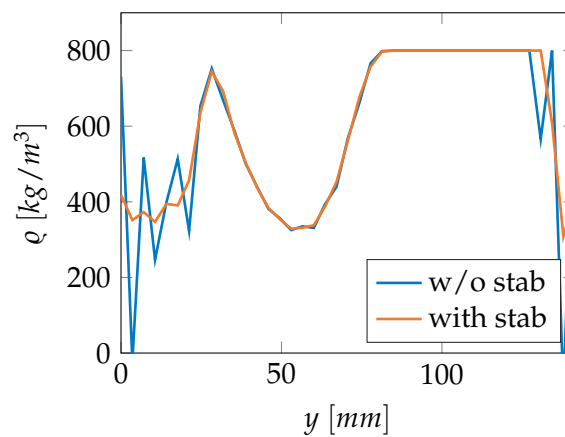
where  $h$  is the nominal fluid height. The surface roughness is chosen as  $\sigma=1 \mu\text{m}$  and the surface hardness as  $H = 900e6 \text{ N/m}^2$ . The tangential shear forces due to the contact pressure are defined by  $\tau_c = \mu_c p_c$  with  $\mu_c = 0.1$ .

Figure 6.5 shows the maximal pressure without contact pressure as well as the maximal fluid and contact pressure respectively, when mixed lubrication is considered. It becomes clear that the contact pressure becomes active only, when the fluid height is very small and then, the load is carried both by the fluid and the contact pressure. In Fig. 6.6, a contour plot of the maximal contact pressure in the bearing is given. By this, highly loaded regions in the bearing can be determined.

### JFO cavitation condition with and without numerical stabilization

This section demonstrates the effect of the SUPG stabilization, when using the JFO cavitation model. As described in Section 2.3.3, an upwind stabilization of the FE discretization is necessary, since the REYNOLDS equation degenerates in the cavitation zone to a pure convection dominated equation for the density.

Figure 6.7 shows a density profile in angular direction of the unwrapped bearing housing with and without stabilization. It can be seen clearly that numerical oscillations are avoided, when the SUPG stabilization is considered.

(a) Maximal pressure  $p_{max}(t)$ (b) Minimal height  $h_{min}(t)$ **Figure 6.5:** Influence of contact pressure on simulation outputs.**Figure 6.6:** Contour plot of maximal contact pressure during simulation.**Figure 6.7:** Density distribution with and without SUPG stabilization.

## 6.2 Experimental validation of a rotor test rig

This section gives an experimental study of a rotor test rig with a journal bearing component. It serves for the comparison of simulation and experimental results and shows further a method on how to determine misalignment of the rotor shaft in the journal bearing. The following sections are already published in the articles of KRINNER et. al. [105, 106].

### Introduction

The dynamic behavior of a rotor system with journal bearings, which operates at steady-state conditions like a constant rotational speed, strongly depends on its equilibrium position. At low rotational speeds, the equilibrium between gravity force, stiffness force and fluid force is found at a larger eccentricity than for higher rotational speeds, meaning that the rotor moves to the bearing center with increasing rotational speed. This fact is illustrated in Fig. 6.8(a) for the case of a vanishing stiffness force. Figure 6.8(a) shows the equilibrium eccentricity  $e$  between shaft and bearing center in dependency of the rotational speed  $\Omega$ , when vertical gravity force and the fluid force are the only acting forces in the bearing with clearance  $h_0$ . The well-known GUEMBEL curve arises, see for instance [64, 68, 174]. In an idealized rotor bearing system, the rotor axis is assumed to be perfectly aligned with the bearing axis. In this case, the equilibrium position can be calculated by the equality of gravity, stiffness and fluid force. However, in reality, the rotor axis can be misaligned in the bearing housing, resulting in a different equilibrium position, since an additional misalignment force has to be considered in the static force equilibrium. As a consequence, misalignment affects the dynamic behavior of the rotor system and hence, it also needs to be considered in simulation models. To illustrate this fact, Fig. 6.8(b) sketches the equilibrium eccentricity in dependency of the rotational speed  $\Omega$  for the case, in which the rotor stiffness and additionally, a misalignment  $a$  between rotor shaft and bearing axis are considered. It occurs a different curve of equilibrium positions compared to the curve of Fig. 6.8(a).

Several contributions to a misaligned rotor system can be found in literature: The interaction between misalignment and wear is investigated by an analytical model in [128] and an experimental study on this interaction is given in [32]. In [182], a theoretical study on a misaligned shaft due to an external preload force is outlined. Angularly misaligned bearings are numerically investigated in [15]. In [86], a design of a test rig with a rotor supported by four journal bearings suitable for the prediction of misalignment is proposed. In [144], simulation models and results for a flexible rotor system with angular and parallel misalignment are presented.

In the following sections, a rotor test rig with journal bearings is investigated with

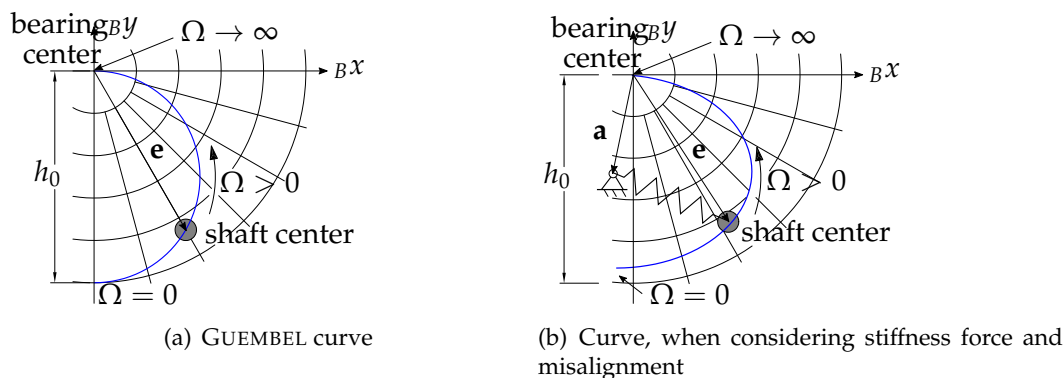


**Figure 6.8:** Equilibrium eccentricity  $e$  in dependency of rotational speed  $\Omega$ .

respect to parallel misalignment of rotor and bearing axis. First, a simple rotor model is applied in order to analyze the misalignment and in a next step, the dynamic behavior of the test rig due to unbalance can be investigated by further rotor models.

### Rotor test rig with two journal bearings

At the Institute of Applied Mechanics, a rotor test rig exists for the investigation of the interaction of the rotor dynamics with fluid forces coming from a journal bearing or a seal. In Fig. 6.9, the experimental setup is shown. It consists of an elastic rotor, which is supported by stiff roller bearings at the two ends. In the middle of the rotor, a rigid disk rotates in a pressurized journal bearing component system. This system consists of two identical journal bearings with external pressure support in the center of the two bearings, see Fig. 6.9. An oil distribution ring ensures an uniform oil flow through the bearings.

When pressurizing the journal bearing system at zero rotational speed, the rotor is lifted in an equilibrium position. In the following, this equilibrium position at zero rotational velocity is denoted by the misalignment parameter  $a$ . Further, it is assumed for simplicity that the lifting force due to the external pressure support remains constant in both its value and directions.

The main properties of the rotor test rig and the journal bearings are listed in Table 6.1. The bending stiffness of the dry rotor was identified by an operational modal analysis by determining the first bending eigenfrequency.

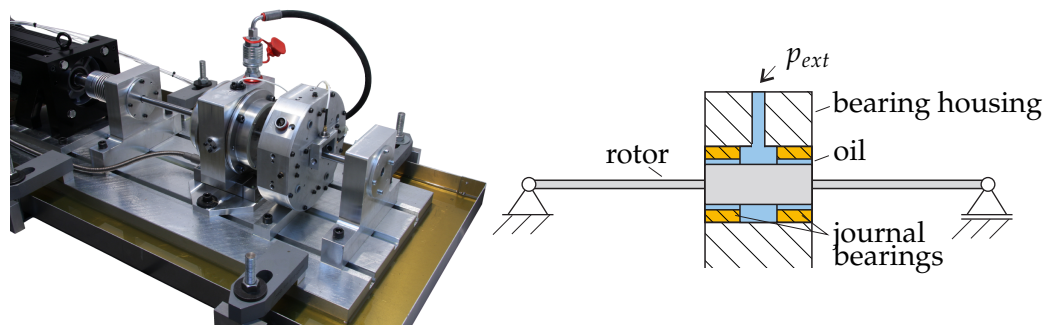


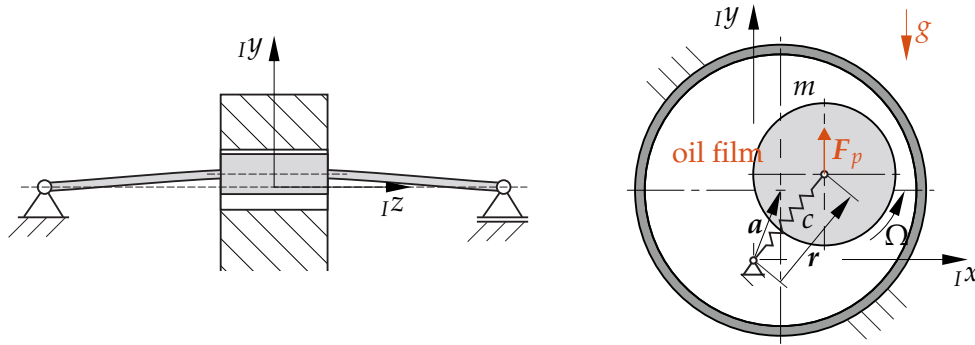
Figure 6.9: Rotor test rig with journal bearings.

Table 6.1: Properties of the test rig.

parameter	value	parameter	value
rotor mass $m$	5.0 kg	radius bearing $R_2$	50 mm
stiffness rotor $c$	295 kN/m	clearance bearing	170 $\mu\text{m}$
length rotor	0.60 m	length bearing	20 mm
1. eigenfrequ. (dry)	38.6 Hz	dyn. viscosity $\eta$	0.021 kg m/m <sup>2</sup>
diameter shaft	15 mm	fluid density $\rho$	880 kg/m <sup>3</sup>
external pressure $p_{ext}$	2.5 bar		

### Rotor modeling

In this section, different rotor models are presented for the validation of the experimental results. As the rotor axis in the test rig is not aligned concentrically to the bearing axis, misalignment is considered for all models. Further, it will be assumed that the gravity force is always compensated due to the external pressure support.



**Figure 6.10:** LAVAL rotor with misalignment, preload force and fluid forces.

Four different complex rotor models are introduced. The first one is a LAVAL rotor with misalignment and fluid forces. This model will be used for the experimental validation of equilibrium positions of the rotor bearing system at different rotational speeds.

The further models are a LAVAL rotor with linearized fluid forces, a complete elastic rotor model with nonlinear and linearized fluid forces, respectively. These models will be used for comparisons with the first rotor model in order to discuss their model discrepancies with respect to experimental measurements.

#### Model A1: LAVAL rotor with misalignment and fluid forces

The first model is a LAVAL rotor as depicted in Fig. 6.10. The rotor is characterized by the mass  $m$  and the stiffness  $c$  and its deflection  $r$  is described in the inertia frame, which is located in the center of the undeformed shaft. The misalignment is considered by the vector  $a$  as relative alignment between bearing axis and rotor axis at zero rotational speed. Then, following dynamic equations can be stated:

$$m \ddot{r} + c r = 2 F_f(r, \dot{r}, \Omega, a) + F_p + F_g + F_{ext}, \quad (6.1)$$

where  $F_f$  is the nonlinear fluid force of one journal bearing depending on the rotational speed  $\Omega$  and the misalignment  $a$ ,  $F_p$  is the preload force coming from the external pressure support and  $F_g$  is the gravity force. In addition, external forces  $F_{ext}$  can act on the rotor.

As mentioned in Section 6.2, the preload force is assumed to be constant. For that reason and when no further forces are acting, the force  $F_p$  has to compensate the gravity force all the time, in order to fulfill the definition of the misalignment  $a$  at zero rotational speed; it gives  $F_p = -F_g$ .

For the model validation, the static equilibrium points at given rotational speeds  $\Omega$  are considered. For the static deflection  $\bar{r}$ , following nonlinear equation has to be solved:

$$c \bar{r} = 2 F_f(\bar{r}, \Omega, a). \quad (6.2)$$

#### Model A2: LAVAL rotor with misalignment and linearized fluid forces

For this rotor model, the LAVAL rotor is still used and the fluid forces are linearized around the equilibrium position  $\bar{r}$ , which is determined by the solution of Eq. (6.2) for a given rotational speed and a known misalignment, leading to:

$$F_f(r, \dot{r}, \Omega, a) \approx F_f(\bar{r}, \Omega, a) - K_f(\bar{r}, \Omega, a) (r - \bar{r}) - D_f(\bar{r}, \Omega, a) \dot{r}, \quad (6.3)$$

with the linearized matrices  $K_f$  and  $D_f$  for the fluid stiffness and damping, respectively. They are assumed to have the following form:

$$\mathbf{K}_f = -\left. \frac{\partial \mathbf{F}_f}{\partial \mathbf{r}} \right|_{\mathbf{r}=\bar{\mathbf{r}}} = \begin{bmatrix} K_{xx} & k_{xy} \\ k_{yx} & K_{yy} \end{bmatrix}, \quad \mathbf{D}_f = -\left. \frac{\partial \mathbf{F}_f}{\partial \dot{\mathbf{r}}} \right|_{\mathbf{r}=\bar{\mathbf{r}}} = \begin{bmatrix} D_{xx} & d_{xy} \\ d_{yx} & D_{yy} \end{bmatrix}, \quad (6.4)$$

where  $K$  is the direct stiffness,  $k$  the coupling stiffness,  $D$  the direct damping and  $d$  the coupling damping coefficient. Inserting Eq. (6.3) in Eq. (6.1) and using Eq. (6.2) gives the dynamic equations of the LAVAL rotor with misalignment and linearized fluid forces:

$$m \ddot{\mathbf{r}} + c(\mathbf{r} - \bar{\mathbf{r}}) + 2\mathbf{K}_f(\bar{\mathbf{r}}, \Omega, \mathbf{a})(\mathbf{r} - \bar{\mathbf{r}}) + 2\mathbf{D}_f(\bar{\mathbf{r}}, \Omega, \mathbf{a})\dot{\mathbf{r}} = \mathbf{F}_{ext}. \quad (6.5)$$

### Model B1: Elastic rotor with misalignment and fluid forces

In a more detailed simulation model, the elastic deformation of the rotor is described by a set of mode shapes (Ritz ansatz). These mode shapes come from a finite element discretization of the rotor by using Bernoulli beam elements. For a better distinction from the LAVAL rotor, the elastic deformation is now described by the vector  $\mathbf{q}$  representing the modal coordinates. The dynamic behavior of the rotor is then characterized by the modal mass matrix  $\mathbf{M}$  and the modal stiffness matrix  $\mathbf{C}$ , leading for the rotor bearing system to:

$$\mathbf{M} \ddot{\mathbf{q}} + \mathbf{C}(\mathbf{q} - \bar{\mathbf{q}}) = \mathbf{F}_{f,1}(\mathbf{q}, \dot{\mathbf{q}}, \Omega, \mathbf{a}) + \mathbf{F}_{f,2}(\mathbf{q}, \dot{\mathbf{q}}, \Omega, \mathbf{a}) + \mathbf{F}_{ext}. \quad (6.6)$$

The fluid forces  $\mathbf{F}_{f,1}$  and  $\mathbf{F}_{f,2}$  of the two bearings as well as the external forces  $\mathbf{F}_{ext}$  represent forces projected on the modes, although the same notation as in Eq. (6.1) is used. Similar to the rotor models A1 and A2,  $\bar{\mathbf{q}}$  is the equilibrium position. Damping or gyroscopic effects of the rotor are not considered.

### Model B2: Elastic rotor with misalignment and linearized fluid forces

Similar to model A2, the fluid forces are linearized like in Eq. (6.3). Considering this in Eq. (6.6), following linear differential equation for the elastic rotor is obtained:

$$\mathbf{M} \ddot{\mathbf{q}} + \mathbf{C}(\mathbf{q} - \bar{\mathbf{q}}) + [\mathbf{K}_{f,1} + \mathbf{K}_{f,2}](\mathbf{q} - \bar{\mathbf{q}}) + [\mathbf{D}_{f,1} + \mathbf{D}_{f,2}]\dot{\mathbf{q}} = \mathbf{F}_{ext}, \quad (6.7)$$

which describes the motion of the rotor around the equilibrium position  $\bar{\mathbf{q}}$ .

## Experimental validation

In this section, an experimental validation of the rotor system of Section 6.2 is given by applying adequate simulation models of Section 6.2 depending on the specific accuracy requirements. A first experiment (static rotor equilibrium positions) is performed in order to determine the parallel misalignment between rotor and bearing axis. After having analyzed the misalignment, measurement data of a second experiment (rotor orbit at unbalance) is validated by simulation results of the four different simulation models of Section 6.2.

### Experiment 1: Static rotor equilibrium positions

The first experiment serves to determine the misalignment  $\mathbf{a}$  between rotor and bearing axis, which can not be identified by an absolute measurement.

On the test rig, the relative equilibrium positions of the rotor in the bearing can be measured for different rotational speeds  $\Omega$ . Since the absolute position of the rotor can

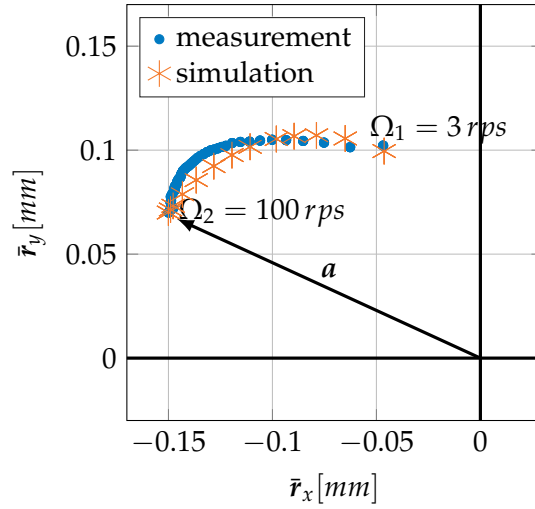


**Figure 6.11:** Measured and simulated curve of equilibrium positions with misalignment parameter  $\mathbf{a} = [-0.15 \text{ mm}, 0.07 \text{ mm}]$ .

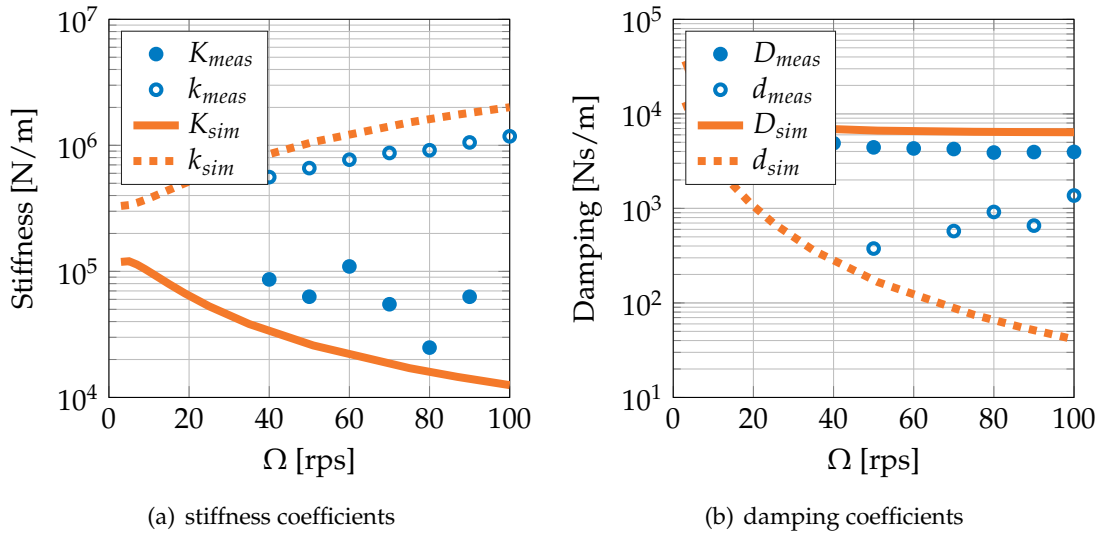


**Figure 6.12:** Calculated and measured stiffness and damping coefficients for different rotational speeds.

not be measured, the equilibrium positions are measured with respect to a reference position. The latter is chosen as the equilibrium position at high rotational speed, since it is known from theory that the rotor will be centered in the bearing housing for high rotational speeds [64].

The LAVAL-rotor model A1 with Eq. (6.2) for the equilibrium position  $\bar{\mathbf{r}}$  is used for the experimental validation. With this model, an optimal misalignment parameter  $\mathbf{a}$  can be determined in such a way that the relative curve of equilibrium positions of the experiment is well approximated by the equilibrium positions calculated by Eq. (6.2).

In Fig. 6.11, the curve of equilibrium positions of the experiment and of the simulation can be seen. The misalignment parameter is chosen as  $\mathbf{a} = [-0.15 \text{ mm}, 0.07 \text{ mm}]$ . The measurement and the simulation start at  $\Omega_1 = 3 \text{ rps}$  and move with increasing rotational speed to the reference position identical with the bearing center at  $\Omega_2 = 100 \text{ rps}$ .

When the equilibrium positions  $\bar{\mathbf{r}}$  for different rotational speeds are known, the stiffness and damping coefficients of Eq. (6.4) can be calculated in a next step. Here, they

are computed by a finite difference scheme and following mean coefficient can be determined:

$$K = \frac{K_{xx} + K_{yy}}{2}, \quad k = \frac{k_{xy} - k_{yx}}{2}, \quad D = \frac{D_{xx} + D_{yy}}{2}, \quad d = \frac{d_{xy} - d_{yx}}{2}.$$

The calculated as well as the measured mean coefficients are shown in Fig. 6.12. In the experiment, the coefficients are determined by exciting the rotor at different frequencies and measuring the rotor displacements and bearing reaction forces in the frequency domain. A fitting of the measured data by a reduced rotor bearing model gives the mean coefficient. The detailed measurement concept is described by WAGNER et. al. [195].

The dependency of the measured coefficients on the rotational speed shows good agreement with the simulation results for the direct stiffness, direct damping and coupling stiffness coefficients ( $K$ ,  $D$  and  $k$ ). However, for the coupling damping coefficient  $d$ , a discrepancy is observed. The reason could be an angular misalignment of the rotor shaft in the experiment.

### Experiment 2: Rotor orbit at unbalance

After having determined the parallel misalignment, a second experiment is performed in order to discuss the accuracy and efficiency of the four presented simulation models. Therefore, an unbalance is added at the middle of the rotor and the orbit of the rotor is measured at a constant rotational speed  $\Omega = 21 \text{ rps}$ . The measured and simulated orbits are depicted in Fig. 6.13.

In Fig. 6.13(a), the measured and the simulated orbits are shown at their equilibrium positions. It has to be mentioned that the misalignment  $a$  determined by the first experiment is added to the measured orbit in order to get the absolute position of the orbit. The reason for that is that, as already mentioned, the absolute reference point of the measurement is unknown. For the simulation, rotor model A1 is used.

In Fig. 6.13(b), the form of the measured orbit is compared with the orbits obtained by the four simulation models. Note that all orbits are shifted to the origin in order to compare their forms. It can be seen that all four simulation models give nearly the same rotor orbit, meaning the model accuracy is good for all simulation models. The elliptical form of the simulated orbits are characteristic for a rotor, which has an eccentric equilibrium position in the journal bearing. However, the form of the measured orbit

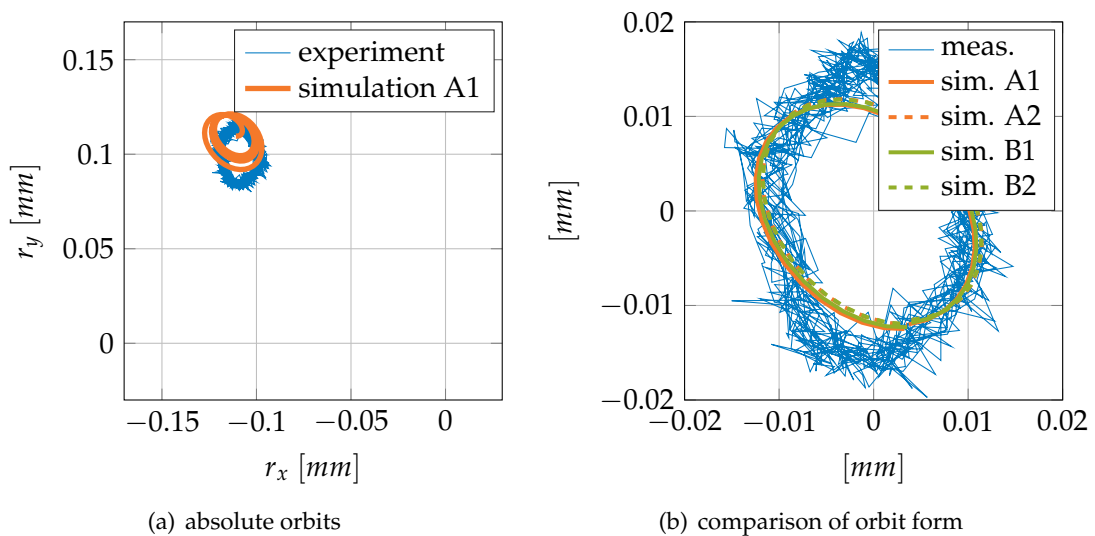


Figure 6.13: Rotor orbits due to unbalance at  $\Omega = 21 \text{ rps}$ .

has a tendency to a squared form. The reason could be that next to the unbalance an excitation with the third harmonic is present, which could cause a squared form, see for instance [188]. A physical source for a third harmonic excitation is the three-jaw chuck during manufacturing of the rotor shaft.

When looking at the simulation time of the models in Table 6.2, it can be seen that the fastest model is model A2 – the LAVAL rotor model with linearized fluid forces. It is followed by the elastic rotor model B2, where the fluid forces are also linearized. A relatively long simulation time is needed for the full elastic rotor model B1 with nonlinear fluid forces. All the four simulation models are integrated with the `ode15s` solver of MATLAB, which uses a variable step size. The absolute and relative tolerances are set to  $1e - 6$ . For the elastic description of the rotor shafts of models B1 and B2, twelve RITZ modes are used.

**Table 6.2:** Simulation time for the different rotor models.

model	sim. time	rel. time
A1	11.7 s	100 %
A2	0.124 s	1.06 %
B1	1343 s	11478 %
B2	4.46 s	38.1 %

## Conclusion

In this section, a rotor test rig with two journal bearings is validated by adequate simulation models. It becomes evident that the misalignment of rotor and bearing axis has to be considered in the simulation models.

When using simulation models with nonlinear fluid forces (models A1 and B1), the misalignment has to be known for the dynamic simulation in order to ensure that the rotor moves in the simulation to the right equilibrium position.

When using simulation models with linearized fluid forces (models A2 and B2), an important step for the dynamic analysis is the determination of the equilibrium position, which again requires the misalignment parameter. When the equilibrium position is known, the fluid forces can be linearized around this equilibrium position.

With respect to the accuracy of the simulation models, the LAVAL rotor model is accurate enough for the experimental validation for the here analyzed test rig. The use of an elastic rotor is not necessary for the described experiments, it only requires a larger modeling effort than the simple LAVAL rotor model.

The simulation costs can be saved significantly, when the fluid forces are linearized, as the evaluation of the FE solution of the nonlinear fluid forces are the most time-consuming part. However, the linearization has to be performed in a preprocessing step as well as the calculation of the equilibrium position. Note that here the amplitude of the rotor motion in the bearing is about  $0.01\text{mm}$  for a clearance of  $0.17\text{mm}$ . It is to be expected that the linearized model will lose their validity when the motion of the rotor in the bearing becomes large.

## Outlook

For the model of the fluid forces, the classical REYNOLDS equation is applied, where effects of the fluid inertia are neglected. This assumption has to be analyzed further and comparisons with the bulk flow equations, usually applied for seals, should be made. Further, the effect of the preload force has to be investigated in more detail.

In this section, only mean stiffness and damping coefficients are determined in the experiment. Their practical relevance is only given for a vanishing eccentricity of the shaft. Usually the anisotropic coefficients have to be determined for a precise dynamic analysis, see the work of GLIENICKE [68] or SOMEYA [174].

The model based determination of the parallel misalignment as described in the first experiment could be further used for rotor diagnostics, similar to concepts described in [162, 188].

### 6.3 EHL point contact

This section outlines the classical simulation example of an EHL point contact. Such simulations may deliver nonlinear stiffness and damping characteristics for the ball contact in full dynamic ball bearing models like [196]. For more details, it is referred to the work of WIJNANT [199]. In the following, the static solution is calculated in order to analyze the developed numerical methods.

The kinematics of the EHL point contact is already introduced in Section 2.4.1. In the following, according to WIJNANT [199], the dimensionless problem is considered. It is characterized by the dimensionless lubricant parameter  $L$  and the dimensionless load parameter  $M$ , as originally defined by MOES [125]:

$$L = \zeta E' \left( \frac{\eta_{p=0} u_s}{E' R_y} \right)^{1/4}, \quad M = \left( \frac{f}{E' R_y^2} \right) \left( \frac{E' R_y}{\eta_{p=0} u_s} \right)^{3/4},$$

with the pressure viscosity coefficient  $\zeta$  of Eq. (2.8), the reduced modulus of elasticity  $E'$ , the sum velocity  $u_s$ , the reduced radius  $R_y$  of curvature in  $y$ -direction and the nominal load  $f$ . For the complete set of dimensionless equation it is referred to WIJNANT [199]. The parameter of the simulation example are chosen similar to those of the article of AHMED et. al. [2]. They are listed in Table 6.3.

The elastic deformation in the point contact is calculated by an elastic half-space (equivalent modulus of elasticity  $E_{eq} = E'/2$ ), similar to HABCHI et. al. [78] and AHMED et. al. [2]. The symmetry of the problem is utilized and only half of the problem is calculated. The unreduced body with the dimensions  $-30 \leq \bar{x} \leq 30$ ,  $-30 \leq \bar{y} \leq 30$  and  $-30 \leq \bar{z} \leq 0$  can be seen in Fig. 6.14. By a CRAIG-BAMPTON reduction, the elastic half-space is reduced to the nodes of the fine inner mesh with typical dimensions  $-4.5 \leq \bar{y} \leq 1.5$  and  $-3 \leq \bar{z} \leq 0$ .

The solution is calculated on a structured mesh with 32 elements in  $\bar{y}$ - and 16 elements in  $\bar{z}$ -direction, respectively. As shape functions the *Quad8Mod* for the pressure and the *Quad8* for the deformation respectively, are chosen. Further, the projection formulation in combination with the Newton-Raphson method as solution technique is used for the calculation.

**Table 6.3:** Parameter for simulation example of EHL point contact.

parameter	value
lubricant parameter $L$	10
load parameter $M$	20
viscosity index $\zeta$	$2.2\text{e-}8 \text{ m}^2/\text{N}$
viscosity $\eta_{p=0}$	$0.04 \text{ Ns}/\text{mm}^2$
sum velocity $u_s$	$1.6 \text{ m}/\text{s}$
reduced modulus of elasticity $E'$	$1.05\text{e}11 \text{ N}/\text{m}^2$
maximum HERTZian pressure $p_H$	$4.95\text{e}8 \text{ N}/\text{m}^2$

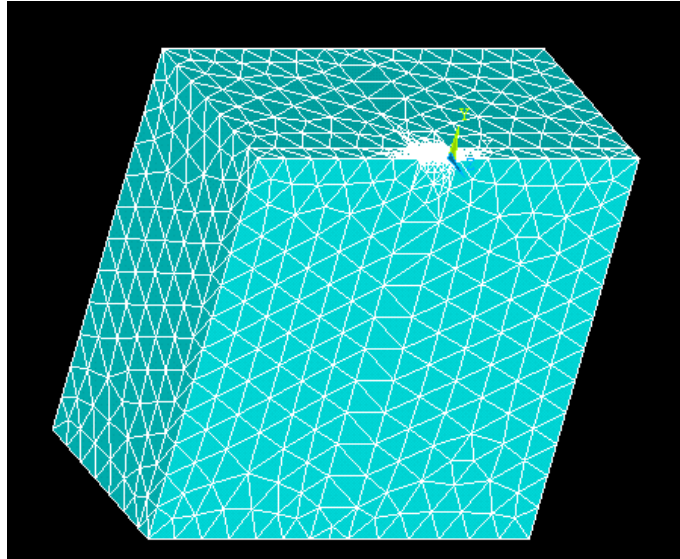


**Figure 6.14:** Elastic half space for EHL point contact.

Figure 6.15 shows the profiles of the pressure and the fluid film height at  $\bar{z} = 0$ . The solution agrees well the solution of AHMED et. al. [2]. In Fig. 6.16, the 3-dimensional pressure distribution is depicted as well as the elastic deformation of the half-space.

In Fig. 6.17, the convergence of the non-smooth Newton-Raphson method is depicted. It can be seen, that the norm of the residual oscillates for the first iterations. The reason is that at the beginning, the cavitation zone is not yet fully converged. After that, linear convergence can be observed.

For this simulation example, also the quasi-Newton method of Section 5.1.2, adapted for the static case, is tested. However, no convergence is achieved. The reason is the strong influence of the elastic deformation on the pressure distribution.

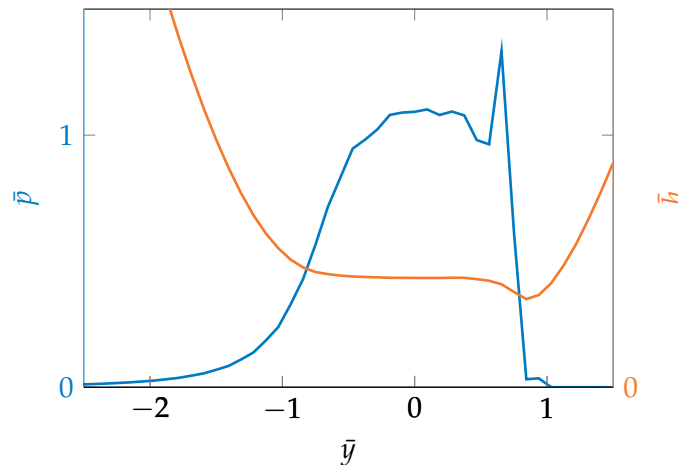


**Figure 6.15:** Profiles of pressure and fluid film height at  $\bar{z} = 0$  for EHL point contact.

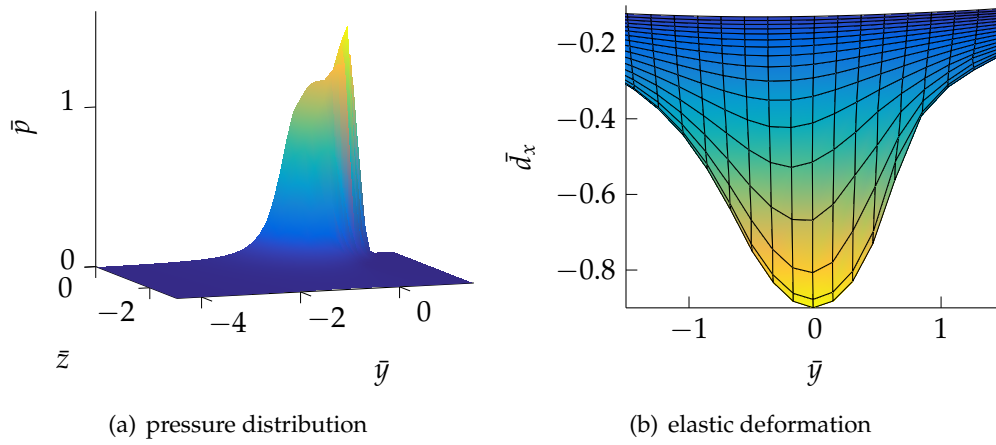


**Figure 6.16:** Pressure distribution and elastic deformation of EHL point contact.

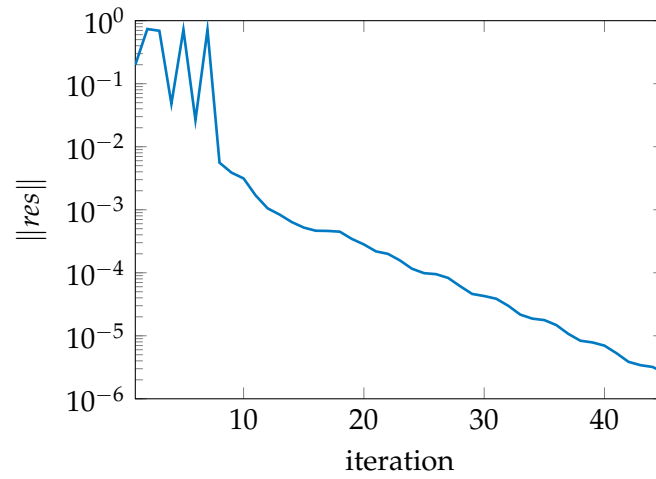


**Figure 6.17:** Convergence of the error of the residual.



## Chapter 7

### Conclusion and outlook

This work treats the modeling and simulation of mechanical systems with EHL contacts. Conformal EHL contacts are addressed in the same way as non-conformal contacts. Numerical methods are developed in order to improve the simulation process of such systems. Hereafter, Section 7.1 shortly summarizes this work and Section 7.2 points out its important contributions. Section 7.3 highlights the main conclusions of this research. Finally, Section 7.4 outlines shortcomings and gives recommendations for future work.

#### 7.1 Summary

This work starts with the outline of the REYNOLDS equation and gives a numerical discretization by the FEM. Two state-of-the-art cavitation conditions – the steady-state SWIFT-STIEBER and the mass-conservative JFO condition – are outlined and their formulation as a complementarity problem is given. Since their describing equations are different, for each model an individual FE treatment is stated. Further, this work describes the fundamental aspects of the fluid film kinematics and forces as well as the incorporation of inertia, temperature and roughness effects into the lubrication theory.

A focus of this work is the numerical coupling of non-conforming meshes in the context of EHL contacts. Existing coupling strategies (consistent, conservative) and transfer methods (nearest neighbor, nearest neighbor projected, weighted residual) are outlined and their convergences are investigated for a numerical example.

As a further topic, this work investigates reduction methods for elastic structures with lubricated interfaces. Two existing CMS-based reduction methods are outlined as well as a load dependent reduction approach is specified for EHL bearings. The three reduction methods are compared for two classical simulation examples with EHL bearings.

This work also deals with different solution strategies and techniques for the coupled system. It compares a state-of-the-art partitioned solution strategy with a monolithic solution strategy. It applies the Newton method as a state-of-the-art solution technique as well as a quasi-Newton method to the solution of the nonlinear equations resulting from the time-discretization. For the quasi-Newton solution technique, appropriate algorithms are developed for both the partitioned and the monolithic solution strategy. The different methods are analyzed for a numerical example.

Finally in this work, numerical and experimental case studies are treated. A detailed study of the physical and numerical behavior of a slider-crank mechanism is outlined. Different fluid and rod models are compared as well as the effect of a contact pressure or the numerical stabilization are demonstrated. An experimental study of a rotor system with journal bearings serves as verification of the simulation tool. A static simulation of a EHL point contact illustrates the applicability of the projection function and the monolithic solution strategy during the solution process.

## 7.2 New contributions

This work puts for the first time the different existing ways of cavitation treatment into one context. Besides, it shows for the first time that the concept of bi-orthogonal element shape functions is applicable to the steady-state cavitation problem. A further novelty of this work is the application of a projection formulation to the complementarity problem of the SWIFT-STIEBER and the JFO cavitation model.

This work also contributes to a thorough analysis of existing interface coupling methods of non-conforming meshes for the EHL problem.

A further novel contribution of this work is a load-dependent reduction method in order to reduce the elastic interface DOFs of flexible journal bearings.

As a new contribution, this work states out a full monolithic formulation for a mechanical system coupled with hydrodynamic equations by using the projection formulation of the cavitation problem.

Further, this work applies the first time the quasi-Newton method of DEGROOTE et. al. to the EHL problem. It modifies the original IQN-ILS method by using a scaled residual and incorporating an incomplete Jacobian. The developments have resulted in new solution algorithms for the discrete equations of motions of a MBS coupled either in a monolithic or a partitioned way with either the steady-state or the mass-conservative cavitation problem.

Finally, this work contributes to a profound understanding of exemplary mechanical system with EHL journal bearings. For instance, the dynamic behavior of slider-crank mechanism with an EHL journal bearing is investigated numerically or a misaligned rotor in journal bearings is investigated numerically as well as experimentally.

## 7.3 Conclusions

Following main conclusions can be derived from this work:

- Applying the projection formulation to the complementarity problem of each cavitation model, results in a nonlinear algebraic equation for each cavitation problem. Its solutions are obtained by a non-smooth Newton scheme, resulting in new cavitation algorithms. The advantage of these new algorithms is that there is no need for pivot-based operations like in the existing cavitation algorithms. A further advantage becomes evident, when focusing on the discretized coupled system: the cavitation condition can be added to the mechanical system by an algebraic equation and a monolithic solution strategy for the coupled system is possible<sup>1</sup>.
- Following a monolithic instead of a partitioned solution strategy for the discretized coupled problem, leads to a faster convergence of the solution. The reason is that the monolithic solution strategy solves the dynamic equilibrium and the cavitation problem simultaneously in one iteration loop. In contrast, the partitioned strategy has an inner iteration loop, which always solves the cavitation problem, even if the outer loop is not yet converged.
- Within the modified IQN-ILS method proposed in this work, an incomplete Jacobian is used when solving the nonlinear equations of the coupled system. This incomplete Jacobian inherits only the parts of the full Jacobian, which are related to the global motion of the body. By this, the complete calculation of the full Jacobian, which is extremely time-consuming, if it is performed numerically, can be avoided.

<sup>1</sup>As far, this was possible only when using a penalization of the cavitation condition; however, in that case, the cavitation condition is not fulfilled mathematically exactly.

- Concerning the different interface coupling methodologies, it follows from a convergence study that a consistent transfer of surface tractions and deformations by either fulfilling the coupling conditions in a weak sense (mortar method) or projecting the field values leads to coupling errors, which do not affect the global discretization errors. In the same way, a conservative transfer by fulfilling the coupling conditions in a weak sense leads to coupling errors, which do not affect the global discretization errors. Other investigated transfer methods like a nearest neighbor method or a conservative transfer by projecting the field values lead to coupling errors, which deteriorate the global discretization error. The conservative transfer with the weighted residual method would be the favorite transfer methodology for long-time simulations, where no artificial energy shall be created nor annihilated.
- Concerning the interface reduction methods, it can be concluded that the load dependent approach is the most suitable to cover the deformation due to the pressure forces. This is logical since the deformation of the elastic interface results from pressure distributions. Further, the load dependent approach allows the incorporation of eventually known pressure distributions during the reduction process. For instance, the infinitely long and short bearing solution can be used for the reduction of the interface DOFs of a finite flexible bearing. In the example of the flexible slider-crank mechanism, the load dependent approach needs much less interface modes compared to the CMS-based approaches.
- The simulation example of the flexible slider-crank mechanism verifies the existing simulation tool and figures out the sensitivities in the modeling process. From the results, it can be concluded that the mass-conservative cavitation model should be used for the dynamic simulation with changing loads. Further, the dependency of the viscosity on the pressure becomes important especially at high pressures. The SUPG stabilization of the FE solution in the cavitation zone avoids oscillations in the density distribution.
- Concerning the simulation and experimental validation of a rotor system, it becomes clear that the parallel misalignment of the rotor axis strongly influences the static equilibrium position and has to be considered in the simulation model. The experimental validation of the the rotor system with misalignment can be achieved by using a LAVAL rotor simulation model with nonlinear fluid forces.
- The simulation example of the EHL point contact emphasizes the applicability of the monolithic solution strategy with the projection function. The convergence of the semi-smooth Newton scheme can be demonstrated.

## 7.4 Recommendations for future work

Due to occasional shortcomings, this work offers possible topics for future work.

As outlined at the beginning of Chapter 2, temperature effects as well as effects due to non-NEWTONian fluid behavior or fluid inertia are not treated in this work. Even though some basic modeling concepts are outlined in Section 2.5, the detailed modeling and numerical treatment of such effects would be a topic of future work. Especially, the effect of the temperature on the fluid parameters is usually not negligible. The effect of the fluid inertia may play an important role, when dealing with high velocities in tangential or fast changing velocities in normal direction. The non-NEWTONian fluid behavior has to be usually considered for the EHL point contact.

Further, the modeling and simulation of the run-up of mechanisms with bearings should be investigated in more detail. In that case, the transition between dry and lu-

bricated contact plays a fundamental role. For the modeling, simulation and also experimental validation of imperfect joints, it is referred for instance to [60, 104, 187].

Concerning the interface coupling methodologies, the numerical example deals only with an one-sided EHL problem. Even though the theory is outlined for the general case, a convergence study for the two-sided EHL problem should be analyzed in a future work. In the same way, the interface reduction methods are only investigated for one-sided EHL problems. Again, although the theory is valid for the two-side case, a numerical example should proof that.

Concerning the monolithic and partitioned solution strategy, the size of the coupled system is an aspect, which has to be also considered, when comparing simulation times: as the partitioned strategy deals with smaller system matrices, this could be an advantage when analyzing large systems with several EHL contacts. A detailed numerical study of such systems could be topic of a future work.

The simulation example of the EHL point contact of Section 6.3 reveals that the quasi-Newton method does not converge for this simulation example. The reason is the strong influence of the elastic deformation on the pressure distribution. Hence, the quasi-Newton method, outlined in this thesis, is well applicable in bearing simulation, meaning conformal EHL contact problems. However, for non-conformal EHL contact problems, the fast convergence is still an open issue. Further, the analysis of reduction methods like the load dependent method for the non-conformal EHL contact could be an outstanding task for future works.

## Appendix A

### Derivation of the REYNOLDS equation

For a better understanding, the derivation of the REYNOLDS equation from the NAVIER-STOKES equations is outlined. A more detailed derivation is given for instance in the textbook of HAMROCK et. al. [81]. In the following, the notations in the fluid film according to Fig. 2.1 are used.

When neglecting convective terms and volume forces and further assuming a small fluid height compared to the characteristic lengths in  $y$ - and  $z$ -direction respectively, the NAVIER-STOKES equations reduces to:

$$0 = -\frac{\partial p}{\partial x'} \quad (\text{A.1})$$

$$0 = -\frac{\partial p}{\partial y} + \frac{\partial}{\partial x} \left( \eta \frac{\partial v}{\partial x} \right), \quad (\text{A.2})$$

$$0 = -\frac{\partial p}{\partial z} + \frac{\partial}{\partial x} \left( \eta \frac{\partial w}{\partial x} \right). \quad (\text{A.3})$$

Equation (A.1) leads to a constant pressure in  $x$ -direction of the fluid height. Equations (A.2) and (A.3) can be integrated twice in  $x$ -direction from  $x = h_1$  to  $x = h_2$ . Then, one obtains parabolic velocity profiles for the velocity components  $v$  and  $w$  respectively, over the fluid height:

$$v = \frac{1}{2\eta} \frac{\partial p}{\partial y} x^2 + \frac{C_1}{\eta} x + C_2, \quad (\text{A.4})$$

$$w = \frac{1}{2\eta} \frac{\partial p}{\partial z} x^2 + \frac{C_3}{\eta} x + C_4, \quad (\text{A.5})$$

with integration constants still to be determined. Setting the non-slip boundary conditions  $v(x = h_1) = v_1$ ,  $v(x = h_2) = v_2$  and  $w(x = h_1) = w_1$ ,  $w(x = h_2) = w_2$  respectively, yields:

$$v = \frac{1}{2\eta} \frac{\partial p}{\partial y} (x^2 - (h_1 + h_2)x + h_1 h_2) + \frac{v_1 - v_2}{h_1 - h_2} (x - h_1) + v_1,$$

$$w = \frac{1}{2\eta} \frac{\partial p}{\partial z} (x^2 - (h_1 + h_2)x + h_1 h_2) + \frac{w_1 - w_2}{h_1 - h_2} (x - h_1) + w_1.$$

With them, the corresponding volume fluxes per unit length in  $y$ - and  $z$ -direction respectively can be determined. With the film height  $h = h_2 - h_1$ , they are defined as:

$$q'_y = \int_{h_1}^{h_2} v \, dx = -\frac{h^3}{12\eta} \frac{\partial p}{\partial y} + \frac{v_1 + v_2}{2} h, \quad (\text{A.6})$$

$$q'_z = \int_{h_1}^{h_2} w \, dx = -\frac{h^3}{12\eta} \frac{\partial p}{\partial z} + \frac{w_1 + w_2}{2} h. \quad (\text{A.7})$$

The conservation of mass in a control volume can be stated as following flux balance:

$$\frac{\partial}{\partial y}(eq'_y) + \frac{\partial}{\partial z}(eq'_z) + \frac{\partial(hq)}{\partial t} = 0, \quad (\text{A.8})$$

which ensures that the temporal change  $\frac{\partial(hq)}{\partial t}$  is caused by the local changes of the corresponding fluxes. Inserting Eqs. (A.6) and (A.7) into Eq. (A.8) gives the REYNOLDS equation:

$$\underbrace{-\nabla \left( \frac{h^3 \varrho}{12\eta} \nabla p \right)}_{\text{POISEUILLE}} + \underbrace{\frac{\partial}{\partial y} \left( \varrho h \frac{v_1 + v_2}{2} \right) + \frac{\partial}{\partial z} \left( \varrho h \frac{w_1 + w_2}{2} \right)}_{\text{COUETTE}} + \underbrace{\varrho \frac{\partial h}{\partial t}}_{\text{squeeze}} + \underbrace{h \frac{\partial \varrho}{\partial t}}_{\text{loc. exp.}} = 0,$$

in similar form as Eq. (2.1) by distinguishing the different fluxes.

## Appendix B

### Finite element shape functions

#### B.1 Dual bi-linear LAGRANGE shape functions

Figure B.1 shows the first two of the four dual bi-linear LAGRANGE shape functions. They are bi-orthogonal to the *Lin4* element shape functions.

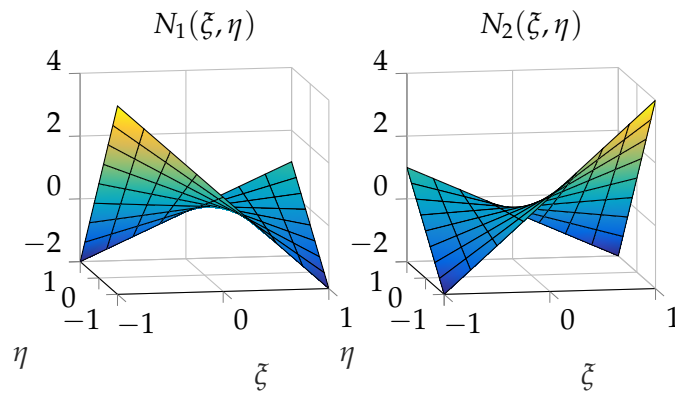


**Figure B.1:** Dual bi-linear LAGRANGE shape functions.

#### B.2 Modified bi-quadratic serendipity shape functions

Figure B.2 shows the first two of the modified bi-quadratic serendipity shape functions (*Quad8Mod*).

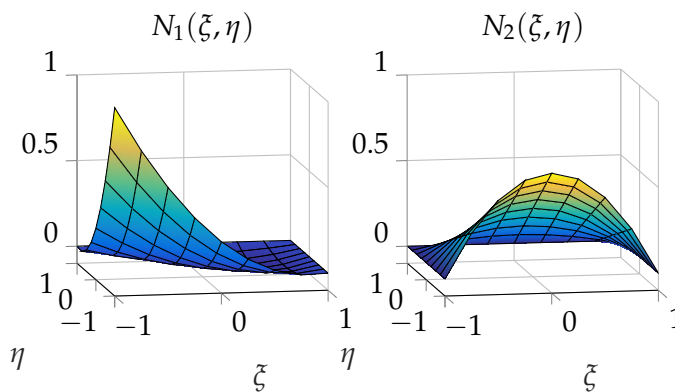


**Figure B.2:** Modified bi-quadratic serendipity shape functions.

### B.3 Dual bi-quadratic serendipity shape functions

Figure B.3 shows the first two of the dual bi-quadratic serendipity shape functions. They are bi-orthogonal to the modified bi-quadratic serendipity shape functions of Fig. B.2.

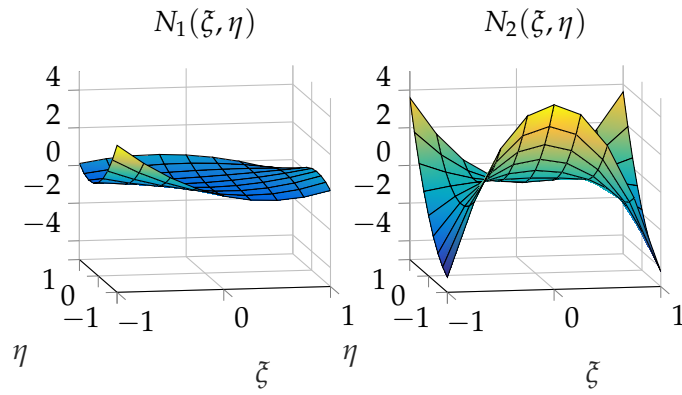


**Figure B.3:** Dual bi-quadratic serendipity shape functions.

## Appendix C

# Finite element discretization of the mass-conservative cavitation problem

### C.1 Standard-GALERKIN discretization

The FE discretization of the strong form of Eqs. (2.67) to (2.73) is given.

The solution and weighting functions of the pressure are defined by the same function spaces  $S^+$  and  $W^+$  as in Eqs. (2.44) and (2.45). The solution space  $D^+$  of the density  $\varrho$  is defined similarly to the already defined space  $Q^+$ , see Eq. (2.46) :

$$D^+ = \{\varrho \in H^{-1}(\Omega) \mid \varrho = \hat{\varrho} \text{ on } \Gamma_p, \int_{\Omega} (f_{\varrho}(p) - \varrho) (p - p_c) \, d\Omega \geq 0, p \in S^+\}. \quad (\text{C.1})$$

With these function spaces, following weak form can be stated: Find  $p \in S^+$  and  $\varrho \in D^+$  such that

$$\begin{aligned} \int_{\Omega} \kappa_d(p, \varrho) \nabla \mathbf{w}^T \nabla p \, d\Omega + \int_{\Omega} \mathbf{w} \left( \mathbf{u}_d^T \nabla \varrho + h \dot{\varrho} \right) \, d\Omega = \\ - \int_{\Omega} \mathbf{w} (q_{\text{stat}} + q_{\text{squ}}) \, d\Omega + \int_{\Gamma_q} \mathbf{w} \hat{q} \, d\Gamma, \quad \forall \mathbf{w} \in W^+, \quad (\text{C.2}) \end{aligned}$$

$$\int_{\Omega} (q - (f_{\varrho}(p) - \varrho)) (p - p_c) \, d\Omega \geq 0, \quad \forall q \in Q^+. \quad (\text{C.3})$$

Here, the GAUSS divergence is already applied. The second equation represents the VI of the complementarity condition, similar to Eq. (2.53).

The discretization is performed on the discrete fluid domain  $\Omega_h$  by using the discrete spaces  $W_h^+$  and  $S_h^+$ . The weighting function and the pressure are approximated like in Eqs. (2.22) and (2.23). In addition, the discrete spaces  $Q_h^+$  and  $D_h^+$  are defined and both the density  $\varrho$  and the weighting function  $q$  are described by the LAGRANGE shape functions  $M_k$ , leading:

$$\varrho(y, z) \approx \varrho_h(y, z) = \sum_{i=1}^{n_{\text{free}}} M_i \varrho_{\text{free},i} + \sum_{j=1}^{n_{\text{dbc}}} M_j \varrho_{\text{dbc},j}, \quad (\text{C.4})$$

$$q(y, z) \approx q_h(y, z) = \sum_{k=1}^{n_{\text{free}}} M_k q_{\text{free},k}, \quad (\text{C.5})$$

For the following discretization, the discrete solution space

$$S_h^+ = \{p_h \in S_h \mid (p_{\text{free},i} - p_c) \geq 0 \, \forall i \in \{1 \dots n_{\text{free}}\}\}$$

is chosen.

Then, the discretization leads to following discretized weak form:

$$\begin{aligned} & \sum_{k=1}^{n_{free}} \left[ w_k \left\{ \int_{\Omega_h} \left( \kappa_Q(p_h, q_h) \nabla N_k^T \sum_{i=1}^{n_{free}} \nabla N_i p_{free,i} + N_k \mathbf{u}_Q^T \sum_{i=1}^{n_{free}} \nabla M_i d_{free,i} \right) d\Omega \right. \right. \\ & + \int_{\Omega_h} h N_k \sum_{i=1}^{n_{free}} M_i \dot{q}_{free,i} d\Omega = - \int_{\Omega_h} N_k (q_{stat,h} + q_{squ,h}) d\Omega + \int_{\Gamma_{q,h}} N_k \hat{q} d\Gamma \\ & \left. \left. - \int_{\Omega_h} \left( \kappa_{Q,h} \nabla N_k^T \sum_{j=1}^{n_{dbc}} \nabla N_j p_{dbc,j} + N_k \mathbf{u}_{Q,h}^T \sum_{j=1}^{n_{dbc}} \nabla M_j q_{dbc,j} \right) d\Omega \right\} \right], \end{aligned} \quad (C.6)$$

$$\sum_{k=1}^{n_{free}} \left[ \int_{\Omega_h} M_k (f_{Q,k} - q_{free,k}) \sum_{i=1}^{n_{free}} N_i (p_{free,i} - p_c) d\Omega \right] = 0, \quad (C.7)$$

$$\sum_{k=1}^{n_{free}} \left[ q_k \int_{\Omega_h} M_k \sum_{i=1}^{n_{free}} N_i (p_{free,i} - p_c) d\Omega \right] \geq 0, \quad (C.8)$$

$$\sum_{k=1}^{n_{free}} \left[ w_k \int_{\Omega_h} N_k \sum_{i=1}^{n_{free}} M_i (f_{Q,i} - q_{free,i}) d\Omega \right] \geq 0, \quad (C.9)$$

with the unknown values  $p_{free,i}$  and  $q_{free,i}$ , which in the following, belong to the  $i$ -th component ( $i = 1 \dots n_{free}$ ) of the discrete vectors  $\mathbf{p}$  and  $\mathbf{q}$ , respectively. The discretized weak form has to be valid for every nonnegative value of  $w_k$ . As the solution space  $S_h^+$  is chosen such that the discrete pressure values  $(p_{free,i} - p_c)$  are nonnegative, following matrix-vector representation can be stated:

$$\begin{aligned} & \mathbf{A}_Q(\mathbf{p}, \mathbf{q}) \mathbf{p} + \mathbf{B}_Q \mathbf{q} + \mathbf{C}_Q \dot{\mathbf{q}} = \mathbf{b}_Q(\mathbf{p}, \mathbf{q}) \\ & \mathbf{0} \leq \mathbf{p} - p_c \perp N(\mathbf{f}_Q(\mathbf{p}) - \mathbf{q}) \geq \mathbf{0}. \end{aligned}$$

In summary, these are two sets of equations for the two unknown vectors  $\mathbf{p}$  and  $\mathbf{d}$ . It becomes clear, that the Eqs. (C.7) to (C.9) of the discrete weak form of the complementarity problem lead to complementarity problem for the discrete values. The matrices and vectors are calculated and assembled element-wise. They are defined as:

$$\begin{aligned} \mathbf{A}_Q &= \bigwedge_{e=1}^{n_{ele}} \mathbf{A}_{k,i}^{(e)}, & \mathbf{A}_{k,i}^{(e)} &= \int_{\Omega^{(e)}} \kappa_Q(p_h, q_h) \nabla N_k^T \nabla N_i d\Omega, \\ \mathbf{B}_Q &= \bigwedge_{e=1}^{n_{ele}} \mathbf{B}_{k,i}^{(e)}, & \mathbf{B}_{k,i}^{(e)} &= \int_{\Omega^{(e)}} N_k \mathbf{u}_Q^T \nabla M_i d\Omega, \\ \mathbf{C}_Q &= \bigwedge_{e=1}^{n_{ele}} \mathbf{C}_{k,i}^{(e)}, & \mathbf{C}_{k,i}^{(e)} &= \int_{\Omega^{(e)}} h N_k M_i d\Omega, \\ \mathbf{b}_Q &= \bigwedge_{e=1}^{n_{ele}} \mathbf{b}_k^{(e)}, & \mathbf{b}_k^{(e)} &= - \int_{\Omega^{(e)}} N_k (q_{stat,h} + q_{squ,h}) d\Omega + \int_{\Gamma_q^{(e)}} N_k \hat{q} d\Gamma \\ & & & - \int_{\Omega^{(e)}} \kappa_{Q,h} \nabla N_k^T \sum_{j=1}^{n_{dbc}} \nabla N_j p_{dbc,j} d\Omega \\ & & & - \int_{\Omega^{(e)}} N_k \mathbf{u}_{Q,h}^T \sum_{j=1}^{n_{dbc}} \nabla M_j q_{dbc,j} d\Omega, \\ \mathbf{N} &= \bigwedge_{e=1}^{n_{ele}} \mathbf{N}_{k,i}^{(e)}, & \mathbf{N}_{k,i}^{(e)} &= \int_{\Omega^{(e)}} N_k M_i d\Omega. \end{aligned}$$

## C.2 PETROV-GALERKIN discretization

The SUPG method is applied to stabilize the FE discretization of the strong form of Eqs. (2.67) to (2.73).

In contrast to the standard BUBNOV-GALERKIN method of the previous subsection, following streamline upwind modified weighting functions for the discretization of the function space  $W_h^+$  are used:

$$\tilde{w}_{\varrho,h} = w_h + v_{\varrho,h} = w_h + \tau_{\varrho} \mathbf{u}_{\varrho,h}^T \nabla w_h, \quad (\text{C.10})$$

with the stabilization parameter  $\tau_{\varrho}$ . The modified weighting function  $\tilde{w}_{\varrho,h}$  is applied to the discretization of Eq. (C.2) of the weak form. For the discretization of Eq. (C.3) still the standard-GALERKIN method with the weighting function  $q$  is used. For the first equation of the stabilized discrete weak form follows for  $p_h \in S_h$  and  $q_h \in D_h$ :

$$\begin{aligned} \int_{\Omega_h} \kappa_{\varrho}(p_h, q_h) \nabla w_h^T \nabla p_h \, d\Omega + \int_{\Omega_h} w_h \left( \mathbf{u}_{\varrho,h}^T \nabla q_h + h \dot{q}_h \right) \, d\Omega = \\ - \int_{\Omega_h} w_h (q_{\text{stat},h} + q_{\text{squ},h}) \, d\Omega + \int_{\Gamma_{q,h}} w_h \hat{q} \, d\Gamma \\ + \sum_{e=1}^{n_{el}} \int_{\Omega_h^{(e)}} v_{\varrho,h}^{(e)} R_{\varrho,h}^{(e)} \, d\Omega, \quad \forall w_h \in W_h^+. \end{aligned} \quad (\text{C.11})$$

The last term represents the stabilization term. The discrete residuum  $R_{\varrho,h}$  is given according to Eq. (2.67):

$$R_{\varrho,h} = -\nabla (\kappa_{\varrho}(p_h, q_h) \nabla p_h) + \mathbf{u}_{\varrho,h}^T \nabla q_h + h \dot{q}_h + q_{\text{stat},h} + q_{\text{squ},h}. \quad (\text{C.12})$$

The further discretization of the stabilization term gives matrices and vectors, which are used to update the original matrices and vectors of the standard-GALERKIN method:

$$\mathbf{A}_{\varrho} \leftarrow \mathbf{A}_{\varrho} + \mathbf{A}_{\varrho,SUPG}, \quad \mathbf{B}_{\varrho} \leftarrow \mathbf{B}_{\varrho} + \mathbf{B}_{\varrho,SUPG}, \quad \mathbf{C}_{\varrho} \leftarrow \mathbf{C}_{\varrho} + \mathbf{C}_{\varrho,SUPG}, \quad \mathbf{b}_{\varrho} \leftarrow \mathbf{b}_{\varrho} + \mathbf{b}_{\varrho,SUPG}.$$



## Appendix D

### Kinematics for cylindrical joint

With the eccentricity  $e$  and the radial deformation  $\delta_r$ , the local geometric and kinematic relations in the cylindrical elastic joint can be derived (Fig. 2.7 of Section 2.4.1). Due to the assumption of a thin fluid film  $h \ll R_2$ , the order of geometric and kinematic properties is characterized as follows:

$$0. \text{ order: } \quad R_1, R_2, \omega_1, \omega_2, \quad (\text{D.1})$$

$$1. \text{ order: } \quad h, e, e_r, e_t, \delta_r, \dot{e}, \dot{e}_r, \dot{e}_t, \dot{\delta}_r, \dot{\delta}_t, \dot{\delta}_z \quad (\text{D.2})$$

$$2. \text{ order: } \quad \bar{h}_1 = -\frac{1}{2} \frac{e_t^2}{R_1} + \mathcal{O}(e_t^3), \bar{v}_1. \quad (\text{D.3})$$

At a point  $(y, z)$  of the fluid domain, the local heights can be evaluated as follows:

$$h_1 = e_r + r_1 = e_r + R_1 + \bar{h}_1, \quad (\text{D.4})$$

$$h_2 = R_2 + \delta_r, \quad (\text{D.5})$$

$$h = h_2 - h_1 = R_2 - R_1 - e_r + \delta_r + \bar{h}_1, \quad (\text{D.6})$$

where  $\bar{h}_1$  is a second order term, see (D.3). For the derivatives with respect to  $y$  and  $z$  follows with (2.82):

$$\frac{\partial h_1}{\partial y} = \frac{\partial e_r}{\partial y} + \frac{\partial \bar{h}_1}{\partial y} = \frac{e_t}{R_2} + \frac{\partial \bar{h}_1}{\partial y} =: \tan(\alpha), \quad (\text{D.7})$$

$$\frac{\partial h_2}{\partial y} = \frac{\partial \delta_r}{\partial y}, \quad (\text{D.8})$$

$$\frac{\partial h_1}{\partial z} = 0, \quad \frac{\partial h_2}{\partial z} = \frac{\partial \delta_r}{\partial z}. \quad (\text{D.9})$$

The absolute velocities in local tangential and normal directions can be calculated as follows, where  $\dot{\delta}_t$  and  $\dot{\delta}_z$  are the velocities in local tangential and  $z$  direction, respectively:

$$u_1 = \dot{x}_{B1} \cos(\varphi) + \dot{y}_{B1} \sin(\varphi) + \omega_1 R_1 \sin(\alpha), \quad (\text{D.10})$$

$$u_2 = \dot{x}_{B2} \cos(\varphi) + \dot{y}_{B2} \sin(\varphi) + \dot{\delta}_r, \quad (\text{D.11})$$

$$v_1 = -\dot{x}_{B1} \sin(\varphi) + \dot{y}_{B1} \cos(\varphi) + \omega_1 R_1 \cos(\alpha) \quad (\text{D.12})$$

$$= -\dot{x}_{B1} \sin(\varphi) + \dot{y}_{B1} \cos(\varphi) + \omega_1 R_1 + \bar{v}_1, \quad (\text{D.13})$$

$$v_2 = -\dot{x}_{B2} \sin(\varphi) + \dot{y}_{B2} \cos(\varphi) + \omega_2 h_2 + \dot{\delta}_t, \quad (\text{D.14})$$

$$w_1 = 0, \quad w_2 = \dot{\delta}_z, \quad (\text{D.15})$$

where  $\bar{v}_1$  is a term of second order, see (D.3). Derivation of the velocities yields:

$$\frac{\partial v_1}{\partial y} = \frac{1}{R_2} (-\dot{x}_{B1} \cos(\varphi) - \dot{y}_{B1} \sin(\varphi)) + \frac{\partial \bar{v}_1}{\partial y}, \quad (\text{D.16})$$

$$\frac{\partial v_2}{\partial y} = \frac{1}{R_2} \left( -\dot{x}_{B2} \cos(\varphi) - \dot{y}_{B2} \sin(\varphi) + \omega_2 \frac{\partial h_2}{\partial y} \right) + \frac{\partial \dot{\delta}_t}{\partial y}, \quad (\text{D.17})$$

$$\frac{\partial w_1}{\partial z} = 0, \quad \frac{\partial w_2}{\partial z} = \frac{\partial \dot{\delta}_z}{\partial z}. \quad (\text{D.18})$$

The kinematic equations (D.5) to (D.18) can be inserted into the flux terms (2.5) to (2.6) of the Reynolds equation (2.2). After neglecting all second order terms by using the order analysis (D.1) to (D.3), the following term  $q_{\text{stat},b}$  for the flexible bearing remains:

$$q_{\text{stat},b} = -\rho \left[ \left( \frac{\partial \delta_r}{\partial y} - \frac{\partial e_r}{\partial y} \right) \frac{\omega_1 R_1 + \omega_2 R_2}{2} - \omega_2 R_2 \frac{\partial \delta_r}{\partial y} + \dot{e}_r + \dot{\delta}_r \right]. \quad (\text{D.19})$$

It is worth noting that the velocity  $\omega_1 R_1$  due to the rotation of the shaft cancels out in the source term  $\frac{\partial h_i}{\partial t}$  of Eq. (2.3). This agrees with the fact that a velocity in the tangential direction of a surface (like it is the velocity  $\omega_1 R_1$ ) causes only a COUETTE flow, but no squeeze effect.

# Appendix E

## Parameter for simulation examples

### E.1 Simulation example of Section 2.6.1

Figure E.1 shows the simulation example and Table E.1 lists the simulation parameter.

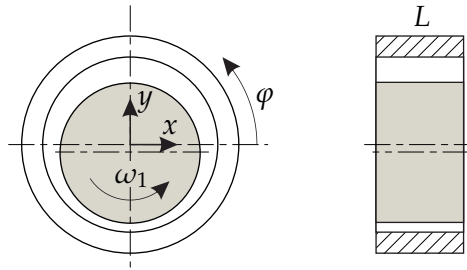


**Figure E.1:** Simulation example of journal bearing with fixed eccentricity.

**Table E.1:** Parameter for simulation example of journal bearing with fixed eccentricity.

parameter	value	parameter	value
$R_2$	2.25 cm	$\rho_{p=0}$	800 kg/m <sup>3</sup>
$L$	2.2 cm	$\eta_{p=0}$	5e-3 kgm/s
$h_0$	17 $\mu$ m	$a$	0.6e-9 m <sup>2</sup> /N
$\omega_1$	500 rad/s	$b$	1.7e-9 m <sup>2</sup> /N
$e_x$	0 $\mu$ m	$\alpha_0$	5.93e-8 m <sup>2</sup> /N
$e_y$	-0.5 $h_0$	$p_c$	0 N/m <sup>2</sup>

### E.2 Simulation example of Section 2.6.2

Figure E.2 shows the simulation example and Table E.2 lists the simulation parameter.

### E.3 Simulation example of Section 2.6.3

Figure E.1 shows the simulation example and Table E.3 lists the simulation parameter.

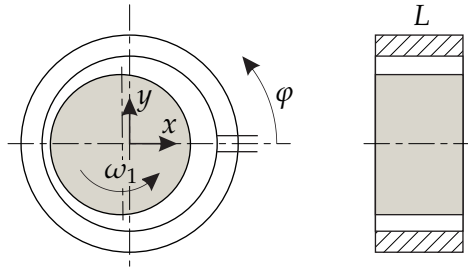


**Figure E.2:** Simulation example of grooved journal bearing with fixed eccentricity.

**Table E.2:** Parameter for simulation example of grooved journal bearing with fixed eccentricity.

parameter	value	parameter	value
$L/R_2$	2	$\bar{a}$	1/40
$e_x/h_0$	-0.6	$\bar{b}$	0
$e_y/h_0$	0	$\bar{p}_c$	0

**Table E.3:** Parameter for simulation example of journal bearing with fixed eccentricity.

parameter	value	parameter	value
$R_2$	2.25 cm	$\rho_{p=0}$	839 kg/m <sup>3</sup>
$L$	2.2 cm	$\eta_{p=0}$	0.414 kgm/s
$h_0$	17 μm	$a$	0.6e-9 m <sup>2</sup> /N
$\omega_1$	500 rad/s	$b$	1.7e-9 m <sup>2</sup> /N
$e_x$	0 μm	$Z_1$	0.43
$e_y$	-0.245 $h_0$	$c_p$	1.96e8 N/m <sup>2</sup>
$p_c$	0 N/m <sup>2</sup>	$\eta_\infty$	6.31e-5 kgm/s

## Appendix F

### Solution techniques

#### F.1 Scheme of solution strategy for DAE formulation with IQN-ILS method

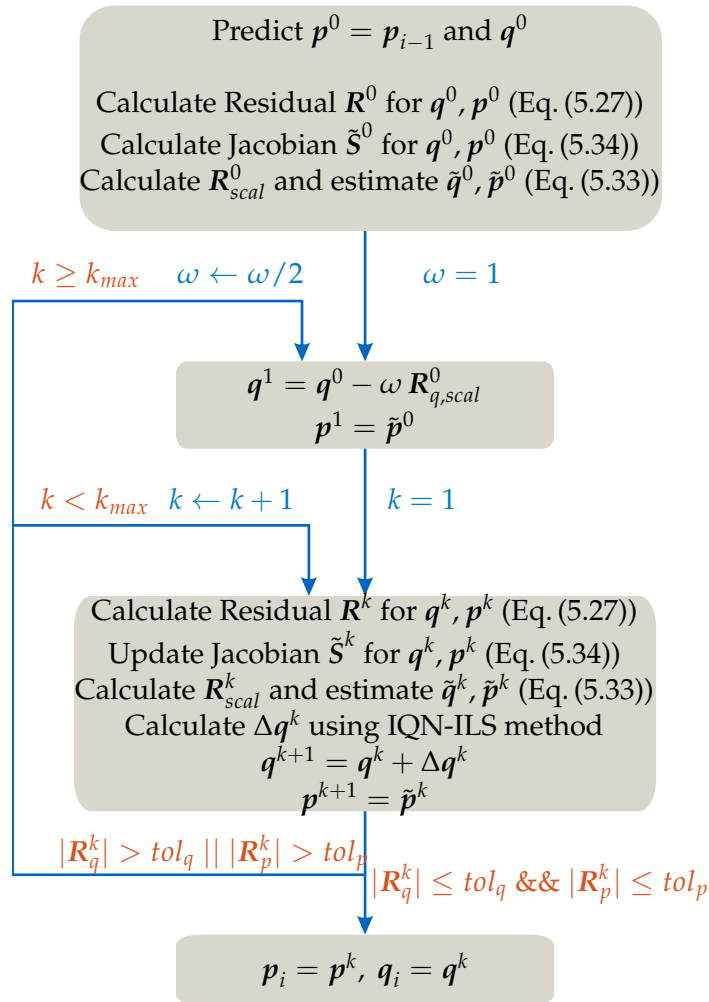


**Figure F.1:** Scheme of solution strategy with IQN-ILS method and reduced Jacobian for DAE formulation for a given time step.



## Bibliography

- [1] V. Acary and B. Brogliato. “Numerical methods for nonsmooth dynamical systems: applications in mechanics and electronics”. In: *Lecture Notes in Applied and Computational Mechanics*. Ed. by P. Wriggers and P. Eberhard. Vol. 35. Berlin Heidelberg: Springer Science & Business Media, 2008.
- [2] S. Ahmed, C. E. Goodyer, and P. K. Jimack. “An efficient preconditioned iterative solution of fully-coupled elastohydrodynamic lubrication problems”. In: *Applied Numerical Mathematics* 62.5 (2012), pp. 649–663.
- [3] S. Alakhramsing, R. van Ostayen, and R. Eling. “Thermo-Hydrodynamic Analysis of a Plain Journal Bearing on the Basis of a New Mass Conserving Cavitation Algorithm”. In: *Lubricants* 3.2 (2015), pp. 256–280.
- [4] P. Alart and A. Curnier. “A mixed formulation for frictional contact problems prone to Newton like solution methods”. In: *Computer methods in applied mechanics and engineering* 92.3 (1991), pp. 353–375.
- [5] H. Allmaier, C. Priestner, D. Sander, and F. Reich. “Friction in automotive engines”. In: *Tribology in engineering* (2013), pp. 149–84.
- [6] H. Allmaier and G. Offner. *Current Challenges and Frontiers for the EHD Simulation of Journal Bearings: a Review*. Tech. rep. SAE Technical Paper, 2016.
- [7] J. Archard and M. Kirk. “Lubrication at point contacts”. In: *Proceedings of the Royal Society of London A: Mathematical, Physical and Engineering Sciences*. Vol. 261. 1307. The Royal Society. 1961, pp. 532–550.
- [8] M. Arnold and O. Bruels. “Convergence of the generalized-alpha scheme for constrained mechanical systems”. In: *Multibody System Dynamics* 18.2 (2007), pp. 185–202.
- [9] M. Bampton and R. Craig. “Coupling of substructures for dynamic analyses”. In: *Aiaa Journal* 6.7 (1968), pp. 1313–1319.
- [10] C. Barus. “Isothermals, isopiestic and isometrics relative to viscosity”. In: *American journal of science* 266 (1893), pp. 87–96.
- [11] G. Bayada, M. Chambat, and M. El Alaoui. “Variational formulations and finite element algorithms for cavitation problems”. In: *Journal of Tribology* 112.2 (1990), pp. 398–403.
- [12] G. Bayada and M. Chambat. “Nonlinear variational formulation for a cavitation problem in lubrication”. In: *Journal of Mathematical Analysis and Applications* 90.2 (1982), pp. 286–298.
- [13] C. Bernardi, Y. Maday, and A. Patera. “A new nonconforming approach to domain decomposition: the mortar element method”. In: *Nonlinear Partial Differential Equations and Their Applications*. Ed. by H. Brezis and J. Lions. London/New York: Pitman/Wiley, 1994, pp. 13–51.

- [14] L. Bertocchi, D. Dini, M. Giacomini, M. T. Fowell, and A. Baldini. "Fluid film lubrication in the presence of cavitation: a mass-conserving two-dimensional formulation for compressible, piezoviscous and non-Newtonian fluids". In: *Tribology International* 67 (2013), pp. 61–71.
- [15] S. Boedo and J. Booker. "Classical bearing misalignment and edge loading: a numerical study of limiting cases". In: *Journal of Tribology* 126.3 (2004), pp. 535–541.
- [16] A. Bogaers, S. Kok, B. Reddy, and T. Franz. "Quasi-Newton methods for implicit black-box FSI coupling". In: *Computer Methods in Applied Mechanics and Engineering* 279 (2014), pp. 113–132.
- [17] D. Bonneau, A. Fatu, and D. Souchet. *Hydrodynamic Bearings*. London: John Wiley & Sons, 2014.
- [18] D. Bonneau, A. Fatu, and D. Souchet. *Internal Combustion Engine Bearings Lubrication in Hydrodynamic Bearings*. London: John Wiley & Sons, 2014.
- [19] D. Bonneau, A. Fatu, and D. Souchet. *Mixed lubrication in hydrodynamic bearings*. London: John Wiley & Sons, 2014.
- [20] J. Booker. "Dynamically loaded journal bearings: mobility method of solution". In: *Journal of Basic Engineering* 87.3 (1965), pp. 537–546.
- [21] J. Booker. "Classic cavitation models for finite element analysis". In: *Current research in cavitating fluid films* (1990), pp. 39–40.
- [22] J. Booker, S. Boedo, and D. Bonneau. "Conformal elastohydrodynamic lubrication analysis for engine bearing design: a brief review". In: *Proceedings of the Institution of Mechanical Engineers-Part C: Journal of Mechanical Engineering Science* 224.12 (2010), pp. 2648–2653.
- [23] C. Bottasso, D. Dopico, and L. Trainelli. "On the optimal scaling of index three DAEs in multibody dynamics". In: *Multibody System Dynamics* 19.1-2 (2008), pp. 3–20.
- [24] F. Bowden and D. Tabor. *The friction and lubrication of solids*. New York: Oxford University Press, 2001.
- [25] M. Braun and W. Hannon. "Cavitation formation and modelling for fluid film bearings: a review". In: *Proceedings of the Institution of Mechanical Engineers, Part J: Journal of Engineering Tribology* 224.9 (2010), pp. 839–863.
- [26] H. Bremer. *Dynamik und Regelung mechanischer Systeme*. Stuttgart: Teubner, 1988.
- [27] H. Bremer. *Elastic multibody dynamics*. Berlin Heidelberg: Springer Science + Business Media, 2008.
- [28] H. Bremer and F. Pfeiffer. *Elastische Mehrkörpersysteme*. Stuttgart: Teubner, 1992.
- [29] A. Brooks and T. Hughes. "Streamline upwind/Petrov-Galerkin formulations for convection dominated flows with particular emphasis on the incompressible Navier-Stokes equations". In: *Computer methods in applied mechanics and engineering* 32.1 (1982), pp. 199–259.
- [30] O. Bruls, P. Duysinx, and J.-C. Golinval. "A unified finite element framework for the dynamic analysis of controlled flexible mechanisms". In: *ECCOMAS Thematic Conference on Advances in Computational Multibody Dynamics*. Madrid, Spain, 2005.
- [31] M. Busch and B. Schweizer. "Coupled simulation of multibody and finite element systems: an efficient and robust semi-implicit coupling approach". In: *Archive of Applied Mechanics* 82.6 (2012), pp. 723–741.

- [32] A. Chasalevris and F. Dohnal. "An Experimental Study on the Additional Harmonics due to Worn Journal Bearings". In: *10. Internationale Tagung Schwingungen in rotierenden Maschinen (SIRM)* (2013).
- [33] H. Cheng and B. Sternlicht. "A numerical solution for the pressure, temperature, and film thickness between two infinitely long, lubricated rolling and sliding cylinders, under heavy loads". In: *Journal of Basic Engineering* 87.3 (1965), pp. 695–704.
- [34] D. G. Christopherson. "A new mathematical method for the solution of film lubrication problems". In: *Proceedings of the Institution of Mechanical Engineers* 146.1 (1941), pp. 126–135.
- [35] J. Chung and G. Hulbert. "A time integration algorithm for structural dynamics with improved numerical dissipation: the generalized-alpha method". In: *Journal of applied mechanics* 60.2 (1993), pp. 371–375.
- [36] T. Conry, S. Wang, and C. Cusano. "A Reynolds-Eyring Equation for Elastohydrodynamic Lubrication in Line Contacts". In: *Journal of Tribology* 109.4 (1987), pp. 648–654.
- [37] V. Constantinescu and S. Galetuse. "On the possibilities of improving the accuracy of the evaluation of inertia forces in laminar and turbulent films". In: *Journal of Lubrication Technology* 96.1 (1974), pp. 69–77.
- [38] R. Craig and C.-J. Chang. *Substructure coupling for dynamic analysis and testing*. Tech. rep. Austin, United States: University of Texas, 1977.
- [39] R. Craig and A. Kurdila. *Fundamentals of structural dynamics*. 2nd ed. Hoboken, New Jersey: John Wiley & Sons, 2006.
- [40] C. Cryer and M. Dempster. "Equivalence of linear complementarity problems and linear programs in vector lattice Hilbert spaces". In: *SIAM Journal on Control and Optimization* 18.1 (1980), pp. 76–90.
- [41] A. De Boer, A. Van Zuijlen, and H. Bijl. "Review of coupling methods for non-matching meshes". In: *Computer methods in applied mechanics and engineering* 196.8 (2007), pp. 1515–1525.
- [42] A. De Boer. "Computational fluid-structure interaction: spatial coupling, coupling shell and mesh deformation". PhD thesis. Netherlands: Delft University of Technology, 2008.
- [43] J. Degroote, K.-J. Bathe, and J. Vierendeels. "Performance of a new partitioned procedure versus a monolithic procedure in fluid–structure interaction". In: *Computers & Structures* 87.11 (2009), pp. 793–801.
- [44] J. Degroote, R. Haelterman, S. Annerel, P. Bruggeman, and J. Vierendeels. "Performance of partitioned procedures in fluid–structure interaction". In: *Computers & structures* 88.7 (2010), pp. 446–457.
- [45] J. Donea and A. Huerta. *Finite element methods for flow problems*. Chichester, United Kingdom: John Wiley & Sons, 2003.
- [46] S. Dousti, P. Allaire, T. Dimond, and J. Cao. "An extended Reynold equation applicable to high reduced Reynolds number operation of journal bearings". In: *Tribology International* 102 (2016), pp. 182–197.
- [47] D. Dowson and G. Higginson. "A numerical solution to the elasto-hydrodynamic problem". In: *Journal of mechanical engineering science* 1.1 (1959), pp. 6–15.
- [48] D. Dowson and G. Higginson. *Elastohydrodynamic Lubrication*. Oxford: Pergamon Press, 1966.

- [49] D. Dowson and C. Taylor. "Cavitation in bearings". In: *Annual Review of Fluid Mechanics* 11.1 (1979), pp. 35–65.
- [50] D. Dowson. *History of Tribology*. 2nd ed. London: Wiley, 1998.
- [51] C. Elcoate, H. Evans, and T. Hughes. "On the coupling of the elastohydrodynamic problem". In: *Proceedings of the Institution of Mechanical Engineers, Part C: Journal of Mechanical Engineering Science* 212.4 (1998), pp. 307–318.
- [52] R. Eling, R. van Ostayen, and D. Rixen. "Multilobe Floating Ring Bearings for Automotive Turbochargers". In: *Proceedings of the 9th IFToMM International Conference on Rotor Dynamics*. Springer International Publishing Switzerland, 2015, pp. 821–833.
- [53] R. Eling, M. te Wierik, R. van Ostayen, and D. Rixen. "Towards Accurate Prediction of Unbalance Response, Oil Whirl and Oil Whip of Flexible Rotors Supported by Hydrodynamic Bearings". In: *Lubricants* 4.3 (2016), pp. 33–51.
- [54] H. Elrod. "A cavitation algorithm". In: *Journal of Tribology* 103.3 (1981), pp. 350–354.
- [55] H. Elrod and M. Adams. "A computer program for cavitation and starvation problems". In: *Cavitation and related phenomena in lubrication* (1974), pp. 37–41.
- [56] H. Evans and R. Snidle. "The elastohydrodynamic lubrication of point contacts at heavy loads". In: *Proceedings of the Royal Society of London A: Mathematical, Physical and Engineering Sciences*. Vol. 382. 1782. The Royal Society. 1982, pp. 183–199.
- [57] C. Farhat, M. Lesoinne, and P. Le Tallec. "Load and motion transfer algorithms for fluid/structure interaction problems with non-matching discrete interfaces: Momentum and energy conservation, optimal discretization and application to aeroelasticity". In: *Computer methods in applied mechanics and engineering* 157.1 (1998), pp. 95–114.
- [58] B. Flemisch and B. Wohlmuth. "Stable Lagrange multipliers for quadrilateral meshes of curved interfaces in 3D". In: *Computer Methods in Applied Mechanics and Engineering* 196.8 (2007), pp. 1589–1602.
- [59] L. Floberg. "On hydrodynamic lubrication with special reference to sub-cavity pressures and number of streamers in cavitation regions (Hydrodynamic bearing lubrication of rotating cylinder with reference to sub-cavity pressure and cavitation regions)". In: *Acta Polytechnica Scandinavica, Mechanical Engineering Series* (1965), pp. 1–35.
- [60] P. Flores, J. Ambrosio, J. Pimenta Claro, and H. Lankarani. "Kinematics and Dynamic of Multibody Systems with Imperfect Joints - Models and Case Studies". In: *Lecture Notes in Applied and Computational Mechanics*. Ed. by F. Pfeiffer and P. Wriggers. Vol. 34. Berlin Heidelberg: Springer Verlag, 2008.
- [61] P. Flores. "Modeling, Analysis and Simulation of 3D Elastohydrodynamic Revolute Joints in Multibody Systems". In: *Multibody Mechatronic Systems*. Springer, 2015, pp. 199–209.
- [62] M. Förg, F. Pfeiffer, and H. Ulbrich. "Simulation of unilateral constrained systems with many bodies". In: *Multibody System Dynamics* 14.2 (2005), pp. 137–154.
- [63] A. Fuchs, J. Schmied, and A. Kosenkov. "High Speed Hydrodynamic Journal Bearings – State of the Art of Calculations". In: *11. Internationale Tagung Schwingungen in rotierenden Maschinen (SIRM)*. Magdeburg, Germany, 2015.
- [64] R. Gasch, R. Nordmann, and H. Pfützner. *Rotordynamik*. Berlin: Springer-Verlag, 2006.

- [65] M. Geradin and D. Rixen. "A 'nodeless' dual superelement formulation for structural and multibody dynamics application to reduction of contact problems". In: *International Journal for Numerical Methods in Engineering* 106.10 (2015), pp. 773–798.
- [66] M. Géradin and D. Rixen. *Mechanical vibrations: theory and application to structural dynamics*. West Sussex, UK: John Wiley & Sons, 2014.
- [67] M. Giacomini, M. Fowell, D. Dini, and A. Strozzi. "A mass-conserving complementarity formulation to study lubricant films in the presence of cavitation". In: *Journal of tribology* 132.4 (2010), p. 041702.
- [68] J. Glienicke. "Feder- und Dämpfungskonstanten von Gleitlagern für Turbomaschinen und deren Einfluß auf das Schwingungsverhalten eines einfachen Rotors". PhD thesis. 1966.
- [69] C. Glocker. *Dynamik von Starrkörpersystemen mit Reibung und Stößen*. VDI-Fortschrittsberichte Reihe 18 Nr. 182. Düsseldorf: VDI-Verlag, 1995.
- [70] P. Goenka. "Dynamically loaded journal bearings: finite element method analysis". In: *Journal of Tribology* 106.4 (1984), pp. 429–437.
- [71] J. Greenwood and J. Tripp. "The contact of two nominally flat rough surfaces". In: *Proceedings of the institution of mechanical engineers* 185.1 (1970), pp. 625–633.
- [72] L. Gümbel. "Das problem der Lagerreibung". In: *Bezirksverband deutscher Ingenieure VDI* 5 (1914), pp. 87–104.
- [73] W. Habchi. "Reduced order finite element model for elastohydrodynamic lubrication: Circular contacts". In: *Tribology International* 71 (2014), pp. 98–108.
- [74] W. Habchi, D. Eyheramendy, P. Vergne, and G. Morales-Espejel. "Stabilized Finite Elements for Elastohydrodynamic Lubrication Problems". In: *Proceedings of the Sixth International Conference on Engineering Computational Technology*. Stirlingshire, Scotland: Citeseer, 2008.
- [75] W. Habchi and J. Issa. "Fast and reduced full-system finite element solution of elastohydrodynamic lubrication problems: Line contacts". In: *Advances in Engineering Software* 56 (2013), pp. 51–62.
- [76] W. Habchi and J. Issa. "An Exact and General Model Order Reduction Technique for the Finite Element Solution of Elastohydrodynamic Lubrication Problems". In: *Journal of Tribology* (2016).
- [77] W. Habchi, I. Demirci, D. Eyheramendy, G. Morales-Espejel, and P. Vergne. "A finite element approach of thin film lubrication in circular EHD contacts". In: *Tribology International* 40.10 (2007), pp. 1466–1473.
- [78] W. Habchi, D. Eyheramendy, P. Vergne, and G. Morales-Espejel. "A full-system approach of the elastohydrodynamic line/point contact problem". In: *Journal of Tribology* 130.2 (2008), pp. 02150-1–10.
- [79] E. Hairer and G. Wanner. *Solving Ordinary Differential Equations II: Stiff and differential-algebraic problems*. Springer Verlag, 1991.
- [80] B. Hamrock and D. Dowson. "Isothermal elastohydrodynamic lubrication of point contacts: Part I — Theoretical formulation". In: *Journal of Lubrication Technology* 98.2 (1976), pp. 223–228.
- [81] B. Hamrock, S. Schmid, and B. Jacobson. *Fundamentals of fluid film lubrication*. New York: CRC press, 2004.

- [82] S. Hartmann and E. Ramm. "A mortar based contact formulation for non-linear dynamics using dual Lagrange multipliers". In: *Finite Elements in Analysis and Design* 44.5 (2008), pp. 245–258.
- [83] J. Herrmann, M. Maess, and L. Gaul. "Substructuring including interface reduction for the efficient vibro-acoustic simulation of fluid-filled piping systems". In: *Mechanical systems and signal processing* 24.1 (2010), pp. 153–163.
- [84] H. Hertz. "Über die Berührung fester elastischer Körper". In: *Journal für die reine Angewandte Mechanik* 92 (1881), pp. 156–171.
- [85] M. Hofer. "Isotherme elastohydrodynamische Kontakte in Mehrkörpersystemen". Semester Thesis. Munich: Technical University of Munich, Chair of Applied Mechanics, May 28, 2015.
- [86] W. Hu, H. Miah, N. Feng, and E. Hahn. "A rig for testing lateral misalignment effects in a flexible rotor supported on three or more hydrodynamic journal bearings". In: *Tribology International* 33.3 (2000), pp. 197–204.
- [87] B. Hübner, E. Walhorn, and D. Dinkler. "A monolithic approach to fluid–structure interaction using space–time finite elements". In: *Computer methods in applied mechanics and engineering* 193.23 (2004), pp. 2087–2104.
- [88] S. Hüeber. "Discretization techniques and efficient algorithms for contact problems". PhD thesis. Stuttgart, 2008.
- [89] S. Hüeber and B. Wohlmuth. "A primal–dual active set strategy for non-linear multibody contact problems". In: *Computer Methods in Applied Mechanics and Engineering* 194.27 (2005), pp. 3147–3166.
- [90] T. Hughes, C. Elcoate, and H. Evans. "A novel method for integrating first-and second-order differential equations in elastohydrodynamic lubrication for the solution of smooth isothermal, line contact problems". In: *International journal for numerical methods in engineering* 44.8 (1999), pp. 1099–1113.
- [91] T. Hughes, C. Elcoate, and H. Evans. "Coupled solution of the elastohydrodynamic line contact problem using a differential deflection method". In: *Proceedings of the Institution of Mechanical Engineers, Part C: Journal of Mechanical Engineering Science* 214.4 (2000), pp. 585–598.
- [92] T. Hughes. *The finite element method: linear static and dynamic finite element analysis*. Mineola, New York: Courier Corporation, 2012.
- [93] B. Jakobsson and L. Floberg. *The finite journal bearing, considering vaporization*. Göteborg: Gumperts Förlag, 1957.
- [94] K. Jansen, C. Whiting, and G. Hulbert. "A generalized-alpha method for integrating the filtered Navier–Stokes equations with a stabilized finite element method". In: *Computer Methods in Applied Mechanics and Engineering* 190.3 (2000), pp. 305–319.
- [95] M. Junge, D. Brunner, J. Becker, and L. Gaul. "Interface-reduction for the Craig–Bampton and Rubin method applied to FE–BE coupling with a large fluid–structure interface". In: *International journal for numerical methods in engineering* 77.12 (2009), pp. 1731–1752.
- [96] N. Kikuchi and J. Oden. *Contact problems in elasticity: a study of variational inequalities and finite element methods*. Vol. 8. Philadelphia, United States: SIAM, 1988.
- [97] H.-G. Kim. "A new coupling strategy for fluid–solid interaction problems by using the interface element method". In: *International journal for numerical methods in engineering* 81.4 (2010), pp. 403–428.

- [98] G. Knoll, R. Schönen, and K. Wilhelm. "Full dynamic analysis of crankshaft and engine block with special respect to elasto-hydrodynamic bearing coupling". In: *ASME ICE* 28.3 (1997), pp. 1–8.
- [99] M. Kostreva. "Elasto-hydrodynamic lubrication: A nonlinear complementarity problem". In: *International Journal for numerical methods in fluids* 4.4 (1984), pp. 377–397.
- [100] A. de Kraker, R. van Ostayen, and D. Rixen. "Development of a texture averaged Reynolds equation". In: *Tribology International* 43.11 (2010), pp. 2100–2109.
- [101] A. de Kraker, R. van Ostayen, and D. Rixen. "Calculation of Stribeck curves for (water) lubricated journal bearings". In: *Tribology International* 40.3 (2007), pp. 459–469.
- [102] A. Krinner and D. Rixen. "Interface reduction methods for mechanical systems with elasto-hydrodynamic lubricated joints". In: *Proceedings of the 27th ISMA, A Conference on Noise and Vibration Engineering*. KU Leuven, 2016.
- [103] A. Krinner, T. Schindler, and D. Rixen. "Fluid-Struktur-Kopplung in elasto-hydrodynamischen Gleitlagern". In: *11. Internationale Tagung Schwingungen in rotierenden Maschinen (SIRM)*. Magdeburg, Germany, 2015.
- [104] A. Krinner and T. Thümmel. "Non-smooth behaviour of a linkage mechanism with revolute clearance joints". In: *New Advances in Mechanisms, Transmissions and Applications*. Springer, 2014, pp. 233–241.
- [105] A. Krinner, W. Tsunoda, C. Wagner, T. Berninger, T. Thümmel, and D. Rixen. "Simulation and experimental validation of a misaligned rotor in journal bearings using different levels of detail". In: *12. Internationale Tagung Schwingungen in rotierenden Maschinen (SIRM), February 15 – 17*. Graz, Austria, 2017.
- [106] A. Krinner, W. Tsunoda, C. Wagner, T. Berninger, T. Thümmel, and D. Rixen. "Simulation and experimental validation of a misaligned rotor in journal bearings using different levels of detail". In: *Technische Mechanik - Scientific Journal for Fundamentals and Applications of Engineering Mechanics* 37.2-5 (2017), pp. 450–459.
- [107] A. Krinner and D. Rixen. "Load Dependent Interface Reduction Method for Flexible Multibody Systems with Elasto-hydrodynamic Lubricated Joints". In: *The 4th Joint international Conference on Multibody Dynamics, May 29 – June 2*. Montreal, Canada, 2016.
- [108] A. Krinner and D. Rixen. "Interface reduction methods for mechanical systems with elasto-hydrodynamic lubricated revolute joints". In: *Multibody System Dynamics* 42.1 (2017), pp. 79–96.
- [109] A. Krinner, T. Schindler, and D. Rixen. "Projection formulation of the cavitation problem in elasto-hydrodynamic lubrication contact". In: *PAMM* 15.1 (2015), pp. 57–58.
- [110] A. Krinner, T. Schindler, and D. Rixen. "Time integration of mechanical systems using Quasi-Newton method and projection formulations". In: *International Journal for Numerical Methods in Engineering* 110.6 (2017), pp. 523–548.
- [111] A. Kumar and J. Booker. "A finite element cavitation algorithm". In: *Journal of Tribology* 113.2 (1991), pp. 276–284.
- [112] G. LaBouff and J. Booker. "Dynamically loaded journal bearings: a finite element treatment for rigid and elastic surfaces". In: *Journal of tribology* 107.4 (1985), pp. 505–513.

- [113] B. Lamichhane and B. Wohlmuth. "Biorthogonal bases with local support and approximation properties". In: *Mathematics of Computation* 76.257 (2007), pp. 233–249.
- [114] B. Lamichhane, R. Stevenson, and B. Wohlmuth. "Higher order mortar finite element methods in 3D with dual Lagrange multiplier bases". In: *Numerische Mathematik* 102.1 (2005), pp. 93–121.
- [115] J. Lang, G. Knoll, C. Thornthwaite, C. Lensch-Franzen, and M. Kronstedt. "Simulation Methods for Elastohydrodynamically Coupled Hydraulic Components". In: *The 9th International Fluid Power Conference, March 24 – 26*. Aachen, Germany, 2014.
- [116] O. Lang and W. Steinhilper. *Gleitlager: Berechnung und Konstruktion von Gleitlagern mit konstanter und zeitlich veränderlicher Belastung*. Ed. by K. Kollmann. Vol. 31. Konstruktionsbücher. Berlin, Heidelberg: Springer-Verlag, 1978.
- [117] J. Lengiewicz, M. Wichrowski, and S. Stupkiewicz. "Mixed formulation and finite element treatment of the mass-conserving cavitation model". In: *Tribology International* 72 (2014), pp. 143–155.
- [118] P. Lesaint and P.-A. Raviart. "On a finite element method for solving the neutron transport equation". In: *Mathematical aspects of finite elements in partial differential equations* 33 (1974), pp. 89–123.
- [119] T. Lohner, A. Ziegltrum, J.-P. Stemplinger, and K. Stahl. "Engineering software solution for thermal elastohydrodynamic lubrication using multiphysics software". In: *Advances in Tribology 2016* (2016).
- [120] H. Lu, M. Berzins, C. Goodyer, and P. Jimack. "High-order discontinuous Galerkin method for elastohydrodynamic lubrication line contact problems". In: *International Journal for Numerical Methods in Biomedical Engineering* 21.11 (2005), pp. 643–650.
- [121] A. Lubrecht. "The numerical solution of the elastohydrodynamically lubricated line and point contact problem, using multigrid techniques". PhD thesis. Netherlands: University of Twente, 1987.
- [122] D. Maier, C. Hager, H. Hetzler, N. Fillot, P. Vergne, D. Dureisseix, and W. Seemann. "A nonlinear model order reduction approach to the elastohydrodynamic problem". In: *Tribology International* 82 (2015), pp. 484–492.
- [123] D. Maier, C. Hager, H. Hetzler, N. Fillot, P. Vergne, D. Dureisseix, and W. Seemann. "Fast Solution of Transient Elastohydrodynamic Line Contact Problems Using the Trajectory Piecewise Linear Approach". In: *Journal of Tribology* 138.1 (2016), p. 011502.
- [124] J. McIvor and D. Fenner. "Finite element analysis of dynamically loaded flexible journal bearings: a fast Newton-Raphson method". In: *Journal of Tribology* 111.4 (1989), pp. 597–604.
- [125] H. Moes. "Discussion on a Paper by D. Dowson". In: *Proceedings of the Institution of Mechanical Engineering* 180 (1965), pp. 244–245.
- [126] A. Mohrenstein-Ertel. "Die Berechnung der hydrodynamischen Schmierung gekrümmter Oberflächen unter hoher Belastung und Relativbewegung (Calculation of the hydrodynamic lubrication for curved surfaces under high load and relative motion)". In: *VDI Fortschritt-Berichte* 1 (1984). First published in 1945 in Russian under the name A. M. Ertel, p. 189.
- [127] K. Murty. "Note on a Bard-type scheme for solving the complementarity problem". In: *Opsearch* 11.2-3 (1974), pp. 123–130.

- [128] P. G. Nikolakopoulos and C. A. Papadopoulos. "A study of friction in worn misaligned journal bearings under severe hydrodynamic lubrication". In: *Tribology International* 41.6 (2008), pp. 461–472.
- [129] S. Nitzschke, E. Woschke, and C. Daniel. "Dynamisches Verhalten von EHD-Kontakten unter Nutzung eines regularisierten, masseerhaltenden Kavitationsalgorithmus". In: Graz, Austria, 2017.
- [130] S. Nitzschke, E. Woschke, C. Daniel, and J. Strackeljan. "Einfluss der masseerhaltenden Kavitation auf gleitgelagerte Rotoren unter instationärer Belastung". In: Berlin, Germany, 2013.
- [131] P. Novotny and V. Pistek. "New efficient methods for powertrain vibration analysis". In: *Proceedings of the Institution of Mechanical Engineers, Part D: Journal of Automobile Engineering* 224.5 (2010), pp. 611–629.
- [132] G. Nowald, R. Schmoll, and B. Schweizer. "Transient run-up simulations of rotors in journal bearings considering mass-conserving cavitation approaches". In: Graz, Austria, 2017.
- [133] P. Ockier. "Modellierung des Festkörperkontaktdruckes in der Simulation von Gleitlagern". Bachelor Thesis. Munich: Technical University of Munich, Chair of Applied Mechanics, Oct. 11, 2016.
- [134] G. Offner and O. Knaus. "A generic friction model for radial slider bearing simulation considering elastic and plastic deformation". In: *Lubricants* 3.3 (2015), pp. 522–538.
- [135] K. Oh. "The numerical solution of dynamically loaded elastohydrodynamic contact as a nonlinear complementarity problem". In: *Journal of Tribology* 106.1 (1984), pp. 88–95.
- [136] K. Oh and P. Goenka. "The elastohydrodynamic solution of journal bearings under dynamic loading". In: *Journal of Tribology* 107.3 (1985), pp. 389–394.
- [137] K. Oh and K. Huebner. "Solution of the elastohydrodynamic finite journal bearing problem". In: *Journal of Lubrication Technology* 95.3 (1973), pp. 342–351.
- [138] K. Oh and S. Rohde. "Numerical solution of the point contact problem using the finite element method". In: *International Journal for Numerical Methods in Engineering* 11.10 (1977), pp. 1507–1518.
- [139] K.-O. Olsson. *Cavitation in dynamically loaded bearings*. Göteborg: Scandinavian University Books, 1965.
- [140] F. Osterle and E. Saibel. "On the effect of lubricant inertia in hydrodynamic lubrication". In: *Zeitschrift für Angewandte Mathematik und Physik* 6 (1955), p. 334.
- [141] P. Panagiotopoulos. *Inequality Problems in Mechanics and Applications: Convex and nonconvex energy functions*. Boston, Basel, Stuttgart: Birkhäuser, 1985.
- [142] N. Patir and H. Cheng. "An average flow model for determining effects of three-dimensional roughness on partial hydrodynamic lubrication". In: *Journal of Lubrication Technology* 100.1 (1978), pp. 12–17.
- [143] A. Pechstein, D. Reischl, and J. Gerstmayr. "A generalized component mode synthesis approach for flexible multibody systems with a constant mass matrix". In: *Journal of Computational and Nonlinear Dynamics* 8.1 (2013), p. 011019.
- [144] P. Pennacchi, A. Vania, and S. Chatterton. "Analysis of the Effects of Parallel and Angular Misalignment in Hyperstatic Rotors Equipped With Oil-Film Bearings". In: *ASME 2011 Turbo Expo: Turbine Technical Conference and Exposition*. American Society of Mechanical Engineers. 2011, pp. 383–390.

- [145] F. Pfeiffer and C. Glocker. *Multibody dynamics with unilateral contacts*. Vol. 9. New York: John Wiley & Sons, 1996.
- [146] F. Pfeiffer and T. Schindler. *Einführung in die Dynamik*. 3rd ed. Berlin, Heidelberg: Springer-Verlag, 2014.
- [147] O. Pinkus and B. Sternlicht. *Theory of Hydrodynamic Lubrication*. New York: McGraw-Hill, 1961.
- [148] O. Pinkus. *Thermal aspects of fluid film tribology*. New York: American Society of Mechanical Engineers, 1990.
- [149] V. Popov. *Contact mechanics and friction: physical principles and applications*. Berlin, Heidelberg: Springer Science & Business Media, 2010.
- [150] E. Popova and V. Popov. "On the history of elastohydrodynamics: The dramatic destiny of Alexander Mohrenstein-Ertel and his contribution to the theory and practice of lubrication". In: *ZAMM* 7.95 (2015), pp. 652–663.
- [151] A. Popp. "Mortar Methods for Computational Contact Mechanics and General Interface Problems". PhD thesis. Munich: Technical University of Munich, Chair of Numerical Mechanics, 2012.
- [152] A. Popp, M. Gee, and W. Wall. "Mortar methods for single-and multi-field applications in computational mechanics". In: *Sustained Simulation Performance 2012*. Springer, 2013, pp. 133–154.
- [153] A. Popp, M. Gitterle, M. W. Gee, and W. A. Wall. "A dual mortar approach for 3D finite deformation contact with consistent linearization". In: *International Journal for Numerical Methods in Engineering* 83.11 (2010), pp. 1428–1465.
- [154] F. Profito and D. Zachariadis. "Partitioned fluid-structure methods applied to the solution of elastohydrodynamic conformal contacts". In: *Tribology International* 81 (2015), pp. 321–332.
- [155] M. Puso. "A 3D mortar method for solid mechanics". In: *International Journal for Numerical Methods in Engineering* 59.3 (2004), pp. 315–336.
- [156] O. Reynolds. "On the Theory of Lubrication and its Application to Mr. Beauchamp Tower's Experiments including an Experimental Determination of the Viscosity of Olive Oil". In: *Philosophical Transactions of the Royal Society of London* 177 (1886), pp. 157–234.
- [157] A. Rienäcker. *Instationäre Elastohydrodynamik von Gleitlagern mit rauhen Oberflächen und inverse Bestimmung der Warmkonturen*. Universität Kassel, Lehrstuhl für Maschinenelemente und Tribologie, 1995.
- [158] D. Rixen and R. van Ostayen. *Jump of Density in EHD reformation region*. Internal report. Chair of Applied Mechanics, Technical University of Munich, 2017.
- [159] C. Roelands. "Correlational aspects of the viscosity-temperature-pressure relationship of lubricating oils". PhD thesis. netherlands: Delft University of Technology, 1966.
- [160] S. Rohde and K. Oh. "A unified treatment of thick and thin film elastohydrodynamic problems by using higher order element methods". In: *Proceedings of the Royal Society of London A: Mathematical, Physical and Engineering Sciences*. Vol. 343. 1634. The Royal Society. 1975, pp. 315–331.
- [161] M. Ross, M. Sprague, C. Felippa, and K. Park. "Treatment of acoustic fluid-structure interaction by localized Lagrange multipliers and comparison to alternative interface-coupling methods". In: *Computer Methods in Applied Mechanics and Engineering* 198.9 (2009), pp. 986–1005.

- [162] M. Roßner. "Modellbasiertes Monitoring von Rotoren mit mehreren gleichzeitigen Fehlern". PhD thesis. Munich: Technical University of Munich, Chair of Applied Mechanics, 2015.
- [163] L. San Andrés and A. Delgado. "A Novel Bulk-Flow Model for Improved Predictions of Force Coefficients in Grooved Oil Seals Operating Eccentrically". In: *Journal of engineering for gas turbines and power* 134.5 (2012), p. 052509.
- [164] T. Schindler, B. Nguyen, and J. Trinkle. "Understanding the difference between prox and complementarity formulations for simulation of systems with contact". In: *Intelligent Robots and Systems (IROS), 2011 IEEE/RSJ International Conference, San Francisco, California*. IEEE. 2011, pp. 1433–1438.
- [165] J. Schmied, M. Perucchi, and J.-C. Pradetto. "Application of MADYN 2000 to rotordynamic problems of industrial machinery". In: *ASME Turbo Expo 2007: Power for Land, Sea, and Air*. American Society of Mechanical Engineers. 2007, pp. 799–810.
- [166] S. Schoeder, H. Ulbrich, and T. Schindler. "Discussion of the Gear-Gupta-Leimkuhler method for impacting mechanical systems". In: *Multibody System Dynamics* 31.4 (2014), pp. 477–495.
- [167] R. Schönen. *Strukturdynamische Mehrkörpersimulation des Verbrennungsmotors mit elasto-hydrodynamischer Grundlagerkopplung*. PhD thesis. Kassel University Press, 2001.
- [168] M. Schouten and H. Van Leeuwen. "Die Elastohydrodynamik: Geschichte und Neuentwicklungen". In: *VDI Bericht 1207* (1995), pp. 1–47.
- [169] B. Schweizer. "Dynamics and stability of turbocharger rotors". In: *Archive of Applied Mechanics* 80.9 (2010), pp. 1017–1043.
- [170] R. Schwertassek and O. Wallrapp. *Dynamik flexibler Mehrkörpersysteme*. in german. Braunschweig: Vieweg, 1999.
- [171] R. Schwertassek, O. Wallrapp, and A. Shabana. "Flexible multibody simulation and choice of shape functions". In: *Nonlinear Dynamics* 20.4 (1999), pp. 361–380.
- [172] A. Shabana. *Dynamics of multibody systems*. 3rd ed. Cambridge, UK: Cambridge University Press, 2005.
- [173] B. Simeon. *Computational Flexible Multibody Dynamics. A Differential-Algebraic Approach*. Heidelberg, 2013.
- [174] T. Someya. *Journal-Bearing Databook*. Berlin, Heidelberg: Springer-Verlag, 1989.
- [175] T. Someya. *Schwingungs- und Stabilitätsverhalten einer in zylindrischen Gleitlagern laufenden Welle mit Unwucht: mit 7 Tafeln*. VDI-Verlag, 1965.
- [176] A. Sommerfeld. "Zur hydrodynamischen Theorie der Schmiermittelreibung". In: *Zeitschrift für Mathematik und Physik* 50 (1904), pp. 97–155.
- [177] H. Spikes. "Sixty years of EHL". In: *Lubrication Science* 18.4 (2006), pp. 265–291.
- [178] A. Stafford, R. Henshell, and B. Dudley. "Finite element analysis of problems in elasto-hydrodynamic lubrication". In: *Proc. 5th Leeds-Lyon Symposium on Tribology*. 1978, pp. 35–41.
- [179] W. Stieber. *Des Schwimmlager: hydrodynamische Theorie des Gleitlagers*. Düsseldorf: VDI-Verlag GmbH, 1933.
- [180] R. Stribeck and M. Schröter. *Die wesentlichen Eigenschaften der Gleit- und Rollenlager: Untersuchung einer Tandem-Verbundmaschine von 1000 PS*. Springer, 1903.

- [181] D. Sun and D. Brewe. "A high speed photography study of cavitation in a dynamically loaded journal bearing". In: *Journal of tribology* 113.2 (1991), pp. 287–292.
- [182] J. Sun and G. Changlin. "Hydrodynamic lubrication analysis of journal bearing considering misalignment caused by shaft deformation". In: *Tribology International* 37.10 (2004), pp. 841–848.
- [183] H. Swift. "The stability of lubricating films in journal bearings". In: 233.1932 (1932), pp. 267–288.
- [184] A. Szeri. *Fluid film lubrication*. 2nd ed. New York: Cambridge University Press, 2011.
- [185] T. Tamarozzi, G. Heirman, and W. Desmet. "An on-line time dependent parametric model order reduction scheme with focus on dynamic stress recovery". In: *Computer Methods in Applied Mechanics and Engineering* 268 (2014), pp. 336–358.
- [186] C. Taylor and J. o'Callaghan. "A numerical solution of the elastohydrodynamic lubrication problem using finite elements". In: *Journal of Mechanical Engineering Science* 14.4 (1972), pp. 229–237.
- [187] T. Thümmel. *Experimentielle Mechanismendynamik - Messung, Modellierung, Simulation, Verifikation, Interpretation und Beeinflussung typischer Schwingungsphänomene an einem Mechanismenprüfstand*. VDI-Forschungsberichte Reihe 11: Schwingungstechnik, Nr. 345. Habilitationsschrift an der TU München, Fakultät für Maschinenwesen. Düsseldorf: VDI-Verlag, 2012.
- [188] T. Thümmel, M. Roßner, H. Ulbrich, and D. Rixen. "Unterscheidung verschiedener Fehlerarten beim modellbasierten Monitoring". In: Magdeburg, Germany, 2015.
- [189] Q. Tian, Y. Sun, C. Liu, H. Hu, and P. Flores. "Elastohydrodynamic lubricated cylindrical joints for rigid-flexible multibody dynamics". In: *Computers & Structures* 114 (2013), pp. 106–120.
- [190] J. Tichy and B. Bou-Said. "Hydrodynamic lubrication and bearing behavior with impulsive loads". In: *Tribology transactions* 34.4 (1991), pp. 505–512.
- [191] B. Tower. "First report on friction experiments". In: *Proceedings of the institution of mechanical engineers* 34.1 (1883), pp. 632–659.
- [192] C. Venner. "Multilevel methods for the EHD line and point contact problems". PhD thesis. Netherlands: University of Twente, 1991.
- [193] D. Vijayaraghavan and T. Keith Jr. "Development and evaluation of a cavitation algorithm". In: *Tribology Transactions* 32.2 (1989), pp. 225–233.
- [194] G. Vogelpohl. *Beiträge zur Kenntnis der Gleitlagerreibung*. Vol. 386. VDI-Forschungsheft. Beilage zur "Forschung auf dem Gebiete des Ingenieurwesens" Ausg. B. VDI-Verlag, 1937.
- [195] C. Wagner, W. Tsunoda, T. Berninger, T. Thümmel, and D. Rixen. "Instability Prediction and Rotordynamic with Seals: Simulations Based on the Bulk-Flow Theory and Experimental Measurements". In: *Proc. of DINAME 2017*. Sao Sebastiao, Sao Paulo, Brasil, 2017.
- [196] C. Wagner, A. Krinner, T. Thümmel, and D. Rixen. "Full Dynamic Ball Bearing Model with Elastic Outer Ring for High Speed Applications". In: *Lubricants* 5.2 (2017), p. 17.
- [197] O. Wallrapp. "Standardization of Flexible Body Modeling in Multibody System Codes, Part I: Definition of Standard Input Data\*". In: *Journal of Structural Mechanics* 22.3 (1994), pp. 283–304.

- [198] T. Wasfy and A. Noor. "Computational strategies for flexible multibody systems". In: *Applied Mechanics Reviews* 56.6 (2003), pp. 553–613.
- [199] Y. Wijnant. "Contact dynamics in the field of elastohydrodynamic lubrication". PhD thesis. Netherlands: University of Twente, 1998.
- [200] K. Wilhelm. *Strukturdynamische Analyse von Kurbelwelle und Motorblock mit elastohydrodynamischen Wechselwirkungen*. Kassel University Press, 1998.
- [201] B. Wohlmuth. "A mortar finite element method using dual spaces for the Lagrange multiplier". In: *SIAM journal on numerical analysis* 38.3 (2000), pp. 989–1012.
- [202] B. Wohlmuth. "Variationally consistent discretization schemes and numerical algorithms for contact problems". In: *Acta Numerica* 20 (2011), pp. 569–734.
- [203] B. Wohlmuth, A. Popp, M. Gee, and W. Wall. "An abstract framework for a priori estimates for contact problems in 3D with quadratic finite elements". In: *Computational Mechanics* 49.6 (2012), pp. 735–747.
- [204] T. Woloszynski, P. Podsiadlo, and G. Stachowiak. "Efficient Solution to the Cavitation Problem in Hydrodynamic Lubrication". In: *Tribology Letters* 58.1 (2015), pp. 1–11.
- [205] E. Woschke, S. Göbel, S. Nitzschke, C. Daniel, and J. Strackeljan. "Influence of bearing geometry of automotive turbochargers on the nonlinear vibrations during run-up". In: *Proceedings of the 9th IFToMM International Conference on Rotor Dynamics*. Springer. 2015, pp. 835–844.
- [206] P. Wriggers. *Computational contact mechanics*. Chichester, UK: John Wiley & Sons, 2002.
- [207] C. Wu and L. Zheng. "An average Reynolds equation for partial film lubrication with a contact factor". In: *Journal of tribology* 111.1 (1989), pp. 188–191.
- [208] S. Wu and J. Oden. "Convergence and error estimates for finite element solutions of elastohydrodynamic lubrication". In: *Computers & Mathematics with Applications* 13.7 (1987), pp. 583–593.
- [209] B. Yang and T. Laursen. "A mortar-finite element approach to lubricated contact problems". In: *Computer Methods in Applied Mechanics and Engineering* 198.47 (2009), pp. 3656–3669.
- [210] Q. Yu and T. Keith Jr. "A boundary element cavitation algorithm". In: *Tribology transactions* 37.2 (1994), pp. 217–226.
- [211] R. Zander, T. Schindler, M. Friedrich, R. Huber, M. Förg, and H. Ulbrich. "Non-smooth dynamics in academia and industry: recent work at TU München". In: *Acta Mechanica* 195.1-4 (2008), pp. 167–183.
- [212] O. Zienkiewicz, R. Tylor, and P. Nithiarasu. *The finite element method for fluid dynamics*. 7th ed. Elsevier, 2009.